UNIVERSITY OF BIRMINGHAM

Exploring Disassembly Challenges: Jamming, Compliance Effects, and Reinforcement Learning in Complex Peg-Holes Processes

By:

Farzaneh Goli

A thesis submitted to the University of Birmingham for the degree of

DOCTOR OF PHILOSOPHY

Department of Mechanical Engineering

School of Engineering

The University of Birmingham

December 2024

UNIVERSITY OF BIRMINGHAM

The University of Birmingham Research Archive

e-theses repository

This thesis is dedicated to

‘HOPE’

“We must accept finite disappointment, but never lose infinite hope.”

Martin Luther King, Jr.

‘Your work is going to fill a large part of your life, and the only way to be truly satisfied is to do what you believe is great work. And the only way to do great work is to love what you do. If you haven’t found it yet, keep looking. Don’t settle.’ Steve Jobs.

Abstract

Disassembly is a prime activity in the remanufacturing chain, promoting recoveries for reuse, hence contributing to sustainable manufacturing. However, being largely a manual and labour-intensive operation, disassembly has poor economic viability. In this thesis, we have focused on investigating and developing robotic disassembly techniques, with special consideration of issues related to dual peg-hole and rectangular peg-hole structures. By incorporating mechanics-based analyses, compliance strategies, and artificial intelligence, this work offers possible solutions for increasing the efficiency, adaptability, and reliability of automated disassembly systems.

Chapter two first explores dual peg-hole disassembly, a typical yet sophisticated operation in remanufacturing. During the extraction process of the peg, the identification of contact states and their geometric conditions are systematically identified to explore the jamming phenomenon, which often disturbs this process. The boundary conditions of jamming are derived based on geometrical and quasistatic analyses, and active compliance strategies are analysed as a solution. Simulation results are presented to investigate the effects of some critical variables such as the amount of compliance, the location of the centre of compliance, and initial position errors. Experimental investigations confirm these results and illustrate how appropriate compliance configurations can reduce the effects of jamming and optimise disassembly.

In the third chapter, rectangular peg-hole structures in three dimensions are examined. The present study finds 26 possible contact states, of which 16 conditions are related to jamming conditions. States are classified according to surface-surface contact interactions with comprehensive interpretations of jamming mechanics. Results indicate that locating the compliance centre at the end of the peg is particularly effective in minimising the risk of jamming and produces a 77.1% reduction in maximum extraction force compared to the less

optimised configurations. This therefore highlights the role of compliance strategies in enabling strong and efficient robotic disassembly.

Chapter four will discuss how reinforcement learning was integrated with compliance strategies to overcome the challenges of disassembling complex peg-hole structures. Reinforcement learning enables the robot to adaptively learn disassembly motions through recurrent training and feedback from environmental sensing, such as force and torque measurements. The proposed Reinforcement learning (RL)--based compliance approach reduces extraction forces by 29.6% compared to manual methods, showcasing the benefits of combining machine learning with mechanical insights. Experimental results confirm that the system dynamically optimises disassembly motions with considerations of material compliance and geometric constraints, reaching a new level of efficiency and adaptability.

In general, this thesis will contribute to the development of intelligent robotic systems for disassembly by incorporating compliance strategies with Artificial intelligence (AI). The research study, through theoretical analysis, computational simulations, and experimental validation, demonstrates how compliance strategy can be employed with AI-driven methods to increase the adaptability and efficiency of robotic disassembly processes, with particular emphasis on reinforcement learning. The compliance strategy used in an innovative way further optimises force control and enhances the system's capability to handle complicated disassembly tasks. These findings provide valuable insights into the potential for automation in remanufacturing and recycling and contribute to more sustainable and economically viable production systems.

Declaration

I hereby declare that except where specific reference is made to the work of others, the contents of this dissertation are original and have not been submitted in whole or in part for consideration for any other degree or qualification in this, or any other university. This dissertation is my own work and contains nothing that is the outcome of work done in collaboration with others, except as specified in the text and acknowledgements.

Some parts of this work have been reproduced from the author's publications along with necessary references where applicable.

This dissertation contains a maximum of 28583 words, including appendices, a bibliography, footnotes, tables, and equations, 83 figures, and 6 tables.

Farzaneh Goli

December 2024

Acknowledgements

I am profoundly grateful to my supervisors, Dr. Yongjing Wang and Dr. Mozafar Saadat for their unwavering guidance, invaluable insights, and constant encouragement throughout the journey of this thesis. Your expertise, patience, and dedication have been instrumental in shaping the direction and quality of this work. Your feedback and constructive criticism have pushed me to reach new heights, and I am truly fortunate to have had the opportunity to learn under your supervision.

My sincere thanks go to Prof. Duc Pham, Dr Mo Qu, Dr Ali Aflakian, and Mr Yue Zang. Also, I would like to thank Dr Yongquan Zhang from the Wuhan University of Technology for his valuable advice and assistance.

Lastly, I wish to express my sincere thanks to my parents and brother for their unconditional love, endless support, and belief in my abilities, without whom none of this would have been possible. Your encouragement has been the driving force behind my aspirations, and I really appreciate you making sacrifices to help me succeed.

I am indebted to my friends and colleagues who provided valuable insights and encouragement during this endeavour. Your discussions, brainstorming sessions, and cooperation have added depth and dimension to my work.

Table of Contents

ABSTRACT IV
ACKNOWLEDGEMENTS VII
TABLE OF CONTENTS VIII
LIST OF FIGURES XI
LIST OF TABLES XX
NOMENCLATURE XXI
CHAPTER 1. GENERAL INTRODUCTION 1
1.1 Introduction 2
1.1.1 Background 2
1.1.2 Remanufacturing and Disassembly 3
1.1.3 Challenges in peg-hole disassembly 4
1.2 Jamming Problems and Effect Compliance Strategy in Peg-Hole Disassembly 5
1.3 Characterising the Mechanics of Dual and Rectangle Peg-Hole Disassembly 7
1.4 Integrating Reinforcement Learning with Mechanical Analysis and Compliance Strategy Contributions 9
1.5 Research Aim and Objective 10
1.5.1 Contributions 11
1.5.2 Publication of this thesis 14
1.6 Thesis Structure 15
1.7 References 17
CHAPTER 2. JAMMING PROBLEMS AND THE EFFECTS OF COMPLIANCE IN DUAL PEG-HOLE DISASSEMBLY 21
2.1 Introduction 24
2.2 Analysis of multiple peg extraction during disassembly 26
2.3 Geometric analysis of dual-peg extraction 27
2.3.1 Extractability 27
2.3.2 Prediction of possible contact states 29
2.4 Force analysis of dual-peg extraction 32
2.4.1 Derivation of force-moment conditions for maintaining contact states 33
2.4.2 Key factors and their effects 47

2.5 Experiment 55
2.5.1 Experimental Design 56
2.5.2 Experimental Results 57
2.6 Conclusion 57
2.7 References 60
2.8 Appendix 62
CHAPTER 3. CHARACTERISING THE MECHANICS OF RECTANGLE PEG-HOLE DISASSEMBLY AND THE EFFECT OF ACTIVE COMPLIANCE CENTRE POSITION ON EXTRACTION FORCE 65
3.1 Introduction 68
3.2 Methodology 72
3.2.1 Geometric analysis 73
3.2.2 Force analysis of Rectangle peg extraction 77
3.3 Results and Discussion 101
3.3.1 Region of extraction depth 102
3.3.2 Key Factors 102
3.4 Experiment 121
3.4.1 Experimental Design 121
3.4.2 Experimental Result 122
3.5 Conclusion 124
3.6 References 126
CHAPTER 4. DISASSEMBLY OF RECTANGLE PEG-HOLE STRUCTURES THROUGH COMPLIANCE STRATEGY AND REINFORCEMENT LEARNING 128
4.1 Introduction 130
4.2 Methodology 133
4.2.1 Peg-Hole disassembly task 133
4.2.2 Robotic disassembly simulation setup 134
4.2.3 Robotic Compliance and Adaptability 135
4.2.4 Reinforcement learning algorithm with compliance strategy 137
4.2.5 Training Parameters 138
4.2.6 Reward System and Analysis 139
4.2.7 Simulation Result 140
4.3 Experimental and Result 144
4.3.1 Experimental Setup 145
4.3.2 Experimental Result 146
4.4 Conclusion 149
4.5 References 150

CHAPTER 5. GENERAL DISCUSSION 153
5.1 Discussion 153
5.2 Conclusion 164
5.3 Future Work 164
5.4 References 165

List of Figures

Figure 1.1 Example of Remanufacturing Process.....3

Figure 1.2 Graphic Overview of Disassembly with Active Compliance Strategy and Reinforcement Learning.....13

Figure 1.3 Overview of Thesis Structure.....16

Figure 2.1. The geometric model of a dual peg-hole.....29

Figure 2.2. Maximum left- and right-side travel cases.....30

Figure 2.3. Typical states of the dual peg-hole disassembly process: (a) no contact, (b) one-point contact, (c) two-point contact, and (d) line contact.....31

Figure 2.4. Three-point contact state of dual peg-in-hole 32

Figure 2.5. Classification of two-point contact states in dual peg-hole disassembly.....33

Figure 2.6. a) Dimensions and reference frame for dual peg-hole, b) Definition of the initial position in the dual peg-hole 34

Figure 2.7. Geometry and forces during the two-point contact in one of the dual peg-holes ..35

Figure 2.8. Geometry and forces during the two-point contact in the external surfaces of pegs contact holes surfaces 39

Figure 2.9. Geometry and forces during two-point contact in the inner surfaces of pegs contact holes surfaces.....43

Figure 2.10. Jamming diagrams for the dual-peg extraction problem based on contact forces[23].....48

Figure 2.11. Dependence of the two-point contact region on the location of the compliance centre with $\delta 0 =$ 2 mm, $\beta 0 = 0$ rad, $KX = 0.4$ N mm^{-1}, $K\theta = 30*10^4$ Nmm rad^{-1}. a) Contact

in one of the dual peg-holes, b) External surfaces of pegs contact holes surfaces, c) Inner surfaces of pegs contact holes surfaces 49

Figure 2.12 The effect of the initial lateral error on the two-point contact region in one of the dual peg-holes: (a) $LC = 0$, $b\ LC = 25$, $c\ LC = 50\ with\ \beta 0 = 0$ rad, $KX = 0.4$ N mm^{-1}, $K\theta = 30*10^4$ Nmm rad^{-1}. 51

Figure 2.13. The effect of initial lateral error on the two-point contact region in the contact of the inner surfaces of the pegs with the holes: (a) $LC = 0$, $b\ LC = 25$, $c\ LC = 50\ with\ \beta 0 = 0$ rad,$KX = 0.4$ N mm^{-1}, $K\theta = 30*10^4$ Nmm rad^{-1}. 51

Figure 2.14. The effect of initial lateral error on the two-point contact region in the contact of the external surfaces of the pegs with the holes: (a) $LC = 0$, $b\ LC = 25$, $c\ LC = 50\ with\ \beta 0 = 0$ rad, $KX = 0.4$ N mm^{-1}, $K\theta = 30*10^4$ Nmm rad^{-1}. 52

Figure 2.15. Dependence of the two-point contact region on the initial angular error: with $LC = 50$ mm, $\delta 0 = 1$ mm, rad, $KX = 0.4$ N mm^{-1}, $K\theta = 30*10^4$ Nmm rad^{-1}.. a) Contact in one of the dual peg-holes, b) External surfaces of pegs contact holes surfaces, c) Inner surfaces of pegs contact holes surfaces 53

Figure 2.16. The effect of the two-point contact region in one of the dual peg-holes on the structural parameters: (a) $Kx = 0.2$ N mm^{-1}, $K\theta = 30*10^4$ Nmm rad^{-1}; (b) $Kx = 0.6$ N mm^{-1}, $K\theta = 30*10^4$ Nmm rad^{-1}; (c) $Kx = 0.4$ N mm^{-1}, $K\theta = 15*10^4$ Nmm rad^{-1}; (d) $Kx = 0.4$ N mm^{-1}, $K\theta = 45*10^4$ Nmm rad^{-1} with $\delta 0 = 2$ mm, $\beta 0 = 0$ rad. 54

Figure 2.17. The effect of the two-point contact region in the contact of the inner surfaces of the pegs with the holes on the structural parameters: (a) $Kx = 0.2$ N mm^{-1}, $K\theta = 30*10^4$ Nmm rad^{-1}; (b) $Kx = 0.6$ N mm^{-1}, $K\theta = 30*10^4$ Nmm rad^{-1}; (c) $Kx = 0.4$ N mm^{-1}, $K\theta = 15*10^4$ Nmm rad^{-1}; (d) $Kx = 0.4$ N mm^{-1}, $K\theta = 45*10^4$ Nmm rad^{-1} with $\delta 0 = 2$ mm, $\beta 0 = 0$ rad. ..54

Figure 2.18. The effect of the two-point contact region in the contact of the external surfaces of the pegs with the holes on the structural parameters: (a) Kx =0.2 N mm^{-1}, $K\theta$ = 30*10^4 Nmm rad^{-1}; (b) Kx =0.6 N mm^{-1}, $K\theta$ = 30*10^4 Nmm rad^{-1}; (c) Kx =0.4 N mm^{-1}, $K\theta$ = 15*10^4 Nmm rad^{-1}; (d) Kx =0.4 N mm^{-1}, $K\theta$ = 45*10^4 Nmm rad^{-1} with $\delta 0$ = 2 mm, $\beta 0$ = 0 rad. ..55

Figure 2.19. The experimental equipment 56

Figure 2.20. Extraction force curves based on compliance centre locations. a) r= 5.7 mm, b) r= 6 mm, and c) r=6.5 mm 59

Figure 3.1. Investigate the impact of Active Compliance Centre (ACC) positions on 16 jamming conditions among 26 possible contact situations both in simulation and experiments. 72

Figure 3.2. The geometric model of a rectangle peg-hole 74

Figure 3.3. Maximum left/right- and down/up-side travel cases 75

Figure 3.4. Typical jamming states of the rectangle peg-hole disassembly process: (a) two-point contact, (b) two-side contact, (c) combined two-side and one-plane contact, (d) two-edge contact, and (e) three-edge contact. 76

Figure 3.5. Dimensions and reference frame for rectangle peg-hole 78

Figure 3.6. Definition of initial errors and position in rectangle peg-hole 79

Figure 3.7. Geometry and forces during the two-point contact in the rectangle peg-hole. 81

Figure 3.8. Geometry and forces during the two-side contact in the rectangle peg-hole 85

Figure 3.9. Geometry and forces during the Two-side and one-plane contact in the rectangle peg-hole 90

Figure 3.10. Geometry and forces during the Two-edge contact in the rectangle peg-hole. ..95

Figure 3.11. Geometry and forces during the Three-edge contact in the rectangle peg-hole. 99

Figure 3.12. Dependence of the two-point contact region on the location of the compliance centre with KX, KY =0.3 N mm^{-1}, $K\theta, K\Phi, K\psi$ = 30*10^4 Nmm rad^{-1}. a) two-point contact, b) two-side contact, c) combined two-side and one-plane contact 104

Figure 3.13. The effect of initial lateral error δX on the two-contact region in the two-point contact with KX, KY =0.3 N mm^{-1}, $K\theta, K\Phi, K\psi$ = 30*10^4 Nmm rad^{-1}, and a) $LC = 0$, $b\ LC = 75$, $c\ LC = 150$..... 105

Figure 3.14. The effect of initial lateral error δX on the two-contact region in the two-side contact with KX, KY =0.3 N mm^{-1}, $K\theta, K\Phi, K\psi$ = 30*10^4 Nmm rad^{-1}, and a) $LC = 0$, $b\ LC = 75$, $c\ LC = 150$..... 106

Figure 3.15. The effect of initial lateral error δX on the two-contact region in the combined two-side and one-plane contact with KX, KY =0.3 N mm^{-1}, $K\theta, K\Phi, K\psi$ = 30*10^4 Nmm rad^{-1}, and a) $LC = 0$, $b\ LC = 75$, $c\ LC = 150$..... 106

Figure 3.16. The effect of initial lateral error δY on the two-contact region in the two-point contact with KX, KY =0.3 N mm^{-1}, $K\theta, K\Phi, K\psi$ = 30*10^4 Nmm rad^{-1}, and a) $LC = 0$, $b\ LC = 75$, $c\ LC = 150$..... 107

Figure 3.17. The effect of initial lateral error δY on the two-contact region in the two-side contact with KX, KY =0.3 N mm^{-1}, $K\theta, K\Phi, K\psi$ = 30*10^4 Nmm rad^{-1}, and a) $LC = 0$, $b\ LC = 75$, $c\ LC = 150$..... 107

Figure 3.18. The effect of initial lateral error δY on the two-contact region in the combined two-side and one-plane contact with KX, KY =0.3 N mm^{-1}, $K\theta, K\Phi, K\psi$ = 30*10^4 Nmm rad^{-1}, and a) $LC = 0$, $b\ LC = 75$, $c\ LC = 150$. 108

Figure 3.19. The effect of initial angular error $\delta\theta$ on the two-contact region in the two-point contact with KX, KY = 0.3 N mm^{-1}, $K\theta, K\Phi, K\psi$ = 30*10^4 Nmm rad^{-1}, and a) $LC = 0$, $b\ LC = 75$, $c\ LC = 150$..... 108

Figure 3.20. The effect of initial angular error $\delta\theta$ on the two-contact region in the two-side contact with KX, KY =0.3 N mm^{-1}, $K\theta, K\Phi, K\psi = 30*10^4$ Nmm rad^{-1}, and 1) $LC = 0$, 2 $LC = 75$, 3 $LC = 150$. 109

Figure 3.21. The effect of initial angular error $\delta\theta$ on the two-contact region in the combined two-side and one-plane contact with KX, KY =0.3 N mm^{-1}, $K\theta, K\Phi, K\psi = 30*10^4$ Nmm rad^{-1}, and a) $LC = 0$, b $LC = 75$, c $LC = 150$.....109

Figure 3.22. The effect of initial angular error $\delta\Phi$ on the two-contact region in the two-point contact with KX, KY =0.3 N mm^{-1}, $K\theta, K\Phi, K\psi = 30*10^4$ Nmm rad^{-1}, and a) $LC = 0$, b $LC = 75$, c $LC = 150$.....110

Figure 3.23. The effect of initial angular error $\delta\Phi$ on the two-contact region in the two-side contact with KX, KY =0.3 N mm^{-1}, $K\theta, K\Phi, K\psi = 30*10^4$ Nmm rad^{-1}, and 1) $LC = 0$, 2 $LC = 75$, 3 $LC = 150$. 110

Figure 3.24. The effect of initial angular error $\delta\Phi$ on the two-contact region in the combined two-side and one-plane contact with KX, KY =0.3 N mm^{-1}, $K\theta, K\Phi, K\psi = 30*10^4$ Nmm rad^{-1}, and a) $LC = 0$, b $LC = 75$, c $LC = 150$.....111

Figure 3.25. The effect of initial angular error $\delta\psi$ on the two-contact region in the two-point contact with KX, KY =0.3 N mm^{-1}, $K\theta, K\Phi, K\psi = 30*10^4$ Nmm rad^{-1}, and a)$LC = 0\ mm$, b $LC = 75\ mm$, c $LC = 150\ mm$. 111

Figure 3.26. The effect of initial angular error $\delta\psi$ on the two-contact region in the two-side contact with KX, KY =0.3 N mm^{-1}, $K\theta, K\Phi, K\psi = 30*10^4$ Nmm rad^{-1}, and 1) $LC = 0\ mm$, 2 $LC = 75\ mm$, 3 $LC = 150\ mm$.....112

Figure 3.27. The effect of initial angular error $\delta\psi$ on the two-contact region in the combined two-side and one-plane contact with KX, KY =0.3 N mm^{-1}, $K\theta, K\Phi, K\psi = 30*10^4$ Nmm rad^{-1}, and a) $LC = 0\ mm$, b $LC = 75\ mm$, c $LC = 150\ mm$.....112

Figure 3.28. The effect of the two-contact region the two-point contact on the structural parameters: (a) KX =0.2 N mm^{-1}; (b) KX =0.3 N mm^{-1}; (c) KX =0.4 N mm^{-1}; (d) KX =0.6 N mm^{-1} with $KY = 0.3\ N\ mm - 1, K\theta, K\Phi, K\psi =$ 30*10^4 Nmm rad^{-1} $\delta X, \delta Y = 2$ mm ,$\delta\theta, \delta\Phi, \delta\psi = 0$ rad. 113

Figure 3.29. The effect of the two-contact region the two-side contact on the structural parameters: (a) KX =0.2 N mm^{-1}; (b) KX =0.3 N mm^{-1}; (c) KX =0.4 N mm^{-1}; (d) KX =0.6 N mm^{-1} with $KY = 0.3\ N\ mm - 1, K\theta, K\Phi, K\psi =$ 30*10^4 Nmm rad^{-1} $\delta X, \delta Y = 2$ mm ,$\delta\theta, \delta\Phi, \delta\psi = 0$ rad. 114

Figure 3.30. The effect of the two-contact region the combined two-side and one-plane contact on the structural parameters: (a) KX =0.2 N mm^{-1}; (b) KX =0.3 N mm^{-1}; (c) KX =0.4 N mm^{-1}; (d) KX =0.6 N mm^{-1} with $KY = 0.3\ N\ mm - 1, K\theta, K\Phi, K\psi =$ 30*10^4 Nmm rad^{-1} $\delta X, \delta Y =$ 2 mm ,$\delta\theta, \delta\Phi, \delta\psi = 0$ rad. 114

Figure 3.31. The effect of the two-contact region the two-point contact on the structural parameters: (a) KY =0.2 N mm^{-1}; (b) KY =0.3 N mm^{-1}; (c) KY =0.4 N mm^{-1}; (d) KY =0.6 N mm^{-1} with $KX = 0.3$ N mm^{-1}, $K\theta, K\Phi, K\psi =$ 30*10^4 Nmm rad^{-1} $\delta X, \delta Y = 2$ mm,$\delta\theta, \delta\Phi, \delta\psi = 0$ rad. 115

Figure 3.32. The effect of the two-contact region the two-side contact on the structural parameters: (a) KY =0.2 N mm^{-1}; (b) KY =0.3 N mm^{-1}; (c) KY =0.4 N mm^{-1}; (d) KY =0.6 N mm^{-1} with $KX = 0.3$ N mm^{-1}, $K\theta, K\Phi, K\psi =$ 30*10^4 Nmm rad^{-1} $\delta X, \delta Y = 2$ mm,$\delta\theta, \delta\Phi, \delta\psi = 0$ 115

Figure 3.33. The effect of the two-contact region of the combined two-side and one-plane contact on the structural parameters: (a) KY =0.2 N mm^{-1}; (b) KY =0.3 N mm^{-1}; (c) KY =0.4 N mm^{-1}; (d) KY =0.6 N mm^{-1} with $KX = 0.3$ N mm^{-1}, $K\theta, K\Phi, K\psi =$ 30*10^4 Nmm rad^{-1} $\delta X, \delta Y =$ 2 mm,$\delta\theta, \delta\Phi, \delta\psi = 0$ 116

Figure 3.34. The effect of the two-contact region two-point contact on the structural parameters: (a) $K\theta$ =15*10^4 Nmm rad^{-1} ; (b) $K\theta$ =30*10^4 Nmm rad^{-1} ; (c) $K\theta$ =45*10^4 Nmm rad^{-1} with $KX, KY = 0.3\ N\ mm - 1$, $K\Phi, K\psi$ = 30*10^4 Nmm rad^{-1} $\delta X, \delta Y =$ 2 mm,$\delta\theta, \delta\Phi, \delta\psi =$ 0 rad. 116

Figure 3.35. The effect of the two-contact region the two-side contact on the structural parameters: (a) $K\theta$ =15*10^4 Nmm rad^{-1} ; (b) $K\theta$ =30*10^4 Nmm rad^{-1} ; (c) $K\theta$ =45*10^4 Nmm rad^{-1} with $KX, KY = 0.3\ N\ mm - 1$, $K\Phi, K\psi =$ 30*10^4 Nmm rad^{-1} $\delta X, \delta Y =$ 2 mm,$\delta\theta, \delta\Phi, \delta\psi =$ 0 rad. 117

Figure 3.36. The effect of the two-contact region the combined two-side and one-plane contact on the structural parameters(a) $K\theta$ =15*10^4 Nmm rad^{-1} ; (b) $K\theta$ =30*10^4 Nmm rad^{-1} ; (c) $K\theta$ =45*10^4 Nmm rad^{-1} with $KX, KY = 0.3\ N\ mm - 1$, $K\Phi, K\psi =$ 30*10^4 Nmm rad^{-1} $\delta X, \delta Y =$ 2 mm,$\delta\theta, \delta\Phi, \delta\psi =$ 0 rad. 117

Figure 3.37. The effect of the two-contact region the two-point contact on the structural parameters: (a) $K\Phi$ =15*10^4 Nmm rad^{-1} ; (b) $K\Phi$ =30*10^4 Nmm rad^{-1} ; (c) $K\Phi$ =45*10^4 Nmm rad^{-1} with $KX, KY = 0.3\ N\ mm - 1$, $K\theta, K\psi =$ 30*10^4 Nmm rad^{-1} $\delta X, \delta Y =$ 2 mm,$\delta\theta, \delta\Phi, \delta\psi =$ 0 rad. 118

Figure 3.38. The effect of the two-contact region the two-side contact on the structural parameters: (a) $K\Phi$ =15*10^4 Nmm rad^{-1} ; (b) $K\Phi$ =30*10^4 Nmm rad^{-1} ; (c) $K\Phi$ =45*10^4 Nmm rad^{-1} with $KX, KY = 0.3\ N\ mm - 1$, $K\theta, K\psi =$ 30*10^4 Nmm rad^{-1} $\delta X, \delta Y =$ 2 mm,$\delta\theta, \delta\Phi, \delta\psi =$ 0 rad. 118

Figure 3.39. The effect of the two-contact region the combined two-side and one-plane contact on the structural parameters: (a) $K\Phi$ =15*10^4 Nmm rad^{-1} ; (b) $K\Phi$ =30*10^4 Nmm rad^{-1} ; (c) $K\Phi$ =45*10^4 Nmm rad^{-1} with $KX, KY = 0.3\ N\ mm - 1$, $K\theta, K\psi =$ 30*10^4 Nmm rad^{-1} $\delta X, \delta Y =$ 2 mm,$\delta\theta, \delta\Phi, \delta\psi =$ 0 rad. 119

Figure 3.40. The effect of the two-contact region the two-point contact on the structural parameters: (a) $K\psi$ =15*10^4 Nmm rad^{-1} ; (b) $K\psi$ =30*10^4 Nmm rad^{-1} ; (c) $K\psi$ =45*10^4 Nmm rad^{-1} with $KX, KY = 0.3\ N\ mm - 1$, $K\theta, K\Phi =$ 30*10^4 Nmm rad^{-1} $\delta X, \delta Y =$ 2 mm,$\delta\theta, \delta\Phi, \delta\psi = 0$ rad. 119

Figure 3.41. The effect of the two-contact region the two-side contact on the structural parameters: (a) $K\psi$ =15*10^4 Nmm rad^{-1} ; (b) $K\psi$ =30*10^4 Nmm rad^{-1} ; (c) $K\psi$ =45*10^4 Nmm rad^{-1} with $KX, KY = 0.3\ N\ mm - 1$, $K\theta, K\Phi =$ 30*10^4 Nmm rad^{-1} $\delta X, \delta Y =$ 2 mm,$\delta\theta, \delta\Phi, \delta\psi = 0$ rad. 120

Figure 3.42. The effect of the two-contact region the combined two-side and one-plane contact on the structural parameters: (a) $K\psi$ =15*10^4 Nmm rad^{-1} ; (b) $K\psi$ =30*10^4 Nmm rad^{-1} ; (c) $K\psi$ =45*10^4 Nmm rad^{-1} with $KX, KY = 0.3\ N\ mm - 1$, $K\theta, K\Phi =$ 30*10^4 Nmm rad^{-1} $\delta X, \delta Y =$ 2 mm,$\delta\theta, \delta\Phi, \delta\psi = 0$ rad. 120

Figure 3.43. The experimental setup. 122

*Figure 3.44. Extraction force curves based on compliance centre locations. a) $w' * v' =$ 59.5*39.5 mm, b) $w' * v' =$ 60*40 mm, and c) $w' * v' =$60.5*40.5 mm* 124

Figure 4.1 A graphic Overview of Disassembly with Active Compliance Strategy and Reinforcement Learning 132

Figure 4.2. Contact stats of rectangle peg-hole disassembly 134

Figure 4.3. A 3D view of rectangle peg-hole 134

Figure 4.4 An environment simulated using PyBullet 135

Figure 4.5. Comparison of extraction forces (Fz) using RL and RL with compliance strategy (CS) 141

Figure 4.6. The average force exerted along the X-Y axis during each episode 142

Figure 4.7. The discounted cumulative reward of each episode 142

Figure 4.8. Trajectory and force dynamics in an RL-controlled disassembly task for Rectangle Peg-Hole 143

Figure 4.9 Overview of Kuka robot with F/T sensor and peg-hole 145

Figure 4.10. Extraction force (Fz) using a reinforcement learning compliance strategy 147

Figure 4.11. Comparison of Fz for the method described in chapters 2 & 3 and compliance strategy using reinforcement learning. 148

Figure 4.12. Extraction Time Comparison for The Method Described in Chapters 2 & 3 vs. RL-Based Compliance Approaches 149

Figure 5.1 Extraction force curves based on compliance centre locations in dual peg-hole with a) r= 5.7 mm, b) r= 6 mm, and c) r=6.5 mm 156

Figure 5.2 Comparison of the extraction force in dual peg-hole based on compliance centre locations with a) r= 5.7 mm, b) r= 6 mm, and c) r=6.5 mm. 158

Figure 5.3 Extraction force curves based on compliance centre locations in the rectangle peg-hole with a) w'*v'= 59.5*39.5 mm, b) w'*v'= 60*40 mm, and c) w'*v'=60.5*40.5 mm 161

Figure 5.4 Comparison of the extraction force in rectangle peg-hole based on compliance centre locations with a) w'*v'= 59.5*39.5 mm, b) w'*v'= 60*40 mm, and c) w'*v'=60.5*40.5 mm 163

List of Tables

TABLE 2.1 Various contact states for dual-peg extractions 30

TABLE 2.2. Parameters for dual peg-hole 55

TABLE 3.1 Various contact states for rectangle peg-hole extractions 75

TABLE 3.2. Parameters for rectangle peg-hole 121

TABLE 4. 1. The Leaning Agent's Specific Parameters 139

TABLE 4. 2. Parameters of rectangle peg-hole disassembly 146

Nomenclature

2D/3D	2/3 dimensional
ACC	Active Compliance Centre
AI	Artificial Intelligence
CNN	convolutional neural network
DA	Dijkstra's algorithm
DCNN	deep convolutional neural network
DL	Deep Learning
DOF	Degree of Freedom
DPP	disassembly process plan
DQN	Deep Q-Network
DRL	Deep Reinforcement Learning
DSP	disassembly sequence plan
EoF	End-of-Life
FRS	fuzzy-rough set
GA	Genetic Algorithm
GRASP	greed randomised adaptive search procedure (GRASP)
HRC	Human-Robot collaboration
HRI	human-robot interactions
IPR	Intellectual property restrictions
LCD	Liquid Crystal Display
ML	Machine Learning
RCC	Remote Compliance Centre

RL	Reinforcement Learning
SAC	Soft Actor-Critic
SARSA	State–action–reward–state–action
SL	supervised learning
SRCC	Spatial Remote Centre Compliance
TCP	Tool Centre Point
TS	Tabu search (TS)
UL	Unsupervised learning
WOS	Web Of Science
YOLO	You Only Look Once
IQR	Inter Quartile Range
CS	Compliance Strategy

Chapter 1. GENERAL INTRODUCTION

Authors Contributions:

A part of this chapter of the alternative thesis format is published in the 27th International Conference on Automation and Computing (ICAC) (2022). I am the first author of this publication. The paper's details and co-authors' contributions are outlined below.

Goli F[1], Wang Y[2] Saadat M[3]; Perspective of self-learning robotics for disassembly automation, The 27th International Conference on Automation and Computing (ICAC) (2022). https://ieeexplore.ieee.org/abstract/document/9911085

[1]Farzaneh Goli: The main author, researched and conducted data analysis and wrote the manuscript.

[2]Yongjing Wang: He provided ongoing supervision and meticulous proofreading support during the entire research process. Her oversight was key in maintaining the project's academic rigour, and her critical feedback helped ensure that the final manuscript was polished and well-structured.

[3] Mozafar Saadat: He provided ongoing supervision and meticulous proofreading support during the entire research process.

General Introduction

1.1 Introduction

1.1.1 Background

Discarded end-of-life (EOL) products pose a global challenge, impacting both the environment and the economy. EOL treatment, encompassing recycling, reuse, and remanufacturing, aims to extract remaining value from materials and components. Remanufacturing, involving stages such as disassembly, cleaning, inspection, repair, reassembly, and testing, plays a crucial role in connecting product return with effective recovery [1], [2]. Disassembly is a crucial step that links product return with product recovery [2].

Disassembly aims to retrieve parts from the returned products. Due to the dimensional uncertainties and geometrical variations in the returned EOL products, disassembly is usually carried out manually. These uncertainties and variations result in operational and planning complexities, making the disassembly processes difficult and time-consuming [3].

As the remanufacturing process grows in scale, there is a need to increase the efficiency of disassembly [2], [3]. Robotic disassembly is a new approach to reducing labour costs and improving productivity. However, industrial robots tend to be used in structured and repetitive tasks and cannot effectively cope with uncertainties and complexities of disassembly [4].

Developments in the areas of industrial automation and robotics can help improve productivity and contribute to creating industrial machines with capabilities beyond simple reasoning [5]. These developments aim to equip industrial machines with capabilities beyond routine operations, potentially revolutionising EOL product treatment.

1.1.2 Remanufacturing and Disassembly

Remanufacturing, which can give products a new life, is currently the most resource-effective, value-added strategy for EoL product recovery than recycling or reuse [6]. During the remanufacturing process, a product is returned to its original specifications to make it look new again. Remanufacturing involves several processes (Fig 1.1) that are commonly performed by experienced and trained workers using conventional methods [7], [8].

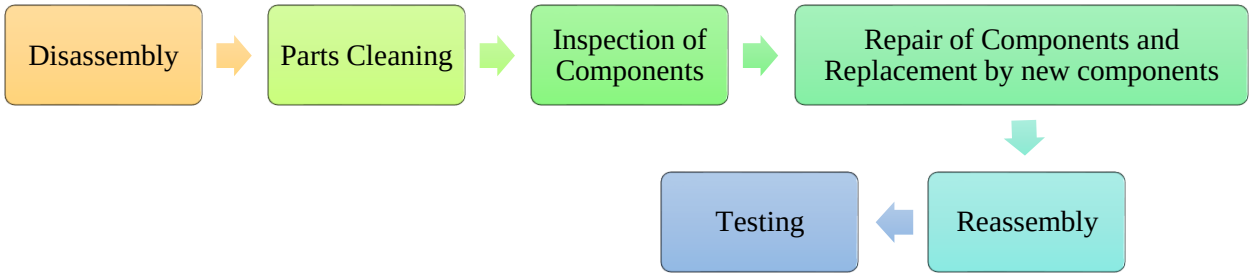

Figure 1.1 Example of Remanufacturing Process

Disassembly of returned products is a key step in remanufacturing [9], [10], [11] and is one of the primary steps of EOL processes. Disassembly involves extracting and separating the desired components, parts, and materials from products [12], [13]. Disassembly is also a key step of repair and maintenance [14]. In a study, Hammond et al. have demonstrated that disassembly is also a remanufacturing concern in addition to parts availability [15]. However, disassembly is not merely the reverse of assembly due to uncertain conditions of the returned products, which makes it more challenging to automate than assembly [16], [17], [18]. It has usually been performed manually and is labour-intensive [3]. There could be various reasons for this. One reason is the high cost of automation. The automated disassembly line may not be flexible enough because there is a wide range of product infrastructures and designs required for remanufacturing [19]. In other cases, such as corroded parts, human intervention is still required to specify suitable tools for removing the affected fasteners [20]. In general, 15 percent of a product's weight is removed for recycling or remanufacturing, while 85 percent is disposed

of in a landfill [21]. For remanufacturing, the product does not have to be dismantled in its entirety. Retrieving only the essential elements, such as high-value cores, thus saves time and eliminates the need for unnecessary procedures. Some research on EOL option decision models assumes that all elements are disassembled; nevertheless, this can lead to unessential disassembly costs [22]. However, due to inefficient disassembly design in many products, disassembling a product manually may not be cost-effective. This increases the time it takes to disassemble, resulting in greater labour costs. It is much more efficient to disassembled and remanufactured products that are specifically designed for this as opposed to remanufacturing products that are not intended for this purpose [23]. To remanufacture an object that was designed for disassembly, the basic requirements are: (1) Make the connection process easier to disassemble, (2) Core retrieval should take precedence over non-remanufacturable pieces, (3) Core protection to retain part integrity, and (4) Incorporate DFD into the product design process as early as feasible to make disassembly operations easier [20].

Disassembly is typically done by human labour using heavy tools rather than automated lines and robots.

However, manual disassembly can be inefficient. To reduce time and labour costs and improve efficiency, automatic disassembly using robotics can be employed [24]. One common task in disassembly is extracting a peg from a clearance-fit hole [25].

The extraction of a peg from a hole is a routine operation in the disassembly of mechanical components, such as detaching a shaft from a bearing in automotive turbochargers [26] and electric motors [27].

1.1.3 Challenges in peg-hole disassembly

While there have been many studies on peg-hole assembly, few studies have focused on disassembly. In the assembly and disassembly process, disassembly has received less attention.

The geometry of assembly parts plays a key role in both processes. Lateral and angular misalignment between separated components can increase reaction forces and cause problems during disassembly. Unbalanced forces can cause jamming and wedging in disassembly, and this is a significant risk in the use of robots in peg-hole disassembly. One of the main challenges in peg-hole disassembly is jamming. This occurs when the peg gets stuck during removal due to improperly applied forces or moments.

Compliance management is another challenge in disassembly operations. Having incorrect settings in compliance can cause unexpected rotation of components, such as pegs, further complicating disassembly. It is imperative to ensure proper compliance control in two-point contact scenarios to mitigate these problems and maintain operational efficiency. Another significant challenge is force control. For smooth disassembly, accurate management of extraction forces and moments is essential. A variation in force application can lead to failed disassembly attempts or damage to the involved parts, which highlights the need for precise force management [28].

1.2 Jamming Problems and Effect Compliance Strategy in Peg-Hole Disassembly

As an important challenge, jamming and wedging can occur due to reaction forces, preventing the successful completion of the task and causing damage to the components and robotics [29].

Whitney analysed the quasistatic assembly of a cylindrical peg into a chamfered hole [30]. By utilising industrial robot strategies such as the remote compliance centre (RCC) [30], [31], [32] [33] the jamming and wedging problem can be solved, allowing for the successful insertion and extraction of pegs [31], [32].

The term Compliance Centre (CC) refers to a mechanism or control system that enables a robotic manipulator to yield or adapt to external forces, thereby enhancing its interaction with the environment. In robotics, a CC represents a controlled, mechanical, or sensor-driven flexibility mechanism that allows a robot to adjust its position or force in response to environmental interactions. In KUKA robots, the CC is defined as the Tool Centre Point (TCP), which specifies the position and orientation of the tool relative to the robot's coordinate system.

Simunovic [34] and Whitney [35] used a compliant manipulator to analyse peg-hole assembly and developed an RCC device to improve accuracy and efficiency. Researchers have also analysed rectangular peg insertion without chamfers [36] and three-dimensional rectangular peg insertion [37], [38]. Sturges et al. also developed Spatial Remote Centre Compliance (SRCC) [39].

Strip [40] developed a hybrid force-position strategy for three-dimensional convex pegs using active compliance. Zhang et al. performed a quasi-static analysis of peg-hole disassembly with a compliance device, exploring the effect of key variables such as the degree of compliance, compliance centre location, and position error [32]. Wang et al. compared passive and active compliance and found that active compliance was more beneficial due to its faster dynamic response [41]. Despite its cost and limited response speed, active compliance is an effective method for improving assembly reliability [42]. Sathirakul and Sturges [43] and Fei and Zhao [44] applied the compliance principle in multi peg-hole assembly tasks to correct lateral and angular misalignments. However, there has been a lack of in-depth investigation into multi-peg-hole disassembly. This has resulted in a knowledge gap regarding the mechanisms and contacts involved in the process.

The effectiveness of the active compliance strategy in robotics for peg-hole assembly and disassembly lies in its adaptability, precise force control [45], sensitivity, safety, efficiency,

versatility, and demonstrated real-world applications. This approach empowers robots to dynamically adjust to their environment, responding in real-time to factors such as misalignments or surface irregularities, thus reducing the length of the jamming area in peg-hole operations. Additionally, by employing force sensing, robots can accurately apply the necessary force for insertion and removal without causing damage to the components. This precision and adaptability make active compliance a valuable and reliable solution, particularly in industrial settings demanding high-precision performance [46].

1.3 Characterising the Mechanics of Dual and Rectangle Peg-Hole Disassembly

Assembling and disassembling peg-holes is a fundamental process in manufacturing/ remanufacturing, robotics, and automation. In spite of extensive research on peg-hole insertion, the disassembly aspect has received comparatively little attention. Peg-hole disassembly mechanics are critical for developing efficient and robust disassembly processes, particularly for delicate components or complex assemblies.

Peg-hole disassembly mechanics describes the factors affecting disassembly forces, friction and clearance, and the effects of different peg and hole geometries on disassembly forces.

In our previous studies [32], [47], we explored contact states within one-peg and one-hole scenarios, characterised by limited contact points typically concentrated at the peg tip and hole's inner surface. These situations featured simpler geometries. In this study, we delve into the intricacies of dual and rectangle peg-hole scenarios, where pegs can establish numerous contact states with their respective holes. These contact points may manifest at various locations along

the pegs, resulting in a more complex contact geometry compared to the one cylindric peg-hole case. This research is motivated by the demand to address these complexities.

This study shows an analysis of dual and rectangle peg-hole extraction problems, highlighting the boundary conditions of jamming and proposing a solution using active compliance to avoid jamming.

The effectiveness of the active compliance strategy in robotics for peg-hole assembly and disassembly lies in its adaptability, precise force control [45], sensitivity, safety, efficiency, versatility, and demonstrated real-world applications. This approach empowers robots to dynamically adjust to their environment, responding in real-time to factors such as misalignments or surface irregularities, thus reducing the length of the jamming area in peg-hole operations. Additionally, by employing force sensing, robots can accurately apply the necessary force for insertion and removal without causing damage to the components. This precision and adaptability make active compliance a valuable and reliable solution, particularly in industrial settings demanding high-precision performance [46].

These traditional methods do not generalise effectively to changes in the environment and are not resistant to uncertainty. The current study has focused on learning disassembly skills directly from interactions with the environment to reduce human participation and increase robustness to uncertainty. Through interactions with their environment and optimising rewards, agents can learn complicated behaviours through Reinforcement Learning (RL) techniques [48]. Consequently, rather than merely imparting human abilities to the robot program, reinforcement learning (RL) can be used to teach robotic agents high-precision assembly/disassembly skills [49], [50].

1.4 Integrating Reinforcement Learning with Mechanical Analysis and Compliance Strategy Contributions

Recently, the rise of reinforcement learning (RL) in robotics provides an exciting new approach, where systems are learning and adapting to their environment through trial-and-error processes and optimising actions based on evaluation of the environment [51]. This paradigm is especially suited for robotic disassembly, in which the tasks are highly variable and therefore call for dynamism in responding to these variations in order to achieve efficiency and minimise damage [52].

The Deconstruction of old items for remanufacturing presents a specific problem in the face of the variability of the used components. Efficient disassembly is critical because it represents the key element of sustainable manufacturing practices that strongly impact waste reduction and environmental efficiency [53], [54]. Recent studies have demonstrated that robotic systems with RL are capable of dealing with variabilities by making real-time decisions that can help to adapt the remanufacturing process [55].

A compliance strategy in the disassembly of robots reduces the risk of damage to the parts even more. Such methods enable the disengagement mechanism to alter its operations dynamically, due to the feedback from the physical interactions the result of which is the enhancement of the precision of the disassembly operation [56]. Hence, such a blend of RL and compliance with robotics addresses the shortcomings of conventional disassembly techniques, which works as a strategy that is adaptive and sensitive to the environment of the task [57].

The literature presents several cases where RL has been deployed successfully in robotic tasks that are more advanced than disassembly, from autonomous driving to robot manipulation tasks requiring dexterity [58], [59], [60]. Through these examples, one can see the range of

possibilities and applications of RL as a powerful tool for dealing with a variety of issues related to robotics and robotics automation.

Nevertheless, RL lacks the specific focus on the disassembled rectangular peg-hole system and also lacks the ability of integrate the compliance strategies. There is a gap in the state of the art in the specification of RL to target solutions that demand exceptional flexibility and robustness to the task environment. Robotic disassembly and compliance are representative of such types of challenges.

1.5 **Research Aim and Objective**

This research focuses on the robotic disassembly of dual and rectangular peg-hole structures in order to address the challenges associated with robotic disassembly. As part of the remanufacturing process, this study explores jamming problems and compliance strategies to maximise efficiency and economic feasibility. A core focus is the integration of reinforcement learning (RL) with mechanical analysis and compliance strategies, in order to optimise disassembly operations dynamically.

This research has the following specific objectives:

Identification and characterisation of disassembly tasks:

- Identification and enumeration of the various contact states and their geometric conditions during the disassembly of dual and rectangular peg-hole.
- To categorise these conditions, focus on understanding the phenomena of jamming and its boundary conditions through geometrical and quasistatic analyses.

Investigate compliance strategies:

- To analyse the role of active compliance in mitigating jamming during the disassembly process.

- To simulate critical variables and examine key parameters such as the degree of compliance, the location of the compliance centre, and initial position errors.
- Experiment with different compliance centre positions in order to assess the effectiveness of each position in reducing jamming and extraction force.

Integrate Reinforcement Learning:

- Developing a method for combining compliance strategies with reinforcement learning (RL) to enhance robotic disassembly efficiency and adaptability.
- RL agents are trained to learn optimal disassembly sequences, incorporating feedback from environmental sensing to adapt disassembly strategies dynamically.

Validation through experimental testing:

- Conduct experiments to verify theory and simulation findings with a 6-DOF-compliant manipulator.

1.5.1 Contributions

The key contributions of this research include:

Characterising Disassembly Mechanics:

During the disassembly of dual and rectangular peg-hole structures, geometrical and quasistatic analyses are conducted to identify the boundary conditions and critical contact states. An understanding of these mechanics is crucial for developing strategies that minimise jamming and increase disassembly efficiency.

Mitigating Jamming with Active Compliance:

This research demonstrates how optimal ACC positioning can reduce extraction force (up to 77.1%) and jamming areas, thus improving robotic disassembly reliability and efficiency.

Enhance precision and minimise destruction by integrating Reinforcement Learning (RL) with a Compliance strategy:

A standout aspect of this research is merging RL with compliance strategies. RL algorithms help robots learn from their environmental feedback and adjust their disassembly methods dynamically. This adaptability results in better disassembly motions, decreasing the extraction force and enhancing overall efficiency.

Figure 1.2 illustrates the structure of this thesis, providing an overview of the Disassembly with Active Compliance Strategy and Reinforcement Learning in a rectangular Peg-Holes structure.

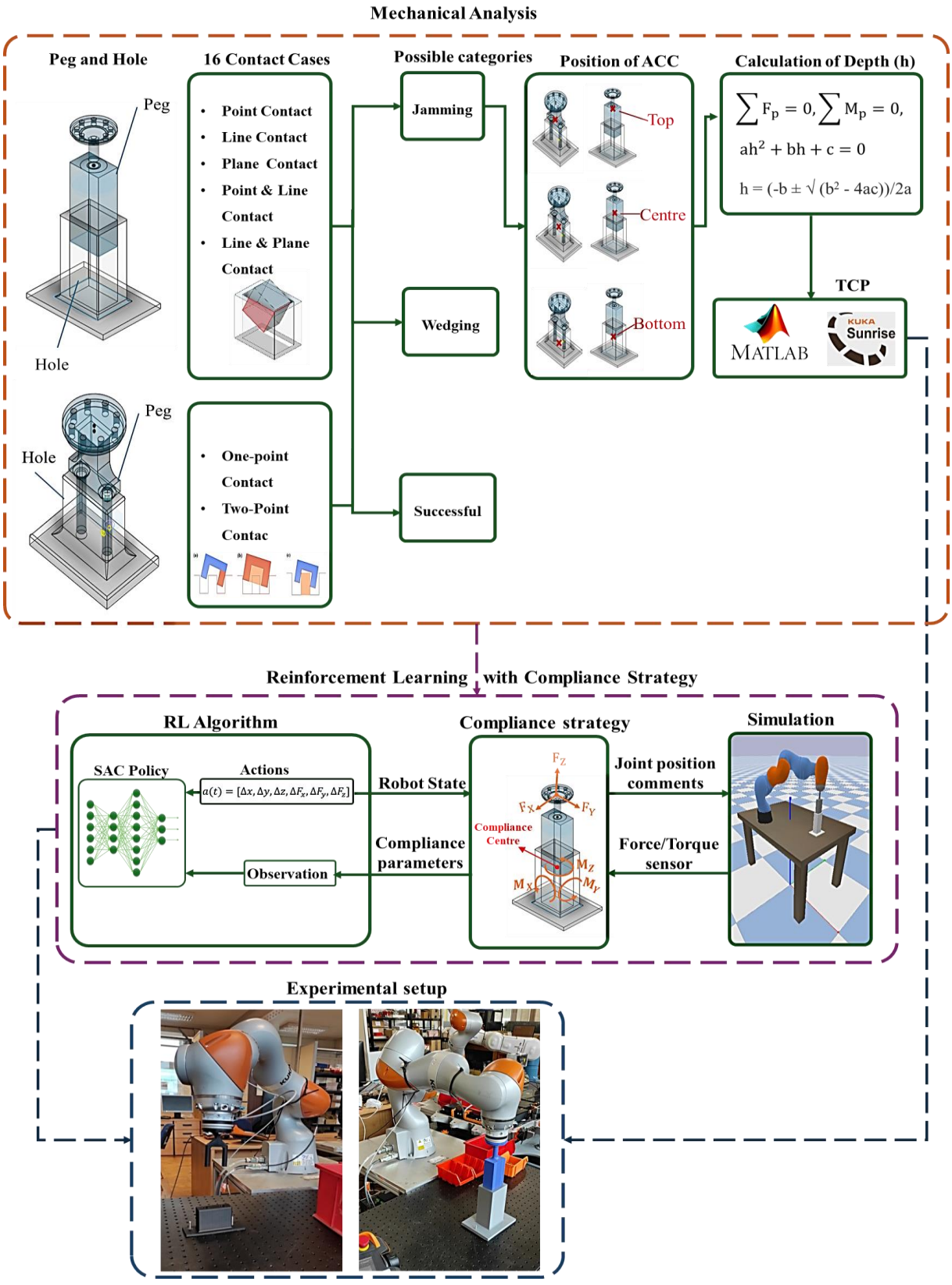

Figure 1.2 Graphic Overview of Disassembly with Active Compliance Strategy and Reinforcement Learning

1.5.2 Publication of this thesis

I. Journal article publications

1. **F. Goli**, A. Aflakian, M. Qu, Y. Zang, M. Saadat, D.T. Pham, Y. Wang, "*Characterising the mechanics of rectangular peg-hole disassembly and the effect of the active compliance centre on the extraction force*", The royal society, Open Science. https://doi.org/10.1098/rsos.240956
2. **F. Goli**, Y. Zhang, M. Qu, Y. Zang, M. Saadat, D.T. Pham, Y. Wang, "*Jamming problems and the effects of compliance in dual peg-hole disassembly*", Proceeding of the royal society A. https://doi.org/10.1098/rspa.2023.0364

II. Conference Proceedings

1. **F. Goli**, Y. Wang, M. Saadat, "*Rectangular Peg-Hole Disassembly Quasi-static with Active Compliance*", IWAR 2024- 8th International Workshop on Autonomous Remanufacturing, October 2024, Detroit, MI, US
2. **F. Goli**, Y. Wang, M. Saadat, "*Disassembly of Rectangle Peg-Hole Structures Through Compliance Strategy and Reinforcement Learning*", CASE 2024- IEEE 20th International Conference on Automation Science and Engineering, August 2024, Bari, Italy. https://ieeexplore.ieee.org/abstract/document/10711423
3. **F. Goli**, Y. Zhang, Y. Wang, M. Saadat, "*An analysis of dual peg-hole disassembly problems*", IWAR 2023- VII International Workshop on Autonomous Remanufacturing, October 2023, Caserta, Italy. https://link.springer.com/chapter/10.1007/978-3-031-52649-7_38
4. **F. Goli**, Y. Wang, M. Saadat, "*Perspective of self-learning robotics for disassembly automation*", 27th International Conference on Automation and Computing (ICAC), September 2022, Bristol, UK. **DOI:** 10.1109/ICAC55051.2022.9911085

III. Poster Presentations

1- Presentation on my PhD project on "Peg-hole disassembly with reinforcement learning and compliance strategy" at the 7th Annual SoE PGR Symposium 2024, University of Birmingham, UK.

2- Presentation on my PhD project on "Peg-hole Disassembly: The Mechanical Analysis and Reinforcement Learning with Compliance Strategy" at the AI and the Future of Engineering Symposium 2024, Dyson Institute Engineering Technology, UK.

1.6 Thesis Structure

This thesis is structured to systematically address the research objectives and provide a comprehensive analysis of the challenges and solutions in robotic disassembly (Fig 1.3):

Chapter 1: General Introduction – Provides an overview of the research background, the importance of remanufacturing, challenges in peg-hole disassembly, and the integration of AI and compliance strategies.

Chapter 2: Jamming problems and the effects of compliance in dual peg-hole disassembly– Explores jamming issues in detail and the effectiveness of compliance strategies, including the Active Compliance Centre (ACC), in addressing these challenges.

Chapter 3: Characterising the mechanics of rectangular peg-hole disassembly and the effect of the active compliance centre on the extraction force– Analyses the mechanical challenges associated with rectangular peg-hole disassembly and identifies optimal Active Compliance Centre (ACC) positions to minimise extraction forces and jamming risks.

Chapter 4: Disassembly of Rectangle Peg-Hole Structures Through Compliance Strategy and Reinforcement Learning – Discusses the application of compliance strategies and reinforcement learning in enhancing the efficiency and adaptability of robotic disassembly processes. This chapter highlights how RL algorithms can optimise disassembly motions and reduce extraction forces based on environmental feedback.

Our goal was to conduct two case studies on peg-hole tasks (rectangular and dual peg-hole configurations). The study was only able to be completed for rectangular peg-holes due to a bug in PyBullet's toolbox that affects collision detection in convex hulls. The optimisation of dual peg-hole insertion using reinforcement learning could be considered in future research with alternative simulators such as CoppeliaSim or Gazebo.

Chapter 5: Conclusions and Future Work – Summarises the research outcomes, highlights the contributions to the field of robotic disassembly, and suggests directions for future research to further advance remanufacturing and recycling technologies.

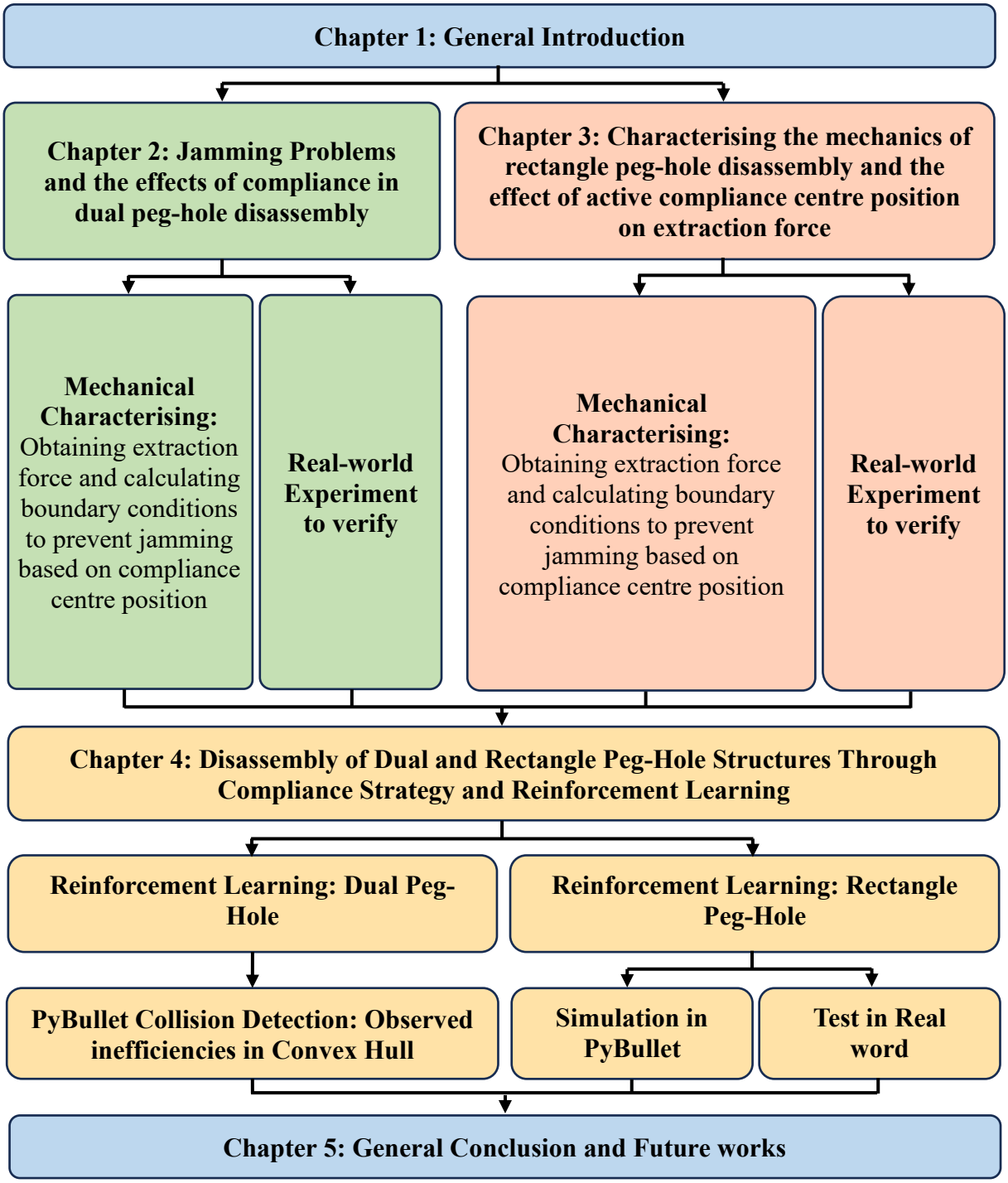

Figure 1.3 Overview of Thesis Structure

1.7 References

[1] W. L. Ijomah, C. A. McMahon, G. P. Hammond, and S. T. Newman, "Development of robust design-for-remanufacturing guidelines to further the aims of sustainable development," *Int J Prod Res*, vol. 45, no. 18–19, pp. 4513–4536, Sep. 2007, doi: 10.1080/00207540701450138.

[2] S. Vongbunyong and W. H. Chen, "Disassembly Automation," in *Disassembly Automation: Automated Systems with Cognitive Abilities*, S. Vongbunyong and W. H. Chen, Eds., Cham: Springer International Publishing, 2015, pp. 25–54. doi: 10.1007/978-3-319-15183-0_3.

[3] J. Li, M. Barwood, and S. Rahimifard, "Robotic disassembly for increased recovery of strategically important materials from electrical vehicles," *Robot Comput Integr Manuf*, vol. 50, pp. 203–212, 2018, doi: 10.1016/j.rcim.2017.09.013.

[4] F. Torres, S. Puente, and C. Díaz, "Automatic cooperative disassembly robotic system: Task planner to distribute tasks among robots," *Control Eng Pract*, vol. 17, no. 1, pp. 112–121, 2009, doi: 10.1016/j.conengprac.2008.05.013.

[5] Yagna. Jadeja, Mahmoud. Shafik, Paul. Wood, and Leonardo. Stella, "An Industrial Self-Learning Robotic Platform Solution for Smart Factories Industrial Applications Using Machine and Deep Imitation Learning," in *Advances in Manufacturing Technology XXXIV*, vol. 15, 2021, ch. 4, pp. 119–124. doi: 10.3233/ATDE210023.

[6] G. D. Hatcher, W. L. Ijomah, and J. F. C. Windmill, "Integrating design for remanufacture into the design process: the operational factors," *J Clean Prod*, vol. 39, pp. 200–208, 2013, doi: https://doi.org/10.1016/j.jclepro.2012.08.015.

[7] D. A. Wahab, E. Blanco-Davis, A. K. Ariffin, and J. Wang, "A review on the applicability of remanufacturing in extending the life cycle of marine or offshore components and structures," *Ocean Engineering*, vol. 169, pp. 125–133, 2018, doi: https://doi.org/10.1016/j.oceaneng.2018.08.046.

[8] S. S. Mad Yusoh, D. Abd Wahab, H. Adil Habeeb, and A. H. Azman, "Intelligent systems for additive manufacturing-based repair in remanufacturing: a systematic review of its potential," *PeerJ Comput Sci*, 2021, doi: https://doi.org/10.7717/peerj-cs.808.

[9] H. Cheng, W. Xu, Q. Ai, Q. Liu, Z. Zhou, and D. T. Pham, "Manufacturing Capability Assessment for Human-Robot Collaborative Disassembly Based on Multi-Data Fusion," *Procedia Manuf*, vol. 10, pp. 26–36, 2017, doi: https://doi.org/10.1016/j.promfg.2017.07.008.

[10] L. Zhang, X. Zhao, Q. Ke, W. Dong, and Y. Zhong, "Disassembly Line Balancing Optimization Method for High Efficiency and Low Carbon Emission," *International Journal of Precision Engineering and Manufacturing-Green Technology*, vol. 8, no. 1, pp. 233–247, 2021, doi: 10.1007/s40684-019-00140-2.

[11] Y. Du, H. Cao, F. Liu, C. Li, and X. Chen, "An integrated method for evaluating the remanufacturability of used machine tool," *J Clean Prod*, vol. 20, no. 1, pp. 82–91, 2012, doi: https://doi.org/10.1016/j.jclepro.2011.08.016.

[12] S. Parsa and M. Saadat, "Intelligent selective disassembly planning based on disassemblability characteristics of product components," *The International Journal of Advanced Manufacturing Technology*, vol. 104, no. 5, pp. 1769–1783, 2019, doi: 10.1007/s00170-019-03857-1.

[13] A. J. D. Lambert, "Disassembly sequencing: A survey," *Int J Prod Res*, vol. 41, no. 16, pp. 3721–3759, 2003, doi: 10.1080/0020754031000120078.

[14] A. Serrano-Muñoz, N. Arana-Arexolaleiba, D. Chrysostomou, and S. Bøgh, "Learning and generalising object extraction skill for contact-rich disassembly tasks: an introductory study," *The International Journal of Advanced Manufacturing Technology*, 2021, doi: 10.1007/s00170-021-08086-z.

[15] R. Hammond, T. Amezquita, B. Bras, and G. W. Woodruff, "Issues in the Automotive Parts Remanufacturing Industry - A Discussion of Results from Surveys Performed among Remanufacturers," 1998.

[16] G. Jin, W. Li, S. Wang, and S. Gao, "A systematic selective disassembly approach for Waste Electrical and Electronic Equipment with case study on liquid crystal display televisions," *Proc Inst Mech Eng B J Eng Manuf*, vol. 231, no. 13, pp. 2261–2278, 2015, doi: 10.1177/0954405415575476.

[17] A. Priyono, W. Ijomah, and U. S. Bititci, "Disassembly for remanufacturing: A systematic literature review, new model development and future research needs," *Journal of Industrial Engineering and Management (JIEM)*, vol. 9, no. 4, pp. 899–932, 2016, doi: 10.3926/jiem.2053.

[18] S. Vongbunyong, P. Vongseela, and J. Sreerattana-aporn, "A Process Demonstration Platform for Product Disassembly Skills Transfer," *Procedia CIRP*, vol. 61, pp. 281–286, 2017, doi: https://doi.org/10.1016/j.procir.2016.11.197.

[19] J. R. Duflou, B. Willems, and W. Dewulf, "Towards self-disassembling products Design solutions for economically feasible large-scale disassembly," in *Innovation in Life Cycle Engineering and Sustainable Development*, D. Brissaud, S. Tichkiewitch, and P. Zwolinski, Eds., Dordrecht: Springer Netherlands, 2006, pp. 87–110. doi: https://doi.org/10.1007/1-4020-4617-0_6.

[20] S. L. Soh, S. K. Ong, and A. Y. C. Nee, "Design for disassembly for remanufacturing: methodology and technology," *Procedia CIRP*, vol. 15, pp. 407–412, 2014, doi: https://doi.org/10.1016/j.procir.2014.06.053.

[21] S. K. Das and S. Naik, "Process planning for product disassembly," *Int J Prod Res*, vol. 40, no. 6, pp. 1335–1355, 2002, doi: 10.1080/00207540110102142.

[22] H. B. Lee, N. W. Cho, and Y. S. Hong, "A hierarchical end-of-life decision model for determining the economic levels of remanufacturing and disassembly under environmental regulations," *J Clean Prod*, vol. 18, no. 13, pp. 1276–1283, 2010, doi: https://doi.org/10.1016/j.jclepro.2010.04.010.

[23] W. Kerr and C. Ryan, "Eco-efficiency gains from remanufacturing: A case study of photocopier remanufacturing at Fuji Xerox Australia," *J Clean Prod*, vol. 9, no. 1, pp. 75–81, 2001, doi: https://doi.org/10.1016/S0959-6526(00)00032-9.

[24] Y. Tang, M. Zhou, E. Zussman, and R. Caudill, "Disassembly modeling, planning, and application," *J Manuf Syst*, vol. 21, no. 3, pp. 200–217, 2002, doi: https://doi.org/10.1016/S0278-6125(02)80162-5.

[25] B.-H. Kim, B.-J. Yi, I. H. Suh, and S.-R. Oh, "Stiffness analysis for effective peg-in/out-hole tasks using multi-fingered robot hands," in *Proceedings. 2000 IEEE/RSJ International Conference on Intelligent Robots and Systems (IROS 2000) (Cat. No.00CH37113)*, 2000, pp. 1229–1236 vol.2. doi: 10.1109/IROS.2000.893187.

[26] B. James, P. Rao, E. Reddy, and V. Mallikarjuna, "DESIGN AND ANALYSIS OF TURBOCHARGERS," Mar. 2016.

[27] M. Bdiwi, A. Rashid, M. Pfeifer, and M. Putz, *Disassembly of Unknown Models of Electrical Vehicle Motors Using Innovative Human Robot Cooperation*. 2017. doi: 10.1145/3029798.3038425.

[28] M. M. Ogot, G. E. Okudan, T. W. Simpson, and J. Lamancusa, “A framework for classifying disassemble/analyse/assemble activities in engineering design education,” *J. of Design Research*, vol. 7, p. 120, 2008, [Online]. Available: https://api.semanticscholar.org/CorpusID:110614897

[29] R. Usubamatov and K. W. Leong, “Analyses of peg-hole jamming in automatic assembly machines,” *Assembly Automation*, vol. 31, no. 4, pp. 358–362, Jan. 2011, doi: 10.1108/01445151111172943.

[30] D. E. Whitney, “Quasi-static assembly of compliantly supported rigid parts,” *J Dyn Syst Meas Control*, vol. 104, no. 1, pp. 65–77, 1982.

[31] B. P. McNelly, R. Leary, S. Brennan, and K. Reichard, “Characterizing successful robotic insertion and removal from a dry storage cask using peg-like jamming and wedging analysis,” in *Pressure Vessels and Piping Conference*, American Society of Mechanical Engineers, 2016, p. V06BT06A064.

[32] Y. Zhang *et al.*, “Peg–hole disassembly using active compliance,” *R Soc Open Sci*, vol. 6, no. 8, p. 190476, 2019, doi: https://doi.org/10.1098/rsos.190476.

[33] H. Asada and Y. Kakumoto, “The dynamic RCC hand for high-speed assembly,” in *Proceedings. 1988 IEEE International Conference on Robotics and Automation*, 1988, pp. 120–125 vol.1. doi: 10.1109/ROBOT.1988.12035.

[34] S. N. ’Simunovi, “an information approach to parts mating,” Massachusetts Institute of Technology, Cambridge, MA, 1979.

[35] J. L. Nevins and D. E. Whitney, “Assembly Research,” *IFAC Proceedings Volumes*, vol. 12, no. 10, pp. 195–214, 1979, doi: https://doi.org/10.1016/S1474-6670(17)65359-X.

[36] M. E. Caine, T. Lozano-Perez, and W. P. Seering, “Assembly strategies for chamferless parts,” in *Proceedings, 1989 International Conference on Robotics and Automation*, 1989, pp. 472–477 vol.1. doi: 10.1109/ROBOT.1989.100031.

[37] R. H. Sturges, “A Three-Dimensional Assembly Task Quantification with Application to Machine Dexterity,” *Int J Rob Res*, vol. 7, pp. 34–78, 1988, [Online]. Available: https://api.semanticscholar.org/CorpusID:32049730

[38] R. H. Sturges Jr. and S. Laowattana, “Virtual Wedging in Three-Dimensional Peg Insertion Tasks,” *Journal of Mechanical Design*, vol. 118, no. 1, pp. 99–105, Mar. 1996, doi: 10.1115/1.2826863.

[39] R. H. Sturges Jr. and S. Laowattana, “Design of an Orthogonal Compliance for Polygonal Peg Insertion,” *Journal of Mechanical Design*, vol. 118, no. 1, pp. 106–114, Mar. 1996, doi: 10.1115/1.2826840.

[40] D. R. Strip, “Insertions using geometric analysis and hybrid force-position control: method and analysis,” in *Proceedings. 1988 IEEE International Conference on Robotics and Automation*, IEEE, 1988, pp. 1744–1751.

[41] W. Wang, R. N. K. Loh, and E. Y. Gu, “Passive compliance versus active compliance in robot-based automated assembly systems,” *Industrial Robot: An International Journal*, vol. 25, no. 1, pp. 48–57, Jan. 1998, doi: 10.1108/01439919810196964.

[42] X. Zhang, Y. Zheng, J. Ota, and Y. Huang, “Peg-in-hole assembly based on two-phase scheme and f/t sensor for dual-arm robot,” *Sensors*, vol. 17, no. 9, p. 2004, 2017.

[43] K. Sathirakul and R. H. Sturges, “Jamming conditions for multiple peg-in-hole assemblies,” *Robotica*, vol. 16, no. 3, pp. 329–345, 1998, doi: DOI: 10.1017/S0263574798000393.

[44] Y. Fei and X. Zhao, “An Assembly Process Modeling and Analysis for Robotic Multiple Peg-in-hole,” *J Intell Robot Syst*, vol. 36, no. 2, pp. 175–189, 2003, doi: 10.1023/A:1022698606139.

[45] Y. Zhang *et al.*, "Peg–hole disassembly using active compliance," *R Soc Open Sci*, vol. 6, no. 8, p. 190476, 2019.
[46] S. Wang, G. Chen, H. Xu, and Z. Wang, "A Robotic Peg-in-Hole Assembly Strategy Based on Variable Compliance Center," *IEEE Access*, vol. 7, pp. 167534–167546, 2019, doi: 10.1109/ACCESS.2019.2954459.
[47] F. Lan, M. Castellani, D. Truong Pham, and Y. Wang, "On the correctness of using two-dimensional representations in the analysis of cylindrical peg–hole insertion and withdrawal," *R Soc Open Sci*, vol. 10, no. 8, Aug. 2023, doi: 10.1098/rsos.221021.
[48] R. S. Sutton and A. G. Barto, "Reinforcement_Learning_second_edition".
[49] C. C. Beltran-Hernandez, D. Petit, I. G. Ramirez-Alpizar, and K. Harada, "Variable Compliance Control for Robotic Peg-in-Hole Assembly: A Deep-Reinforcement-Learning Approach," *Applied Sciences*, vol. 10, no. 19, 2020, doi: 10.3390/app10196923.
[50] C. Yang, C. Zeng, Y. Cong, N. Wang, and M. Wang, "A Learning Framework of Adaptive Manipulative Skills From Human to Robot," *IEEE Trans Industr Inform*, vol. 15, no. 2, pp. 1153–1161, 2019, doi: 10.1109/TII.2018.2826064.
[51] R. S. Sutton and A. G. Barto, *Reinforcement learning: An introduction*. MIT press, 2018.
[52] D. Silver and D. Hassabis, "Alphago: Mastering the ancient game of go with machine learning," *Research Blog*, vol. 9, 2016.
[53] G. Timothy *et al.*, "Note on the Rate and Energy Efficiency Limits for Additive Manufacturing," *J Ind Ecol*, 2017.
[54] E. Sundin and H. M. Lee, "In what way is remanufacturing good for the environment?," in *Design for Innovative Value Towards a Sustainable Society*, M. Matsumoto, Y. Umeda, K. Masui, and S. Fukushige, Eds., Dordrecht: Springer Netherlands, 2012, pp. 552–557.
[55] A. Allagui, I. Belhadj, R. Plateaux, M. Hammadi, O. Penas, and N. Aifaoui, "Reinforcement learning for disassembly sequence planning optimization," *Comput Ind*, vol. 151, p. 103992, 2023, doi: https://doi.org/10.1016/j.compind.2023.103992.
[56] H. Zhu, A. Gupta, A. Rajeswaran, S. Levine, and V. Kumar, "Dexterous Manipulation with Deep Reinforcement Learning: Efficient, General, and Low-Cost," in *2019 International Conference on Robotics and Automation (ICRA)*, 2019, pp. 3651–3657. doi: 10.1109/ICRA.2019.8794102.
[57] Q. Liu, Z. Ji, W. Xu, Z. Liu, B. Yao, and Z. Zhou, "Knowledge-guided robot learning on compliance control for robotic assembly task with predictive model," *Expert Syst Appl*, vol. 234, p. 121037, 2023, doi: https://doi.org/10.1016/j.eswa.2023.121037.
[58] P. Mirowski *et al.*, "Learning to navigate in complex environments," *arXiv preprint arXiv:1611.03673*, 2016.
[59] M. Andrychowicz *et al.*, "Hindsight Experience Replay," in *Advances in Neural Information Processing Systems*, I. Guyon, U. Von Luxburg, S. Bengio, H. Wallach, R. Fergus, S. Vishwanathan, and R. Garnett, Eds., Curran Associates, Inc., 2017. [Online]. Available: https://proceedings.neurips.cc/paper_files/paper/2017/file/453fadbd8a1a3af50a9df4df899537b5-Paper.pdf
[60] F. Goli, Y. Wang, and M. Saadat, "Perspective of self-learning robotics for disassembly automation," in *2022 27th International Conference on Automation and Computing (ICAC)*, 2022, pp. 1–6. doi: 10.1109/ICAC55051.2022.9911085.

Chapter 2. JAMMING PROBLEMS AND THE EFFECTS OF COMPLIANCE IN DUAL PEG-HOLE DISASSEMBLY

Authors Contributions:

This chapter of the alternative thesis format is published in the Journal of Royal Society Proceeding A (2024). I am the first author of this publication. The paper's details and co-authors' contributions are outlined below.

Goli F[1], Zhang Y[2], Qu M[3], Zang Y[4], Saadat M[5], Pham DT[6], Wang Y[7]; Jamming problems and effects of compliance in dual peg-hole disassembly. Royal Society Proceeding A (2024).

https://doi.org/10.1098/rspa.2023.0364

[1] Farzaneh Goli: The main author, designed a Quasi-Static model and executed experiments, and numerical simulations, performed all necessary characterisation and data analysis and wrote the manuscript.

[2] Yongquan Zhang: He contributed to the Quasi-Static model. His contributions involved providing essential theoretical insights and mathematical formulations that enhanced the model's accuracy and robustness.

[3] Mo Qu: He contributed significantly by assisting in setting up the experimental framework. His efforts ensured that all equipment was properly calibrated and that the experimental conditions were optimised for reliable data collection.

[4] **Yue Zang:** He meticulously reviewed the mathematical formulations to ensure their accuracy. Additionally, his detailed inputs both during review and writing ensured that the final document was precise and well-articulated.

[5] **Mozafar Saadat:** He provided ongoing supervision and meticulous proofreading support during the entire research process.

[6] **Duc Truong Pham:** He **was** pivotal in conceptualising the project, contributing significantly by framing the research objectives. In addition, he helped to address reviewers' comments, ensuring that the feedback was carefully considered and effectively integrated into the final manuscript.

[7]**Yongjing Wang:** He provided ongoing supervision and meticulous proofreading support during the entire research process. Her oversight was key in maintaining the project's academic rigour, and her critical feedback helped ensure that the final manuscript was polished and well-structured.

Jamming Problems and the effects of compliance in dual peg-hole disassembly

Abstract

Disassembly is a crucial step in remanufacturing and is currently mainly performed by humans. Automating disassembly can reduce labour costs and make remanufacturing more economically attractive. This paper focuses on identifying and characterising a common disassembly task, dual peg-hole disassembly, with the aim of building a robotic disassembly system for this task. We enumerate the possible contact states and their geometric conditions during the extraction of two studs in a dual peg-hole. This paper focuses on jamming in the extraction and conducts geometrical and quasistatic analyses to determine the boundary conditions of jamming. Based on the analyses, this paper also investigates the role of active compliance as a solution to avoid jamming. We also simulate critical variables and examine key parameters such as the degree of compliance, the location of the compliance centre, and initial position errors. Finally, we conduct experimental studies on dual peg-hole extraction with different compliance centres obtained using active compliance.

Key words: Dual peg-hole extraction, Disassembly, Active compliance centre, Robotic, Force analysis, Jamming

2.1 Introduction

The disposal of end-of-life (EOL) products presents a global challenge with a profound impact on both the environment and the economy[1]. To mitigate these impacts, EOL products are often recycled, reused, and remanufactured so that their components and materials can be separated non-destructively for future reuse[2].

Remanufacturing involves several stages, including disassembly, cleaning, inspection, repair or replacement of damaged parts, reassembly, and testing [3]. Disassembly is a crucial step that links product return with product recovery [4]. However, manual disassembly can be inefficient. To reduce time and labour costs and improve efficiency, automatic disassembly using robotics can be employed [5]. One common task in disassembly is extracting a peg from a clearance-fit hole [6].

The extraction of a peg from a hole is a routine operation in the disassembly of mechanical components, such as detaching a shaft from a bearing in automotive turbochargers [7] and electric motors [8]. This procedure extends to the disassembly of assemblies with multiple peg-holes or dual peg-holes, as seen in examples such as electric plugs, capacitors, and resistors.

While there have been many studies on peg-hole assembly, few studies have focused on disassembly. In the assembly and disassembly process, disassembly has received less attention. The geometry of assembly parts plays a key role in both processes. Lateral and angular misalignment between separated components can increase reaction forces and cause problems during disassembly. Unbalanced forces can cause jamming and wedging in disassembly, and this is a significant risk in the use of robots in peg-hole disassembly.

Jamming and wedging can occur due to reaction forces, preventing the successful completion of the task and causing damage to the components and robotics [9]. Whitney analysed the quasistatic assembly of a cylindrical peg into a chamfered hole [10]. By utilising

industrial robot strategies such as the remote compliance centre (RCC) [10], [11], [12], [13], the jamming and wedging problem can be solved, allowing for successful insertion and extraction of pegs [11], [12].

Simunovic [14] and Whitney [15] used a compliant manipulator to analyse peg-hole assembly and developed an RCC device to improve accuracy and efficiency. Researchers have also analysed rectangular peg insertion without chamfers [16] and three-dimensional rectangular peg insertion [17], [18]. Sturges *et al.* also developed Spatial Remote Centre Compliance (SRCC) [19].

Strip [20] developed a hybrid force-position strategy for three-dimensional convex pegs using active compliance. Zhang *et al*. performed a quasi-static analysis of peg-hole disassembly with a compliance device, exploring the effect of key variables such as the degree of compliance, compliance centre location, and position error [12]. Wang *et al*. compared passive and active compliance and found that active compliance was more beneficial due to its faster dynamic response [21]. Despite its cost and limited response speed, active compliance is an effective method for improving assembly reliability [22]. Sathirakul and Sturges [23] and Fei and Zhao [24] applied the compliance principle in multi peg-hole assembly tasks to correct lateral and angular misalignments. However, there has been a lack of in-depth investigation into multi-peg-hole disassembly. This has resulted in a knowledge gap regarding the mechanisms and contacts involved in the process.

In our previous studies [12], [25], we explored contact states within one-peg and one-hole scenarios, characterised by limited contact points typically concentrated at the peg tip and hole's inner surface. These situations featured simpler geometries. In this paper, we delve into the intricacies of dual peg-hole scenarios, where each of the two pegs can establish numerous contact states with their respective holes. These contact points may manifest at various locations

along the pegs, resulting in a more complex contact geometry compared to the one-peg-one-hole case. This research is motivated by the demand to address these complexities.

This paper shows an analysis of dual peg-hole extraction problems in two dimensions, highlighting the boundary conditions of jamming and proposing a solution using active compliance to avoid jamming.

The effectiveness of the active compliance strategy in robotics for peg-hole assembly and disassembly lies in its adaptability, precise force control [12], sensitivity, safety, efficiency, versatility, and demonstrated real-world applications. This approach empowers robots to dynamically adjust to their environment, responding in real time to factors such as misalignments or surface irregularities, thus reducing the length of the jamming area in peg-hole operations. Additionally, by employing force sensing, robots can accurately apply the necessary force for insertion and removal without causing damage to the components. This precision and adaptability make active compliance a valuable and reliable solution, particularly in industrial settings demanding high-precision performance [26].

Section 2.2 presents an analysis of multiple peg extraction during disassembly. Section 2.3 provides a geometric analysis of dual-peg extraction. Section 2.4 describes the force analysis of dual-peg extraction. Section 2.5 presents the experimental design and the results that confirm the theoretical disassembly model.

2.2 Analysis of multiple peg extraction during disassembly

Dual peg-hole extraction is a disassembly task in which two pegs are held together, moved together, and removed from their respective holes at the same time (Figure 2.1). Although peg-hole disassembly is a three-dimensional problem, it can be schematically illustrated and analysed in two dimensions for simplicity [6]. To ensure that the simplified 2D model can represent 3D contact conditions, Lan *et al* [25] investigated the correctness of using two-

dimensional instead of three-dimensional models for peg-hole system analysis and compared the results obtained from 2D and 3D models. The authors concluded that the 2D model can be used to represent the challenges in 3D if the following conditions are met:

1. The peg and hole are circular and axisymmetric.
2. The peg and hole are aligned.
3. The peg is not tilted.
4. The clearance between the peg and hole is smaller than the peg size.

Given these insights, we also adopted the simplified 2D model for our analysis, which focuses on the geometry and contact states of dual peg-holes. The analysis assumes two pegs of equal length and makes the following assumptions: (a) the pegs are stiff, (b) extraction occurs only vertically upwards, and (c) the active compliance centre is located along the extraction axis between the two holes.

Based on the assumptions stated above, the forces and moments generated by contacts between pegs and holes can be calculated. Predicting force and torque during disassembly helps identify configurations in which the compliant devices supporting the pegs, such as a remote centre compliance (RCC), spatial RCC (SRCC), or active compliance centre, may fail to avoid wedging and jamming [23]. The force/torque analysis provides a better understanding of the physics of multiple peg-out-hole extractions using compliance mechanisms. The extraction phase of the dual-peg extraction problem is thoroughly examined in the following sections.

2.3 Geometric analysis of dual-peg extraction

2.3.1 Extractability

Consider a dual peg-hole set with dimensions as shown in Figure 2.1. Peg 1 and Peg 2 have radii of r_{P_1} and r_{P_2}, respectively. Hole 1 and Hole 2 have radii of R_{H_1} and R_{H_2}, respectively.

The distance between the axes of the pegs is D_P,and the distance between the axes of the holes is D_H.The distance between Peg 1 and Hole 1 is C_1, and the distance between Peg 2 and Hole 2 is C_2. The current extraction depth is represented by h.

The necessary conditions for dual peg-hole disassembly are as follows:

a) The pegs must be smaller than their corresponding holes:

$$r_{P_1} < R_{H_1}, \text{ and } r_{P_2} < R_{H_2} \tag{2.1}$$

b) The distance between the outer edges of the pegs must be less than the distance between the outer edges of the holes:

$$D_P + r_{P_1} + r_{P_2} < D_H + R_{H_1} + R_{H_2} \tag{2.2}$$

c) The distance between the inner edges of the pegs must be greater than the distance between the inner edges of the holes:

$$D_P - r_{P_1} - r_{P_2} > D_H - R_{H_1} - R_{H_2} \tag{2.3}$$

Conditions b and c can be written as $-(C_1+C_2) < D_H + D_P < C_1+C_2$, where C_1 and C_2 are the clearances, e.g., $C_1 = R_{H_1} - r_{P_1}$ and $C_2 = R_{H_2} - r_{P_2}$. For the dual pegs to be extracted, all these conditions must be met at the same time. The ability of pegs to be extracted from their corresponding holes is referred to as extractability.

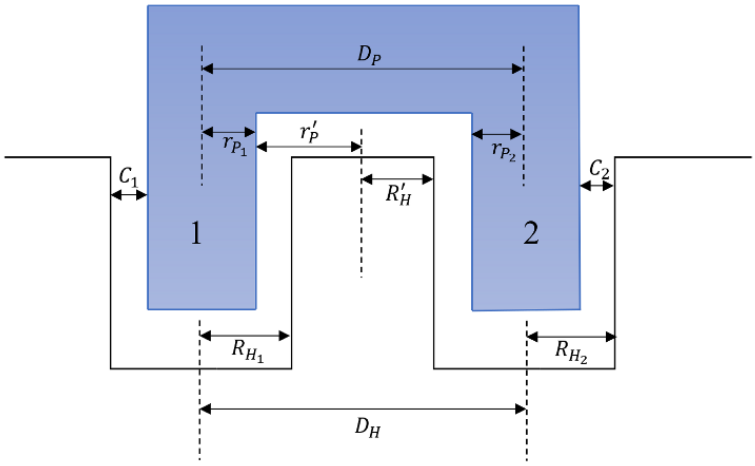

Figure 2.1. The geometric model of a dual peg-hole

2.3.2 Prediction of possible contact states

Figure 2.2 shows dual pegs that are extractable based on their maximum left and right travels. The pegs are rotated clockwise and anticlockwise while maintaining their current contact to produce other possible contact states. There are 13 possible contact states [23] that can exist in a dual peg-hole disassembly process (Table 2.1). The contact states can be divided into four main groups: (a) no contact, (b) one-point contact, (c) two-point contact, and (d) line contact, as shown in Figure 2.3.

Ideally, the pegs should be in a state of no contact, but this rarely happens. The process typically begins with two-point contact due to compliant manipulation and the presence of lateral and angular errors. This occurs when a compliant manipulator grips a peg, causing it to shift and rotate (Figure 2.3c). As the peg is extracted, the errors may decrease due to compliance, and the process may transfer to one-point contact (Figure 2.3b) or line contact (Figure 2.3d). To transfer from the two-point to one-point contact, the peg must rotate during the extraction process (Figure 2.3b). The one-point contact state is maintained until the peg is completely extracted from the hole.

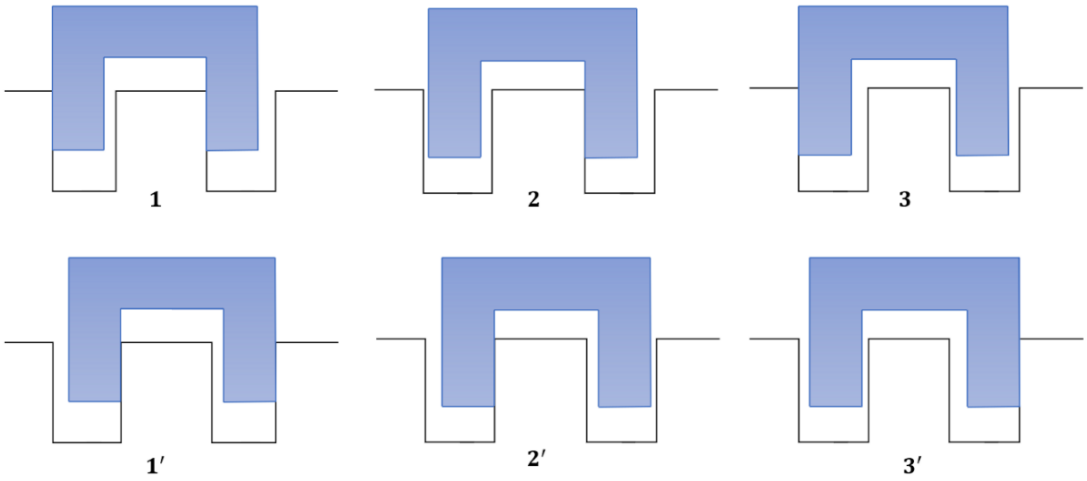

Figure 2.2. Maximum left- and right-side travel cases

TABLE 2.1 Various contact states for dual-peg extractions

	One-point contact	Two-point contact	Line contact
One of the dual pegs	1, 2, 3, 4	5, 6	7, 8
Inner		9	
Outer		10	
Both pegs		11, 12	13

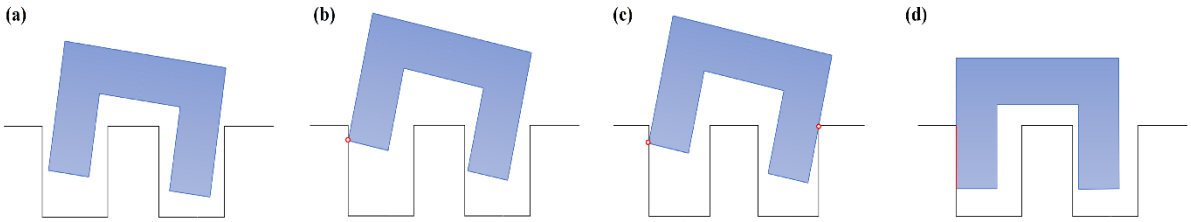

Figure 2.3. Typical states of the dual peg-hole disassembly process: (a) no contact, (b) one-point contact, (c) two-point contact, and (d) line contact

Sathirakul and Sturges [23] and Fei and Zhao [27] found that in 2D cases, the three-point and four-point contact states during peg-in-hole insertion can only exist when certain conditions are met, such as given dimensions and associated insertion depth. As a result, these contact states are considered transient and unimportant in peg-hole insertion. Peg-hole insertion and extraction follow the same geometric analysis.

A three-point contact can occur if equations (2.4) and (2.4) are satisfied simultaneously (θ is the tilt angle of the peg).

$$h \sin\theta + 2r_{P_1} \cos\theta = 2R_{H_1} \tag{2.4}$$

and,

$$h \sin\theta + \left(2r_{P_1} + 2r'_P + 2r_{P_2}\right) \cos\theta = 2R_{H_1} + 2R'_H + 2R_{H_2} \tag{2.5}$$

Similarly, four-point contact can only occur if equations (2.4) and (2.6) are both satisfied (Figure 2.4).

$$h_2 \sin\theta + \left(2r_{P_2}\right) \cos\theta = 2R_{H_2} \tag{2.6}$$

Therefore, three-point and four-point contacts are considered transitory and insignificant, as they only occur at specific insertion depth points rather than in a depth region [23], [27].

Jamming is a common problem in peg-hole disassembly. Jamming occurs when a peg is unable to move due to improperly applied forces and moments. It can occur in the two-point contact state and can be avoided by reducing the two-point contact region and controlling the position where two-point contact occurs [28]. In the case of three-point and four-point contacts,

these issues are minimal because they occur at specific depth points rather than at specific regions. As a result, this study focuses on jamming analysis in two-point contact states.

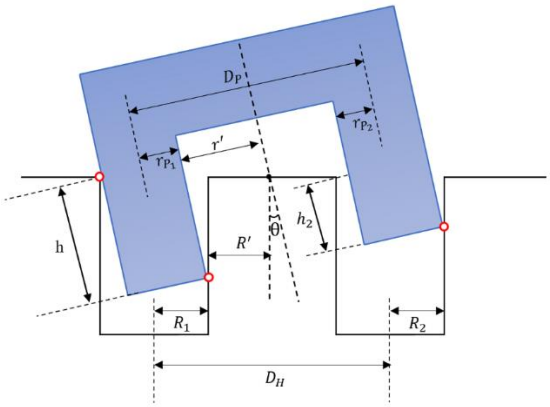

Figure 2.4. Three-point contact state of dual peg-in-hole

2.4 Force analysis of dual-peg extraction

Analysing forces and moments during dual-peg extraction is important for planning fine motions. Several conditions must be met for the successful extraction of dual pegs from their holes. During extraction, the dual pegs may experience various contact states, some of which may be more desirable than others. To maintain each contact state, it is necessary to derive the conditions of applied forces and moments. A two-dimensional dual-peg problem may have 13 possible states (Table 2.1), but contact states with more than two-point contacts are insignificant in jamming, as explained in Section 3. In general, dual peg-hole problems can be considered similar to one peg-hole problem in terms of two-point contact states (Figure 2.5). Two-point contact states in dual peg-holes can be categorised into three groups: a) contact in one of the dual peg-holes, b) external surfaces of pegs contacting hole surfaces, and c) inner surfaces of pegs contacting hole surfaces. This section analyses a contact from each category.

2.4.1 Derivation of force-moment conditions for maintaining contact states

Consider two pegs of the same length with dimensions, as shown in Figure 2.6.a. The reference frame for the dual pegs in each state is located at the end of the selected peg (shown in orange). All forces and moments acting on the pegs are prescribed with respect to this reference frame. It is assumed that the dual pegs and the hole are initially in two-point contact and that the angle is small to simplify the calculations. This assumption is valid because, in practice, the peg's angular error is typically only a few degrees at most.

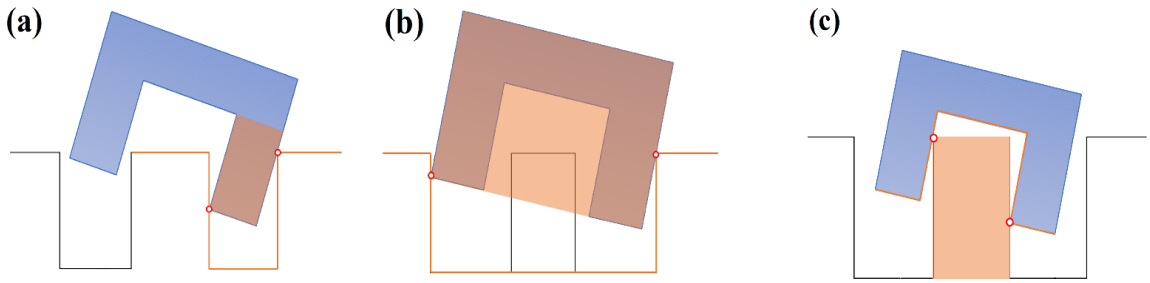

Figure 2.5. Classification of two-point contact states in dual peg-hole disassembly.

As shown in Figure 2.6.b , δ_0 and β_0 represent the initial lateral and angular errors, respectively. The compliance centre and the tip of the peg are located at distances U_0 and ε_0 from the axis of the hole, respectively.

I. Contact in one of the dual peg-holes

In this section, the contact states of two points that occur in one of the peg-holes (Figure 2.5.a) are analysed. There are 4 possible contact states in this situation. The force analysis of one of these contact states is presented here as an example. Consider the quasistatic equilibrium condition of double pegs in contact mode 5 (Table 2.1), as shown in Figure 2.7.

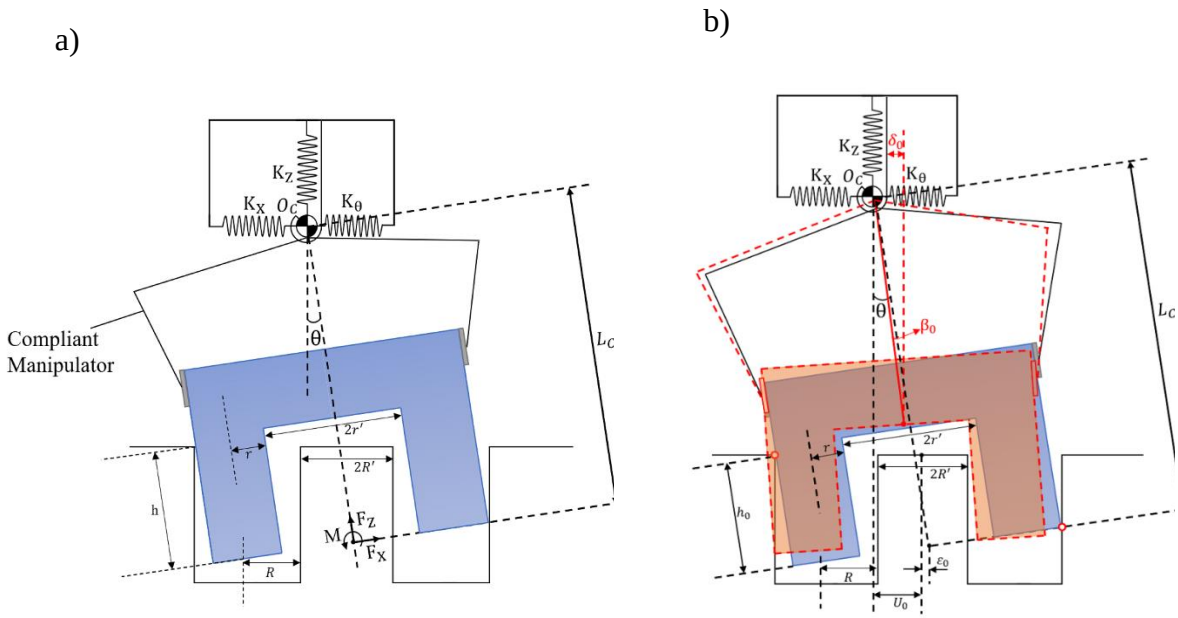

Figure 2.6. a) Dimensions and reference frame for dual peg-hole, b) Definition of the initial position in the dual peg-hole

Extraction forces (F_z), (F_x) and moments (M) are applied to the studs at point O, which is the origin of the reference frame. The distances U and ε vary continuously during disassembly. The path of the compliance centre can be deduced as follows:

$$U + \varepsilon = L_C \sin\theta$$

$$U - U_0 + (\varepsilon - \varepsilon_0) = L_C(\theta - \theta_0)$$

$$\varepsilon = r' \cos\theta - R'$$

$$U - U_0 = L_C(\theta - \theta_0) \tag{2.7}$$

In this equation, L_C is the distance between the compliance centre and the tip of the pegs, and h is the depth of peg extraction.

During two-point contact, the geometrical relations are as follows, based on geometrical constraints between the dual peg-holes:

$$R = \frac{h \sin\theta}{2} + r \cos\theta \tag{2.8}$$

In the case of small clearances between pegs and holes, equation (2.8) can be simplified as:

$$h\theta = 2CR\,, \qquad C = \frac{R - r}{R} \;\; ; \; C\text{: Clearance ratio for first peg} - \text{hole} \tag{2.9}$$

Whitney's [10] method can be re-expressed contact and supporting forces at and around the compliance centre in the coordinate frame fixed at the tip of the selected peg.

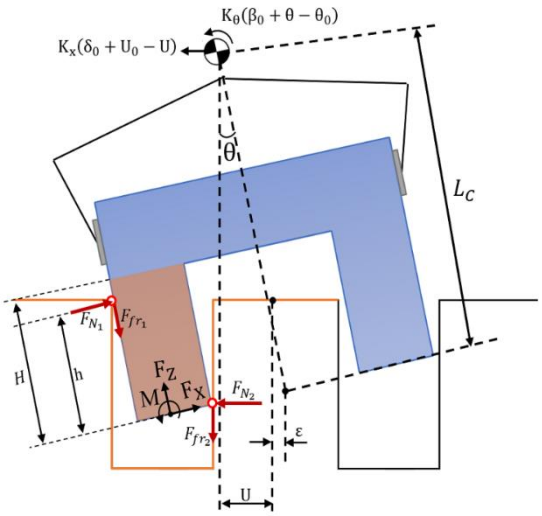

Figure 2.7. Geometry and forces during the two-point contact in one of the dual peg-holes

$$F_x = F_{N2} - F_{N1}$$

$$F_z = \mu(F_{N1} + F_{N2}) \tag{2.10}$$

$$M = (h - \mu r)F_{N1} + \mu r F_{N2}$$

The following is the applied force and moment by the compliance centre:

$$F_x = -K_x(\delta_0 + U_0 - U)$$

$$M = K_x L_C(\delta_0 + U_0 - U) + K_\theta(\beta_0 + \theta - \theta_0) \tag{2.11}$$

By assuming $F_{N2} = 0$ for the contact force at point 2, it is possible to calculate the boundary conditions for the two-point contact. Accordingly, the contact forces are as follows:

$$F_x = -F_{N1}$$

$$F_z = \mu F_{N1} \tag{2.12}$$

$$M = (h - \mu r)F_{N1}$$

The path of the centre of compliance in the boundary conditions of the two-point contact state is expressed as follows using equations (2.7) and (2.12).

$$\theta = \theta_0 - \beta_0 + \frac{K_x(h - \mu r - L_C)(L_C\beta_0 + \delta_0)}{K_x L_C(h - \mu r) - K_x L_C^2 + K_\theta}$$

and

$$U = U_0 + \delta_0 - \frac{K_\theta(L_C\beta_0 + \delta_0)}{K_x L_C(h - \mu r) - K_x L_C^2 + K_\theta} \tag{2.13}$$

By substituting equations (2.8) and (2.9) into equation (2.13), a quadratic equation can be generated, which will be the roots of the equation for extraction depth h:

$$\alpha h^2 + \beta h + \gamma = 0 \tag{2.14}$$

where

$$\alpha = A + K_x L_C B$$

$$\beta = (E - \mu r K_x L_C)B - (L_C + \mu r)A - 2cRK_x L_C$$

$$\gamma = 2cR(\mu r K_x L_C - E)$$

$$A = K_x(L_C\beta_0 + \delta_0)$$

$$B = \theta_0 - \beta_0$$

$$E = K_\theta - K_x L_C^2$$

The roots (extraction depth[1]) of equation (2.14) are:

$$h_2 = \frac{-\beta + \sqrt{\beta^2 - 4\alpha\gamma}}{2\alpha}, h_2' = \frac{-\beta - \sqrt{\beta^2 - 4\alpha\gamma}}{2\alpha} \tag{2.15}$$

[1] The period of the equation's roots (h_2 & h_2') is discussed in section IV.

The roots h_2 and h_2', which represent the beginning and end of a two-point contact zone, can be found by solving equation (2.14).

In the one-point contact state, the geometrical parameters are as follows ($\theta \approx 0$):

$$\begin{aligned} U &= L_C\theta - \varepsilon \\ \varepsilon &= r'\cos\theta - R' \\ U &= L_C\theta - r' + R' \end{aligned} \tag{2.16}$$

The equations for U and θ and of the one-point contact can be obtained by combining equations (2.11) and (2.12) in a coordinate frame fixed to the selected peg tip.

$$\begin{aligned} U &= \delta_0 + U_0 - \frac{N_2 + K_\theta\theta}{K_x(h - \mu r - L_C)} \\ \theta &= \frac{N_2 - K_x N_1(h - \mu r - L_C)}{-K_x L_C(h - \mu r - L_C) - K_\theta} \end{aligned} \tag{2.17}$$

where:

$$\begin{aligned} N_1 &= \delta_0 + U_0 - R' + r' \\ N_2 &= K_\theta(\beta_0 - \theta_0) \end{aligned} \tag{2.18}$$

The reaction force and extraction force during the two-point contact can be obtained from equation (2.10), which is composed of three equations and three unknown parameters:

$$\begin{aligned} F_{N1} &= -\frac{\mu r}{h}F_x + \frac{1}{h}M \\ F_{N2} &= \frac{h - \mu r}{h}F_x + \frac{1}{h}M \\ F_z &= \frac{M}{\lambda r} - \frac{\mu}{\lambda}(1 - \lambda)F_x \quad ; \quad \lambda = \frac{h}{2r\mu} \end{aligned} \tag{2.19}$$

Equation (2.11) with equations (2.7) and (2.9) substituted produces $F_x$and M for the two-point contact state.

$$F_x = -k_x\left(\delta_0 + L_C\theta_0 - \frac{cDL_C}{h}\right)$$

$$M = k_x L_C(\delta_0 + L_C\theta_0) - \frac{k_x {L_C}^2 CD}{h} + k_\theta(\beta_0 - \theta_0) + \frac{k_\theta CD}{h} \tag{2.20}$$

where $h\theta = 2CR = CD; D = 2R$

By substituting equation (2.13) into equation (2.12), the extraction force in the one-point contact state is calculated.

$$F_z = \frac{\mu k_\theta(\theta - \theta_0 + \beta_0)}{(h - \mu r - L_C)} \tag{2.21}$$

II. External surfaces of pegs contacting hole surfaces

In this part, the states where the external surfaces of the pegs contact the hole surfaces are analysed, as shown in Figure 2.5.b. There are 4 possible contact states in this situation, and one of these contact states is presented as an example. Consider the quasistatic equilibrium condition in contact mode 10, as shown in Table 2.1. Extraction forces, F_X and F_z, and moments, M, are applied to the stud at point O, which is the origin of the reference frame. The distances U and ε (Figure 2.8) are very continuous during disassembly.

where in this case, $2R = 2R_{H_1} + 2R_{H_2} + 2R'$ and $2r = 2r_{p_1} + 2r_{p_2} + 2r'$.

The path of the compliance centre can be deduced as follows:

$$U + \varepsilon = L_C \sin\theta \;;\; \varepsilon = \frac{h\theta}{2}$$

$$U - U_0 + \left(\frac{h\theta}{2} - \varepsilon_0\right) = L_C(\theta - \theta_0) \tag{2.22}$$

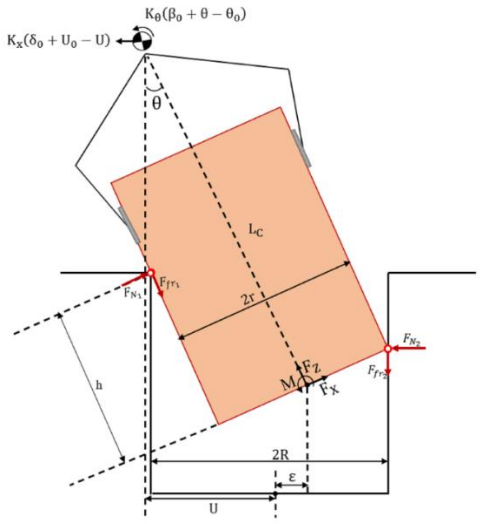

Figure 2.8. Geometry and forces during the two-point contact in the external surfaces of pegs contact holes surfaces

During two-point contact, the geometrical relations are as follows, based on geometrical constraints between the dual peg-holes:

$$R = \left(\frac{h}{2}\right)\sin\theta + r\cos\theta \tag{2.23}$$

In the case of small clearances between pegs and holes, equation (2.23) can be simplified as

$$h\theta = 2CR \;; \quad C = \frac{(R-r)}{R} \;;\; C\text{: Clearance ratio for both peg} - \text{hole} \tag{2.24}$$

Contact forces and supporting forces at and about the compliance centre in the coordinate frame fixed at the tip of the peg:

$$F_x = F_{N2} - F_{N1}$$

$$F_z = \mu(F_{N1} + F_{N2}) \tag{2.25}$$

$$M = (h - \mu r)F_{N1} + \mu r F_{N2}$$

The following is the applied force and moment by the compliance centre:

$$F_x = -K_x(\delta_0 + U_0 - U)$$

$$M = K_x L_C(\delta_0 + U_0 - U) + K_\theta(\beta_0 + \theta - \theta_0) \tag{2.26}$$

Boundary conditions of two-point contact when $F_{N2} = 0$:

$$F_x = -F_{N1}$$

$$F_z = \mu F_{N1} \tag{2.27}$$

$$M = (h - \mu r)F_{N1}$$

The path of the compliance centre in the boundary conditions of the two-point contact state is expressed as follows using equations (2.22) and (2.27):

$$\theta = \theta_0 - \beta_0 + \frac{K_x(h - \mu r - L_C)(L_C\beta_0 + \delta_0 + CR - \varepsilon_0)}{K_x L_C(h - \mu r) - K_x L_C^2 + K_\theta}$$

$$U = U_0 + \delta_0 - \frac{K_\theta(L_C\beta_0 + \delta_0 + CR - \varepsilon_0)}{K_x L_C(h - \mu r) - K_x L_C^2 + K_\theta} \tag{2.28}$$

A quadratic equation can be generated by substituting equations (2.23) and (2.24) into equation (2.28), which will be the roots of the equation for extraction depth[1] (h):

$$\alpha h^2 + \beta h + \gamma = 0 \tag{2.29}$$

where

$$\alpha = A + K_x L_C B$$

[1] The period of the equation's roots (h_2 & h_2') is discussed in section IV.

$$\beta = (E - \mu r K_x L_C)B - (L_C + \mu r)A - 2cRK_x L_C$$

$$\gamma = 2CR(\mu r K_x L_C - E)$$

$$A = K_x(L_C\beta_0 + \delta_0 + CR - \varepsilon_0)$$

$$B = \theta_0 - \beta_0$$

$$E = K_\theta - K_x L_C^2$$

The solutions of equation (2.29):

$$h_2 = \frac{-\beta + \sqrt{\beta^2 - 4\alpha\gamma}}{2\alpha} \quad , \quad h_2' = \frac{-\beta - \sqrt{\beta^2 - 4\alpha\gamma}}{2\alpha} \tag{2.30}$$

The geometrical constraints during one-point contact ($\theta \approx 0$):

$$U = L_C\theta - h\theta + CR \tag{2.30}$$

The path of the compliance centre during one-point contact by using equations (2.26) and (2.27):

$$U = \delta_0 + U_0 - \frac{N_2 + K_\theta\theta}{K_x(h - \mu r - L_C)}$$

$$\theta = \frac{N_2 - K_x N_1(h - \mu r - L_C)}{-K_x(L_C - h)(h - \mu r - L_C) - K_\theta} \tag{2.31}$$

where

$$N_1 = \delta_0 + U_0 - CR$$

$$N_2 = K_\theta(\beta_0 - \theta_0) \tag{2.32}$$

The reaction force and extraction force during the two-point contact can be obtained from equation (2.25):

$$F_{N1} = -\frac{\mu r}{h}F_x + \frac{1}{h}M$$

$$F_{N2} = \frac{h - \mu r}{h}F_x + \frac{1}{h}M$$

$$F_z = \frac{M}{\lambda r} - \frac{\mu}{\lambda}(1-\lambda)F_x \quad ; \quad \lambda = \frac{h}{2r\mu} \tag{2.33}$$

F_x and M for two-point contact by using equations (2.22), (2.24) and (2.26):

$$F_x = -k_x\left(\delta_0 - \varepsilon_0 + L_C\theta_0 + CD/2 - \frac{cDL_C}{h}\right)$$

$$M = k_x L_C(\delta_0 - \varepsilon_0 + L_C\theta_0 + CD/2) - \frac{k_x L_C^2 CD}{h} + k_\theta(\beta_0 - \theta_0) + \frac{k_\theta CD}{h} \tag{2.34}$$

The extraction force in the one-point contact state is calculated by substituting equation (2.31) into equation (2.27).

$$F_z = \frac{\mu k_\theta(\theta - \theta_0 + \beta_0)}{(h - \mu r - L_C)} \tag{2.35}$$

III. Inner surfaces of pegs contacting holes surfaces

This section analyses the two-point contact state where the inner surfaces of pegs contact holes. As shown in Figure 5. c, an inverted peg-hole is considered. There are 2 possible contact states in this situation. As in the previous sections, the force analysis of one of these contact states is presented as an example. Consider the quasistatic equilibrium condition of the dual pegs in contact mode 9, as shown in Table 2.1. The distances U and ε (Figure 2.9) are very continuous during disassembly. The path of the compliance centre can be deduced as follows:

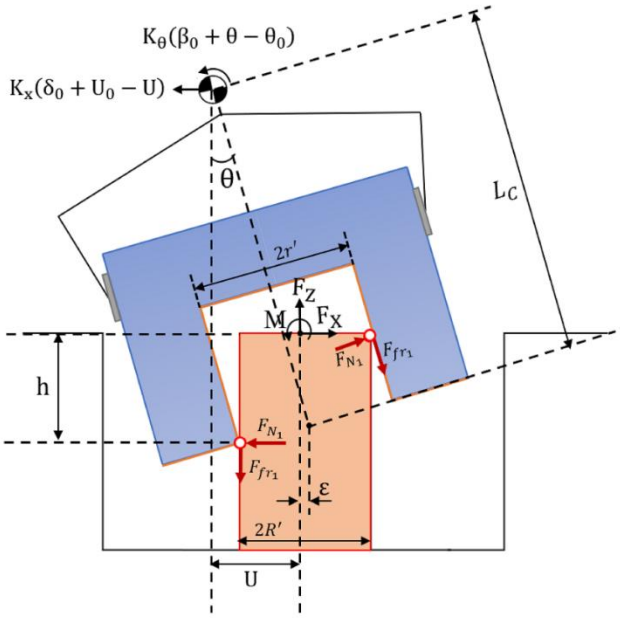

Figure 2.9. Geometry and forces during two-point contact in the inner surfaces of pegs contact holes surfaces

$$U + \varepsilon = L_C \sin\theta$$

$$\varepsilon = r'\cos\theta - R'$$

$$U - U_0 = L_C(\theta - \theta_0) \tag{2.36}$$

Considering an inverted peg-hole, the radius of the hole, which is considered in this section as the radius of the peg, is as follows:

$$R' = \frac{r'}{\cos\theta} - \frac{h}{2}\tan\theta \tag{2.37}$$

For small clearances between pegs and holes, equation (2.37) can be simplified as follows:

$$h\theta = 2R'C \;\; ; \quad C = \frac{(r' - R')}{r'} \; ; \; C\text{: Clearance ratio for both peg} - \text{hole} \tag{2.38}$$

Contact forces and supporting forces at and about the compliance centre in the coordinate frame fixed at the tip of the peg are given by

$$F_x = F_{N2} - F_{N1}$$

$$F_z = \mu(F_{N1} + F_{N2})$$
$$M = (h - \mu R')F_{N1} + \mu R' F_{N2} \tag{2.39}$$

The following is the applied force and moment by the compliance centre:

$$F_x = -K_x(\delta_0 + U_0 - U)$$
$$M = K_x(L_C - h)(\delta_0 + U_0 - U) + K_\theta(\beta_0 + \theta - \theta_0) \tag{2.40}$$

Boundary conditions of two-point contact when $F_{N1} = 0$:

$$F_x = F_{N2}$$
$$F_z = \mu F_{N2}$$
$$M = \mu R' F_{N2} \tag{2.41}$$

The path of the compliance centre in the boundary conditions of the two-point contact state is expressed as follows using equations (4.3.1), (4.3.5) and (4.3.6):

$$\theta = \theta_0 - \beta_0 + \frac{K_x(h - \mu R' - L_C)(\delta_0 + L_C\beta_0)}{K_x L_C(h - \mu R') - K_x {L_C}^2 + K_\theta}$$
$$U = U_0 + \delta_0 - \frac{K_\theta(L_C\beta_0 + \delta_0)}{K_x L_C(h - \mu R') - K_x {L_C}^2 + K_\theta} \tag{2.42}$$

A quadratic equation can be generated by substituting equations (2.37) and (2.38) into equation (2.42), which will be the roots of the equation for extraction depth[1] h:

$$\alpha h^2 + \beta h + \gamma = 0 \tag{2.43}$$

where

$$\alpha = A + K_x L_C B$$
$$\beta = \left(E - K_x L_C^2\right)B - (\mu R' + L_C)A - (-2R'C)K_x L_C$$
$$\gamma = (-2R'C)\left(K_x L_C^2 - E\right)$$

[1] The period of the equation's roots (h_2 & h_2') is discussed in section IV.

$$A = K_x(\delta_0 + L_C\beta_0)$$

$$B = \theta_0 - \beta_0$$

$$E = K_\theta - \mu R' K_x L_C$$

So,

$$(A + K_x L_C B)h^2 + \left(\left(E - K_x L_C^2\right)B - (\mu R' + L_C)A - (-2R'C)K_x L_C\right)h + (-2R'C)\left(K_x L_C^2 - E\right) = 0$$

The solutions of equation (2.43):

$$h_2 = \frac{-\beta + \sqrt{\beta^2 - 4\alpha\gamma}}{2\alpha} \quad , \quad h_2' = \frac{-\beta - \sqrt{\beta^2 - 4\alpha\gamma}}{2\alpha} \tag{2.44}$$

The geometrical constraints during one-point contact ($\theta \approx 0$):

$$U = L_C\theta - \varepsilon$$

$$\varepsilon = r' - R'$$

$$U = L_C\theta - r' + R' \tag{2.45}$$

The path of the compliance centre during one-point contact by using equations (2.40) and (2.41) and θ is obtained using equations (2.45) and U:

$$U = \delta_0 + U_0 - \frac{N_2 + K_\theta\theta}{K_x(h - \mu R' - L_C)}$$

$$\theta = \frac{N_2 - K_x N_1(h - \mu R' - L_C)}{-K_x L_C(h - \mu R' - L_C) - K_\theta} \tag{2.46}$$

where

$$N_1 = \delta_0 + U_0 - R' + r', N_2 = K_\theta(\beta_0 - \theta_0) \tag{2.47}$$

The reaction force and extraction force during the two-point contact can be obtained from equation (2.39):

$$F_{N1} = -\frac{\mu R'}{h} F_x + \frac{1}{h} M$$

$$F_{N2} = \frac{h - \mu R'}{h} F_x + \frac{1}{h} M$$

$$F_z = \frac{M}{\lambda R'} - \frac{\mu}{\lambda}(1-\lambda)F_x \quad ; \quad \lambda = \frac{h}{2R'\mu} \tag{2.48}$$

F_x and M for two-point contact by using equations (2.36), (2.38) and (2.40):

$$F_x = -k_x\left(\delta_0 + L_C\theta_0 - \frac{L_C(-2R'C)}{h}\right)$$

$$M = k_x L_C(\delta_0 + L_C\theta_0 - h\theta - 2R'C) - \frac{k_x {L_C}^2(-2R'C)}{h} - k_x h\delta_0 + k_\theta(\beta_0 - \theta_0)$$

$$+ \frac{k_\theta(-2R'C)}{h} \qquad (4.3.14)$$

The extraction force in the one-point contact state is calculated by substituting equation (2.46) into equation (2.41):

$$F_z = \frac{-\mu k_\theta(\theta - \theta_0 + \beta_0)}{(h - \mu R' - L_C)} \tag{2.49}$$

IV. Region of extraction depth

In equations (2.14), (2.29), and (2.43), h_2 and h_2' are the two roots representing the depth of extraction (h). The parameters h_2 and h_2' represent the beginning and end of the two-point contact region, respectively. If $h_2' < h_0$, the peg and hole would be in the two-point contact area at the start of the disassembly process. If $h_0 < h_2' < h_2$, the peg-hole is initially in one-point contact, and there is at least one transformation between the one-point contact and two-point contact states. Two-point contact cannot occur during disassembly if the equations have no solution. If $h_0 < h_2' = h_2$, the peg-hole has a two-point contact state at a certain depth point. The height and position of the two-point contact region are influenced by many parameters,

including the geometrical parameters of the hole-peg system, the location of the compliance centre, initial position errors, and the degree of compliance.

V. Jamming region

Jamming can be determined using equilibrium equations for rigid pegs [10]. Combining equations (2.10), (2.25), or (2.39) reveals the linear relationship for a peg in two-point contact:

$$\frac{M}{hF_Z} = \frac{h}{2r\mu} - \frac{F_X}{F_Z}\left(\frac{h}{2r} - \mu\right) \tag{2.50}$$

$$\frac{F_X}{F_Z} = \pm\frac{1}{\mu} \tag{2.51}$$

Based on (2.50) and (2.51),

$$\frac{M}{hF_Z} = \pm\left(\frac{h}{2r\mu} + 1\right) \tag{2.52}$$

As illustrated in Figure 2.10, equations (2.50) and (2.52) define the equilibrium instance (shown by the outline of the parallelogram) where the pegs are extracted from the holes based on the combination of F_X, F_Z, and M. Jamming occurs when combinations of F_X, F_Z, and M falls outside the parallelogram, while successful extraction occurs when they fall within the parallelogram. As h decreases, the peg is closer to the mouths of the hole, and the probability of jamming decreases [11]. Jamming becomes less likely as the peg is extracted from the hole.

2.4.2 Key factors and their effects

In the two-point contact state, the reaction forces applied to the pegs increase the risk of extraction failure, especially at the mouth of the hole. Two-point contact also increases the extraction force due to angular and lateral errors. This section identifies the most influential parameters for reducing the two-point region and their effect on its location.

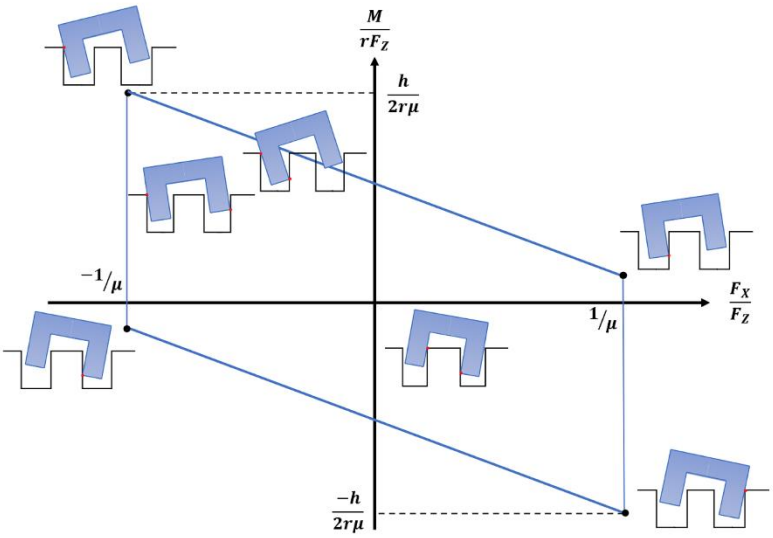

Figure 2.10. Jamming diagrams for the dual-peg extraction problem based on contact forces[23].

Parameters L_C, δ_0, K_x, and k_θ have been examined to demonstrate their impacts on the two-point contact region. These investigations are discussed in the following sections.

I. Location of compliance centre

A key design parameter is the placement of the compliance centre along the central axis of the pegs. When a compliant manipulator grasps a peg, initial position errors between the manipulator and the dual peg-hole system cause the peg to shift and rotate. Assuming that the dual peg-hole is solid (Figure 2.6), the black figure shows the initial location of the peg before the initial angular error. However, the initial lateral error causes the peg to displace and rotate around the compliance centre (red figure). If the compliance centre is positioned far from the peg tip, the peg rotates anticlockwise around it. In this case, the one-point contact state might change into a two-point contact. If the compliance centre is positioned at the peg tip, it rotates clockwise around it when grasped, resulting in one-point or line contact between the pegs and holes. These characteristics can help minimise the two-point contact region during disassembly. Figure 2.11 shows the boundary conditions of the two-point contact region based on the equations of extraction depth (h_2 & h_2'). It is clear that when the

compliance centre is near the tip of the peg, the two-point contact area is significantly smaller. Additionally, as L_C decreases, the two-point contact region shifts to the hole mouth.

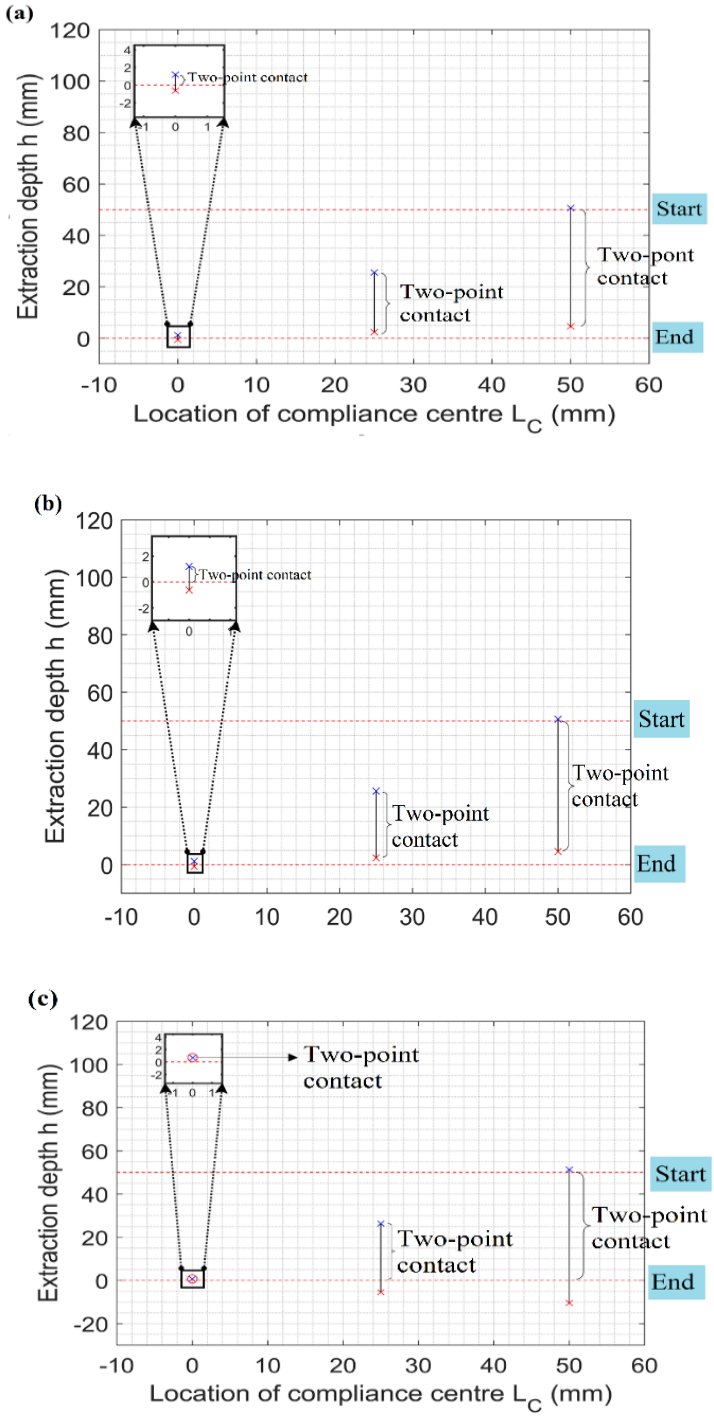

Figure 2.11. Dependence of the two-point contact region on the location of the compliance centre with $\delta_0 = 2$ mm, $\beta_0 = 0$ rad, $K_X = 0.4$ N mm^{-1}, $K_\theta = 30*10^4$ Nmm rad^{-1}. a) Contact in one of the dual peg-holes, b) External surfaces of pegs contact holes surfaces, c) Inner surfaces of pegs contact holes surfaces

II. Initial position errors

The two-point contact region can be influenced by initial position errors, including lateral and angular errors between the compliant manipulator and the peg-hole system. When the compliance centre is located far from the tip, a large lateral δ_0 error can cause the peg to rotate anticlockwise significantly. If δ_0 is large enough, the peg and hole will remain in two-point contact during disassembly. If the compliance centre is at the tip, the peg rotates clockwise during disassembly. From the two-point contact, the hole and peg transition to one-point contact or line contact [12]. Figures 2.12, 2.13, and 2.14 show the effects of the initial lateral error on the two-point contact region for various compliance centre locations. The two-point contact region decreases as the lateral error increases when the compliance centre is near the tip of the peg. Angle errors affect the disassembly process both in magnitude and direction. When the compliance centre is far from the peg tip and the initial angular error is opposite to the rotation of the peg, as shown in Figure 2.15, a two-point contact region can be reduced. Otherwise, the two-point contact region increases. The effects of the initial angular error are similar when the compliance centre is at the tip of the peg.

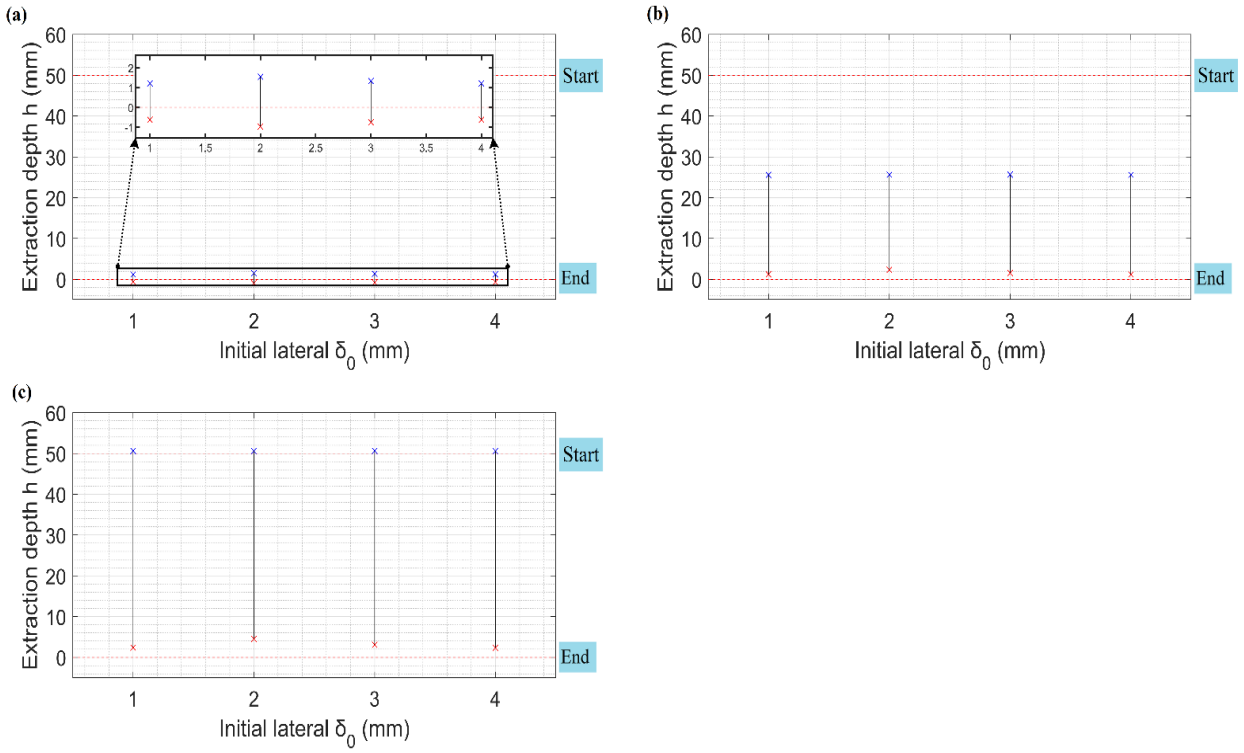

Figure 2.12 The effect of the initial lateral error on the two-point contact region in one of the dual peg-holes: (a) $L_C = 0$ *,(b)* $L_C = 25$*, (c)* $L_C = 50$ *with* $\beta_0 = 0$ *rad,* $K_X = 0.4$ *N mm*$^{-1}$*,* $K_\theta = 30*10^4$ *Nmm rad*$^{-1}$*.*

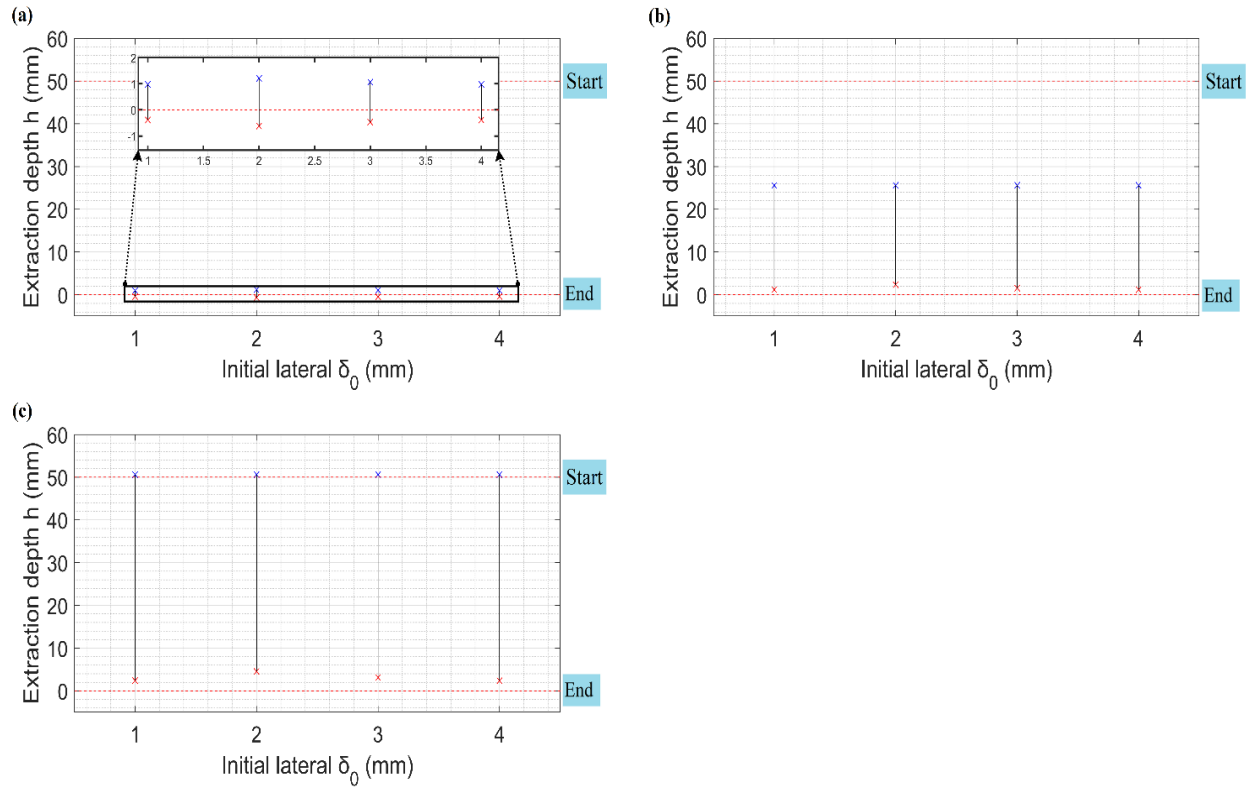

Figure 2.13. The effect of initial lateral error on the two-point contact region in the contact of the inner surfaces of the pegs with the holes: (a) $L_C = 0$ *,(b)* $L_C = 25$*, (c)* $L_C = 50$ *with* $\beta_0 = 0$ *rad,*$K_X = 0.4$ *N mm*$^{-1}$*,* $K_\theta = 30*10^4$ *Nmm rad*$^{-1}$*.*

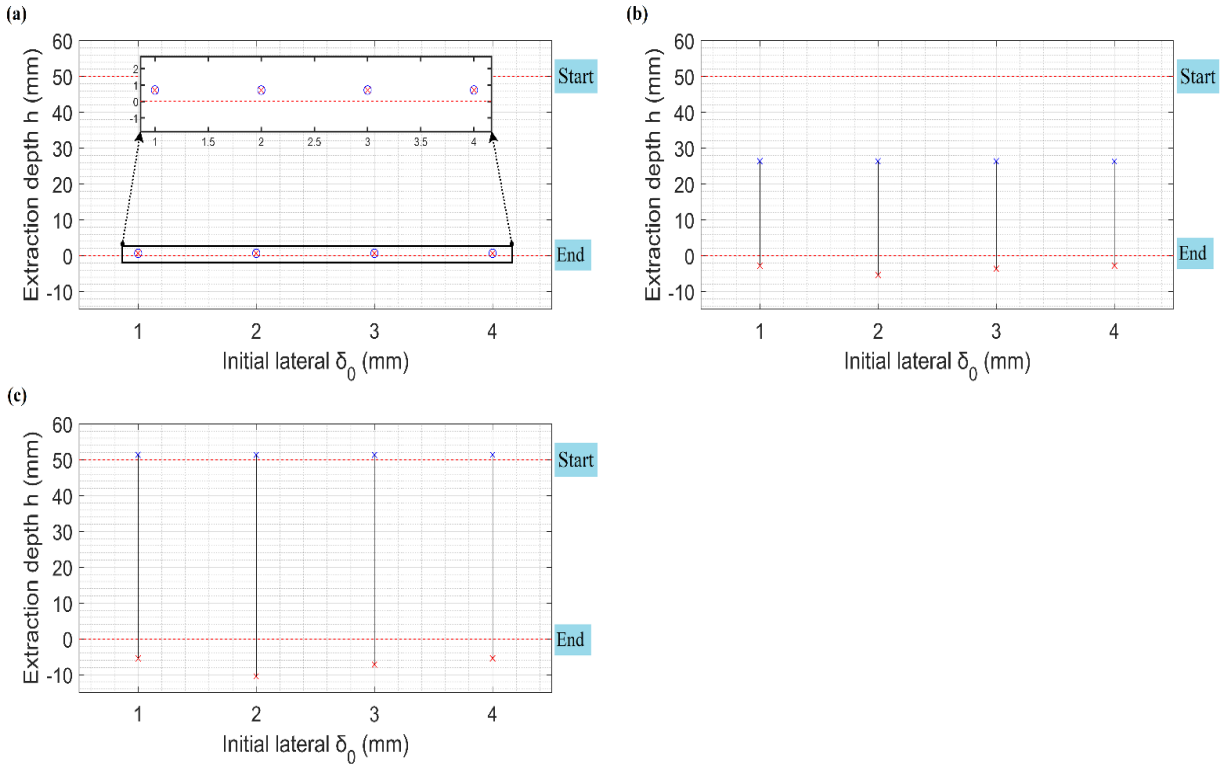

Figure 2.14. The effect of initial lateral error on the two-point contact region in the contact of the external surfaces of the pegs with the holes: (a) $L_C = 0$, (b) $L_C = 25$, (c) $L_C = 50$ with $\beta_0 = 0$ rad, $K_X = 0.4$ N mm^{-1}, $K_\theta = 30*10^4$ Nmm rad^{-1}.

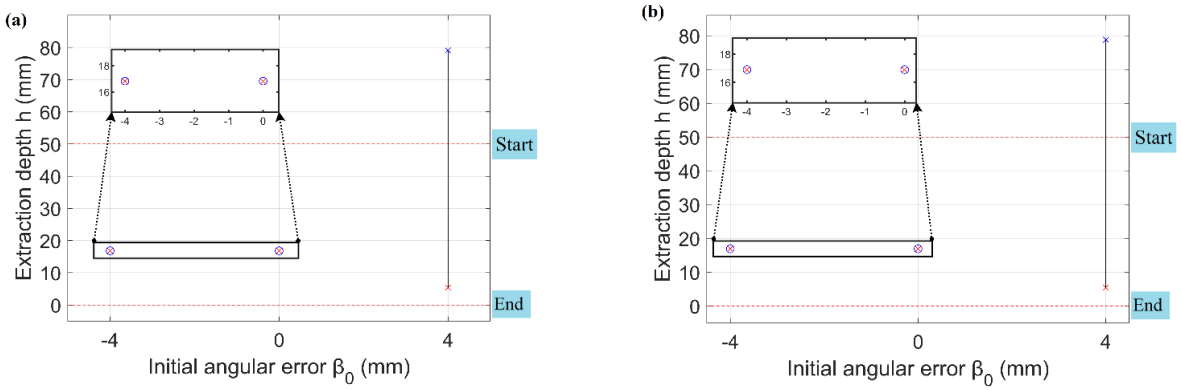

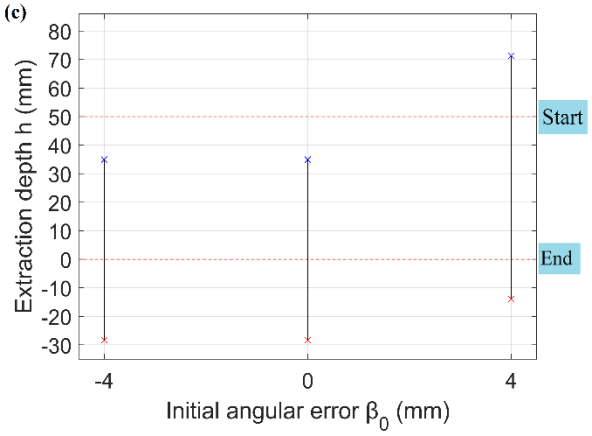

Figure 2.15. Dependence of the two-point contact region on the initial angular error: with $L_C = 50$ mm, $\delta_0 = 1$ mm, rad, $K_X = 0.4\ N\,mm^{-1}$, $K_\theta = 30*10^4$ Nmm rad^{-1}.. a) Contact in one of the dual peg-holes, b) External surfaces of pegs contact holes surfaces, c) Inner surfaces of pegs contact holes surfaces

III. Stiffness

A successful disassembly task depends on the location of the compliance centre on the peg and the coupling stiffness element between the translational and rotational directions [6]. Compliant manipulators define lateral and angular compliance based on their rotational and lateral stiffnesses. Figures 2.16, 2.17 and 2.18 (a and b) show that as the lateral stiffness and location of the centre of compliance increase, the two-point contact region decreases. This is because increased lateral stiffness causes the pegs to rotate less for similar positional errors, reducing the two-point contact region.

The two-point contact region, on the other hand, increases with increasing angular stiffness regardless of the location of the compliance centre (Figures 2.16, 2.17 and 2.18 (c and d)). According to these figures, stiffness does not significantly influence the two-point contact region.

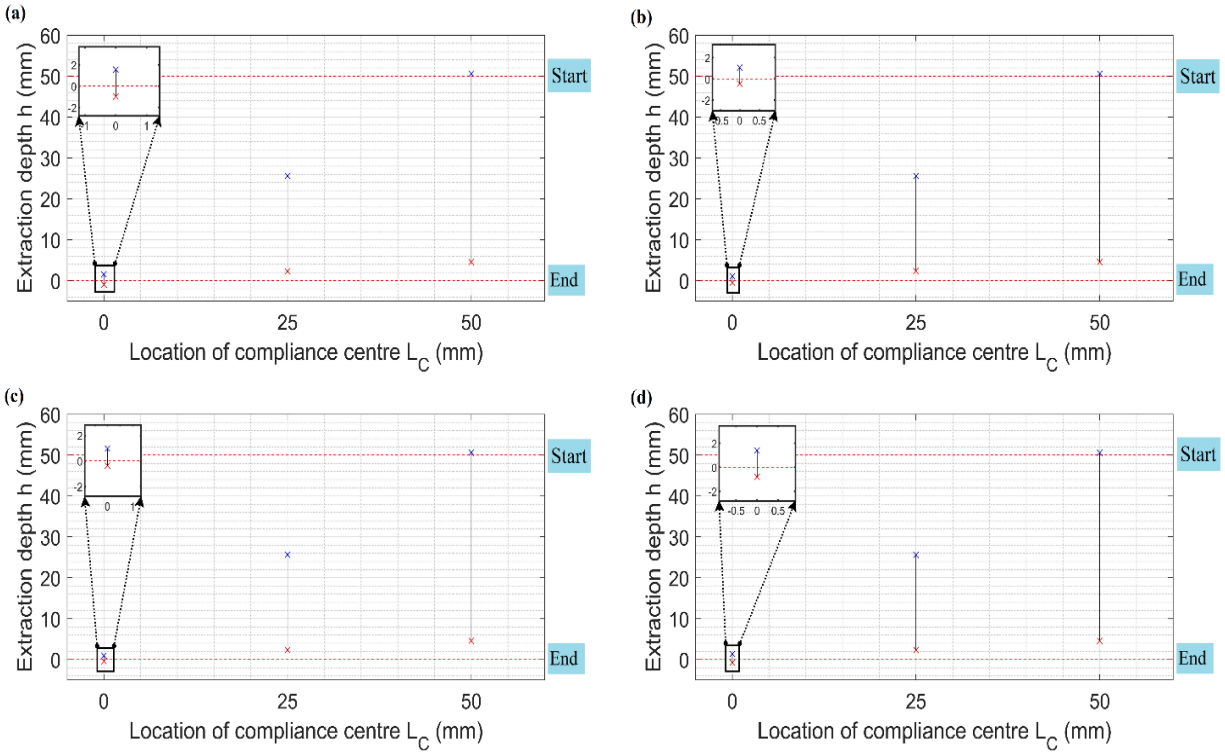

*Figure 2.16. The effect of the two-point contact region in one of the dual peg-holes on the structural parameters: (a) K_x =0.2 N mm^{-1}, K_θ = 30*10^4 Nmm rad^{-1}; (b) K_x =0.6 N mm^{-1}, K_θ = 30*10^4 Nmm rad^{-1}; (c) K_x =0.4 N mm^{-1}, K_θ = 15*10^4 Nmm rad^{-1}; (d) K_x =0.4 N mm^{-1}, K_θ = 45*10^4 Nmm rad^{-1} with δ_0 = 2 mm, β_0 = 0 rad.*

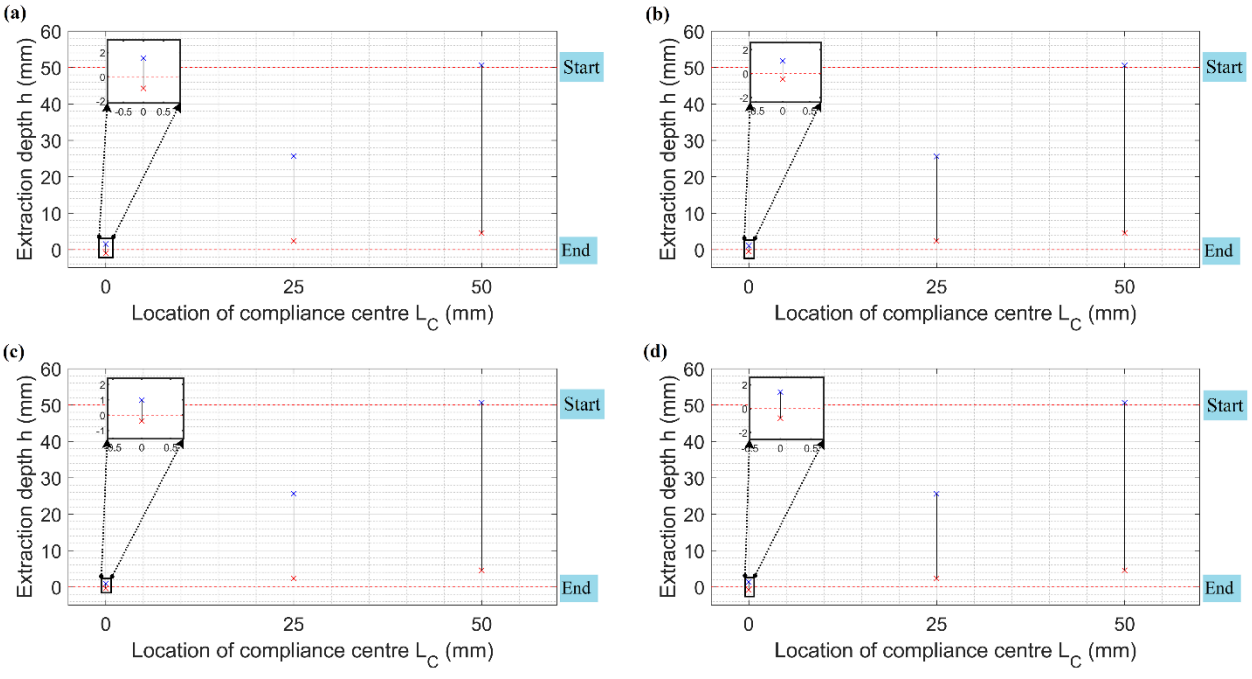

*Figure 2.17. The effect of the two-point contact region in the contact of the inner surfaces of the pegs with the holes on the structural parameters: (a) K_x =0.2 N mm^{-1}, K_θ = 30*10^4 Nmm rad^{-1}; (b) K_x =0.6 N mm^{-1}, K_θ = 30*10^4 Nmm rad^{-1}; (c) K_x =0.4 N mm^{-1}, K_θ = 15*10^4 Nmm rad^{-1}; (d) K_x =0.4 N mm^{-1}, K_θ = 45*10^4 Nmm rad^{-1} with δ_0 = 2 mm, β_0 = 0 rad.*

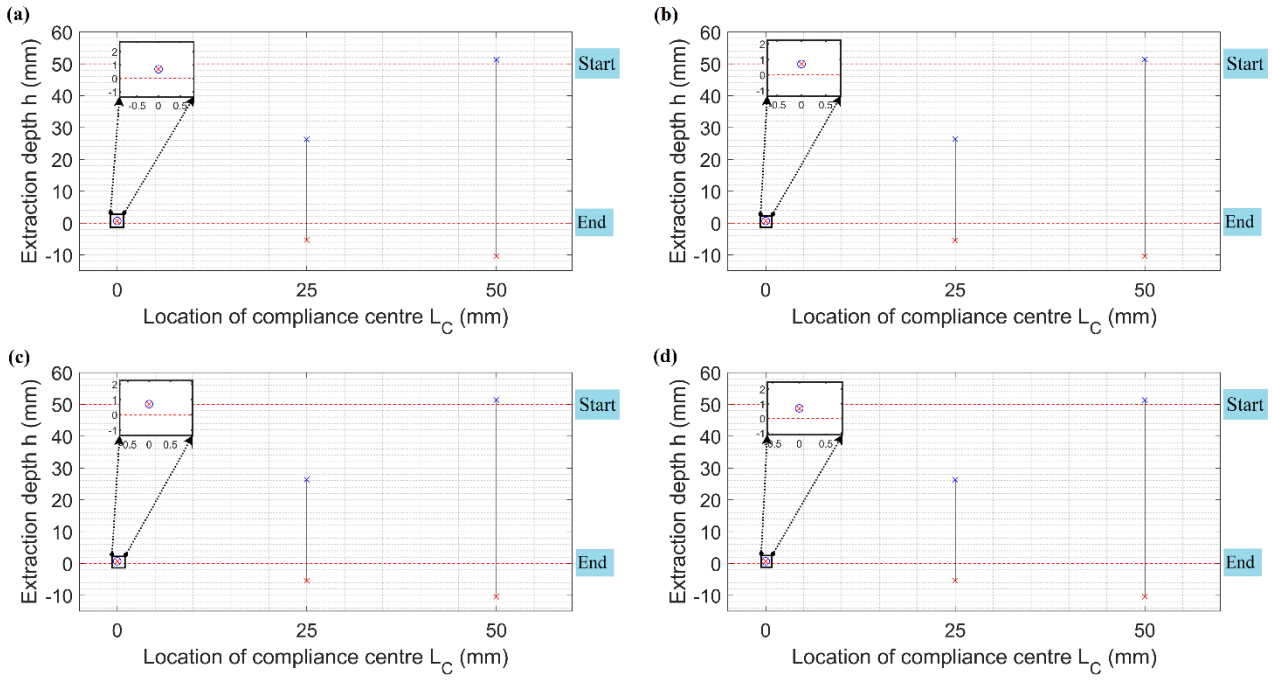

*Figure 2.18. The effect of the two-point contact region in the contact of the external surfaces of the pegs with the holes on the structural parameters: (a) K_x =0.2 N mm^{-1}, K_θ = 30*10^4 Nmm rad^{-1}; (b) K_x =0.6 N mm^{-1}, K_θ = 30*10^4 Nmm rad^{-1}; (c) K_x =0.4 N mm^{-1}, K_θ = 15*10^4 Nmm rad^{-1}; (d) K_x =0.4 N mm^{-1}, K_θ = 45*10^4 Nmm rad^{-1} with δ_0 = 2 mm, β_0 = 0 rad.*

2.5 Experiment

In this section, an experiment is performed with three samples with different radii to verify the results of the above analysis. Dual peg-holes have the following geometric dimensions (Table II).

TABLE 2.2. Parameters for dual peg-hole

Category	Parameter	Value
Friction Characteristics	Static Coefficient of friction	$\mu = 0.01$
Geometrical parameters	Pegs mass	m= 0.6 kg
	Pegs radius	r= 5.7, 6 and 6.5 mm
	Holes radius	R=6.1 mm
	Pegs length	L= 50 mm
	Distance between two centres of pegs/holes	D= 40 mm
	Clearance ratio	C= 0.01639 , 0.06557, 0.00819
Initial position/angle	Depth	$h_0 = 50$ mm
	Angle	$\theta_0 = -0.9$ rad

2.5.1 Experimental Design

The experiment presented in this section uses a six-degree-of-freedom KUKA LBR iiwa robot [29] and a force/torque sensor (Figure 2.19). The experimental video can be found at [30]. In this experiment, the force and moment were sampled accordingly. The hole block was positioned on a table while the peg was attached to the media flange of a robot arm.

The exclusion of a gripper in this setup facilitates the examination of the compliance centre's impact. It is noteworthy that established literature, including Zhang et al's work[12], frequently utilises the approach of affixing the workpiece to the robot's end effector.

The peg and hole were made of thermoplastic material. The experiment was repeated 18 times for each sample, with six repetitions for each compliance centre location (L_C = 50 mm, L_C = 25 mm, L_C =0 mm).

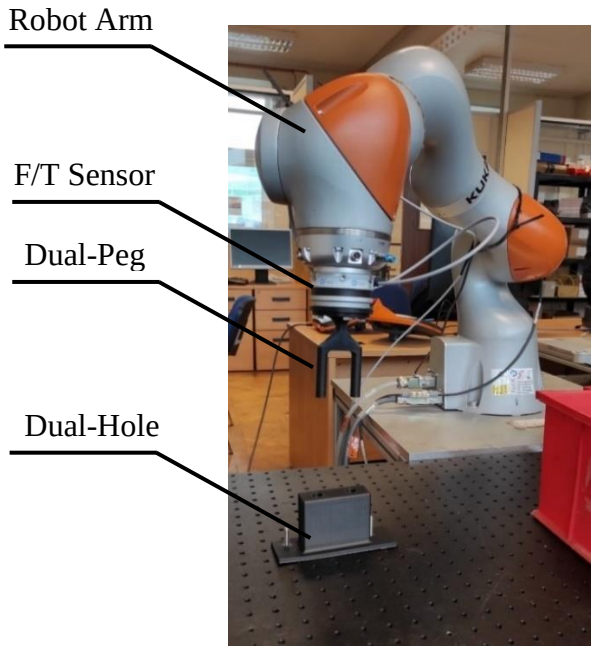

Figure 2.19. The experimental equipment

The tool centre point (TCP) was also created using active compliance. In this experiment, the peg could rotate around the TCP without changing its position. To simulate the different

locations of the compliance centre, several TCPs were configured. Lateral and angular stiffness could also be controlled [29].

2.5.2 Experimental Results

The experimental parameters are listed in Table II. Along the extraction direction, a stiffness of $K_x = 0.3$ N.mm^{-1} is set. A Savitzky–Golay filter was used to remove noise before plotting extraction force measurements. Figure 2.20 shows the effects of the compliance centre location on extraction forces with depth or three samples with different radii. The area of two-point contact increases with increasing extraction force. It is evident that both in theory and practice, the contact states significantly differ based on the position of the compliance centre. The blue curve shows that when the compliance centre was far from the tip of the dual-peg, the two-point contact region was the largest. The orange and green curves show narrower and lower peaks when L_C decreases, corresponding to a smaller two-point contact region.

2.6 Conclusion

This paper presents a geometric and static force analysis for the dual-peg extraction jamming problem, considering all geometric variations. In a dual peg jamming problem, all 13 contact states are identified.

The applied geometric and quasistatic force analysis approach proves effective in studying the jamming phenomenon and exhibits potential for application to other assembly and disassembly problems.

The incorporation of compliant manipulators offers the opportunity to establish geometric and force/moment conditions for each contact state, underscoring the potential for developing more precise and reliable robotic systems tailored for disassembly and remanufacturing tasks. In this investigation, we delve into several factors, including the location of the compliance centre, initial lateral and angular errors, and manipulator stiffness,

to assess their influence on the area of the two-point contact. Of particular note, our results emphasise the pivotal role played by the location of the compliance centre.

Our theoretical exploration demonstrates striking similarities between the dual peg-hole extraction process and its single peg-hole counterpart. This suggests that techniques developed for single peg-hole scenarios, such as the compliance centre approach, can be viably applied to the dual peg-hole case as well, providing an effective strategy.

To corroborate our theoretical findings, we conducted experiments. Our research confirms that the application of appropriate compliance strategies, such as adjusting stiffness and the remote centre of compliance, can significantly reduce disassembly forces. While it is true that the jamming conditions differ between single and dual peg-holes, as illustrated in Table 2.1, with 13 contact states compared to the 3 contact states in a single peg-hole [12], the judicious use of remote compliance strategies proves effective in mitigating disassembly forces in both scenarios. The experimental outcomes align with the predictions of the theoretical model concerning the disassembly of dual-peg-hole assemblies, further reinforcing the credibility and reliability of the study's findings.

a)

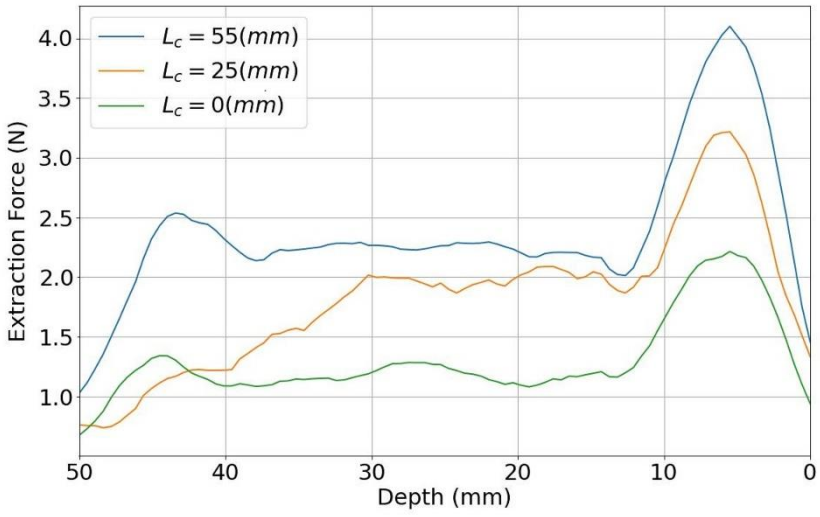

b)

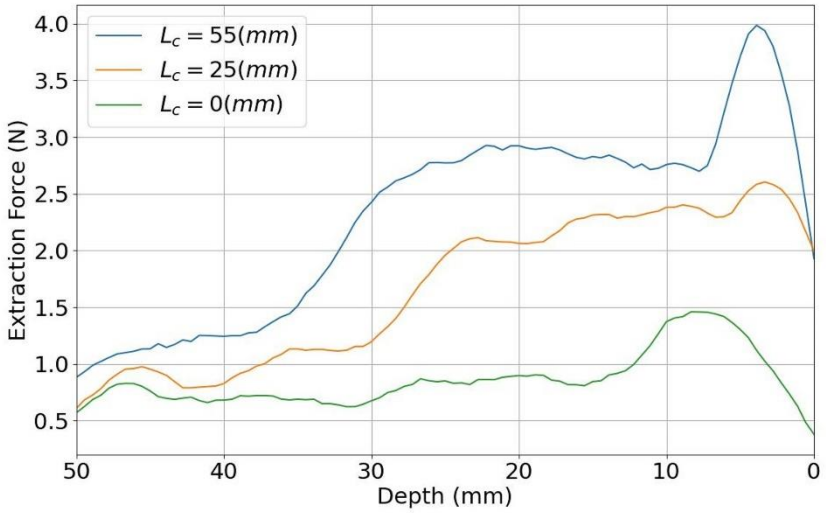

c)

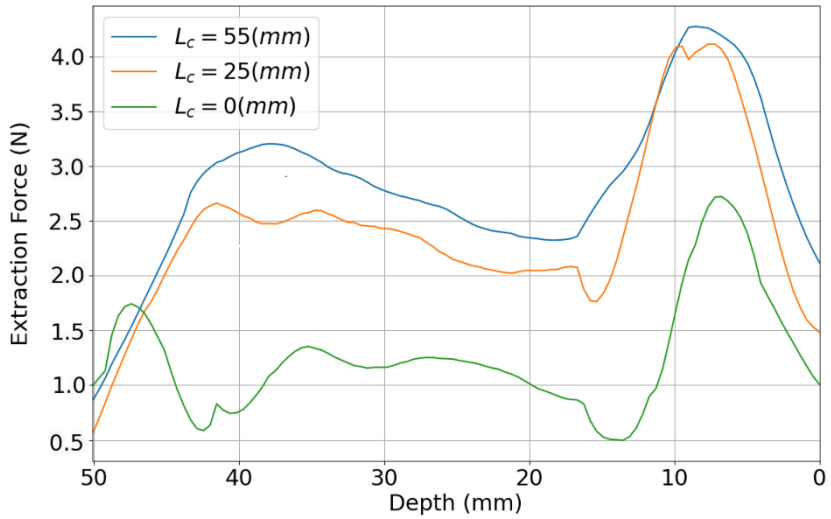

Figure 2.20. Extraction force curves based on compliance centre locations. a) r= 5.7 mm, b) r= 6 mm, and c) r=6.5 mm

Acknowledgement

This work was supported by the Engineering and Physical Sciences Research Council (EPSRC) under Grant EP/W00206X/1.

2.7 References

[1] F. Goli, Y. Wang, and M. Saadat, "Perspective of self-learning robotics for disassembly automation," in *2022 27th International Conference on Automation and Computing (ICAC)*, 2022, pp. 1–6. doi: 10.1109/ICAC55051.2022.9911085.

[2] J. Y. Mule, "Design for Disassembly Approaches on Product Development," 2012.

[3] W. L. Ijomah, C. A. McMahon, G. P. Hammond, and S. T. Newman, "Development of robust design-for-remanufacturing guidelines to further the aims of sustainable development," *Int J Prod Res*, vol. 45, no. 18–19, pp. 4513–4536, Sep. 2007, doi: 10.1080/00207540701450138.

[4] S. Vongbunyong and W. H. Chen, "Disassembly Automation," in *Disassembly Automation: Automated Systems with Cognitive Abilities*, S. Vongbunyong and W. H. Chen, Eds., Cham: Springer International Publishing, 2015, pp. 25–54. doi: 10.1007/978-3-319-15183-0_3.

[5] Y. Tang, M. Zhou, E. Zussman, and R. Caudill, "Disassembly modeling, planning, and application," *J Manuf Syst*, vol. 21, no. 3, pp. 200–217, 2002, doi: https://doi.org/10.1016/S0278-6125(02)80162-5.

[6] B.-H. Kim, B.-J. Yi, I. H. Suh, and S.-R. Oh, "Stiffness analysis for effective peg-in/out-hole tasks using multi-fingered robot hands," in *Proceedings. 2000 IEEE/RSJ International Conference on Intelligent Robots and Systems (IROS 2000) (Cat. No.00CH37113)*, 2000, pp. 1229–1236 vol.2. doi: 10.1109/IROS.2000.893187.

[7] B. James, P. Rao, E. Reddy, and V. Mallikarjuna, "DESIGN AND ANALYSIS OF TURBOCHARGERS," Mar. 2016.

[8] M. Bdiwi, A. Rashid, M. Pfeifer, and M. Putz, *Disassembly of Unknown Models of Electrical Vehicle Motors Using Innovative Human Robot Cooperation*. 2017. doi: 10.1145/3029798.3038425.

[9] R. Usubamatov and K. W. Leong, "Analyses of peg-hole jamming in automatic assembly machines," *Assembly Automation*, vol. 31, no. 4, pp. 358–362, Jan. 2011, doi: 10.1108/01445151111172943.

[10] D. E. Whitney, "Quasi-static assembly of compliantly supported rigid parts," *J Dyn Syst Meas Control*, vol. 104, no. 1, pp. 65–77, 1982.

[11] B. P. McNelly, R. Leary, S. Brennan, and K. Reichard, "Characterizing successful robotic insertion and removal from a dry storage cask using peg-like jamming and wedging analysis," in *Pressure Vessels and Piping Conference*, American Society of Mechanical Engineers, 2016, p. V06BT06A064.

[12] Y. Zhang *et al.*, "Peg–hole disassembly using active compliance," *R Soc Open Sci*, vol. 6, no. 8, p. 190476, 2019.

[13] H. Asada and Y. Kakumoto, "The dynamic RCC hand for high-speed assembly," in *Proceedings. 1988 IEEE International Conference on Robotics and Automation*, 1988, pp. 120–125 vol.1. doi: 10.1109/ROBOT.1988.12035.

[14] S. N. 'Simunovi, "an information approach to parts mating," Massachusetts Institute of Technology, Cambridge, MA, 1979.

[15] J. L. Nevins and D. E. Whitney, "Assembly Research," *IFAC Proceedings Volumes*, vol. 12, no. 10, pp. 195–214, 1979, doi: https://doi.org/10.1016/S1474-6670(17)65359-X.

[16] M. E. Caine, T. Lozano-Perez, and W. P. Seering, "Assembly strategies for chamferless parts," in *Proceedings, 1989 International Conference on Robotics and Automation*, 1989, pp. 472–477 vol.1. doi: 10.1109/ROBOT.1989.100031.

[17] R. H. Sturges, "A Three-Dimensional Assembly Task Quantification with Application to Machine Dexterity," *Int J Rob Res*, vol. 7, no. 4, pp. 34–78, Aug. 1988, doi: 10.1177/027836498800700403.

[18] R. H. Sturges Jr. and S. Laowattana, "Virtual Wedging in Three-Dimensional Peg Insertion Tasks," *Journal of Mechanical Design*, vol. 118, no. 1, pp. 99–105, Mar. 1996, doi: 10.1115/1.2826863.

[19] R. H. Sturges Jr. and S. Laowattana, "Design of an Orthogonal Compliance for Polygonal Peg Insertion," *Journal of Mechanical Design*, vol. 118, no. 1, pp. 106–114, Mar. 1996, doi: 10.1115/1.2826840.

[20] D. R. Strip, "Insertions using geometric analysis and hybrid force-position control: method and analysis," in *Proceedings. 1988 IEEE International Conference on Robotics and Automation*, IEEE, 1988, pp. 1744–1751.

[21] W. Wang, R. N. K. Loh, and E. Y. Gu, "Passive compliance versus active compliance in robot-based automated assembly systems," *Industrial Robot: An International Journal*, vol. 25, no. 1, pp. 48–57, Jan. 1998, doi: 10.1108/01439919810196964.

[22] X. Zhang, Y. Zheng, J. Ota, and Y. Huang, "Peg-in-hole assembly based on two-phase scheme and f/t sensor for dual-arm robot," *Sensors*, vol. 17, no. 9, p. 2004, 2017.

[23] K. Sathirakul and R. H. Sturges, "Jamming conditions for multiple peg-in-hole assemblies," *Robotica*, vol. 16, no. 3, pp. 329–345, 1998, doi: DOI: 10.1017/S0263574798000393.

[24] Y. Fei and X. Zhao, "An Assembly Process Modeling and Analysis for Robotic Multiple Peg-in-hole," *J Intell Robot Syst*, vol. 36, no. 2, pp. 175–189, 2003, doi: 10.1023/A:1022698606139.

[25] F. Lan, M. Castellani, D. Truong Pham, and Y. Wang, "On the correctness of using two-dimensional representations in the analysis of cylindrical peg–hole insertion and withdrawal," *R Soc Open Sci*, vol. 10, no. 8, Aug. 2023, doi: 10.1098/rsos.221021.

[26] S. Wang, G. Chen, H. Xu, and Z. Wang, "A Robotic Peg-in-Hole Assembly Strategy Based on Variable Compliance Center," *IEEE Access*, vol. 7, pp. 167534–167546, 2019, doi: 10.1109/ACCESS.2019.2954459.

[27] Y. Fei and X. Zhao, "Jamming analyses for dual peg-in-hole insertions in three dimensions," *Robotica*, vol. 23, no. 1, pp. 83–91, 2005, doi: DOI: 10.1017/S0263574704000578.

[28] D. N. Trong, M. Betemps, and A. Jutard, "Analysis of dynamic assembly using passive compliance," in *Proceedings of 1995 IEEE International Conference on Robotics and Automation*, 1995, pp. 1997–2002 vol.2. doi: 10.1109/ROBOT.1995.525556.

[29] "System Software KUKA Sunrise.OS 1.11 KUKA Sunrise.Workbench 1.11 Operating and Programming Instructions for System Integrators," 2016.

[30] Goli F, "Dual peg-hole disassembly process with active compliance centre." [Online]. Available: https://youtube.com/shorts/hDh6vXg1Vx4

2.8 Appendix

Variable	Description	Formula	State No
C	clearance ratio	$C= (R-r)/R$	
D	diameter of the hole (mm)	Camera	
$\mathbf{F_x}$	lateral force (N)	$F_X = -K_x\left(\delta_0 + L_C\theta_0 - \frac{CDL_C}{h}\right)$ $F_x = -k_x\left(\delta_0 - \varepsilon_0 + L_C\theta_0 + cD/2 - \frac{cDL_C}{h}\right)$ $F_x = -k_x\left(\delta_0 + L_C\theta_0 - \frac{L_C(-2R'C)}{h}\right)$	5 10 9
$\mathbf{F_{fr1}}$	friction force at contact point 1 (N)		
$\boldsymbol{F_{fr2}}$	friction force at contact point 2 (N)		
$\boldsymbol{F_{N1}}$	reaction force at contact point 1 (N)		
$\boldsymbol{F_{N2}}$	reaction force at contact point 2 (N)		
$\boldsymbol{F_z}$	extraction force (N)	$F_Z = \frac{M}{\lambda r} - \frac{\mu}{\lambda}(1-\lambda)F_x \quad , \quad \lambda = h/(2r\mu)$	
$\boldsymbol{F_z}$ one-point contact	extraction force (N)	$F_z = \frac{\mu k_\theta(\theta - \theta_0 + \beta_0)}{(h - \mu r - L_C)}$	
h	extraction depth (mm)	$h = (2R - 2r\cos\theta)/\sin\theta$	
$\mathbf{h_0}$	initial depth of the peg in the hole (mm)	$h_0 = (2R - 2r\cos\theta_0)/\sin\theta_0$	
H	height of each peg (mm)		
$\boldsymbol{K_x}$	lateral stiffness of the compliant manipulator (N mm^{-1})		
$\boldsymbol{K_z}$	vertical stiffness of the compliant manipulator (N mm^{-1})		
$\boldsymbol{K_\theta}$	rotational stiffness of the compliant manipulator (N.mm rad^{-1})		

L_C	location of the compliance centre (mm)		
M	moment applied on the peg (Nmm)		
r	the radius of each peg (mm)	Camera	
R	the radius of each hole (mm)	R=D/2	
2R'	Distance between two holes (mm)	Camera	
2r'	Distance between two pegs (mm)	Camera	
$\mathbf{U_0}$	the initial distance between the compliance centre and the hole axis (mm)	$\lvert X_{hole} - X_C \rvert$	
U	distance between the compliance centre and the hole axis (mm)	$U = U_0 + \delta_0 - \frac{K_\theta(L_C\beta_0 + \delta_0)}{K_x L_C(h - \mu r) - K_x L_C^2 + K_\theta}$	5
		$U = U_0 + \delta_0 - \frac{K_\theta(L_C\beta_0 + \delta_0 + cR - \varepsilon_0)}{K_x L_C(h - \mu r) - K_x L_C^2 + K_\theta}$	10
		$U = U_0 + \delta_0 - \frac{K_\theta(L_C\beta_0 + \delta_0)}{K_x L_C(h - \mu R') - K_x L_C^2 + K_\theta}$	9
$\boldsymbol{\beta_0}$	initial angular error (rad)		
$\boldsymbol{\delta_0}$	initial lateral error (mm)		
$\boldsymbol{\varepsilon}$	distance between the selected peg tip and the hole axis (mm)		
$\boldsymbol{\varepsilon_0}$	the initial distance between the selected peg tip and the hole axis (mm)	$\varepsilon_0 = L_C \sin\theta_0 - U_0$	
$\boldsymbol{\theta}$	the tilt angle of the peg (rad)	$\theta = \theta_0 - \beta_0 + \frac{K_x(h - \mu r - L_C)(L_C\beta_0 + \delta_0)}{K_x L_C(h - \mu r) - K_x L_C^2 + K_\theta}$	5
		$\theta = \theta_0 - \beta_0 + \frac{K_x(h - \mu r - L_C)(L_C\beta_0 + \delta_0 + cR - \varepsilon_0)}{K_x L_C(h - \mu r) - K_x L_C^2 + K_\theta}$	10
		$\theta = \theta_0 - \beta_0 + \frac{K_x(h - \mu R' - L_C)(\delta_0 + L_C\beta_0)}{K_x L_C(h - \mu R') - K_x {L_C}^2 + K_\theta}$	9
$\boldsymbol{\theta_0}$	the initial tilt angle of the peg (rad)		
$\boldsymbol{\mu}$	coefficient of friction		

Data accessibility. All data sources are conveniently accessible through the electronic supplementary materials hosted on Figshare at the following URL https://figshare.com/s/9a9df1ea0a0a4c535aa7.. This ensures that the data associated with the study can be readily accessed for reference, transparency, and reproducibility.

Chapter 3. CHARACTERISING THE MECHANICS OF RECTANGLE PEG-HOLE DISASSEMBLY AND THE EFFECT OF ACTIVE COMPLIANCE CENTRE POSITION ON EXTRACTION FORCE

Authors Contributions:

This chapter of the alternative thesis format is published in the Journal of Royal Society Open Science (2024). I am the first author of this publication. The paper's details and co-authors' contributions are outlined below.

Goli F[1], Aflakian A[2], Qu M[3], Zang Y[4], Saadat M[5], Pham DT[6], Wang Y[7]; Characterising the mechanics of rectangle pe-hole disassembly and the effect of active compliance centre position on extraction force. Royal Society Open Science (2024). *https://doi.org/10.1098/rsos.240956*

[1] **Farzaneh Goli:** The main author, designed a Quasi-Static model and executed experiments, and numerical simulations, performed all necessary characterisation and data analysis and wrote the manuscript

[2] **Ali Aflakian:** He contributed to the Quasi-Static model. His contributions involved providing essential theoretical insights and mathematical formulations that enhanced the model's accuracy and robustness.

[3] **Mo Qu:** He contributed significantly by assisting in setting up the experimental framework. His efforts ensured that all equipment was properly calibrated and that the experimental conditions were optimised for reliable data collection.

[4] **Yue Zang:** He meticulously reviewed the mathematical formulations to ensure their accuracy. Additionally, his detailed inputs both during review and writing ensured that the final document was precise and well-articulated.

[5] **Mozafar Saadat:** He provided ongoing supervision and meticulous proofreading support during the entire research process.

[6] **Duc Truong Pham:** He was pivotal in conceptualising the project, contributing significantly by framing the research objectives. In addition, he helped to address reviewers' comments, ensuring that the feedback was carefully considered and effectively integrated into the final manuscript

[7]**Yongjing Wang:** He provided ongoing supervision and meticulous proofreading support during the entire research process. Her oversight was key in maintaining the project's academic rigour, and her critical feedback helped ensure that the final manuscript was polished and well-structured.

Characterising the mechanics of rectangle peg-hole disassembly and the effect of active compliance centre position on extraction force

Abstract

This paper aimed at facilitating robotised disassembly for remanufacturing by focussing on the challenge of rectangular peg-hole disassembly.

The study explores all potential contact states during the rectangular peg-hole disassembly process and identifies 26 distinct conditions, 16 of which are related to jamming. The contact conditions are categorised into five groups based on the number of contacts with the surface. Thereafter, it provides an in-depth analysis of jamming phenomena during the extraction process, employing both geometrical and quasistatic analyses to establish boundary conditions for jamming.

Furthermore, the efficacy of the active compliance centre position in preventing jamming areas is explored, considering critical variables such as compliance degree, centre location, and initial position errors. The outcomes highlight that positioning the compliance centre at the end of the peg is the most effective strategy for reducing the jamming area and extraction force. Finally, the simulated results are confirmed by experiments and demonstrated 77.1% deduction to the maximum extraction force with the correct active compliance centre position, as opposed to when it is placed at the top of the peg. The findings contribute insights into the intricate dynamics of disassembly, revealing potential avenues for optimising automated robotic systems in remanufacturing.

Key words: Quasi-static, robotic disassembly, remanufacturing, active compliance, rectangle peg–hole disassembly

3.1 Introduction

The disposal of end-of-life (EOL) products creates both environmental and economic challenges [1]. To address these challenges, EOL products often undergo processes of remanufacturing, ensuring non-destructive separation of components and materials for prospective reuse [2].

Remanufacturing, a multi-stage process involving disassembly, cleaning, inspection, repair or replacement of damaged parts, reassembly, and testing, has emerged as a pivotal link connecting product return with product recovery [3], [4]. However, the manual disassembly process has proven to be inefficient, prompting the adoption of automatic disassembly facilitated by robots to enhance efficiency, reduce time and labour costs, and mitigate the dangers associated with human involvement [5]. A particular challenge in disassembly lies in the extraction of pegs from clearance-fit holes [6].

This routine operation, prevalent in the disassembly of mechanical components like shaft-hub connections in machinery, gears and sprockets, and pump and motor connections, extends to the disassembly of assemblies with rectangle peg-holes. This routine operation, prevalent in the disassembly of mechanical components such as shaft-hub connections in machinery, gears and sprockets, and pump and motor couplings, extends to the dismantling of assemblies with rectangular peg-holes. While previous research has extensively explored the peg-hole assembly, disassembly presents unique challenges due to the reverse nature of the process. Unlike the assembly of new products, which is deterministic because the components to be assembled are of known geometries, dimensions and states, disassembly is stochastic as

it has to contend with used products of uncertain shapes, sizes and conditions. They introduce uncertainties in tolerances and misalignments between the peg and hole in separation processes and may lead to increased extraction forces and potential damage to the components[7].

Lateral and angular misalignment between separated components can amplify reaction forces, resulting in problems during disassembly, including jamming and wedging [8].

It should be mentioned that in robotic disassembly, jamming describes the peg becoming lodged at an angle, complicating disassembly with misalignment issues, while wedging refers to the peg becoming tightly stuck in the hole due to friction or deformation. The use of robots in peg-hole disassembly should consider jamming and wedging due to unbalanced forces, which can cause damage to components and robots[8].

Lateral and angular misalignment between separated components can amplify reaction forces, resulting in problems during disassembly, including jamming and wedging[8].

To address these challenges, researchers have explored various strategies, such as the remote compliance centre (RCC)[9], [10], [11], [12], to avoid jamming and wedging during disassembly [10], [11]. Despite these efforts, there is a notable absence of comprehensive investigations into multiple peg-hole disassembly, leaving a gap in understanding the mechanisms and contacts involved in this process. Simunovic[13] and Whitney [14], in their exploration of peg-hole assembly dynamics, employed a compliant manipulator, advancing the field by introducing an RCC device to enhance precision and efficiency. The investigation extended to various dimensions, encompassing rectangular peg insertion without chamfers[15] and three-dimensional scenarios [16], [17]. Sturges et al. contributed to the discourse by developing the Spatial Remote Centre Compliance (SRCC) [18]. Strip [19] innovatively devised a hybrid force-position strategy tailored for three-dimensional convex pegs, integrating active compliance. Zhang et al. investigated the intricacies of peg-hole disassembly by conducting a quasistatic analysis with a compliance device. Their inquiry scrutinised critical

variables such as compliance degree, the position of the compliance centre, and positional errors[11]. Wang et al. undertook a comparative study, of pitting passive against active compliance and concluding that the latter, despite its costs and restricted response speed, outshines in improving dynamic response and assembly reliability [20].

This paper builds on prior studies [11], [21] that investigated contact states within one-peg and one-hole scenarios.

These scenarios are characterised by limited contact points concentrated at the peg tip and hole's inner surface. In [7], [22], we also explored the extension of techniques from single peg-holes to dual peg-holes, indicating the potential for more accurate robotic systems. The study underscores the potential applicability of single peg-hole techniques, such as the compliance centre approach, to the dual peg-hole case, with experimental results supporting the proposed claim.

The complexities of rectangle peg-hole scenarios are less explored in the existing literature. These kind of pegs and their mating holes are commonly utilised in mechanical products, including industrial components, furniture, toys, and electronic devices. One of the complexities and differences in such configurations, compared to cylinder peg-hole assemblies, arises from the fact that a rectangular peg can establish multiple contact states with its corresponding hole, leading to complex jamming conditions.

While cylinder pegs typically exhibit rotational symmetry, reducing the variety of contact points during extraction, rectangular pegs can contact the hole on multiple planes and edges. This significantly increases the complexity of disassembly for rectangular pegs, making control of lateral and angular misalignment more critical. Cylindrical peg-hole configurations generally require less extraction force and experience minimal friction. The geometry and symmetry of the cylinder make alignment, control, and sensing easier, often demanding precise tolerances but with predictable forces. In contrast, disassembly tasks involving polygonal

shapes face more complex forces, higher friction, and require more advanced robotic control strategies due to the increased complexity of surface interactions and mechanical constraints.

The extraction force required to remove a rectangular peg from a mating hole constitutes another critical complexity within such configurations. Dismantling these assemblies typically demands substantial force, rendering the process challenging, time-consuming, and costly. A deep understanding of the mechanics involved in rectangular peg-hole disassembly becomes essential for enhancing the efficiency of disassembly processes. In this study, the mechanics of rectangular peg-hole disassembly are investigated, and the effect of the active compliance centre (ACC) position on the extraction force in three dimensions is analysed. Specifically, the relationships between the geometrical parameters of the peg and hole, the frictional properties of the contact surfaces, and the extraction force required to remove the peg from the hole are characterised. Thereafter, the effect of the ACC position on the extraction force is explored, and the optimal ACC position that minimises the force required for disassembly is identified. The geometrical boundary conditions (specifically, depths of extraction) of jamming are highlighted, and a solution using ACC to minimise the jamming area is proposed.

Figure 3.1 illustrates the structure of this study, which delves into the robotic disassembly of a 3D rectangle peg from a hole.

Two categories of contact states are listed, jamming and wedging, which are situations where the peg cannot be extracted from the hole smoothly. This study explores the influence of ACC positions on 16 jamming conditions using the formula derived from the quasi-static analysis. Finally, the Kuka LBR arm is utilised to validate the theoretical approach for practical application.

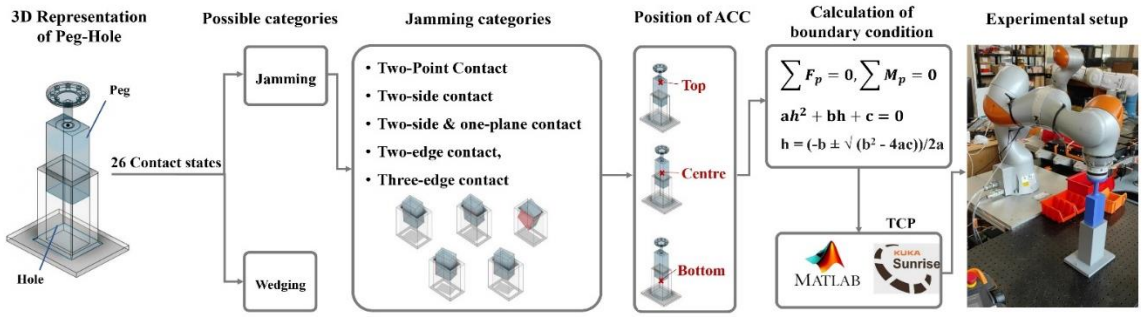

Figure 3.1. Investigate the impact of Active Compliance Centre (ACC) positions on 16 jamming conditions among 26 possible contact situations both in simulation and experiments.

Our findings provide insights into the mechanics of rectangle peg-hole disassembly and highlight the importance of considering the ACC position in optimising disassembly processes. This knowledge can be applied to a wide range of mechanical systems and can lead to significant improvements in efficiency, cost, and sustainability.

Section 3.2 provides an analysis of rectangle peg extraction during disassembly, encompassing geometric analysis, and delves into the force analysis of rectangle peg-hole extraction as a methodology. Section 3.3 presents the results and discussion of the analysis. Section 3.4 details the experimental design and results, confirming the theoretical disassembly model.

3.2 Methodology

Extracting a rectangular peg from a hole is a common task in disassembly applications. Considering the forces and moments involved in the extraction of a rectangular peg from a hole is necessary to successfully complete the common task of extracting the peg from the hole. This analysis is based on the following main assumptions:

- The pegs are stiff,
- There is only one extraction direction: vertically upwards.
- The ACC is located along the axis of extraction and the hole.

- The stiffness parameters (K_X, K_Y and K_θ, K_Φ, K_Ψ) define the resistance of the system to lateral and rotational displacements during extraction. Higher stiffness values correspond to lower compliance, leading to reduced rotations and minimised two-contact regions.
- Adhesive forces, such as parts being bonded by glue or due to corrosion, are not considered.

Predicting force and torque during disassembly helps us identify configurations in which compliant devices supporting the pegs, such as RCC, SRCC, or ACC, may fail to avoid wedging and jamming [23]. This information provides a better understanding of the characteristics of the rectangle peg-hole disassembly using compliance mechanisms.

The forces and moments acting on the peg can be used to predict the likelihood of wedging and jamming during extraction. If not properly controlled, the peg can wedge in the hole or jam against the sides of the hole. This knowledge can be used to design and control extraction processes to minimise the risk of these problems.

In a rectangular peg-hole problem, the use of an ACC is expected to result in successful extraction with an appropriate initial configuration. The ACC will mitigate the likelihood of wedging and jamming by adjusting the forces and moments acting on the peg in real-time. This allows for a smooth and safe extraction process. The extracting phase of the rectangular peg-hole extraction problem is thoroughly examined in the following sections.

3.2.1 Geometric analysis

The main dimensions of a rectangular peg-hole are shown in Figure 3.2. A hole's length and width are w and v, respectively, and a peg's length and width are w' and v'. The distance between the peg and the hole in the rectangle's length is C_1, and the distance between the peg and the hole in its width is C_2 ; h represents the current extraction depth.

$$C_1 = w - w' \text{ and } C_2 = v - v'$$

Due to incompatible dimensions, the peg cannot be extracted from the hole in some cases. The rectangular peg can be extracted from the hole if the following condition is met:

$$w' < w \;\&\; v' < v$$

The ability of a peg to be extracted from its hols is referred to as extractability.

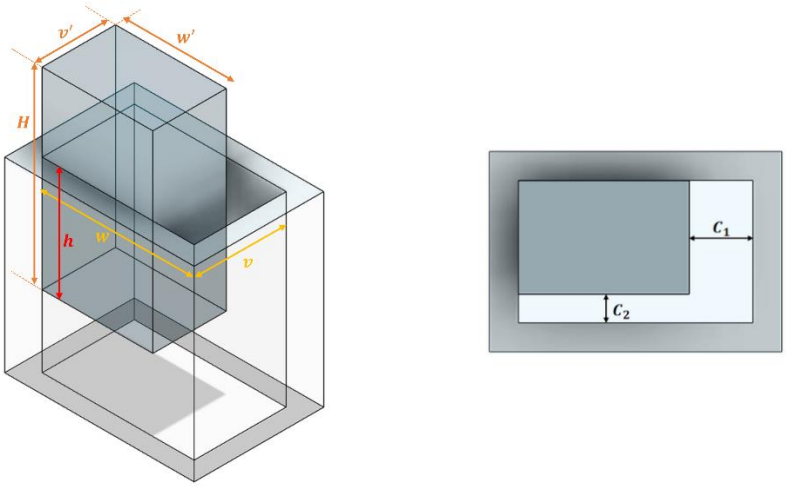

Figure 3.2. The geometric model of a rectangle peg-hole

Figure 3.3 illustrates the rectangular peg-hole that is removable based on its maximum left or right, or left and right displacements. The pegs undergo three types of rotation: yaw, pitch, and roll while maintaining their current contact positions to generate various potential contact states. Disassembly of the rectangular peg from the corresponding hole can lead to a total of 26 potential contact states; however, after eliminating redundant states (with the same initial conditions), 16 distinct contact states remain in Table 3.1. These contact states can be categorised into five primary groups: (a) no contact, (b) point contact, (c) line contact, (d) combined point and line contact, and (e) combined line and plane contact.

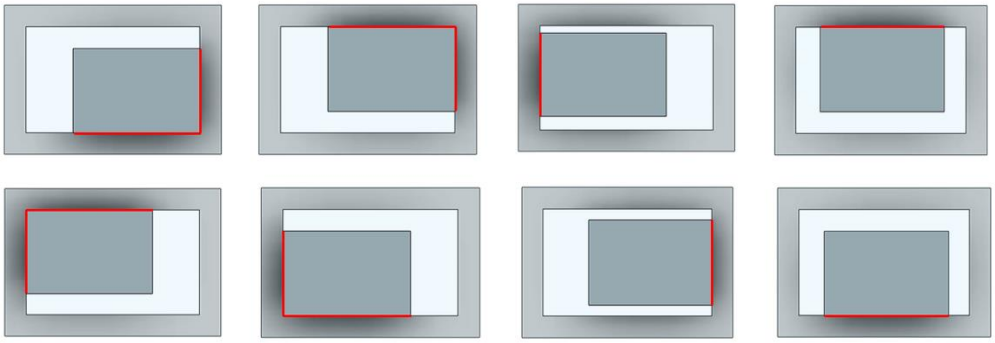

Figure 3.3. Maximum left/right- and down/up-side travel cases

TABLE 3.1 Various contact states for rectangle peg-hole extractions

	One contact state	*Two contact state*	*Three contact state*
Point Contact			
Line Contact	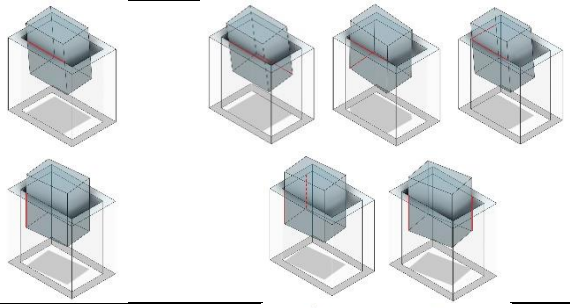		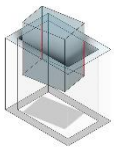
Point & Line Contact		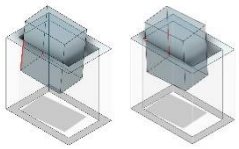	
Line & Plane Contact		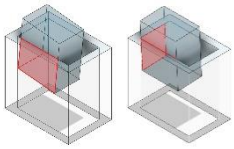	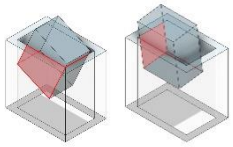

Ideally, the desired state for the peg is one of the states in the “no contact” group; nevertheless, in practice, this state is rarely achieved due to the small clearance between the peg and the hole. The disassembly process typically commences in a two-contact state, attributed to the compliant nature of manipulation and the presence of lateral and angular errors. Such a two-contact state occurs when a compliant manipulator grasps the peg, leading to slight

shifts and rotations. As the peg is progressively extracted, compliance may help reduce the errors, and the process can transition into one-contact states or states involving line or plane contact.

In rectangular peg-hole disassembly, jamming is observed within 8 out of the 16 distinct contact modes. These states can be categorised into five primary groups: 1) two-point contact, 2) two-sided contact, 3) combined two-sided and one-plane contact, 4) two-edge contact, and 5) three-edge contact, as shown in Figure 3.4.

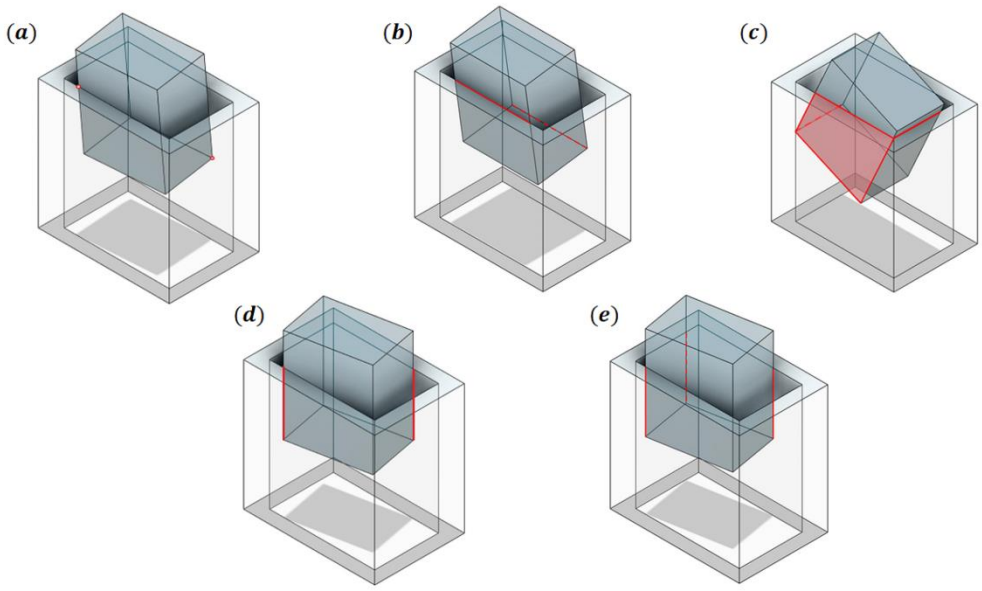

Figure 3.4. Typical jamming states of the rectangle peg-hole disassembly process: (a) two-point contact, (b) two-side contact, (c) combined two-side and one-plane contact, (d) two-edge contact, and (e) three-edge contact.

Jamming is a prevalent challenge in the context of peg-hole disassembly. Jamming arises when a peg becomes immobile due to forces and moments that are incorrectly applied. This issue primarily manifests in the two-contact state and can be mitigated by reducing the extent of the two-contact area and by carefully controlling the location at which the two-contact state occurs [24]. Notably, the concern of jamming is relatively minimal in cases of four-line contact, as it manifests as wedging rather than jamming occurring at specific angles. R. H. Sturges studied four-point contacts during peg-hole insertion, also known as wedging [16],

[17]. This study is centred on the analysis of jamming within two- and three-contact states, recognising the distinct nature of the issue in these scenarios.

3.2.2 Force analysis of Rectangle peg extraction

Analysing the forces and moments involved in the extraction of a rectangular peg is crucial for planning precise motions. The insertion of peg-hole followed the same geometric analysis as extraction. Successful removal of the rectangular peg from its corresponding hole hinges on meeting specific conditions. Throughout the extraction process, the rectangular peg encounters various contact states, some of which are more favourable than others.

As explained previously, in the context of a three-dimensional (3D) rectangular peg-hole problem, a total of 16 potential states can be identified Table 3.1. Among these states, eight are linked to contact situations that may lead to jamming Figure 3.4, and these eight states have been categorised into five distinct groups, as elucidated in the preceding subsection. This subsection will proceed to conduct an in-depth analysis of each of these categorised groups.

Considering the rectangular peg-hole system as modelled in Figure 3.5, a consistent reference frame is utilised for the rectangular peg throughout all states, positioned at the end of the peg. All the forces and moments applied to the pegs are specified with respect to this established reference frame. Now, consider rotation angles θ around the X-axis, ϕ around the Y-axis and ψ around the Z-axis.

It is assumed that both the peg and the hole are initially in a jamming state, and for the sake of computational simplification, it is further assumed that angular deviations are relatively

small. This assumption holds valid in practice, as the peg's angular errors typically remain within a few degrees at most.

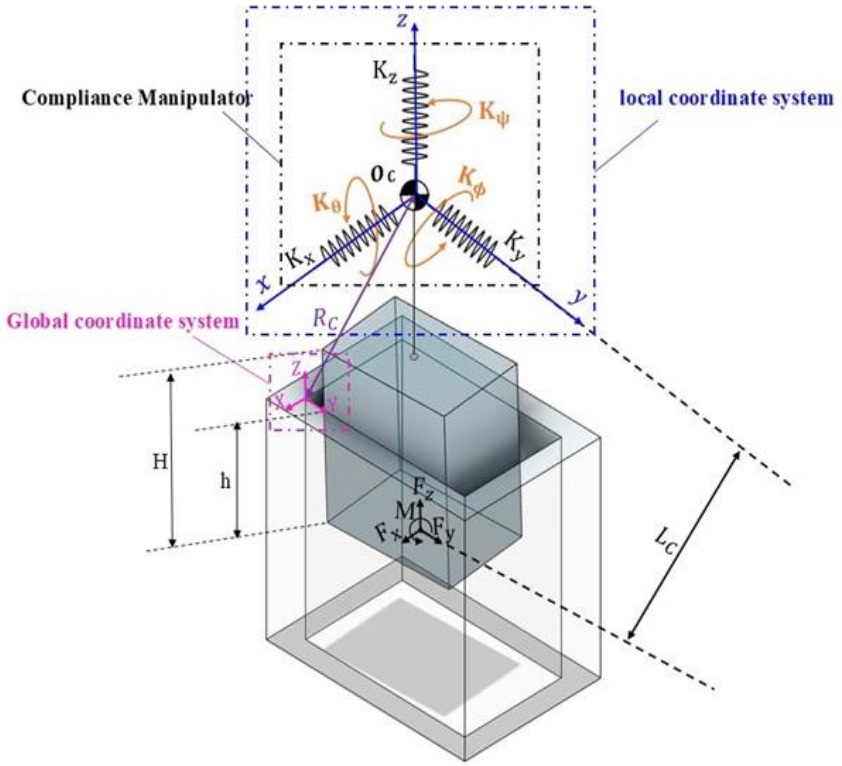

Figure 3.5. Dimensions and reference frame for rectangle peg-hole

As depicted in Figure 3.6, $\vec{\delta} = [\delta_X, \delta_Y, \delta_Z, \delta_\theta, \delta_\phi, \delta_\psi]'$ corresponds to the initial errors, and $\vec{r}_0 = [X_0, Y_0, Z_0, \theta_0, \phi_0, \psi_0]'$ denotes the initial distances from the axis of the hole to the compliance centre and the peg's tip.

The initial state of the compliance centre moves concurrently with the manipulator, and the new position of the compliance centre can change the configuration of the springs. The position and orientation used are considered relative to the coordinate reference system that is related to the hole. The coordinate of the compliance centre is $\vec{r}_m = [X_m, Y_m, Z_m, \theta_m, \phi_m, \psi_m]'$.

The disparity between the new state of the compliance centre and its initial state gives rise to state errors, defined as:

$$\vec{\delta} = \vec{r}_o - \vec{r}_m \tag{3.1}$$

It can be asserted that the linear and torsional springs undergo greater changes when the compliance centre's initial position is more distant from the hole axis, and the rotation angle is larger after extracting the peg from the hole.

In addition, due to the differences in states between the peg's state and the manipulator, the manipulator creates forces and torques, which are defined as follows:

$$\vec{f} = K\vec{\Delta} \tag{3.2}$$

In which $\vec{f} = [f_{sX}, f_{sY}, f_{sZ}, \tau_{s\theta}, \tau_{s\phi}, \tau_{s\psi}]'$ is the force/torque vector, K = *diag*$[k_X, k_Y, k_Z, k_\theta, k_\phi, k_\psi]$ is the gain matrix and $\vec{\Delta} = \vec{\delta} + \vec{r} - \vec{r}_o$, in which r is the current distance from the axis of the hole to the compliance centre and the peg's tip.

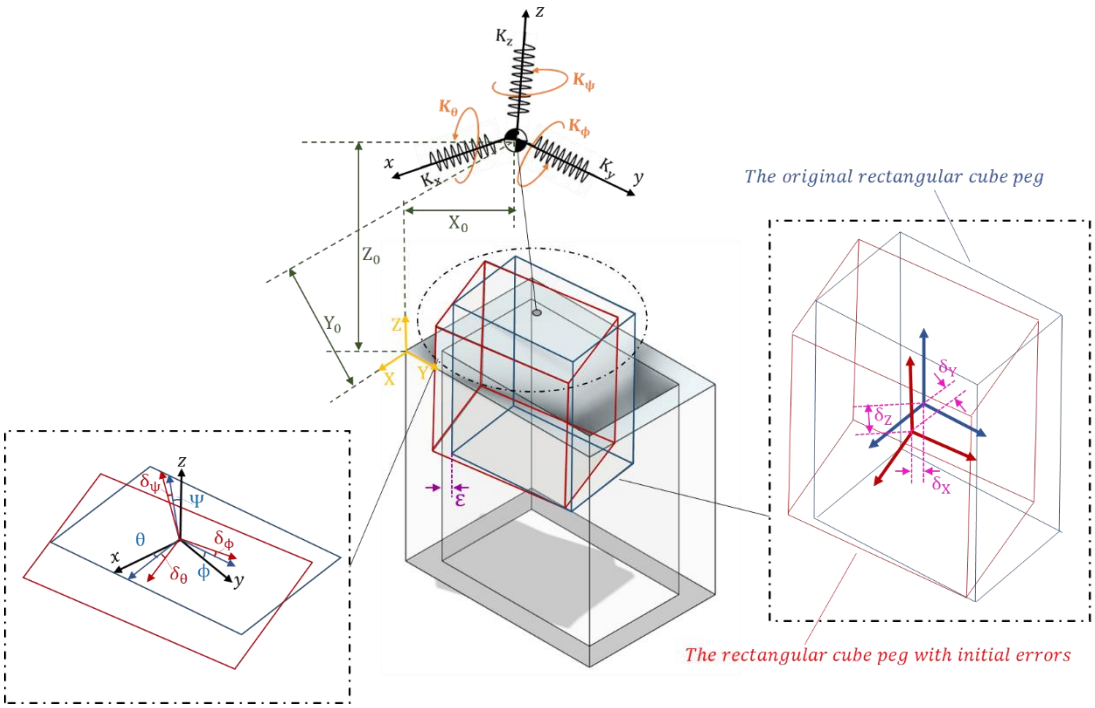

Figure 3.6. Definition of initial errors and position in rectangle peg-hole

I. Case 1: Two-point contact

In this case, we scrutinise the contact scenario where two points of the peg contact the surfaces of the hole (Figure 3.4.a).

In this case, the coordinate transformation matrix is formulated as follows:

$$T_p^h = \begin{bmatrix} c\psi c\phi & s\theta c\psi s\phi - s\psi c\theta & s\theta s\psi + c\theta c\psi s\phi \\ s\psi c\phi & s\theta s\psi s\phi + c\psi c\theta & c\theta s\psi s\phi - s\theta c\psi \\ -s\phi & c\psi s\theta & c\phi c\theta \end{bmatrix} \quad (3.3)$$

$$T_h^p = \begin{bmatrix} c\psi c\phi & s\psi c\phi & -s\phi \\ s\theta c\psi s\phi - s\psi c\theta & s\theta s\psi s\phi + c\psi c\theta & c\psi s\theta \\ s\theta s\psi + c\theta c\psi s\phi & c\theta s\psi s\phi - s\theta c\psi & c\phi c\theta \end{bmatrix} \quad (3.4)$$

A kinematic constraint in the closed-loop kinematic chain is characterised based on the spatial arrangement of the peg relative to the hole.

$$R_1 - T_p^h r_1 = R_C, \quad R_2 - T_p^h r_2 = R_C \quad (3.5)$$

Where,

$$R_1 = \begin{bmatrix} 0 \\ \varepsilon_1 \\ 0 \end{bmatrix}, \quad R_2 = \begin{bmatrix} -v \\ w - \varepsilon_2 \\ -h' \end{bmatrix}, \quad r_1 = \begin{bmatrix} \frac{v'}{2} \\ -\frac{w'}{2} \\ -(H + L_C - h) \end{bmatrix}_p, \quad r_2 = \begin{bmatrix} -\frac{v'}{2} \\ \frac{w'}{2} \\ -(H + L_C) \end{bmatrix}_p \quad (3.6)$$

Therefore,

$$T_p^h (r_1 - r_2) + R_2 - R_1 = 0 \quad (3.7)$$

where ε_1 represents the distance along the Y-axis from the left wall, and ε_2 denotes the distance from the right wall. Additionally, h' signifies the vertical distance from the second contact point to the upper surface of the hole (Figure 3.7).

Conducting a thorough force analysis involves considering the forces and torques from the peg-hole contact, as well as those at the compliance centre due to spring length variations. This analysis allows for the determination of the force F_z in relation to other variables.

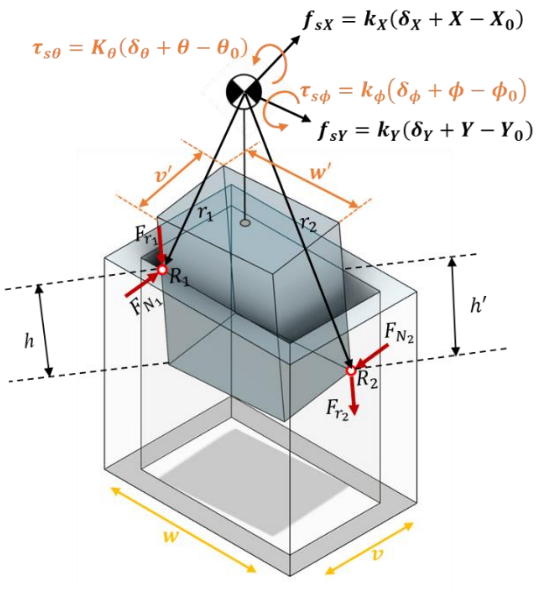

Figure 3.7. Geometry and forces during the two-point contact in the rectangle peg-hole.

The frictional force and the applied force are as follows:

$$F_{N1} = -F_{N1}T_h^p\hat{e}_h \times \hat{e}_p = F_{N1}\begin{bmatrix} -s\theta s\psi s\phi - c\psi c\theta \\ s\psi c\phi \\ 0 \end{bmatrix}_p,$$

$$F_{N2} = F_{N2}T_h^p\hat{I} = F_{N2}\begin{bmatrix} c\psi c\phi \\ s\theta c\psi s\phi - s\psi c\theta \\ s\theta s\psi + c\theta c\psi s\phi \end{bmatrix}_p \quad (3.8)$$

$$F_{r1} = -\mu F_{N1}\hat{k} \quad , \quad F_{r2} = -\mu F_{N2}\begin{bmatrix} -s\phi \\ c\psi s\theta \\ c\phi c\theta \end{bmatrix} = -\mu F_{N2}\hat{K} \quad (3.9)$$

Considering $\sum F_p = 0$ and $\sum M_p = 0$, the following is the applied force and moment by the compliance centre:

$$F + T_h^p f_s + F_{N1} + F_{N2} + F_{r1} + F_{r2} = 0 \quad (3.10)$$

$$M + r_1 \times (F_{N1} + F_{r1}) + r_2 \times (F_{N2} + F_{r2}) + T_h^p \tau_s = 0 \quad (3.11)$$

in which $F = [F_x, F_y, F_z]$`, $f_s = [f_{sx}, f_{sy}, f_{sz}]$ $M = [M_x, M_y, M_z]$`, $\tau_s = [\tau_{s\theta}, \tau_{s\phi}, \tau_{s\psi}]$.

In instances involving small clearances between peg and hole, equations (3.10) and (3.11) can be formulated as:

$$\begin{bmatrix} F_x \\ F_y \\ F_z \end{bmatrix} + \begin{bmatrix} 1 & \psi & -\phi \\ -\psi & 1 & \theta \\ \phi & -\theta & c\phi c\theta \end{bmatrix} \begin{bmatrix} f_{sX} \\ f_{sY} \\ f_{sZ} \end{bmatrix} + F_{N1} \begin{bmatrix} -1 \\ \psi \\ 0 \end{bmatrix} + F_{N2} \begin{bmatrix} 1 \\ -\psi \\ \phi \end{bmatrix} + \begin{bmatrix} 0 \\ 0 \\ -\mu F_{N1} \end{bmatrix} - \mu F_{N2} \begin{bmatrix} -\phi \\ \theta \\ 1 \end{bmatrix} = 0 \tag{3.12}$$

$$\begin{bmatrix} M_x \\ M_y \\ M_z \end{bmatrix} + r_1 \times \begin{bmatrix} -F_{N1} \\ \psi F_{N1} \\ -\mu F_{N1} \end{bmatrix} + r_2 \times \begin{bmatrix} F_{N2} + \phi\mu F_{N2} \\ -\psi F_{N2} - \theta\mu F_{N2} \\ \phi F_{N2} - \mu F_{N2} \end{bmatrix} + \begin{bmatrix} 1 & \psi & -\phi \\ -\psi & 1 & \theta \\ \phi & -\theta & c\phi c\theta \end{bmatrix} \begin{bmatrix} \tau_{s\theta} \\ \tau_{s\phi} \\ \tau_{s\psi} \end{bmatrix} = 0 \tag{3.13}$$

To solve the equations, the force F_z is applied in the z-direction (F_x, $F_Y = 0$), and compliance is incorporated along the y and θ directions ($f_{sZ} = 0$):

$$F_z = -\phi f_{sX} + \theta f_{sY} - \psi F_{N1} + \psi F_{N2} + \theta\mu F_{N2} \tag{3.14}$$

$$\begin{bmatrix} F_{N1} \\ F_{N2} \end{bmatrix} = \begin{bmatrix} -1 & 1+\phi\mu \\ \psi & -\psi-\theta\mu \end{bmatrix}^{-1} \begin{bmatrix} -f_{sX} - \psi f_{sY} \\ \psi f_{sX} - f_{sY} \end{bmatrix} = \frac{\begin{bmatrix} -\psi-\theta\mu & -1-\phi\mu \\ -\psi & -1 \end{bmatrix}}{\theta\mu-\psi\phi\mu} \begin{bmatrix} -f_{sX} - \psi f_{sY} \\ \psi f_{sX} - f_{sY} \end{bmatrix} \tag{3.15}$$

By using (3.14) and (3.15), there is:

$$\begin{bmatrix} M_x \\ M_y \\ M_z \end{bmatrix} = -\begin{bmatrix} \frac{w'}{2}\mu F_{N1} + (H + L_C - h)\psi F_{N1} \\ (H + L_C - h)F_{N1} + \frac{v'}{2}\mu F_{N1} \\ \frac{v'}{2}\psi F_{N1} - \frac{w'}{2}F_{N1} \end{bmatrix} -$$

$$\begin{bmatrix} \frac{w'}{2}(\phi F_{N2} - \mu F_{N2}) - (H + L_C)(\psi F_{N2} + \theta\mu F_{N2}) \\ -(H + L_C)(F_{N2} + \phi\mu F_{N2}) + \frac{v'}{2}(\phi F_{N2} - \mu F_{N2}) \\ \frac{v'}{2}(\psi F_{N2} + \theta\mu F_{N2}) - \frac{w'}{2}(F_{N2} + \phi\mu F_{N2}) \end{bmatrix} - \begin{bmatrix} 1 & \psi & -\phi \\ -\psi & 1 & \theta \\ \phi & -\theta & 1 \end{bmatrix} \begin{bmatrix} \tau_{s\theta} \\ \tau_{s\phi} \\ \tau_{s\psi} \end{bmatrix} \tag{3.16}$$

In this scenario, when $F_{N2} = 0$, it signifies the limited state of contact. Consequently, the boundary condition can be established as follows.

$$\begin{bmatrix} 0 \\ 0 \\ F_z \end{bmatrix} + \begin{bmatrix} 1 & \psi & -\phi \\ -\psi & 1 & \theta \\ \phi & -\theta & 1 \end{bmatrix} \begin{bmatrix} f_{sX} \\ f_{sY} \\ f_{sZ} \end{bmatrix} + \begin{bmatrix} -F_{N1} \\ \psi F_{N1} \\ -\mu F_{N1} \end{bmatrix} = 0 \tag{3.17}$$

$$f_{sX} + \psi f_{sY} - \phi f_{sZ} - F_{N1} = 0 \tag{3.18}$$

$$-\psi f_{sX} + f_{sY} + \theta f_{sZ} + \psi F_{N1} = 0 \tag{3.19}$$

Using the above two equations and two unknowns, we can find:

$$F_{sY} + \theta f_{sZ} + \psi^2 f_{sY} - \phi\psi f_{sZ} = 0 \tag{3.20}$$

$$F_{N1} = f_{sX} + \psi f_{sY} - \phi f_{sZ} \tag{3.21}$$

$$\frac{w'}{2}\mu(k_X(\delta_X + X - X_0) + \psi k_Y(\delta_Y + Y - Y_0) - \phi k_Z(\delta_Z + Z - Z_0)) + (H + L_C - h)\psi(k_X(\delta_X + X - X_0) + \psi k_Y(\delta_Y + Y - Y_0) - \phi k_Z(\delta_Z + Z - Z_0)) + k_\theta(\delta_\theta + \theta - \theta_0) + \psi k_\phi(\delta_\phi + \phi - \phi_0) - \phi(\delta_\psi + \psi - \psi_0) = 0 \tag{3.22}$$

Now, a quadratic equation can be formulated to determine the roots corresponding to the extraction depth h:

$$ah^2 + bh + c = 0 \tag{3.23}$$

in which:

$$a \triangleq k_Y\left(\delta_Y + 2w - \frac{3w'}{2} - Y_0\right)$$

$$b \triangleq -\frac{w'}{2}\mu k_Y\left(\delta_Y + 2w - \frac{3w'}{2} - Y_0\right) - k_Y\left(\delta_Y + 2w - \frac{3w'}{2} - Y_0\right)(H + L_C) + k_Y(w - w')(H + L_C) - (w - w')\mu k_X\left(\delta_X - \frac{v'}{2} - X_0\right)\frac{1}{2} + k_\theta(\delta_\theta - \theta_0)$$

$$c \triangleq \frac{w'}{2}\mu k_Y(w - w')(H + L_C) + \frac{w'}{2}\mu(w - w')\mu k_X\left(\delta_X - \frac{v'}{2} - X_0\right) + k_Y(w - w')(H + L_C)^2 + k_\theta(w - w')$$

The roots (extraction depth[1]) of the equation is:

$$h_1 = \frac{-b + \sqrt{b^2 - 4ac}}{2a}, h_2 = \frac{-b - \sqrt{b^2 - 4ac}}{2a} \tag{3.24}$$

II. Case 2: Two-side contact

In this section, we conduct an analysis of the contact state wherein two lines of the peg come into contact with the inner surfaces of the hole (Figure 3.4.b). In this scenario, the rigidity inherent in both the peg and the hole results in a uniform distribution of the vertical force along

[1] The period of the equation's roots (h_1 & h_2) is discussed in section 3.3.1.

the contact lines. Consequently, the vertical force and the friction force, which are initially distributed forces, are treated as concentrated forces acting at the centre of the contact lines.

Based on the relative position of the peg in relation to the hole, kinematic constraints can be delineated as follows. Kinematic constraints represent equations that govern the motion of solids, faces, edges, or points and can be formulated utilising predefined coordinate systems or custom coordinate systems.

$$R_1 - T_p^h r_1 = R_C \ , \ \ R_2 - T_p^h r_2 = R_C \tag{3.25}$$

Let $R_C = [X, Y, Z]`$, R_1 and R_2 denote the midpoints of two contact lines in the hole coordinates, and r_1 and r_2 represent the midpoints of two contact lines in the peg coordinates.

In this scenario, it is evident that ψ=0 , and ϕ is contingent on the extraction depth, denoted as h. The calculation for ϕ is as follows:

$$v = h \sin\phi + v' \cos\phi \tag{3.26}$$

For small clearances and angles between pegs and holes, Equation (3.26) can be simplified as $v = h\phi + v'$ and, therefore:

$$\phi = \frac{v - v'}{h} \tag{3.27}$$

Using the same assumption, the coordinate transformation matrix is also calculated as follows:

$$T_p^h = \begin{bmatrix} c\phi & 0 & s\phi \\ 0 & 1 & 0 \\ -s\phi & 0 & c\phi \end{bmatrix} \ , \ T_h^p = \begin{bmatrix} c\phi & 0 & -s\phi \\ 0 & 1 & 0 \\ s\phi & 0 & c\phi \end{bmatrix} \tag{3.28}$$

Additionally, the peg exhibits an offset in the Y-direction from the hole wall, denoted as ε. Consequently, the following equations can be formulated:

$$R_1 = \left(\varepsilon + \frac{w'}{2}\right)\hat{j} \ , \ R_2 = \left(\varepsilon + \frac{w'}{2}\right)\hat{j} - v'\hat{i} - h\hat{k} \ , \ r_1 = \frac{v'}{2}\hat{i} - (H + L_C - h)\hat{k} \ ,$$

$$r_2 = -\frac{v'}{2}\hat{i} - (H + L_C)\hat{k} \tag{3.29}$$

Using Equation (3.25), R_C will result is:

$$R_C = \begin{bmatrix} s\phi(H + L_C - h) - \frac{c\phi v'}{2} \\ \varepsilon + \frac{w'}{2} \\ c\phi(H + L_C - h) + \frac{s\phi v'}{2} \end{bmatrix} = \begin{bmatrix} X \\ Y \\ Z \end{bmatrix} \tag{3.30}$$

A comprehensive force analysis can be conducted by considering forces and torques arising from the peg-hole contact, alongside forces and torques at the compliance centre attributed to spring length variations. The force F_z can therefore be determined by other relevant variables (Figure 3.8).

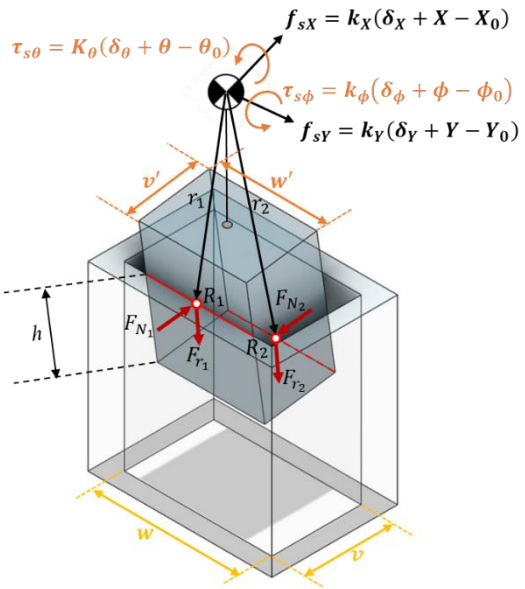

Figure 3.8. Geometry and forces during the two-side contact in the rectangle peg-hole

The frictional force and the applied force are as follows:

$$F_{N1} = -F_{N1}\hat{\imath} \quad , \quad F_{N2} = T_h^p F_{N2}\hat{I} \tag{3.31}$$

$$F_{r1} = -F_{r1}\hat{k} = -\mu F_{N1}\hat{k} \quad , \quad F_{r2} = -F_{r2}\hat{K} = -\mu F_{N2}\hat{K} \tag{3.32}$$

The following is the applied force and moment by the compliance centre:

$$\sum F_p = 0$$

$$F + T_h^p f_{sx} + \begin{bmatrix} -F_{N1} \\ 0 \\ -\mu F_{N1} \end{bmatrix} + \begin{bmatrix} F_{N2}c\phi \\ 0 \\ F_{N2}s\phi \end{bmatrix} + \begin{bmatrix} \mu F_{N2}s\phi \\ 0 \\ -\mu F_{N2}c\phi \end{bmatrix} = 0 \tag{3.33}$$

$$\sum M_p = 0$$

$$M + r_1 \times (F_{N1} + F_{r1}) + r_2 \times (F_{N2} + F_{r2}) + T_h^p \tau_s = 0 \tag{3.34}$$

In the case of small clearances between pegs and holes, equations (3.33) and (3.34) can be simplified as:

$$\begin{bmatrix} F_x - F_{N1} + F_{N2} + \mu F_{N2}\phi \\ F_y \\ F_z - \mu F_{N1} + F_{N2}\phi - \mu F_{N2} \end{bmatrix} + \begin{bmatrix} f_{sX} - f_{sZ}\phi \\ f_{sY} \\ f_{sX}\phi + f_{sZ} \end{bmatrix} = 0 \tag{3.35}$$

$$M + \begin{bmatrix} 0 \\ F_{N1}\left(H + L_C - h + \frac{\mu v'}{2}\right) \\ 0 \end{bmatrix} + \begin{bmatrix} 0 \\ F_{N2}\left(-(H + L_C)(1 + \mu\phi) + \frac{v'}{2}(\phi - \mu)\right) \\ 0 \end{bmatrix} +$$

$$\begin{bmatrix} \tau_{s\theta} - \tau_{s\psi}\phi \\ \tau_{s\phi} \\ \tau_{s\theta}\phi + \tau_{s\psi} \end{bmatrix} = 0 \tag{3.36}$$

Equations can be expressed in the following way:

$$-F_{N1} + F_{N2}(1 + \mu\phi) + f_{sX} = 0 \tag{3.37}$$

$$F_z - \mu F_{N1} + F_{N2}(\phi - \mu) + f_{sX}\phi = 0 \tag{3.38}$$

$$F_{N1}\left(H + L_C - h + \frac{\mu v'}{2}\right) + F_{N2}\left(-(H + L_C)(1 + \mu\phi) + \frac{v'}{2}(\phi - \mu)\right) + \tau_{s\phi} = 0 \tag{3.39}$$

Utilising equations (3.37) and (3.38), one can calculate the vertical forces acting on the surface as F_z.

$$\begin{bmatrix} F_{N1} \\ F_{N2} \end{bmatrix} = \frac{\begin{bmatrix} -(H+L_C)(1+\mu\phi)+\frac{v'}{2}(\phi-\mu) & -1-\mu\phi \\ -H-L_C+h-\frac{\mu v'}{2} & -1 \end{bmatrix}}{-\frac{v'}{2}\phi+h+h\mu\phi-\frac{\mu\phi\mu v'}{2}} \begin{bmatrix} -f_{sX} \\ -\tau_{s\phi} \end{bmatrix} \tag{3.40}$$

As a result, there are:

$$F_z = \mu F_{N1} - F_{N2}(\phi - \mu) - f_{sX}\phi \tag{3.41}$$

where

$$\delta_X + X - X_0 = \delta_X + s\phi(H + L_C - h) - c\phi v' - X_0 \tag{3.42}$$

Also,

$$\begin{bmatrix} F_x \\ F_y \\ F_z \end{bmatrix} = -\begin{bmatrix} -F_{N1} + F_{N2} + \mu F_{N2}\phi + f_{sX} - f_{sZ}\phi \\ f_{sY} \\ -\mu F_{N1} + F_{N2}\phi - \mu F_{N2} + f_{sX}\phi + f_{sZ} \end{bmatrix} \tag{3.43}$$

$$\begin{bmatrix} M_x \\ M_y \\ M_z \end{bmatrix} = -\begin{bmatrix} 0 \\ F_{N1}\left(H + L_C - h + \frac{\mu v'}{2}\right) \\ 0 \end{bmatrix} - \begin{bmatrix} 0 \\ F_{N2}\left(-(H + L_C)(1 + \mu\phi) + \frac{v'}{2}(\phi - \mu)\right) \\ 0 \end{bmatrix} -$$

$$\begin{bmatrix} \tau_{s\theta} - \tau_{s\psi}\phi \\ \tau_{s\phi} \\ \tau_{s\theta}\phi + \tau_{s\psi} \end{bmatrix} \tag{3.44}$$

By assuming $F_{N2}=0$ for the contact force at line 2, it is possible to calculate the boundary conditions for the two-side contact. Accordingly, the h are as follows:

$$h = \frac{\tau_{s\phi}}{f_{sX}} + H + L_C + \frac{\mu v'}{2} \tag{3.45}$$

h is expressed as follows using equations (3.42) and (3.45).

$$h = \frac{k_\phi(\delta_\phi h + v - v' - h\phi_0)}{k_X[h(\delta_X - v - X_0) + (v - v')(H + L_C)]} + \left(H + L_C + \frac{\mu v'}{2}\right) \tag{3.46}$$

Now, a quadratic equation can be formulated to determine the roots corresponding to the extraction depth h:

$$ah^2 + bh + c = 0 \tag{3.47}$$

in which:

$$a \triangleq k_X(\delta_X - v - X_0)$$

$$b \triangleq k_X(v - v')(H + L_C) - k_\phi(\delta_\phi - \phi_0) - k_\phi(v - v') - k_X\left(H + L_C + \frac{\mu v'}{2}\right)(\delta_X - v - X_0)$$

$$c \triangleq -\left(H + L_C + \frac{\mu v'}{2}\right)k_X(v - v')(H + L_C)$$

The roots (extraction depth[1]) of equation (3.47) are.

[1] The period of the equation's roots (h_1 & h_2)is discussed in section 3.3.1.

$$h_1 = \frac{-b+\sqrt{b^2-4ac}}{2a}, h_2 = \frac{-b-\sqrt{b^2-4ac}}{2a} \tag{3.48}$$

III. Case 3: Two-side and one-plane contact

In this section, we scrutinise the contact scenario where two lines and one plane of the peg contact the inner surfaces of the hole (Figure 3.4.c). In the context of plane contact, the vertical force of the surface is oriented perpendicular to both planes, and the friction force direction exhibits two components within the contact plane, which are determined by the direction of movement. However, due to the small angles involved, the direction of the friction force can be approximated as vertical. Consequently, all forces are applied at the centre of the contact surface, considering the uniformity of the vertical force along the contact lines. Additionally, both the vertical force and the friction force, which are initially distributed forces, are treated as concentrated forces applied at the centre of the contact lines.

A kinematic constraint/kinematic loop can be defined according to the position of the peg in relation to the hole.

$$R_1 - T_p^h r_1 = R_C \ , \quad R_2 - T_p^h r_2 = R_C \tag{3.49}$$

Where,

$$r_1 = \begin{bmatrix} 0 \\ -\frac{w'}{2} \\ -(H + L_C) \end{bmatrix}_p, r_2 = \begin{bmatrix} 0 \\ \frac{w'}{2} \\ -(H + L_C - h) \end{bmatrix}_p, r_3 = \begin{bmatrix} \frac{v'}{2} \\ -\frac{w'}{2} + \bar{y} \\ -(H + L_C - \bar{z}) \end{bmatrix}_p \tag{3.50}$$

Here, $\bar{y}$ and $\bar{z}$ denote the centre of the third contact surface in relation to the bottom corner of the peg. The contact surface consistently takes the shape of a trapezoid with a side length of *h* and height w'. However, given the negligible rotation angle of the peg within the hole, the contact surface can be approximated as a rectangle with sides h and w'.

$$\bar{y} = \frac{w'}{2} \quad , \quad \bar{z} = \frac{h}{2} \quad , \quad r_3 = \begin{bmatrix} \frac{v'}{2} \\ 0 \\ -\left(H + L_C - \frac{h}{2}\right) \end{bmatrix}_p \tag{3.51}$$

As illustrated in Figure 3.9 the peg is constrained to rotate solely around adapter X to preserve the contact state. Consequently, ϕ and ψ are both zero, and θ can be expressed in terms of h as follows.

$$h\theta = w - w' \quad , \quad \theta = \frac{w - w'}{h} \tag{3.52}$$

The coordinate transformation matrix and compliance centre position are calculated as follows:

$$T_p^h = \begin{bmatrix} 1 & 0 & 0 \\ 0 & c\theta & -s\theta \\ 0 & s\theta & c\theta \end{bmatrix} \quad , \quad T_h^p = \begin{bmatrix} 1 & 0 & 0 \\ 0 & c\theta & s\theta \\ 0 & -s\theta & c\theta \end{bmatrix} \tag{3.53}$$

$$R_C = R_2 - T_p^h r_2 = \begin{bmatrix} -\frac{v'}{2} \\ w - \frac{w'}{2} - \theta(H + L_C - h) \\ -\theta\frac{w'}{2} + (H + L_C - h) \end{bmatrix} = \begin{bmatrix} X \\ Y \\ Z \end{bmatrix} \tag{3.54}$$

A thorough force analysis can be undertaken by considering the forces and torques originating from the peg-hole contact, as well as the forces and torques at the compliance centre associated with variations in spring length. Consequently, the force F_z can be expressed in terms of other pertinent variables.

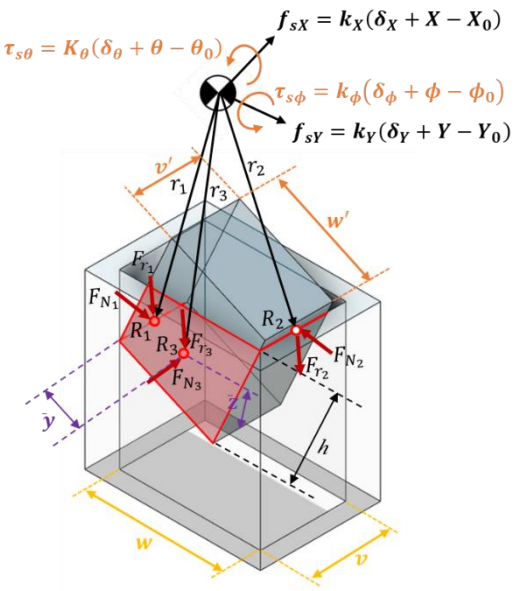

Figure 3.9. Geometry and forces during the Two-side and one-plane contact in the rectangle peg-hole

The frictional force and the applied force are as follows:

$$\mathrm{F_{N1}} = \mathrm{F_{N1}T_h^p\hat{j}} = \mathrm{F_{N1}}\begin{bmatrix} 0 \\ \mathrm{c\theta} \\ -\mathrm{s\theta} \end{bmatrix} \quad , \quad \mathrm{F_{N2}} = -\mathrm{F_{N2}\hat{j}} \quad , \quad \mathrm{F_{N3}} = -\mathrm{F_{N3}\hat{i}} \tag{3.55}$$

$$\mathrm{F_{r1}} = -\mathrm{F_{r1}T_h^p\hat{k}} = -\mu\mathrm{F_{N1}}\begin{bmatrix} 0 \\ \mathrm{s\theta} \\ \mathrm{c\theta} \end{bmatrix}, \mathrm{F_{r2}} = -\mathrm{F_{r2}\hat{k}} = -\mu\mathrm{F_{N2}\hat{k}}\ ,\mathrm{F_{r3}} = -\mathrm{F_{r3}T_h^p\hat{k}} = -\mu\mathrm{F_{N3}}\begin{bmatrix} 0 \\ \mathrm{s\theta} \\ \mathrm{c\theta} \end{bmatrix} \tag{3.56}$$

The following is the applied force and moment by the compliance centre:

$$\sum \mathrm{F_p} = 0$$

$$\mathrm{F} + \mathrm{T_h^p f_s} + \mathrm{F_{N1}} + \mathrm{F_{N2}} + \mathrm{F_{N3}} + \mathrm{F_{r1}} + \mathrm{F_{r2}} + \mathrm{F_{r3}} = 0 \tag{3.57}$$

$$\sum \mathrm{M_p} = 0$$

$$\mathrm{M} + \mathrm{r_1} \times (\mathrm{F_{N1}} + \mathrm{F_{r1}}) + \mathrm{r_2} \times (\mathrm{F_{N2}} + \mathrm{F_{r2}}) + \mathrm{r_3} \times (\mathrm{F_{N3}} + \mathrm{F_{r3}}) + \mathrm{T_h^p}\tau_\mathrm{s} = 0 \tag{3.58}$$

in which:

$$\mathrm{r_1} = \begin{bmatrix} 0 \\ -\frac{\mathrm{w'}}{2} \\ -(\mathrm{H} + \mathrm{L_C}) \end{bmatrix}_\mathrm{p} , \mathrm{r_2} = \begin{bmatrix} 0 \\ \frac{\mathrm{w'}}{2} \\ -(\mathrm{H} + \mathrm{L_C} - \mathrm{h}) \end{bmatrix}_\mathrm{p}, \mathrm{r_3} = \begin{bmatrix} \frac{\mathrm{v'}}{2} \\ 0 \\ -\left(\mathrm{H} + \mathrm{L_C} - \frac{\mathrm{h}}{2}\right) \end{bmatrix}_\mathrm{p} \tag{3.59}$$

In instances involving small clearances between peg and hole, equations (3.57) and (3.59) can be streamlined as:

$$\begin{bmatrix} F_x \\ F_y \\ F_z \end{bmatrix} + \begin{bmatrix} f_{sX} \\ f_{sY} + f_{sZ}\theta \\ -f_{sY}\theta + f_{sZ} \end{bmatrix} + \begin{bmatrix} -F_{N3} \\ F_{N1} - F_{N2} - \theta\mu F_{N1} - \theta\mu F_{N3} \\ -\theta F_{N1} - \mu F_{N1} - \mu F_{N2} - \mu F_{N3} \end{bmatrix} = 0 \tag{3.60}$$

$$\begin{bmatrix} M_x \\ M_y \\ M_z \end{bmatrix} + \begin{bmatrix} \frac{w'}{2} F_{N1}(\theta + \mu) + F_{N1}(H + L_C)(1 - \theta\mu) \\ 0 \\ 0 \end{bmatrix} + \begin{bmatrix} -\frac{w'}{2}\mu F_{N2} - F_{N2}(H + L_C - h) \\ 0 \\ 0 \end{bmatrix} -$$

$$\begin{bmatrix} \theta\mu F_{N3}\left(H + L_C - \frac{h}{2}\right) \\ -F_{N3}\left(H + L_C - \frac{h}{2}\right) - \frac{v'}{2}\mu F_{N3} \\ \frac{v'}{2}\theta\mu F_{N3} \end{bmatrix} + \begin{bmatrix} \tau_{s\theta} \\ \tau_{s\phi} + \tau_{s\psi}\theta \\ -\tau_{s\phi}\theta + \tau_{s\psi} \end{bmatrix} = 0 \tag{3.61}$$

To address the equations, the F_z force is introduced in the z-direction, while Compliance is applied in the y and θ directions. Thus, the equations can be conceptualised as follows. Moreover, in the absence of compliance in the x-direction, the vertical force on the F_{N3} surface would be zero. Therefore, it is presumed that compliance exists in the x-direction, and the force is represented as $F_{N3} = f_{sX}$.

$$\begin{bmatrix} 0 \\ 0 \\ F_z \end{bmatrix} + \begin{bmatrix} f_{sX} \\ f_{sY} \\ -f_{sY}\theta \end{bmatrix} + \begin{bmatrix} -f_{sX} \\ F_{N1} - F_{N2} - \theta\mu F_{N1} - \theta\mu f_{sX} \\ -\theta F_{N1} - \mu F_{N1} - \mu F_{N2} - \mu f_{sX} \end{bmatrix} = 0 \tag{3.62}$$

$$\begin{bmatrix} 0 \\ 0 \\ 0 \end{bmatrix} + \begin{bmatrix} \frac{w'}{2} F_{N1}(\theta + \mu) + F_{N1}(H + L_C)(1 - \theta\mu) \\ 0 \\ 0 \end{bmatrix} + \begin{bmatrix} -\frac{w'}{2}\mu F_{N2} - F_{N2}(H + L_C - h) \\ 0 \\ 0 \end{bmatrix} -$$

$$\begin{bmatrix} \theta\mu f_{sX}\left(H + L_C - \frac{h}{2}\right) \\ -f_{sX}\left(H + L_C - \frac{h}{2}\right) - \frac{v'}{2}\mu f_{sX} \\ \frac{v'}{2}\theta\mu f_{sX} \end{bmatrix} + \begin{bmatrix} \tau_{s\theta} \\ \tau_{s\phi} \\ -\tau_{s\phi}\theta \end{bmatrix} = 0 \tag{3.63}$$

As a result, there are:

$$F_{N1}(1 - \theta\mu) - F_{N2} = -f_{sY} + \theta\mu f_{sX} \tag{3.64}$$

$$F_{N1}\left(\frac{w'}{2}(\theta+\mu)+(H+L_C)(1-\theta\mu)\right)+F_{N2}\left(-\frac{w'}{2}\mu-(H+L_C-h)\right)=\theta\mu f_{sX}\left(H+L_C-\frac{h}{2}\right)-\tau_{s\theta} \quad (3.65)$$

$$F_z=f_{sY}\theta+\theta F_{N1}+\mu F_{N1}+\mu F_{N2}+\mu f_{sX} \quad (3.66)$$

By solving the three equations with three unknowns, namely F_{N1} ،F_{N2} and F_z, their respective values can be determined.

$$\begin{bmatrix}F_{N1}\\F_{N2}\end{bmatrix}=\frac{\begin{bmatrix}-\frac{w'}{2}\mu-(H+L_C-h) & 1\\ -\frac{w'}{2}(\theta+\mu)-(H+L_C)(1-\theta\mu) & 1-\theta\mu\end{bmatrix}}{(1-\theta\mu)\left(-\frac{w'}{2}\mu-(H+L_C-h)\right)+\frac{w'}{2}(\theta+\mu)+(H+L_C)(1-\theta\mu)}\begin{bmatrix}-f_{sY}+\theta\mu f_{sX}\\ \theta\mu f_{sX}\left(H+L_C-\frac{h}{2}\right)-\tau_{s\theta}\end{bmatrix} \quad (3.67)$$

$$\begin{bmatrix}F_x\\F_y\\F_z\end{bmatrix}=-\begin{bmatrix}f_{sX}\\f_{sY}\\-f_{sY}\theta\end{bmatrix}-\begin{bmatrix}-f_{sX}\\F_{N1}-F_{N2}-\theta\mu F_{N1}-\theta\mu f_{sX}\\-\theta F_{N1}-\mu F_{N1}-\mu F_{N2}-\mu f_{sX}\end{bmatrix} \quad (3.68)$$

$$\begin{bmatrix}M_x\\M_y\\M_z\end{bmatrix}=-\begin{bmatrix}\frac{w'}{2}F_{N1}(\theta+\mu)+F_{N1}(H+L_C)(1-\theta\mu)\\0\\0\end{bmatrix}-\begin{bmatrix}-\frac{w'}{2}\mu F_{N2}-F_{N2}(H+L_C-h)\\0\\0\end{bmatrix}+\begin{bmatrix}\theta\mu f_{sX}\left(H+L_C-\frac{h}{2}\right)\\-f_{sX}\left(H+L_C-\frac{h}{2}\right)-\frac{v'}{2}\mu f_{sX}\\\frac{v'}{2}\theta\mu f_{sX}\end{bmatrix}-\begin{bmatrix}\tau_{s\theta}\\\tau_{s\phi}\\-\tau_{s\phi}\theta\end{bmatrix} \quad (3.69)$$

In this scenario, when $F_{N1}=0$, it signifies the limited state of contact. Consequently, the boundary condition can be established as follows.

$$F_{N2}=f_{sY}-\theta\mu f_{sX} \quad (3.70)$$

$$-\frac{w'}{2}\mu F_{N2}-F_{N2}(H+L_C-h)-\theta\mu f_{sX}\left(H+L_C-\frac{h}{2}\right)+\tau_{s\theta}=0 \quad (3.71)$$

where;

$$\tau_{s\theta} = k_\theta(\delta_\theta + \theta - \theta_0)\,;\ \begin{bmatrix} X \\ Y \\ Z \end{bmatrix} = \begin{bmatrix} -\frac{v'}{2} \\ w - \frac{w'}{2} - \theta(H + L_C - h) \\ -\theta\frac{w'}{2} + (H + L_C - h) \end{bmatrix} \tag{3.72}$$

The following results can be obtained by using equations (3.70) and (3.71):

$$\begin{aligned} &-\frac{w'}{2}\mu k_Y\left[\left(\delta_Y + w - \frac{w'}{2} - Y_0 + w - w'\right)h - (w - w')(H + L_C)\right] \\ &\quad + \frac{w'}{2}\mu(w - w')\mu k_X\left(\delta_X - \frac{v'}{2} - X_0\right) \\ &\quad - k_Y\left[\left(\delta_Y + w - \frac{w'}{2} - Y_0 + w - w'\right)h - (w - w')(H + L_C)\right](H + L_C - h) \\ &\quad - (w - w')\mu k_X\left(\delta_X - \frac{v'}{2} - X_0\right)\frac{h}{2} + k_\theta(\delta_\theta - \theta_0)h + k_\theta(w - w') = 0 \end{aligned} \tag{3.73}$$

Now, a quadratic equation ($ah^2 + bh + c = 0$) can be formulated to determine the roots corresponding to the extraction depth h, in which:

$$a \triangleq k_Y\left(\delta_Y + 2w - \frac{3w'}{2} - Y_0\right)$$

$$b \triangleq -\frac{w'}{2}\mu k_Y\left(\delta_Y + 2w - \frac{3w'}{2} - Y_0\right) - k_Y\left(\delta_Y + 2w - \frac{3w'}{2} - Y_0\right)(H + L_C)$$
$$+ k_Y(w - w')(H + L_C) - (w - w')\mu k_X\left(\delta_X - \frac{v'}{2} - X_0\right)\frac{1}{2} + k_\theta(\delta_\theta - \theta_0)$$

$$c \triangleq \frac{w'}{2}\mu k_Y(w - w')(H + L_C) + \frac{w'}{2}\mu(w - w')\mu k_X\left(\delta_X - \frac{v'}{2} - X_0\right)$$
$$+ k_Y(w - w')(H + L_C)^2 + k_\theta(w - w')$$

The roots (extraction depth[1]) of the equation is:

$$h_1 = \frac{-b + \sqrt{b^2 - 4ac}}{2a}, h_2 = \frac{-b - \sqrt{b^2 - 4ac}}{2a} \tag{3.74}$$

[1] The period of the equation's roots (h_1 & h_2)is discussed in section 3.3.1.

IV. Case 4: Two-edge contact

In this section, we analyse the contact scenario in which two edges of the peg come into contact with the surfaces of the hole (Figure 3.4.d). Both the vertical force and the friction force initially span along the contact lines but are treated as concentrated forces positioned at the midpoint of the contact line. The maintenance of the contact state involves the peg moving both vertically and in the Y direction. In this scenario, the angles θ and ϕ are negligible, and for simplification, we consider them to be zero.

In this case, the coordinate transformation matrix is formulated as follows:

$$T_p^h = \begin{bmatrix} c\psi & -s\psi & 0 \\ s\psi & c\psi & 0 \\ 0 & 0 & 1 \end{bmatrix} \quad , \quad T_h^p = \begin{bmatrix} c\psi & s\psi & 0 \\ -s\psi & c\psi & 0 \\ 0 & 0 & 1 \end{bmatrix} \tag{3.75}$$

Also,

$$w' \sin\psi + v' \cos\psi = v \tag{3.76}$$

The ψ angle can be obtained in this manner.

A kinematic constraint or kinematic loop can be characterised based on the spatial arrangement of the peg relative to the hole.

$$R_1 - T_p^h r_1 = R_C \quad , \quad R_2 - T_p^h r_2 = R_C \tag{3.77}$$

Where,

$$r_1 = \begin{bmatrix} \frac{v'}{2} \\ -\frac{w'}{2} \\ -\left(H + L_C - \frac{h}{2}\right) \end{bmatrix}_p \quad , \quad r_2 = \begin{bmatrix} -\frac{v'}{2} \\ \frac{w'}{2} \\ -\left(H + L_C - \frac{h}{2}\right) \end{bmatrix}_p \tag{3.78}$$

The forthcoming steps involve the calculation of the coordinate transformation matrix and the determination of the compliance centre position through the following procedures:

$$R_C = R_1 - T_p^h r_1 = \begin{bmatrix} -\frac{v'}{2} - \psi\frac{w'}{2} \\ \varepsilon + \frac{w'}{2} - \psi\frac{v'}{2} \\ H + L_C - h \end{bmatrix} = \begin{bmatrix} X \\ Y \\ Z \end{bmatrix} \tag{3.79}$$

Anticipating the ensuing steps, an exhaustive force analysis entails the consideration of forces and torques stemming from the interaction between the peg and the hole, along with those affecting the compliance centre due to variations in spring length. The outcome of this analysis will facilitate the determination of the force F_z relative to other pertinent variables (Figure 3.10).

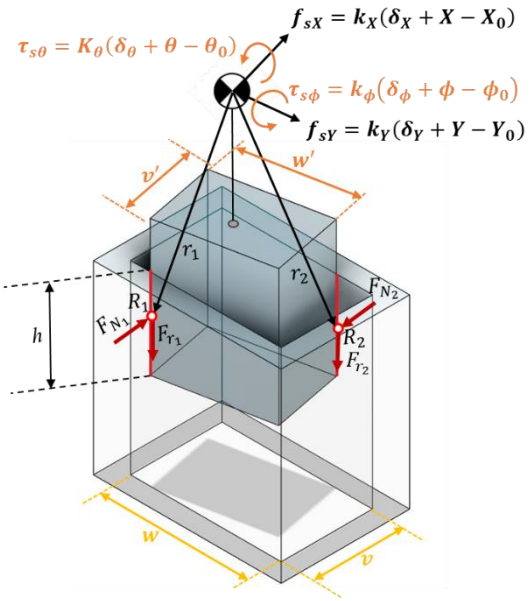

Figure 3.10. Geometry and forces during the Two-edge contact in the rectangle peg-hole.

The frictional force and the applied force are as follows:

$$F_{N1} = -F_{N1}T_h^p\hat{\imath} \quad , \quad F_{N2} = F_{N2}T_h^p\hat{\imath} \tag{3.80}$$

$$F_{r1} = -\mu F_{N1}\hat{k} \quad , \quad F_{r2} = -\mu F_{N2}\hat{k} \tag{3.81}$$

As the peg continues its extraction from the hole, the contact line diminishes, leading to a reduction in the friction force. Consequently, the friction coefficient can be regarded as a function of h and is expressed as follows.

$$\mu = \mu' h \tag{3.82}$$

The following is the applied force and moment by the compliance centre:

$$\sum F_p = 0$$

$$F + T_h^p f_s + F_{N1} + F_{N2} + F_{r1} + F_{r2} = 0 \tag{3.83}$$

$$\sum M_p = 0$$

$$M + r_1 \times (F_{N1} + F_{r1}) + r_2 \times (F_{N2} + F_{r2}) + T_h^p \tau_{s\theta} = 0 \tag{3.84}$$

In this scenario, under the assumption of negligible clearance between the peg and the hole, and considering a small angle of rotation, the equations can be reformulated as follows:

$$\begin{bmatrix} F_x \\ F_y \\ F_z \end{bmatrix} + \begin{bmatrix} f_{sX} + f_{sY}\psi \\ -f_{sX}\psi + f_{sY} \\ f_{sZ} \end{bmatrix} - F_{N1} \begin{bmatrix} 1 \\ -\psi \\ \mu' h \end{bmatrix} + F_{N2} \begin{bmatrix} 1 \\ -\psi \\ -\mu' h \end{bmatrix} = 0 \tag{3.85}$$

$$\begin{bmatrix} M_x \\ M_y \\ M_z \end{bmatrix} + F_{N1} \begin{bmatrix} \frac{w'}{2}\mu' h + \left(H + L_C - \frac{h}{2}\right)\psi \\ \left(H + L_C - \frac{h}{2}\right) + \frac{v'}{2}\mu' h \\ \frac{v'}{2}\psi - \frac{w'}{2} \end{bmatrix} + F_{N2} \begin{bmatrix} -\frac{w'}{2}\mu' h - \left(H + L_C - \frac{h}{2}\right)\psi \\ -\left(H + L_C - \frac{h}{2}\right) - \frac{v'}{2}\mu' h \\ \frac{v'}{2}\psi - \frac{w'}{2} \end{bmatrix} +$$

$$\begin{bmatrix} \tau_{s\theta} + \tau_{s\phi}\psi \\ -\tau_{s\theta}\psi + \tau_{s\phi} \\ \tau_{s\psi} \end{bmatrix} = 0 \tag{3.86}$$

To resolve the equations, the force F_z is introduced in the z-direction, and compliance is applied in the y and θ directions. Consequently, the equations can be formulated as follows. Additionally, in the absence of compliance in the x-direction, the vertical force on the F_{N3} surface would be zero. Thus, it is presumed that compliance exists in the x-direction, and the force is expressed as $F_{N3} = f_{sX}$

$$\begin{bmatrix} 0 \\ 0 \\ F_z \end{bmatrix} + \begin{bmatrix} f_{sX} + f_{sY}\psi \\ -f_{sX}\psi + f_{sY} \\ 0 \end{bmatrix} + \begin{bmatrix} -(F_{N1} - F_{N2}) \\ \psi(F_{N1} - F_{N2}) \\ -\mu' h(F_{N1} + F_{N2}) \end{bmatrix} = 0 \tag{3.87}$$

$$\begin{bmatrix} 0 \\ 0 \\ 0 \end{bmatrix} + \begin{bmatrix} (F_{N1} - F_{N2})\left(\frac{w'}{2}\mu' h + H\psi + L_C\psi - \frac{h}{2}\psi\right) \\ (F_{N1} - F_{N2})\left(\frac{v'}{2}\mu' h + H + L_C - \frac{h}{2}\right) \\ (F_{N1} + F_{N2})\left(\frac{v'}{2}\psi - \frac{w'}{2}\right) \end{bmatrix} + \begin{bmatrix} \tau_{s\theta} + \tau_{s\phi}\psi \\ -\tau_{s\theta}\psi + \tau_{s\phi} \\ \tau_{s\psi} \end{bmatrix} = 0 \tag{3.88}$$

Utilising equations (3.87) and (3.88), one can calculate the vertical forces acting on the surface as F_z.

$$f_{sX} + f_{sY}\psi - (F_{N1} - F_{N2}) = 0 \tag{3.89}$$

$$(F_{N1} + F_{N2})\left(\frac{v'}{2}\psi - \frac{w'}{2}\right) + \tau_{s\psi} = 0 \tag{3.90}$$

Equations can be expressed in the following way:

$$F_{N1} = \frac{f_{sX}+f_{sY}\psi}{2} - \frac{\tau_{s\psi}}{v'\psi - w'} \tag{3.91}$$

$$F_{N2} = -\frac{\tau_{s\psi}}{v'\psi - w'} - \frac{f_{sX}+f_{sY}\psi}{2} \tag{3.92}$$

$$F_z = \mu' h(F_{N1} + F_{N2}) = -\frac{2\mu' h\tau_{s\psi}}{v'\psi - w'} \tag{3.93}$$

$$\begin{bmatrix} F_x \\ F_y \\ F_z \end{bmatrix} = -\begin{bmatrix} f_{sX} + f_{sY}\psi \\ -f_{sX}\psi + f_{sY} \\ 0 \end{bmatrix} - \begin{bmatrix} -(F_{N1} - F_{N2}) \\ \psi(F_{N1} - F_{N2}) \\ -\mu' h(F_{N1} + F_{N2}) \end{bmatrix} \tag{3.94}$$

$$\begin{bmatrix} M_x \\ M_y \\ M_z \end{bmatrix} = -\begin{bmatrix} (F_{N1} - F_{N2})\left(\frac{w'}{2}\mu' h + H\psi + L_C\psi - \frac{h}{2}\psi\right) \\ (F_{N1} - F_{N2})\left(\frac{v'}{2}\mu' h + H + L_C - \frac{h}{2}\right) \\ (F_{N1} + F_{N2})\left(\frac{v'}{2}\psi - \frac{w'}{2}\right) \end{bmatrix} - \begin{bmatrix} \tau_{s\theta} + \tau_{s\phi}\psi \\ -\tau_{s\theta}\psi + \tau_{s\phi} \\ \tau_{s\psi} \end{bmatrix} \tag{3.96}$$

In this instance, it is evident that the contact boundary condition is solely dependent on the ψ angle. Assuming F_{N2}=0, the contact forces can be computed as follows:

$$F_{N1} = \frac{f_{sX}+f_{sY}\psi}{2} - \frac{\tau_{s\psi}}{v'\psi - w'} = 0 \tag{3.96}$$

By formulating a cubic equation as

$$a\psi^3 + b\psi^2 + c\psi + d = 0 \tag{3.97}$$

we can determine the corresponding roots of the angle ψ.

$$a \triangleq -\frac{k_Y v'^2}{2}$$

$$b \triangleq -\frac{k_X v' w'}{2} + k_Y v'\left(\delta_Y + \varepsilon + \frac{w'}{2} - Y_0\right) + \frac{k_Y w' v'}{2}$$

$$c \triangleq k_X v'\left(\delta_X - \frac{v'}{2} - X_0\right) + \frac{k_X w'^2}{2} - k_Y w'\left(\delta_Y + \varepsilon + \frac{w'}{2} - Y_0\right) - 2k_\psi$$

$$d \triangleq -k_X w'\left(\delta_X - \frac{v'}{2} - X_0\right) - 2k_\psi(\delta_\psi - \psi_0)$$

It is obvious that, in this particular case, the roots of the quadratic equation remain unaffected by the ACC's location, indicating a unique scenario where the contact geometry dominates the extraction dynamics. This observation underscores the robustness and independence of the extraction process from the ACC position in this specific contact configuration. In another way, the position of the ACC becomes inconsequential to the extraction depth.

V. Case 5: Three-edge contact

In this section, we investigate the contact situation where three edges of the peg make contact with the surfaces of the hole (Figure 3.4.e). Initially, both the vertical force and the friction force extend along the contact lines but are simplified as concentrated forces located at the midpoint of the contact line. Preserving the contact state requires vertical and lateral movement of the peg. In this context, the angles θ and ϕ are deemed negligible, and for simplicity, we assume their values to be zero.

In this case, the coordinate transformation matrix is formulated as follows:

$$T_p^h = \begin{bmatrix} c\psi & -s\psi & 0 \\ s\psi & c\psi & 0 \\ 0 & 0 & 1 \end{bmatrix}, \quad T_h^p = \begin{bmatrix} c\psi & s\psi & 0 \\ -s\psi & c\psi & 0 \\ 0 & 0 & 1 \end{bmatrix} \tag{3.98}$$

Also,

$$w' \sin\psi + v' \cos\psi = v \tag{3.99}$$

A kinematic constraint or kinematic loop can be characterised based on the spatial arrangement of the peg relative to the hole.

$$R_1 - T_p^h r_1 = R_C \quad , \quad R_2 - T_p^h r_2 = R_C \quad , \quad R_3 - T_p^h r_3 = R_C \tag{3.100}$$

Where,

$$r_1 = \begin{bmatrix} \frac{v'}{2} \\ -\frac{w'}{2} \\ -\left(H + L_C - \frac{h}{2}\right) \end{bmatrix}_p, r_2 = \begin{bmatrix} -\frac{v'}{2} \\ \frac{w'}{2} \\ -\left(H + L_C - \frac{h}{2}\right) \end{bmatrix}_p, r_3 = \begin{bmatrix} -\frac{v'}{2} \\ -\frac{w'}{2} \\ -\left(H + L_C - \frac{h}{2}\right) \end{bmatrix}_p \tag{3.101}$$

The upcoming stages encompass the computation of the coordinate transformation matrix and establishing the position of the compliance centre, achieved through the subsequent processes:

$$R_C = R_3 - T_p^h r_3 = \begin{bmatrix} -\psi\frac{w'}{2} - \frac{v'}{2} \\ \frac{v'}{2}\psi + \frac{w'}{2} \\ H + L_C - h \end{bmatrix} = \begin{bmatrix} X \\ Y \\ Z \end{bmatrix} \quad (3.102)$$

Foreseeing the next phases, an in-depth examination of forces involves taking into account the forces and torques originating from the interaction between the peg and the hole, as well as those influencing the compliance centre due to changes in spring length. The result of this analysis will aid in establishing the force F_z in relation to other relevant variables (Figure 3.11).

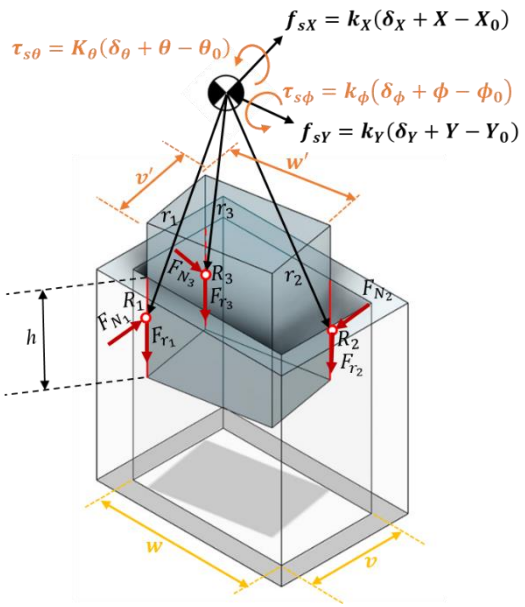

Figure 3.11. Geometry and forces during the Three-edge contact in the rectangle peg-hole.

The frictional force and the applied force are as follows:

$$F_{N1} = -F_{N1}T_h^p\hat{i} \quad , \quad F_{N2} = F_{N2}T_h^p\hat{i} \quad , \quad F_{N3} = F_{N3}T_h^p\hat{j} \quad (3.103)$$

$$F_{r1} = -\mu F_{N1}\hat{k} \quad , \quad F_{r2} = -\mu F_{N2}\hat{k} \quad , \quad F_{r3} = -\mu F_{N3}\hat{k} \quad (3.104)$$

when the peg is extracted from the hole, the contact line diminishes, resulting in a decrease in the friction force. As a result, the friction coefficient can be considered a function of h and is articulated as follows:

$$\mu = \mu' h \tag{3.105}$$

The following is the applied force and moment by the compliance centre:

$$\sum F_p = 0$$

$$F + T_h^p f_s + F_{N1} + F_{N2} + F_{N3} + F_{r1} + F_{r2} + F_{r3} = 0 \tag{3.106}$$

$$\sum M_p = 0$$

$$M + r_1 \times (F_{N1} + F_{r1}) + r_2 \times (F_{N2} + F_{r2}) + r_3 \times (F_{N3} + F_{r3}) + T_h^p \tau_s = 0 \tag{3.107}$$

In this situation, assuming minimal clearance between the peg and the hole and considering a slight rotation angle, the equations can be rephrased as follows:

$$\begin{bmatrix} 0 \\ 0 \\ F_z \end{bmatrix} + \begin{bmatrix} f_{sX} + f_{sY}\psi \\ -f_{sX}\psi + f_{sY} \\ f_{sZ} \end{bmatrix} + \begin{bmatrix} -F_{N1} + F_{N2} + \psi F_{N3} \\ \psi F_{N1} - \psi F_{N2} + F_{N3} \\ -\mu F_{N1} - \mu' h F_{N2} - \mu' h F_{N3} \end{bmatrix} = 0 \tag{3.108}$$

$$\begin{bmatrix} 0 \\ 0 \\ 0 \end{bmatrix} + \begin{bmatrix} \left(H\psi + L_C\psi - \frac{h}{2}\psi + \frac{w'}{2}\mu' h\right)(F_{N1} - F_{N2} + F_{N3}) \\ \left(H + L_C - \frac{h}{2} + \frac{v'}{2}\mu' h\right)(F_{N1} - F_{N2} - F_{N3}) \\ \frac{v'}{2}(F_{N1}\psi + F_{N2}\psi - F_{N3}) - (F_{N1} + F_{N2} - F_{N3}\psi)\frac{w'}{2} \end{bmatrix} + \begin{bmatrix} \tau_{s\theta} + \tau_{s\phi}\psi \\ -\tau_{s\theta}\psi + \tau_{s\phi} \\ \tau_{s\psi} \end{bmatrix} = 0 \tag{3.109}$$

Utilising equations (3.108) and (3.109), one can calculate the vertical forces acting on the surface as F_z.

$$F_{N1} - F_{N2} - \psi F_{N3} = f_{sX} + f_{sY}\psi \tag{3.110}$$

$$\psi F_{N1} - \psi F_{N2} + F_{N3} = f_{sX}\psi - f_{sY} \tag{3.111}$$

$$\frac{v'}{2}(F_{N1}\psi + F_{N2}\psi - F_{N3}) - (F_{N1} + F_{N2} - F_{N3}\psi)\frac{w'}{2} = -\tau_{s\psi} \tag{3.112}$$

Equations can be expressed in the following way:

$$\begin{bmatrix} F_{N1} \\ F_{N2} \\ F_{N3} \end{bmatrix} = \frac{\begin{bmatrix} \frac{v'}{2}\psi^2-\frac{w'}{2}\psi-\frac{v'}{2}\psi+\frac{w'}{2} & \frac{v'}{2}\psi^2-\frac{w'}{2}\psi+\frac{v'}{2}\psi-\frac{w'}{2} & v'\psi^2-w'\psi \\ -\frac{v'}{2}\psi^2+\frac{w'}{2}\psi-\frac{v'}{2}\psi+\frac{w'}{2} & \frac{v'}{2}\psi^2-\frac{w'}{2}\psi-\frac{v'}{2}\psi+\frac{w'}{2} & -v'\psi+w' \\ -\psi^2-1 & -\psi^2-1 & 0 \end{bmatrix}}{-v'\psi^3+w'\psi^2-v'\psi+w'} \begin{bmatrix} f_{sX}+f_{sY}\psi \\ f_{sX}\psi-f_{sY} \\ -\tau_{s\psi} \end{bmatrix} \tag{3.113}$$

$$F_z = -f_{sZ} + \mu' h(F_{N1} + F_{N2} + F_{N3}) \tag{3.114}$$

$$\begin{bmatrix} F_x \\ F_y \\ F_z \end{bmatrix} = -\begin{bmatrix} f_{sX}+f_{sY}\psi \\ -f_{sX}\psi+f_{sY} \\ f_{sZ} \end{bmatrix} - \begin{bmatrix} -F_{N1}+F_{N2}+\psi F_{N3} \\ \psi F_{N1}-\psi F_{N2}+F_{N3} \\ -\mu F_{N1}-\mu' h F_{N2}-\mu' h F_{N3} \end{bmatrix} \tag{3.115}$$

$$\begin{bmatrix} M_x \\ M_y \\ M_z \end{bmatrix} = -\begin{bmatrix} \left(H\psi + L_C\psi - \frac{h}{2}\psi + \frac{w'}{2}\mu' h\right)(F_{N1}-F_{N2}+F_{N3}) \\ \left(H + L_C - \frac{h}{2} + \frac{v'}{2}\mu' h\right)(F_{N1}-F_{N2}-F_{N3}) \\ \frac{v'}{2}(F_{N1}\psi + F_{N2}\psi - F_{N3}) - (F_{N1}+F_{N2}-F_{N3}\psi)\frac{w'}{2} \end{bmatrix} - \begin{bmatrix} \tau_{s\theta}+\tau_{s\phi}\psi \\ -\tau_{s\theta}\psi+\tau_{s\phi} \\ \tau_{s\psi} \end{bmatrix} \tag{3.116}$$

In this instance, it is evident that the contact boundary condition is solely dependent on the ψ angle. Assuming F_{N3}=0, the contact forces can be computed as follows:

$$f_{sX} + f_{sY}\psi + f_{sX}\psi - f_{sY} = 0 \tag{3.117}$$

By formulating $a\psi^2 + b\psi + c = 0$ as the quadratic equation, we have:

$$a \triangleq -k_X\frac{w'}{2} + k_Y\frac{v'}{2}$$

$$b \triangleq k_X\left(\delta_X - X_0 - \frac{v'}{2} - \frac{w'}{2}\right) + k_Y\left(\delta_Y - Y_0 - \frac{v'}{2} + \frac{w'}{2}\right)$$

$$c \triangleq k_X\left(\delta_X - X_0 - \frac{v'}{2}\right) - k_Y\left(\delta_Y - Y_0 + \frac{w'}{2}\right)$$

we can determine the corresponding roots of the angle ψ as:

$$\psi_{1,2} = \frac{-b \pm \sqrt{b^2-4ac}}{2a} \tag{3.118}$$

3.3 Results and Discussion

3.3.1 Region of extraction depth

The two roots in Case 1, 2 and 3, h_1 and h_2, denote the depth of extraction (h). The two roots in Case 4 and 5, ψ_1 and ψ_2, represent the rotation angles as ψ around the Z-axis. Here, h_1 and h_2 represent the initial and final points of the two-contact region, respectively. If $h_2 < h_0$, the peg and hole are initially in the two-contact area at the commencement of the disassembly process. When $h_0 < h_2 < h_1$, the peg-hole initially undergoes one-contact, and there is at least one transition between the one-contact and two-contact states. If the equations have no solution, then no contact occurs during the extraction. When $h_0 < h_2 = h_1$, the peg-hole exhibits a two-contact state at a specific depth. The dimensions and position of the two-contact region are influenced by various factors, including the geometric parameters of the hole-peg system, the compliance centre's location, initial position errors, and the level of compliance.

3.3.2 Key Factors

In the two-contact state, the reaction forces exerted on the peg increase the susceptibility to extraction failure, particularly at the entrance of the hole. Additionally, two contact states contribute to an increase in the extraction force attributed to angular and lateral errors. This section delves into the identification of key parameters crucial for minimising the two-contact region and elucidates their influence on its location. The parameters under scrutiny, namely compliance centre position (L_C), initial lateral ($\delta_X, \delta_Y, \delta_Z$) and angular errors ($\delta_\theta, \delta_\Phi, \delta_\psi$), and stiffness ($K_X, K_Y, K_\theta, K_\Phi$ and K_ψ), are subjected to analysis to elucidate their impacts on the two-contact region, with detailed discussions presented in subsequent sections.

I. Location of Compliance Centre

One crucial design parameter involves determining the optimal placement of the compliance centre along the central axis of the peg. When the manipulator secures a peg, initial

positional discrepancies between the manipulator and the rectangular peg-hole system induce shifts and rotations in the peg. Assuming the rigidity of the rectangular peg-hole (Figure 3.6), the blue figure illustrates the initial position of the peg before angular errors occur. However, initial lateral errors cause the peg to displace and rotate around the compliance centre (depicted in the red figure).

If the compliance centre is situated far from the peg tip, the peg rotates towards the contact side around the axis parallel to the contact line. For instance, if the intersection aligns with the length of the peg, rotation occurs around the Y-axis, potentially altering a single-contact state to a two-contact state. Conversely, when the compliance centre is positioned at the peg tip, rotation occurs around the parallel axis when gripped in the opposite direction to the line of contact, resulting in a single contact between the peg and the hole.

These characteristics play a pivotal role in minimising the two-point contact region during disassembly. As illustrated in Figure 3.12, the boundary conditions of the two-contact region are presented based on the extraction depth equations (h_1 & h_2) for the initial three categories. It becomes evident that when the compliance centre is near the peg tip, the two-contact area is significantly reduced. Furthermore, as L_C decreases, the two-point contact region shifts towards the hole mouth.

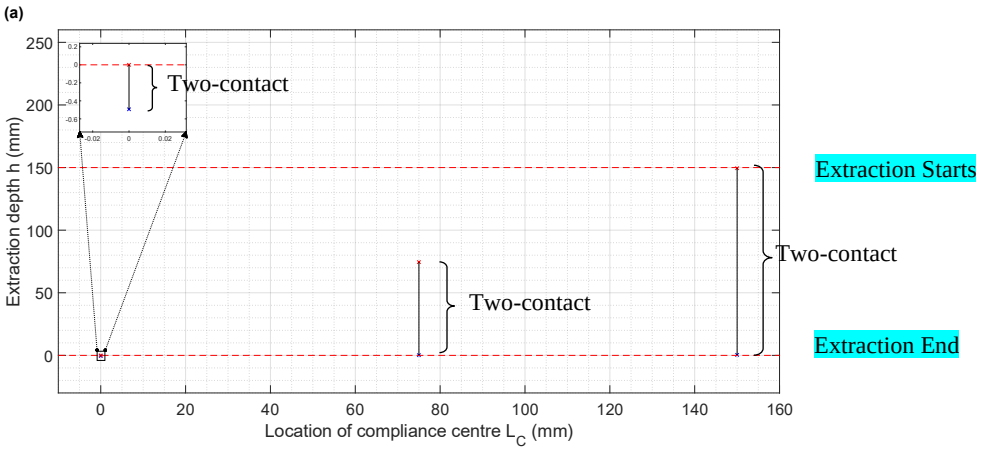

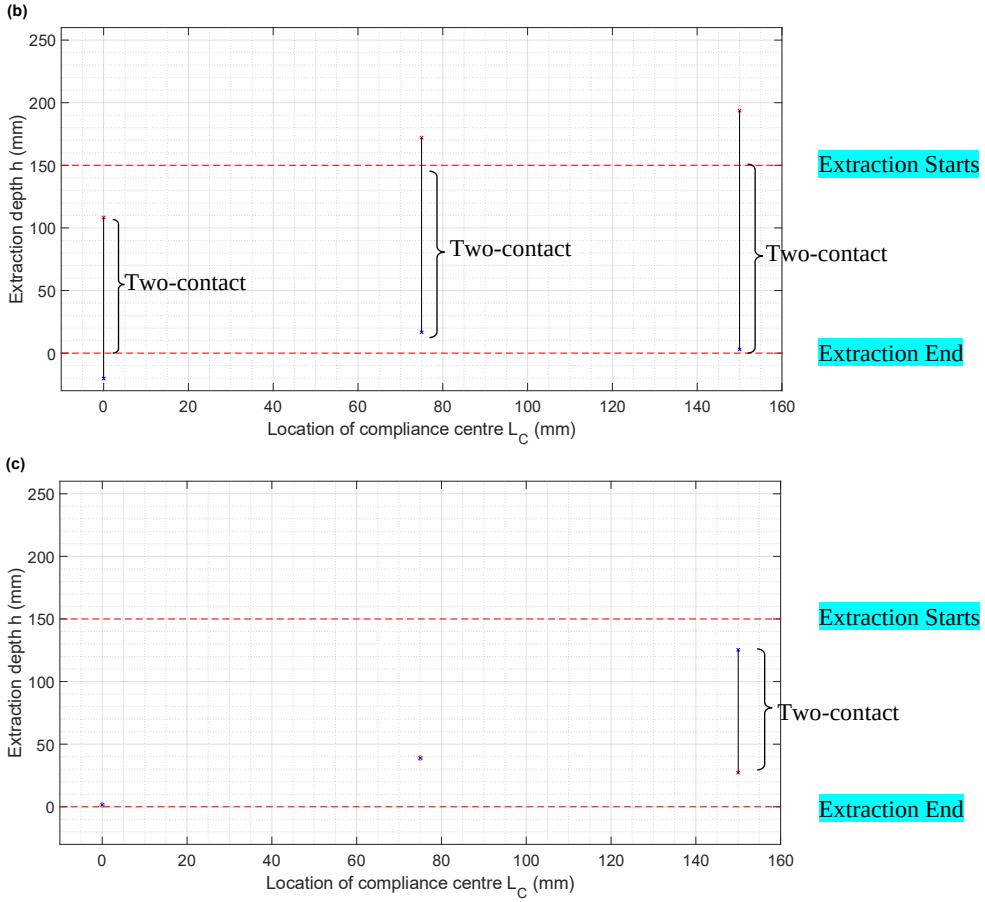

*Figure 3.12. Dependence of the two-point contact region on the location of the compliance centre with K_X, K_Y =0.3 N mm^{-1}, K_θ, K_Φ, K_ψ = 30*10^4 Nmm rad^{-1}. a) two-point contact, b) two-side contact, c) combined two-side and one-plane contact*

II. Initial errors

The two-contact region is susceptible to influence from initial position errors, encompassing lateral and angular deviations between the compliant manipulator and the peg-hole system. Notably, when the compliance centre is positioned far from the tip, substantial lateral errors (δ_X and δ_Y) can induce significant rotation of the peg in the opposite direction to the axes of rotation. In instances where δ_X and δ_Y reach considerable magnitudes; the peg and hole persist in a two-contact region throughout the disassembly process. Conversely, if the compliance centre is situated at the tip, the peg rotation is in alignment with the axes of rotation during disassembly. The transition from two-point contact to one-contact is observed as a consequence of these dynamics [12]. Figures 3.13 - 3.18 illustrate the impact of initial lateral

errors on the two-contact region for diverse compliance centre locations. The two-contact region diminishes with increasing lateral errors when the compliance centre is in close proximity to the tip of the peg.

Angular errors ($\delta_\theta, \delta_\Phi$ *and* δ_ψ) play a pivotal role in influencing the disassembly process both in terms of magnitude and direction. When the compliance centre is distant from the peg tip and the initial angular error opposes the peg's rotation, as depicted in Figures 3.19-3.27, a reduction in the two-contact region is evident. Conversely, if the initial angular error aligns with the rotation of the peg, the two-contact region expands. Similar effects of initial angular errors are observed when the compliance centre is located at the tip of the peg.

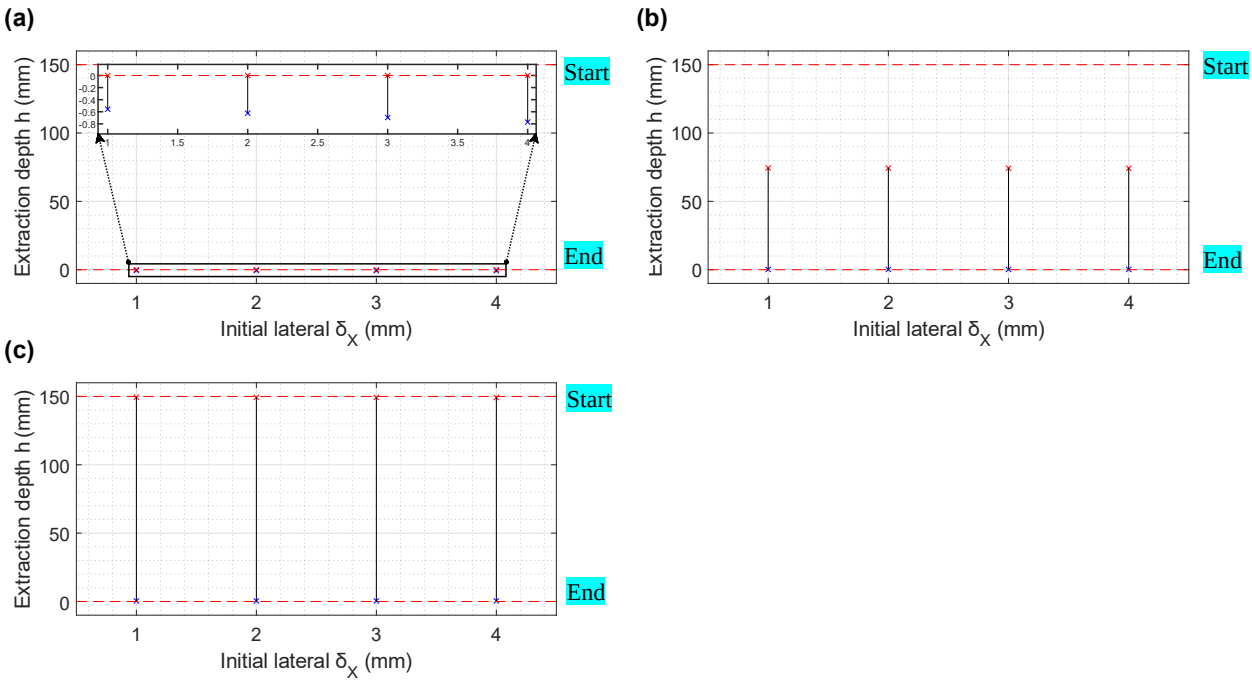

Figure 3.13. The effect of initial lateral error δ_X on the two-contact region in the two-point contact with K_X, K_Y =0.3 N mm^{-1}, $K_\theta, K_\Phi, K_\psi = 30*10^4$ Nmm rad^{-1} ,and a) $L_C = 0$, (b) $L_C = 75$, (c) $L_C = 150$.

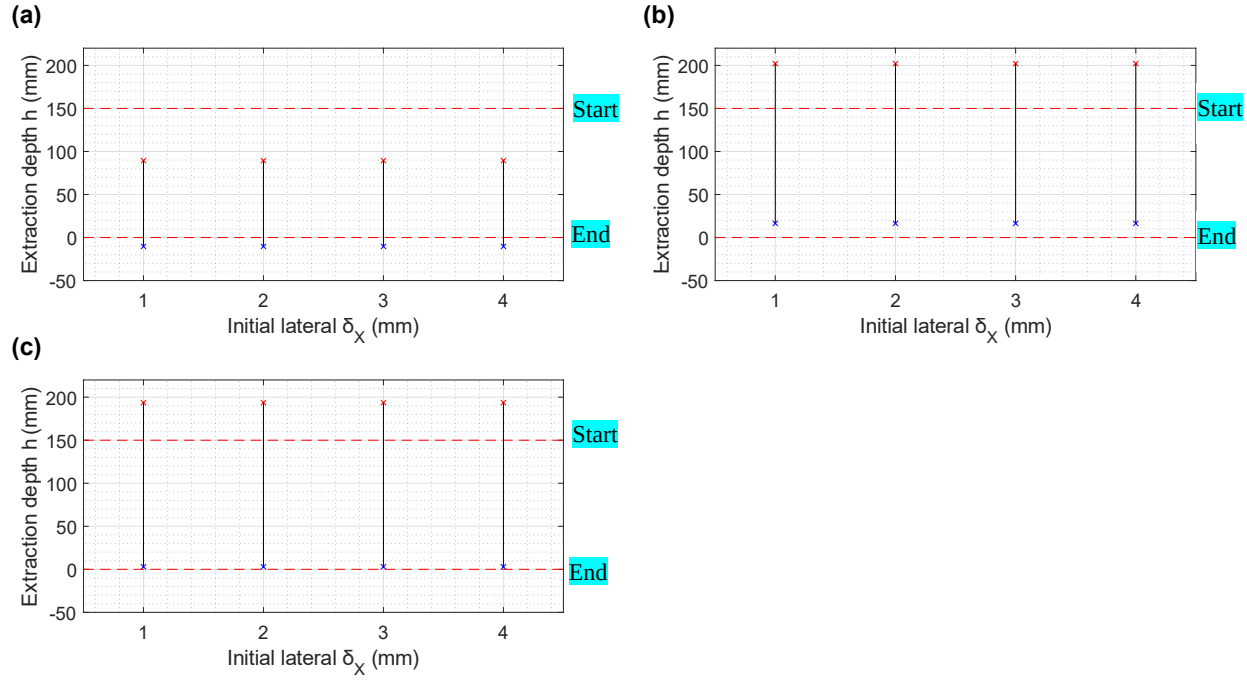

*Figure 3.14. The effect of initial lateral error δ_X on the two-contact region in the two-side contact with K_X, K_Y =0.3 N mm^{-1}, K_θ, K_Φ, K_ψ = 30*10^4 Nmm rad^{-1} ,and a) $L_C = 0$, (b) $L_C = 75$, (c) $L_C = 150$.*

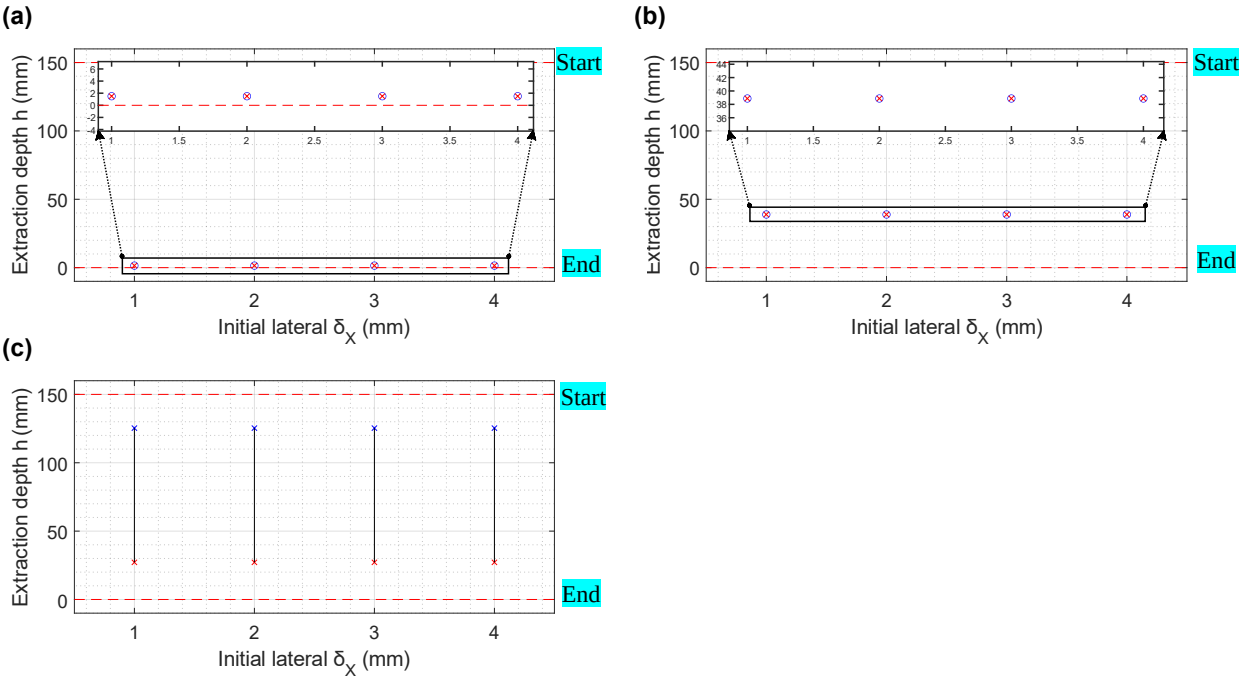

*Figure 3.15. The effect of initial lateral error δ_X on the two-contact region in the combined two-side and one-plane contact with K_X, K_Y =0.3 N mm^{-1}, K_θ, K_Φ, K_ψ = 30*10^4 Nmm rad^{-1} ,and a) $L_C = 0$, (b) $L_C = 75$, (c) $L_C = 150$.*

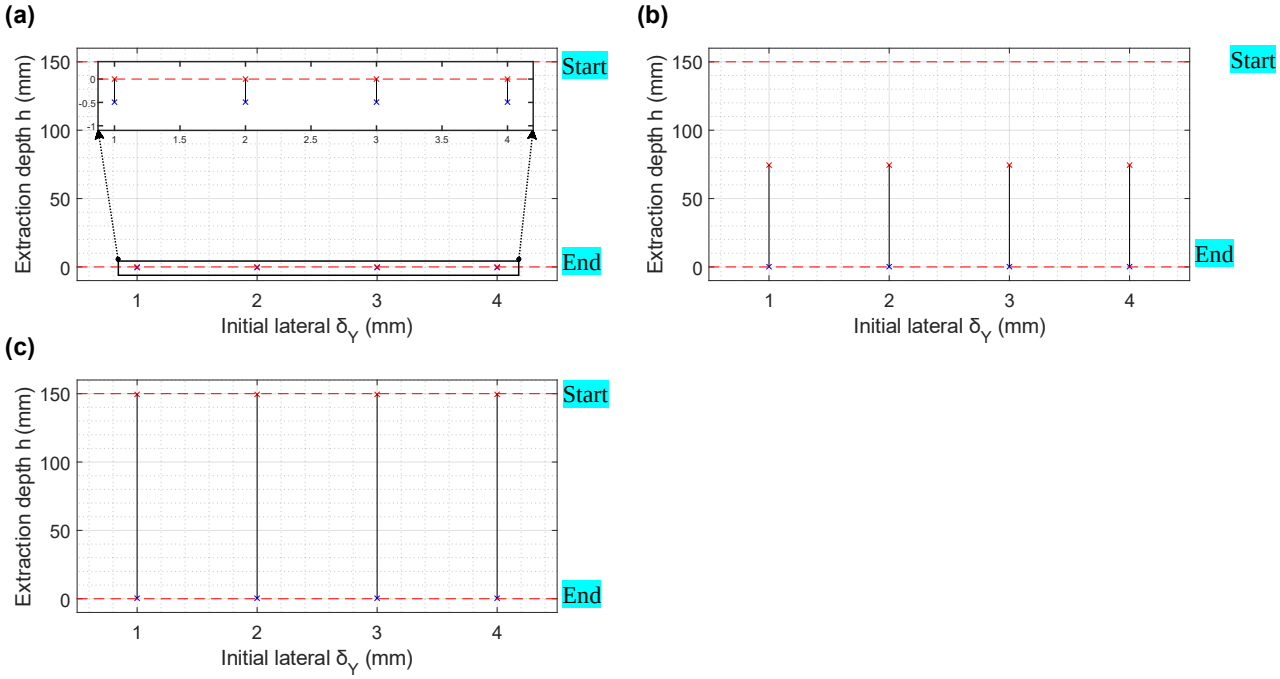

*Figure 3.16. The effect of initial lateral error δ_Y on the two-contact region in the two-point contact with K_X, K_Y =0.3 N mm^{-1}, K_θ, K_Φ, K_ψ = 30*10^4 Nmm rad^{-1}, and a) $L_C = 0$, (b) $L_C = 75$, (c) $L_C = 150$.*

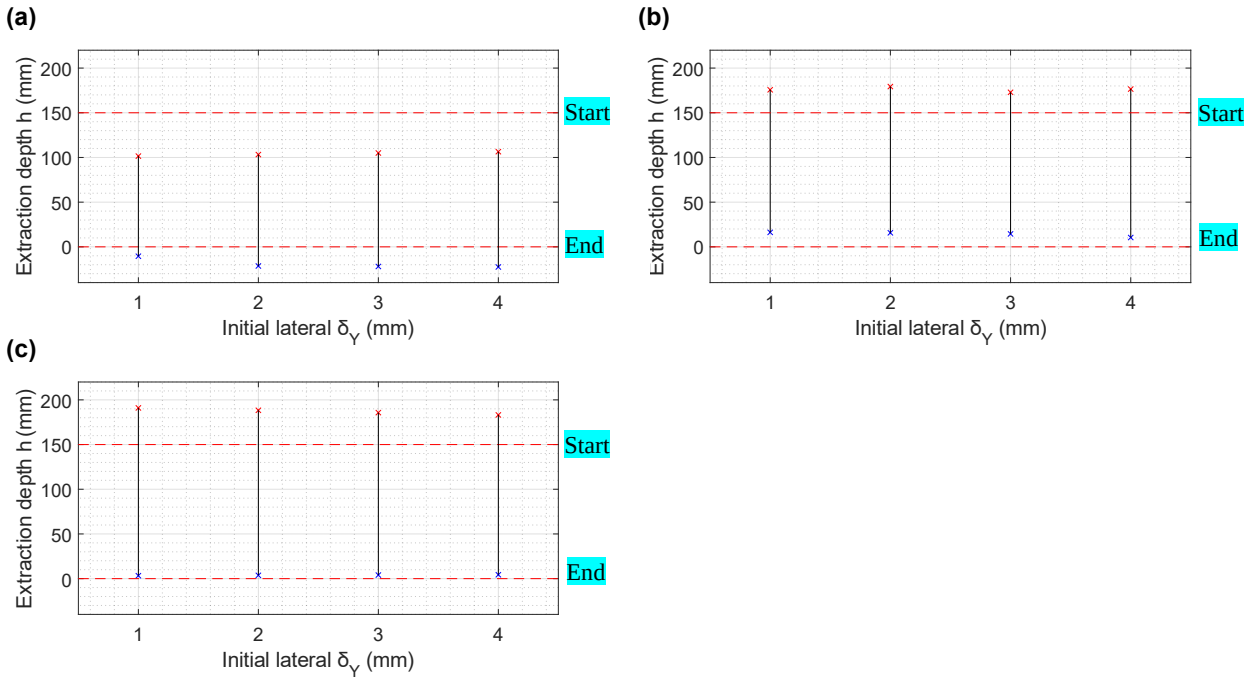

*Figure 3.17. The effect of initial lateral error δ_Y on the two-contact region in the two-side contact with K_X, K_Y =0.3 N mm^{-1}, K_θ, K_Φ, K_ψ = 30*10^4 Nmm rad^{-1}, and a) $L_C = 0$, (b) $L_C = 75$, (c) $L_C = 150$.*

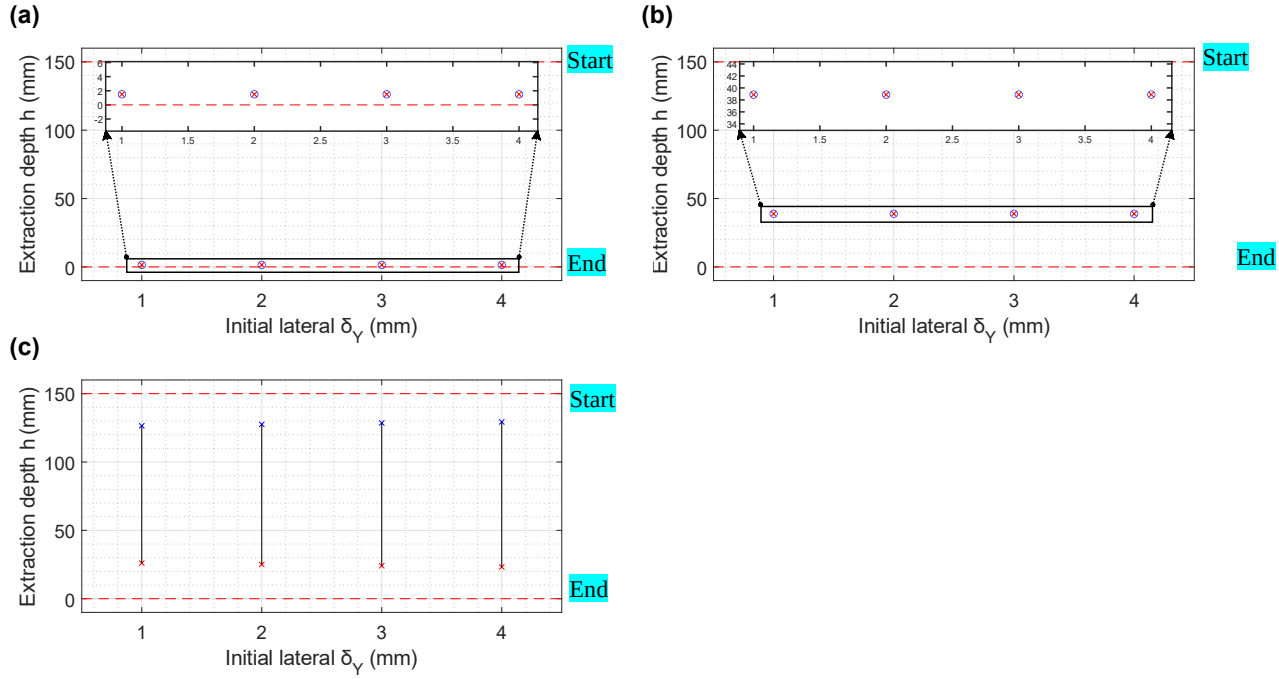

Figure 3.18. The effect of initial lateral error δ_Y on the two-contact region in the combined two-side and one-plane contact with K_X, K_Y =0.3 N mm^{-1}, $K_\theta, K_\Phi, K_\psi = 30*10^4$ Nmm rad^{-1} ,and a) $L_C = 0$, (b) $L_C = 75$, (c) $L_C = 150$.

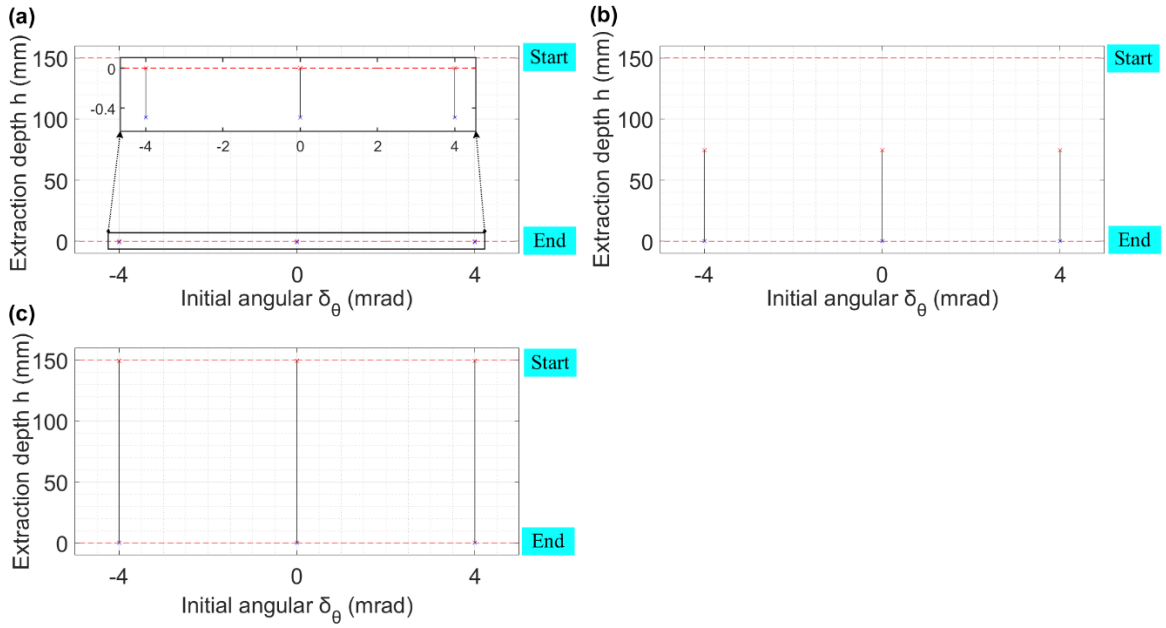

Figure 3.19. The effect of initial angular error δ_θ on the two-contact region in the two-point contact with $K_X, K_Y = 0.3$ N mm^{-1}, $K_\theta, K_\Phi, K_\psi = 30*10^4$ Nmm rad^{-1} ,and a) $L_C = 0$, (b) $L_C = 75$, (c) $L_C = 150$.

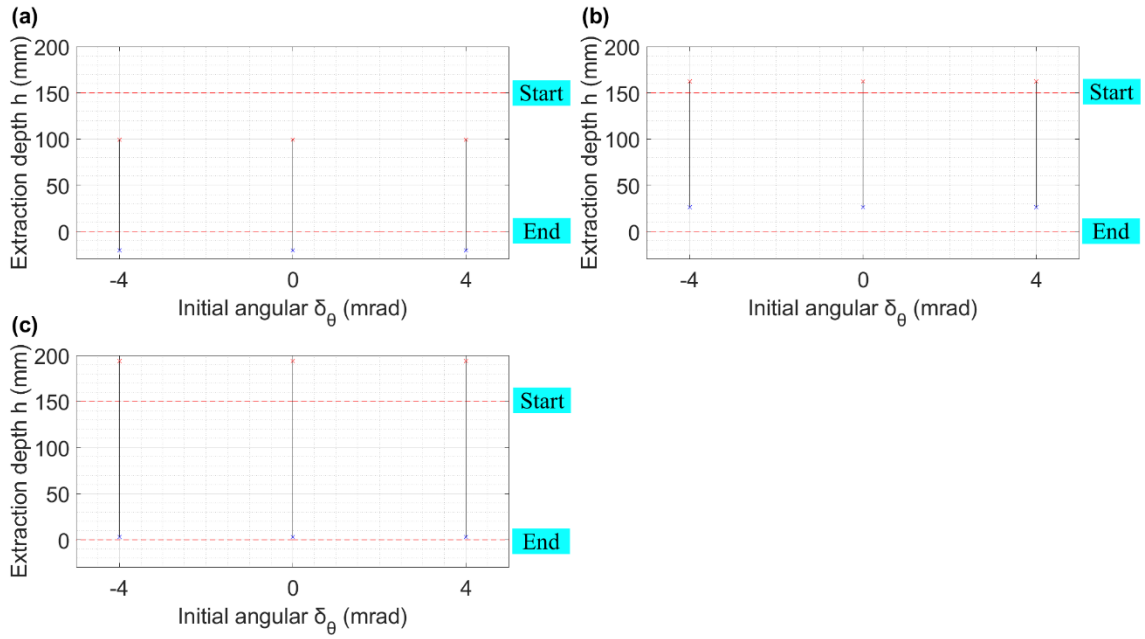

*Figure 3.20. The effect of initial angular error δ_θ on the two-contact region in the two-side contact with K_X, K_Y =0.3 N mm^{-1}, K_θ, K_Φ, K_ψ = 30*10^4 Nmm rad^{-1} and 1) $L_C = 0$, (2) $L_C = 75$, (3) $L_C = 150$.*

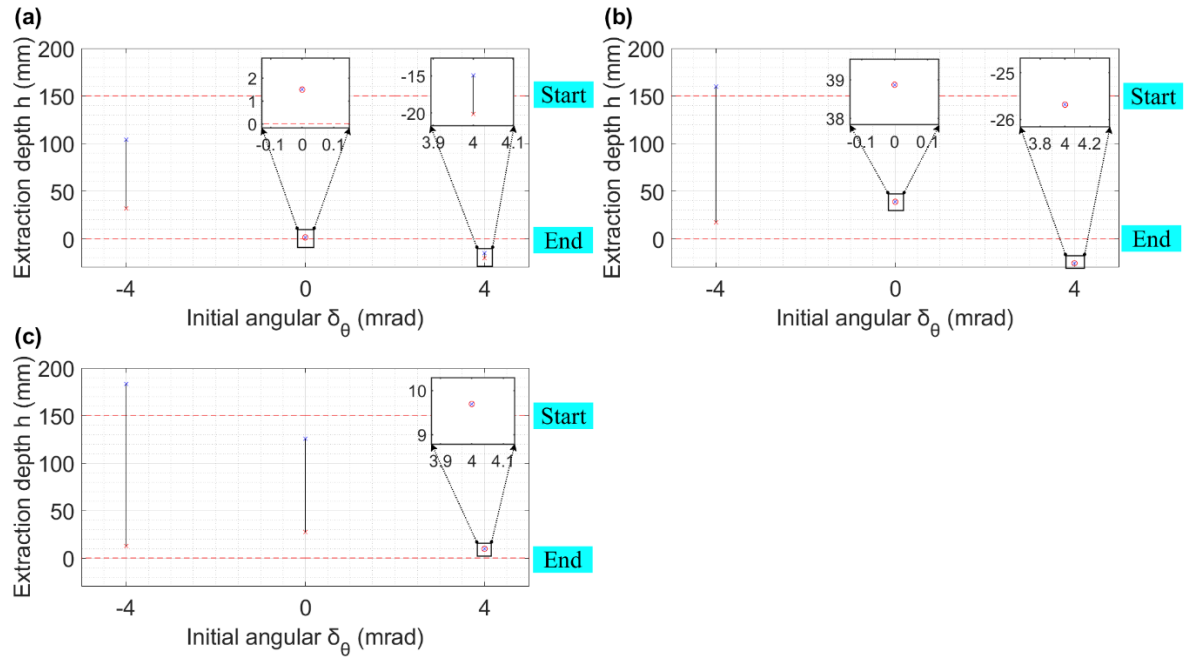

*Figure 3.21. The effect of initial angular error δ_θ on the two-contact region in the combined two-side and one-plane contact with K_X, K_Y =0.3 N mm^{-1}, K_θ, K_Φ, K_ψ = 30*10^4 Nmm rad^{-1} and a) $L_C = 0$, (b) $L_C = 75$, (c) $L_C = 150$.*

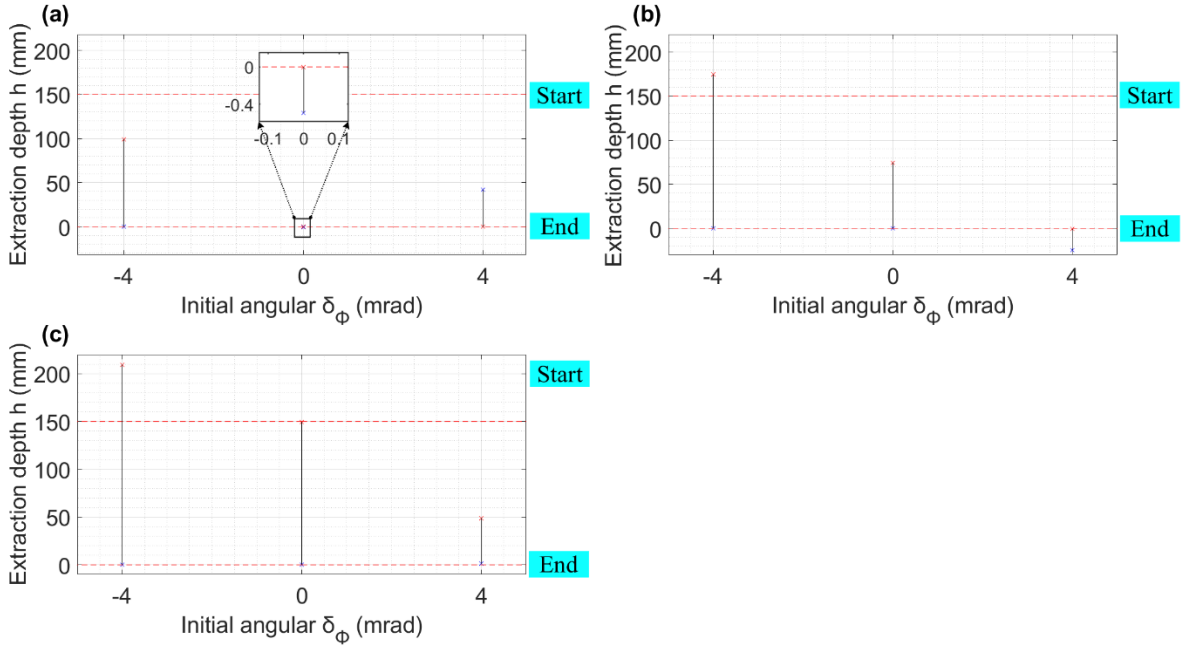

*Figure 3.22. The effect of initial angular error δ_Φ on the two-contact region in the two-point contact with K_X, K_Y =0.3 N mm^{-1}, K_θ, K_Φ, K_ψ = 30*10^4 Nmm rad^{-1}, and a) $L_C = 0$, (b) $L_C = 75$, (c) $L_C = 150$.*

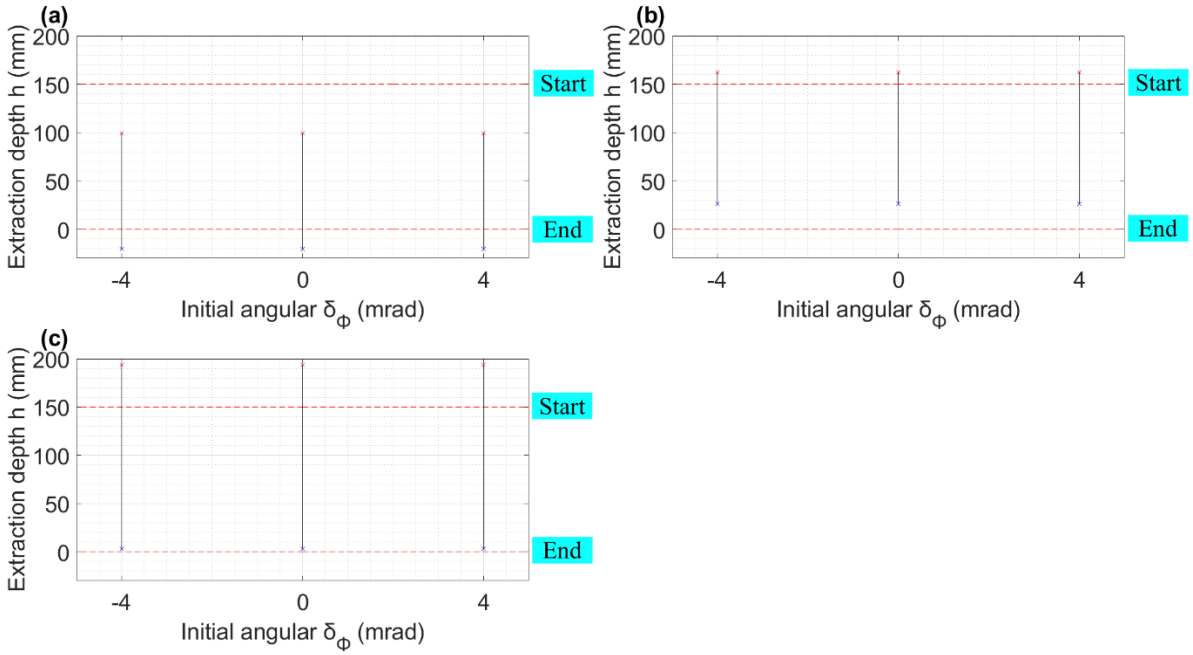

*Figure 3.23. The effect of initial angular error δ_Φ on the two-contact region in the two-side contact with K_X, K_Y =0.3 N mm^{-1}, K_θ, K_Φ, K_ψ = 30*10^4 Nmm rad^{-1}, and 1) $L_C = 0$, (2) $L_C = 75$, (3) $L_C = 150$.*

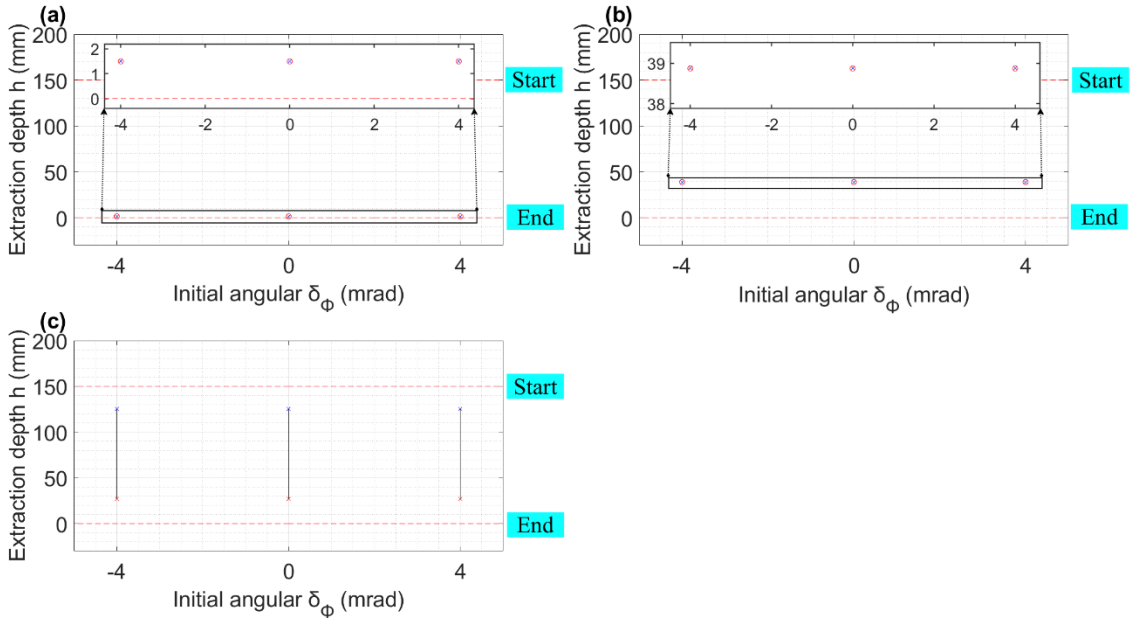

*Figure 3.24. The effect of initial angular error δ_Φ on the two-contact region in the combined two-side and one-plane contact with K_X, K_Y =0.3 N mm^{-1}, K_θ, K_Φ, K_ψ = 30*10^4 Nmm rad^{-1} ·and a) $L_C = 0$, (b) $L_C = 75$, (c) $L_C = 150$.*

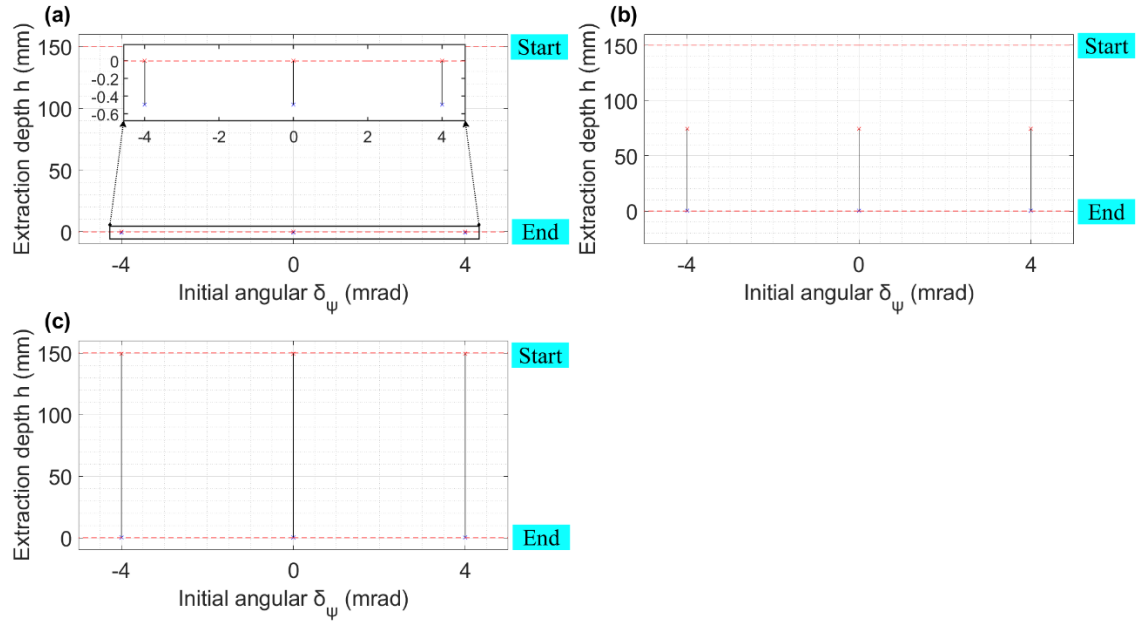

*Figure 3.25. The effect of initial angular error δ_ψ on the two-contact region in the two-point contact with K_X, K_Y =0.3 N mm^{-1}, K_θ, K_Φ, K_ψ = 30*10^4 Nmm rad^{-1} ·and a)L_C = 0 mm, (b) $L_C = 75$ mm, (c) $L_C = 150$ mm.*

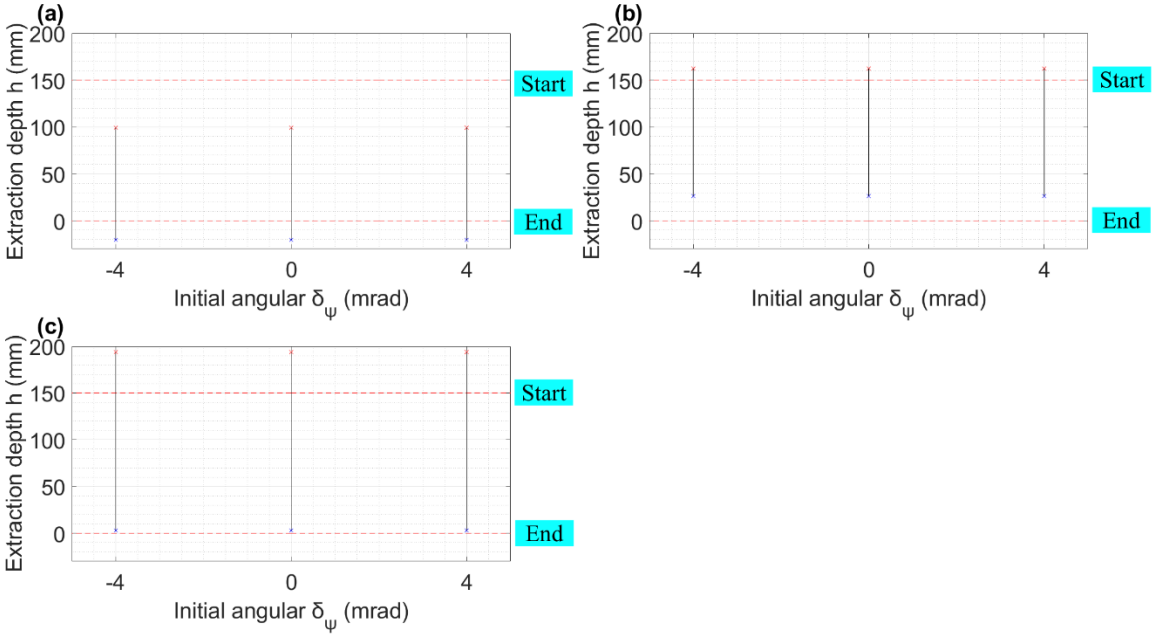

Figure 3.26. The effect of initial angular error δ_ψ on the two-contact region in the two-side contact with K_X, K_Y =0.3 N mm^{-1}, $K_\theta, K_\Phi, K_\psi = 30*10^4$ Nmm rad^{-1}, and 1) $L_C = 0\ mm$, (2) $L_C = 75\ mm$, (3) $L_C = 150\ mm$.

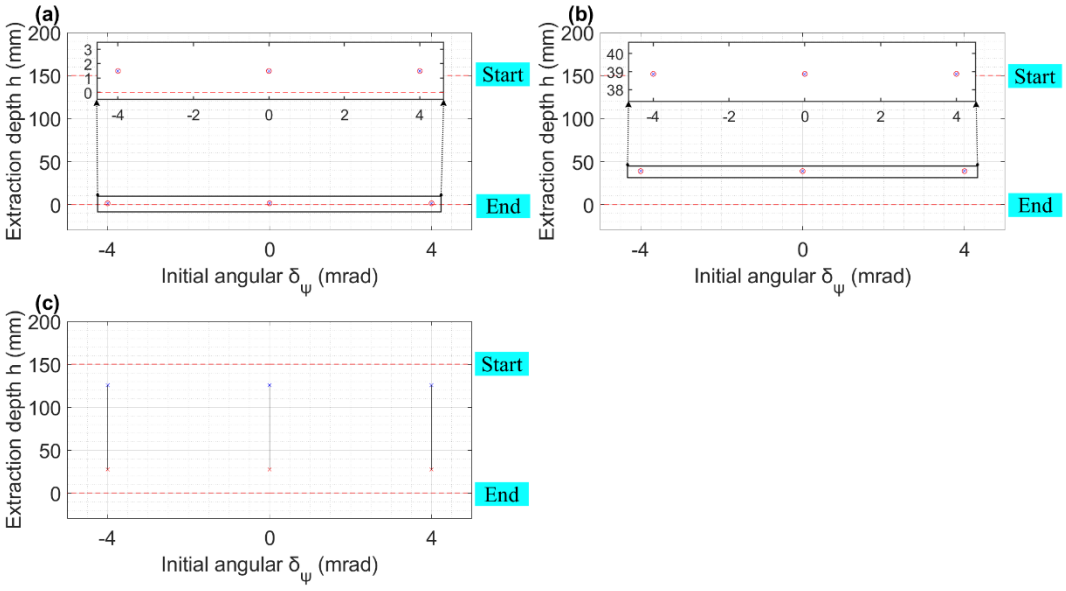

Figure 3.27. The effect of initial angular error δ_ψ on the two-contact region in the combined two-side and one-plane contact with K_X, K_Y =0.3 N mm^{-1}, $K_\theta, K_\Phi, K_\psi = 30*10^4$ Nmm rad^{-1}, and a) $L_C = 0\ mm$, (b) $L_C = 75\ mm$, (c) $L_C = 150\ mm$.

III. Stiffness

The success of a disassembly task is contingent upon the positioning of the compliance centre on the peg and the coupling stiffness elements between translational and rotational

directions [6]. Compliant manipulators exhibit lateral and angular compliance determined by their rotational and lateral stiffness. Figures 3.28-3.33 show that as the lateral stiffness K_X, K_Y (N mm^{-1})) and Figures 3.34-3.42 increase, the angular stiffnesses (K_θ, K_Φ, K_ψ) and the location of the compliance centre and the two-contact region diminishes very slightly. This phenomenon is attributed to heightened lateral stiffness, which results in reduced peg rotation for equivalent positional errors, thereby minimising the two-point contact region. According to these figures, the stiffness has a limited impact on the two-contact region.

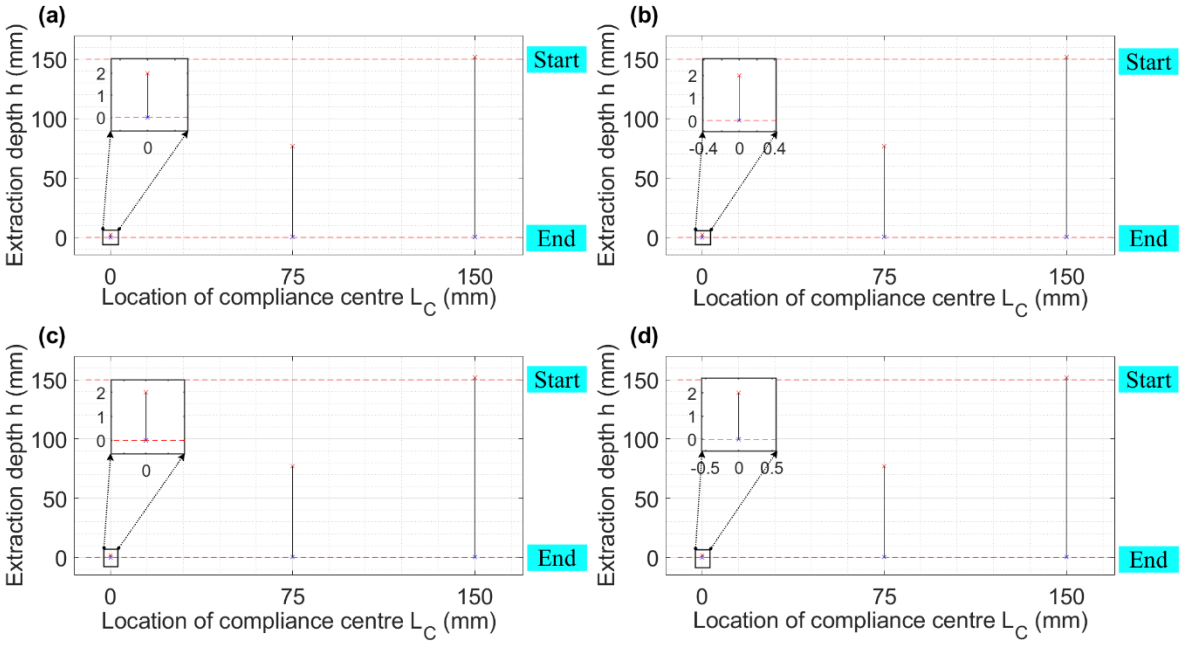

Figure 3.28. The effect of the two-contact region the two-point contact on the structural parameters: (a) K_X =0.2 N mm^{-1}; (b) K_X =0.3 N mm^{-1}; (c) K_X =0.4 N mm^{-1}; (d) K_X =0.6 N mm^{-1} with $K_Y = 0.3\ N\ mm^{-1}, K_\theta, K_\Phi, K_\psi = 30*10^4$ Nmm rad^{-1} $\delta_X, \delta_Y =$ 2 mm ,$\delta_\theta, \delta_\Phi, \delta_\psi =$ 0 rad.

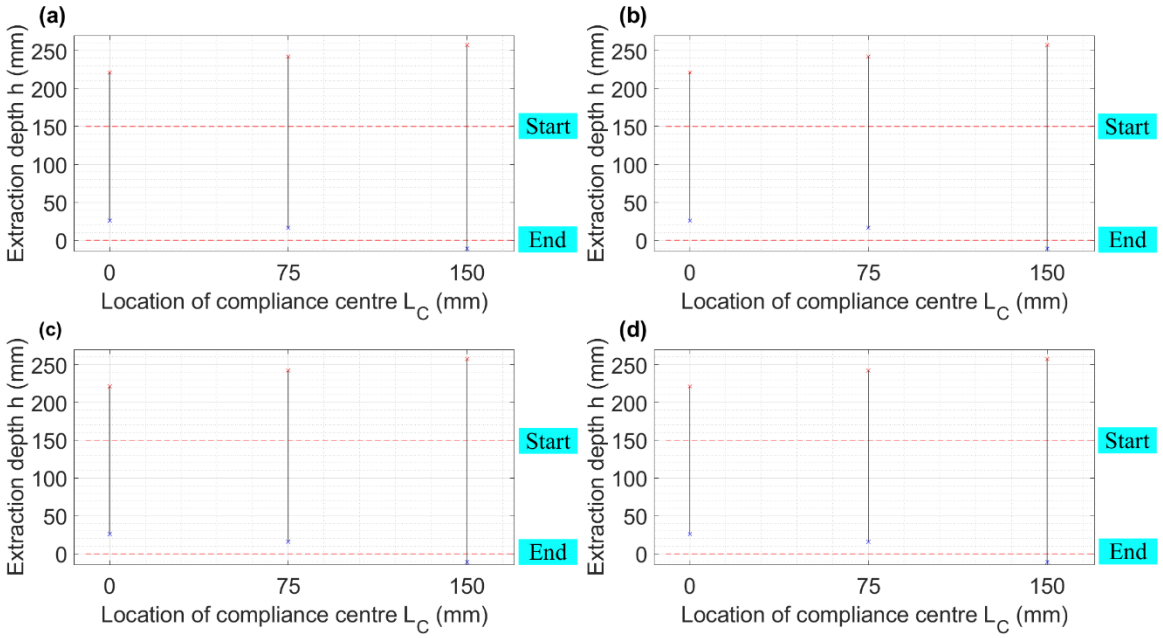

Figure 3.29. The effect of the two-contact region the two-side contact on the structural parameters: (a) K_X =0.2 N mm^{-1}; (b) K_X =0.3 N mm^{-1}; (c) K_X =0.4 N mm^{-1}; (d) K_X =0.6 N mm^{-1} with $K_Y = 0.3\ N\ mm^{-1}, K_\theta, K_\Phi, K_\psi = 30*10^4$ Nmm rad^{-1} $\delta_X, \delta_Y = 2$ mm ,$\delta_\theta, \delta_\Phi, \delta_\psi = 0$ rad.

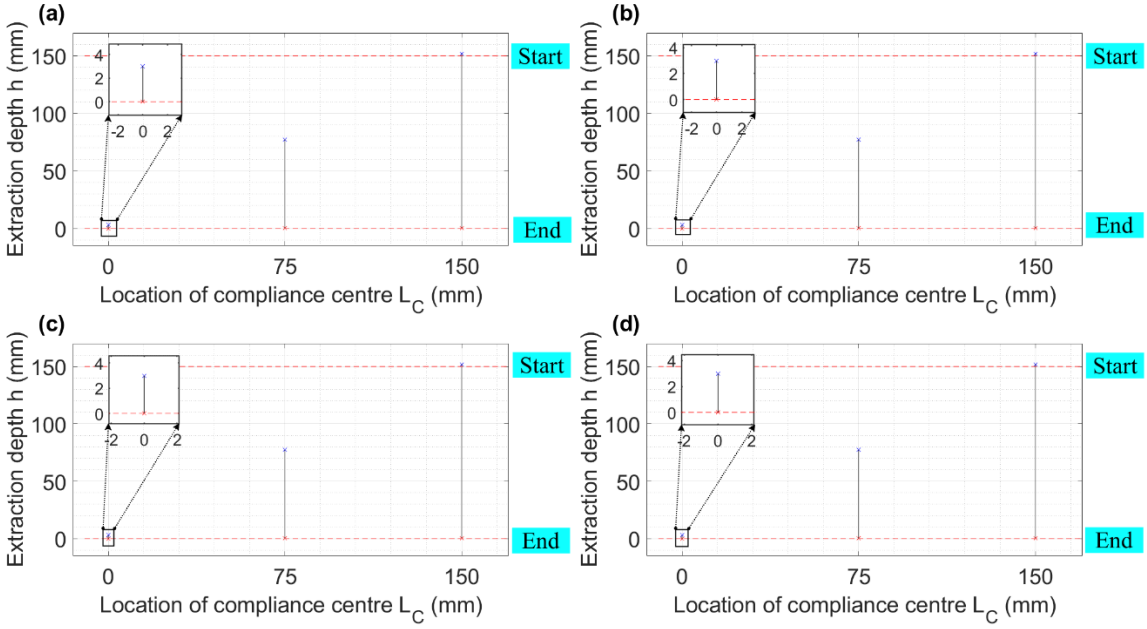

Figure 3.30. The effect of the two-contact region the combined two-side and one-plane contact on the structural parameters: (a) K_X =0.2 N mm^{-1}; (b) K_X =0.3 N mm^{-1}; (c) K_X =0.4 N mm^{-1}; (d) K_X =0.6 N mm^{-1} with $K_Y = 0.3\ N\ mm^{-1}, K_\theta, K_\Phi, K_\psi = 30*10^4$ Nmm rad^{-1} $\delta_X, \delta_Y = 2$ mm ,$\delta_\theta, \delta_\Phi, \delta_\psi = 0$ rad.

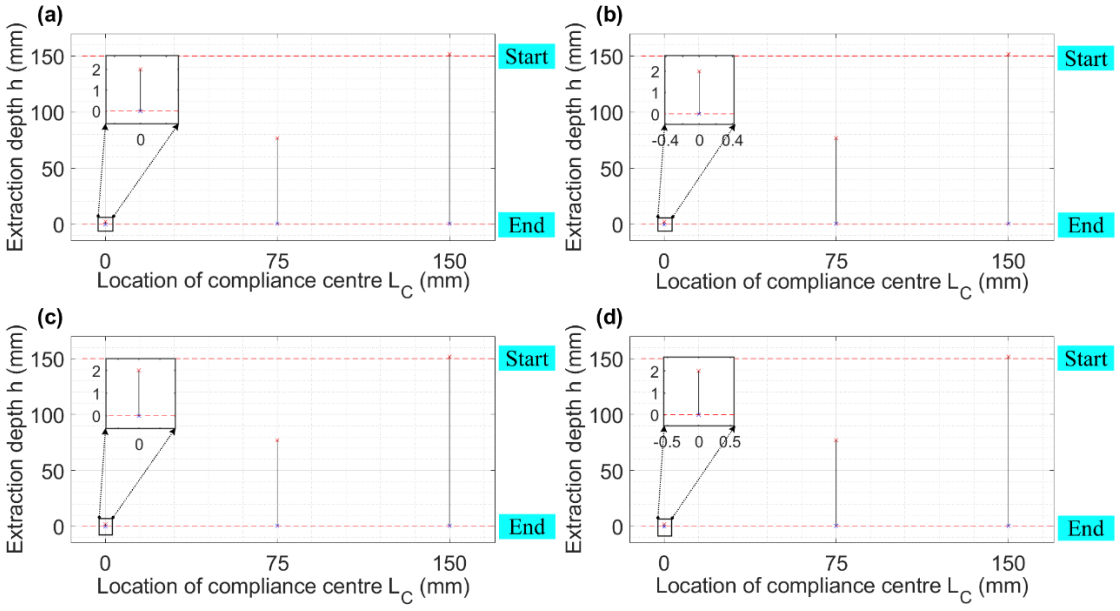

*Figure 3.31. The effect of the two-contact region the two-point contact on the structural parameters: (a) K_Y =0.2 N mm^{-1}; (b) K_Y =0.3 N mm^{-1}; (c) K_Y =0.4 N mm^{-1}; (d) K_Y =0.6 N mm^{-1} with K_X = 0.3 N mm^{-1}, K_θ, K_Φ, K_ψ = 30*10^4 Nmm rad^{-1} δ_X, δ_Y = 2 mm,$\delta_\theta, \delta_\Phi, \delta_\psi$ = 0 rad.*

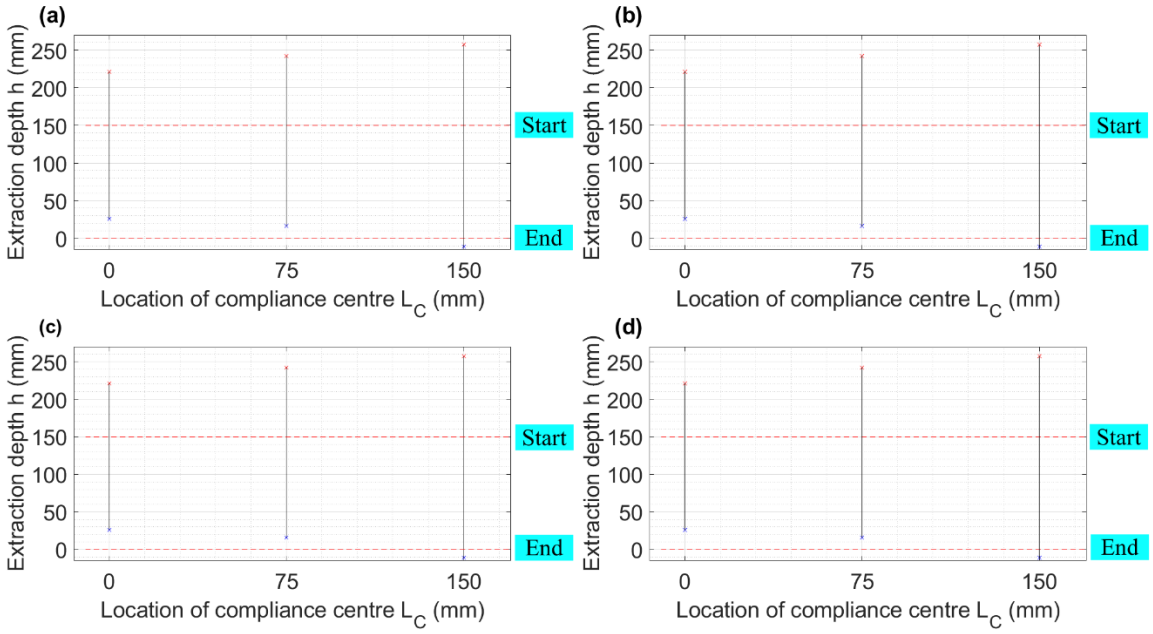

*Figure 3.32. The effect of the two-contact region the two-side contact on the structural parameters: (a) K_Y =0.2 N mm^{-1}; (b) K_Y =0.3 N mm^{-1}; (c) K_Y =0.4 N mm^{-1}; (d) K_Y =0.6 N mm^{-1} with K_X = 0.3 N mm^{-1}, K_θ, K_Φ, K_ψ = 30*10^4 Nmm rad^{-1} δ_X, δ_Y = 2 mm,$\delta_\theta, \delta_\Phi, \delta_\psi$ = 0*

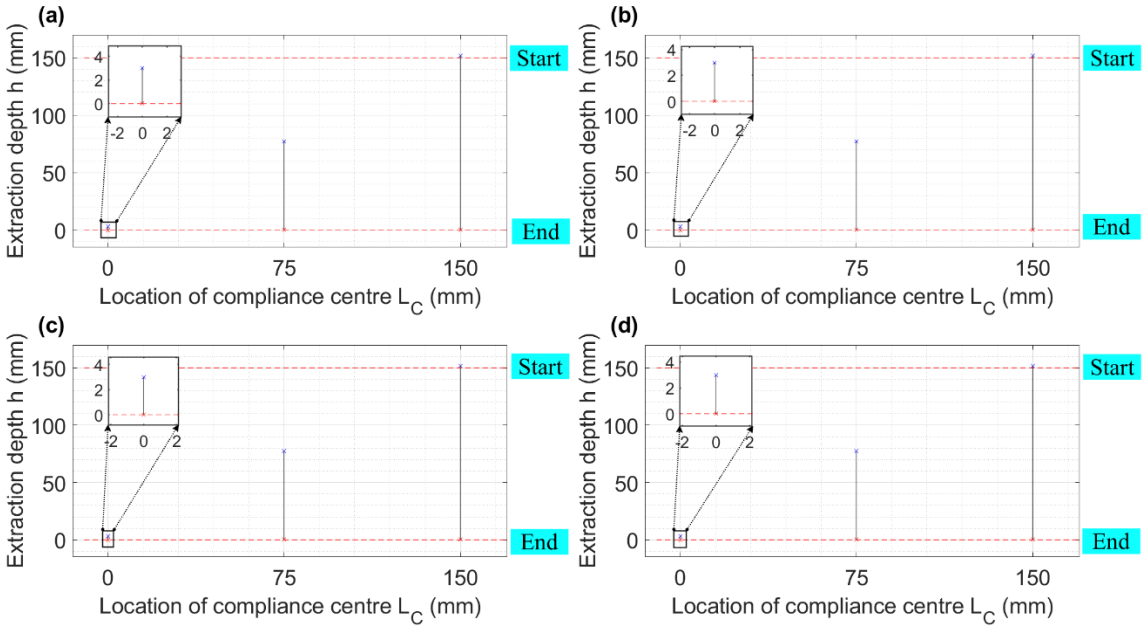

Figure 3.33. The effect of the two-contact region of the combined two-side and one-plane contact on the structural parameters: (a) K_Y =0.2 N mm^{-1}; (b) K_Y =0.3 N mm^{-1}; (c) K_Y =0.4 N mm^{-1}; (d) K_Y =0.6 N mm^{-1} with $K_X = 0.3$ N mm^{-1}, $K_\theta, K_\Phi, K_\psi = 30*10^4$ Nmm rad^{-1} $\delta_X, \delta_Y = 2$ mm, $\delta_\theta, \delta_\Phi, \delta_\psi = 0$

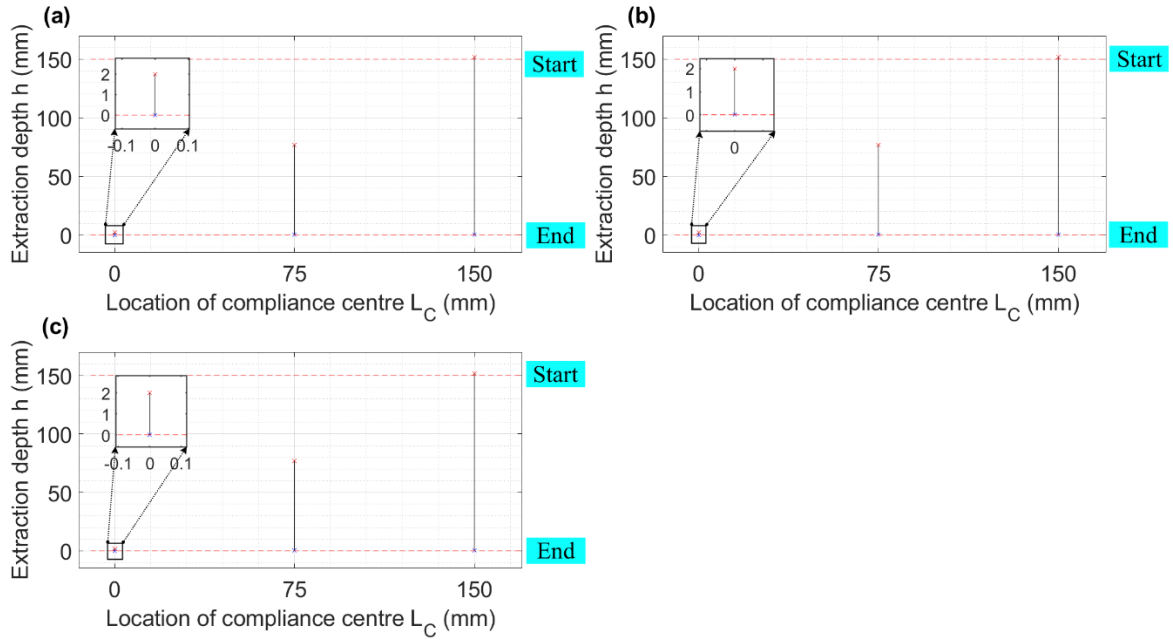

*Figure 3.34. The effect of the two-contact region two-point contact on the structural parameters: (a) K_θ =15*10^4 Nmm rad^{-1} ; (b) K_θ =30*10^4 Nmm rad^{-1} ; (c) K_θ =45*10^4 Nmm rad^{-1} with $K_X, K_Y = 0.3$ N mm^{-1}, $K_\Phi, K_\psi = 30*10^4$ Nmm rad^{-1} $\delta_X, \delta_Y = 2$ mm, $\delta_\theta, \delta_\Phi, \delta_\psi = 0$ rad.*

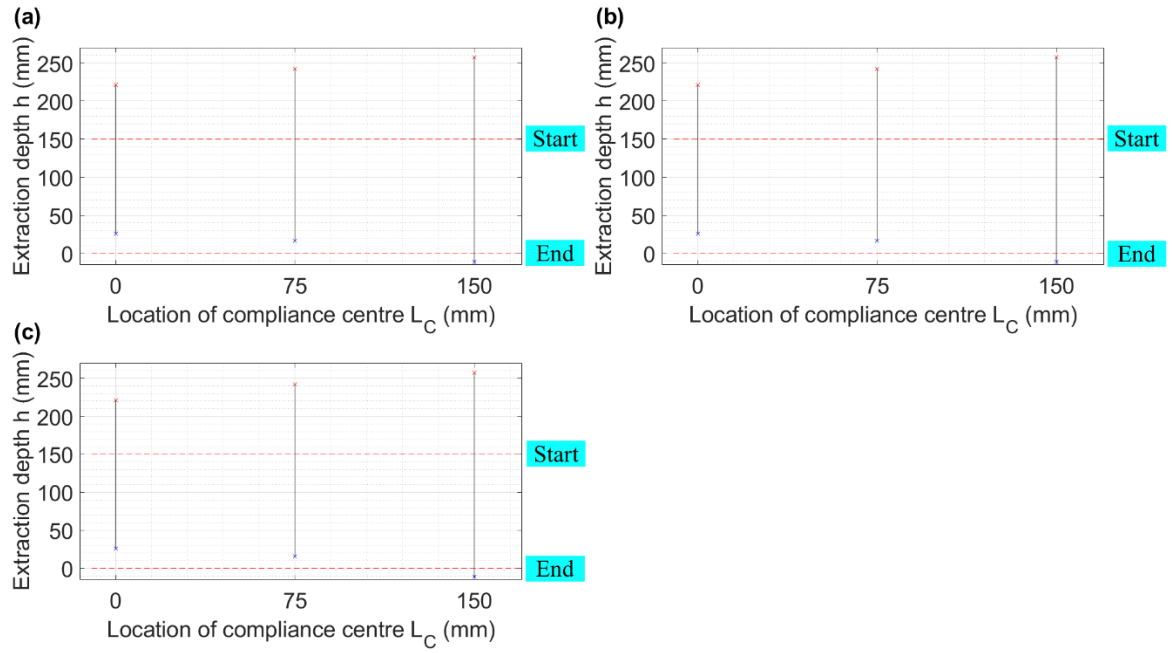

*Figure 3.35. The effect of the two-contact region the two-side contact on the structural parameters: (a) K_θ =15*10^4 Nmm rad^{-1} ; (b) K_θ =30*10^4 Nmm rad^{-1} ; (c) K_θ =45*10^4 Nmm rad^{-1} with $K_X, K_Y = 0.3\ N\ mm^{-1}$, $K_\Phi, K_\psi = 30*10^4$ Nmm rad^{-1} $\delta_X, \delta_Y =$ 2 mm,$\delta_\theta, \delta_\Phi, \delta_\psi = 0$ rad.*

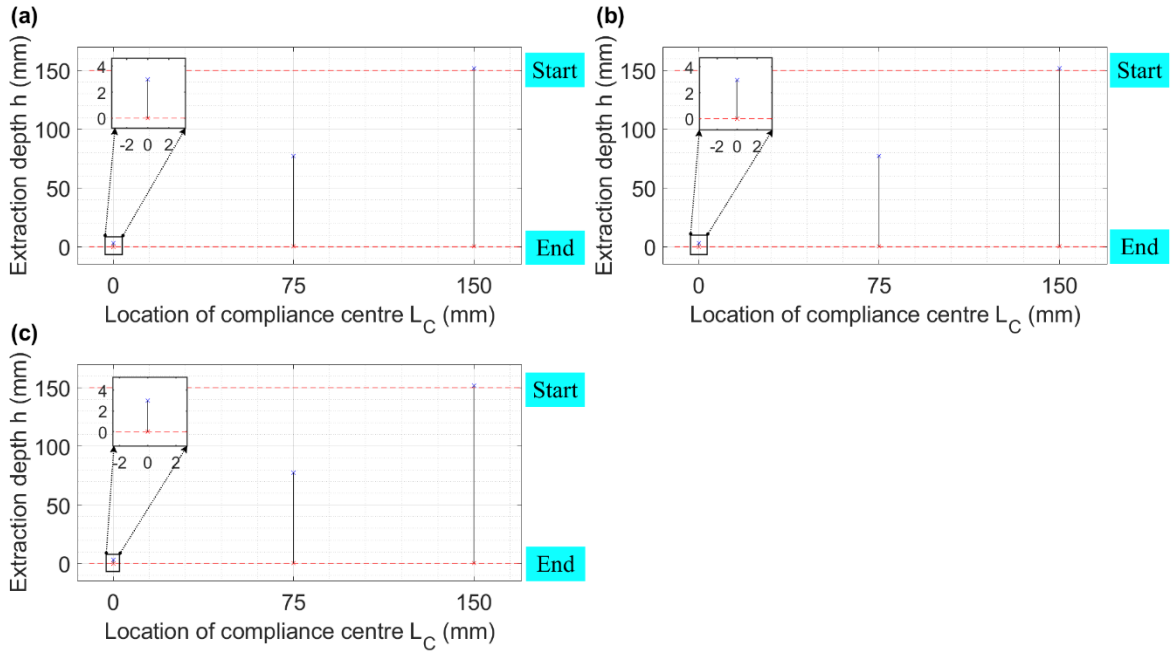

*Figure 3.36. The effect of the two-contact region the combined two-side and one-plane contact on the structural parameters(a) K_θ =15*10^4 Nmm rad^{-1} ; (b) K_θ =30*10^4 Nmm rad^{-1} ; (c) K_θ =45*10^4 Nmm rad^{-1} with $K_X, K_Y = 0.3\ N\ mm^{-1}$, $K_\Phi, K_\psi = 30*10^4$ Nmm rad^{-1} $\delta_X, \delta_Y =$ 2 mm,$\delta_\theta, \delta_\Phi, \delta_\psi = 0$ rad.*

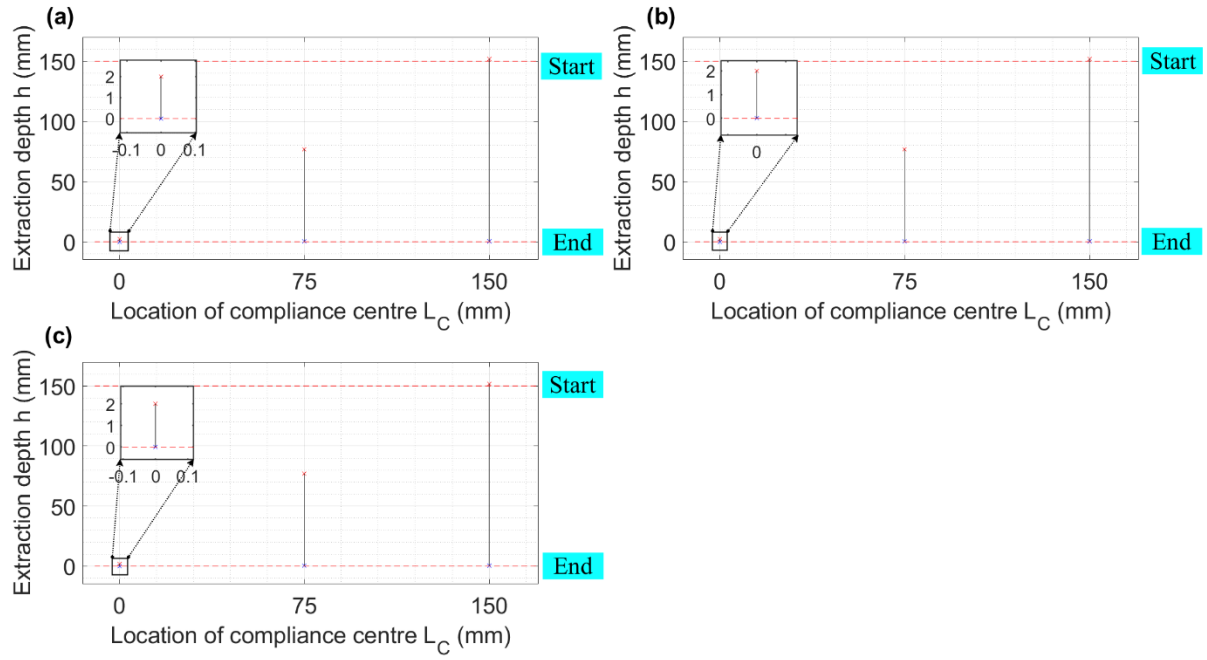

*Figure 3.37. The effect of the two-contact region the two-point contact on the structural parameters: (a) K_Φ =15*10^4 Nmm rad^{-1} ; (b) K_Φ =30*10^4 Nmm rad^{-1} ; (c) K_Φ =45*10^4 Nmm rad^{-1} with $K_X, K_Y = 0.3\ N\ mm^{-1}$, $K_\theta, K_\psi = 30*10^4$ Nmm rad^{-1} $\delta_X, \delta_Y = 2$ mm,$\delta_\theta, \delta_\Phi, \delta_\psi = 0$ rad.*

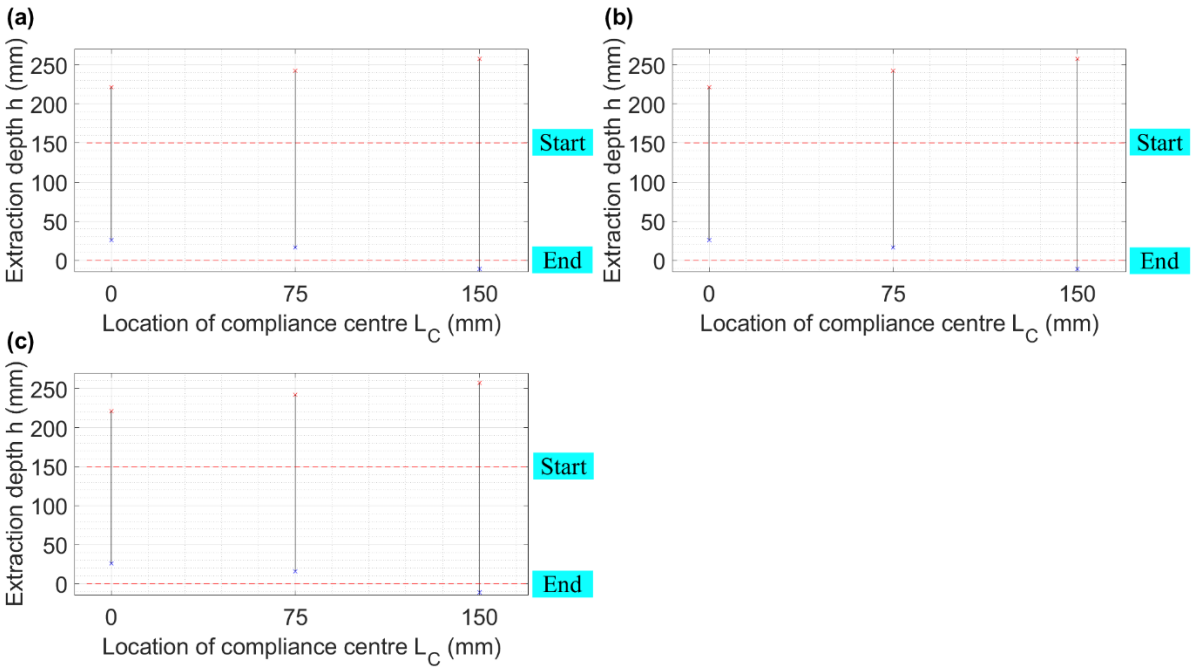

*Figure 3.38. The effect of the two-contact region the two-side contact on the structural parameters: (a) K_Φ =15*10^4 Nmm rad^{-1} ; (b) K_Φ =30*10^4 Nmm rad^{-1} ; (c) K_Φ =45*10^4 Nmm rad^{-1} with $K_X, K_Y = 0.3\ N\ mm^{-1}$, $K_\theta, K_\psi = 30*10^4$ Nmm rad^{-1} $\delta_X, \delta_Y = 2$ mm,$\delta_\theta, \delta_\Phi, \delta_\psi = 0$ rad.*

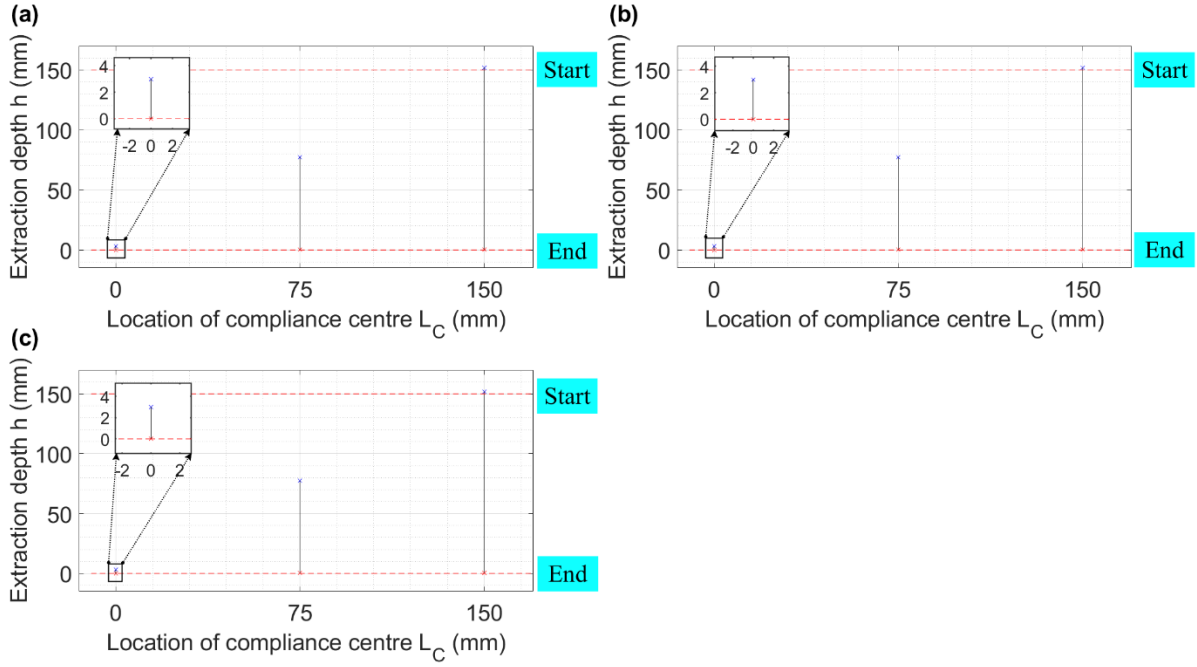

*Figure 3.39. The effect of the two-contact region the combined two-side and one-plane contact on the structural parameters: (a) K_Φ =15*10^4 Nmm rad^{-1} ; (b) K_Φ =30*10^4 Nmm rad^{-1} ; (c) K_Φ =45*10^4 Nmm rad^{-1} with $K_X, K_Y = 0.3\ N\ mm^{-1}$, K_θ, K_ψ = 30*10^4 Nmm rad^{-1} δ_X, δ_Y = 2 mm,$\delta_\theta, \delta_\Phi, \delta_\psi$ = 0 rad.*

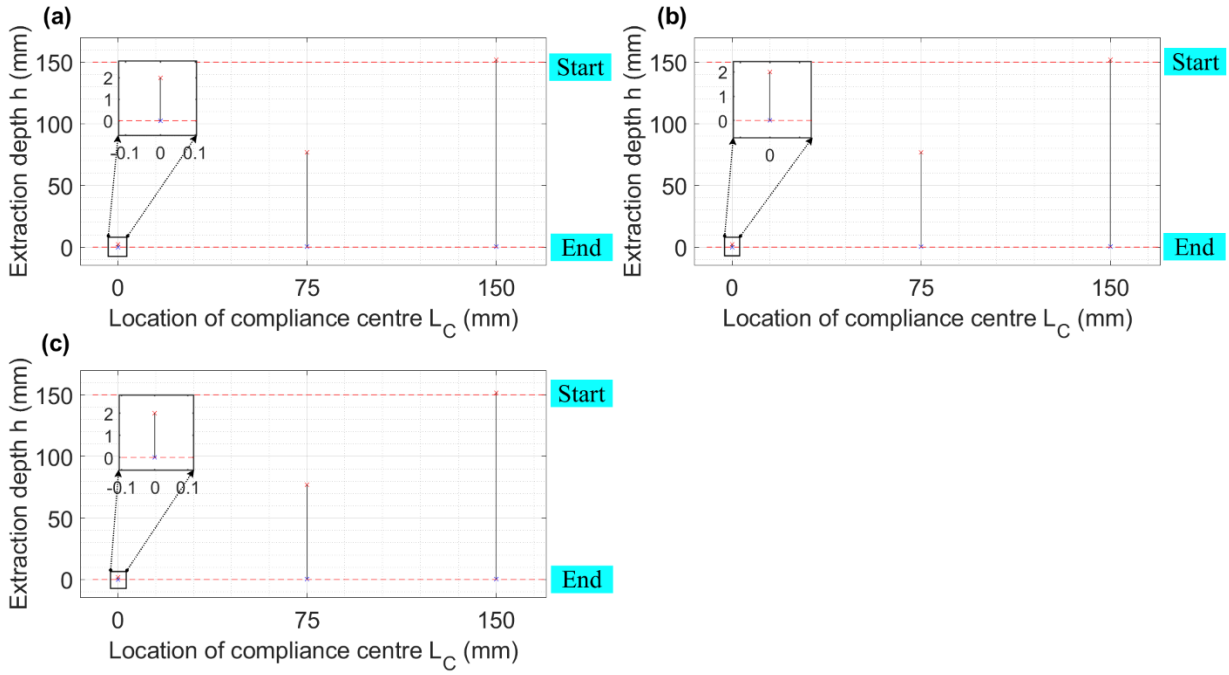

*Figure 3.40. The effect of the two-contact region the two-point contact on the structural parameters: (a) K_ψ =15*10^4 Nmm rad^{-1} ; (b) K_ψ =30*10^4 Nmm rad^{-1} ; (c) K_ψ =45*10^4 Nmm rad^{-1} with $K_X, K_Y = 0.3\ N\ mm^{-1}$, K_θ, K_Φ = 30*10^4 Nmm rad^{-1} δ_X, δ_Y = 2 mm,$\delta_\theta, \delta_\Phi, \delta_\psi$ = 0 rad.*

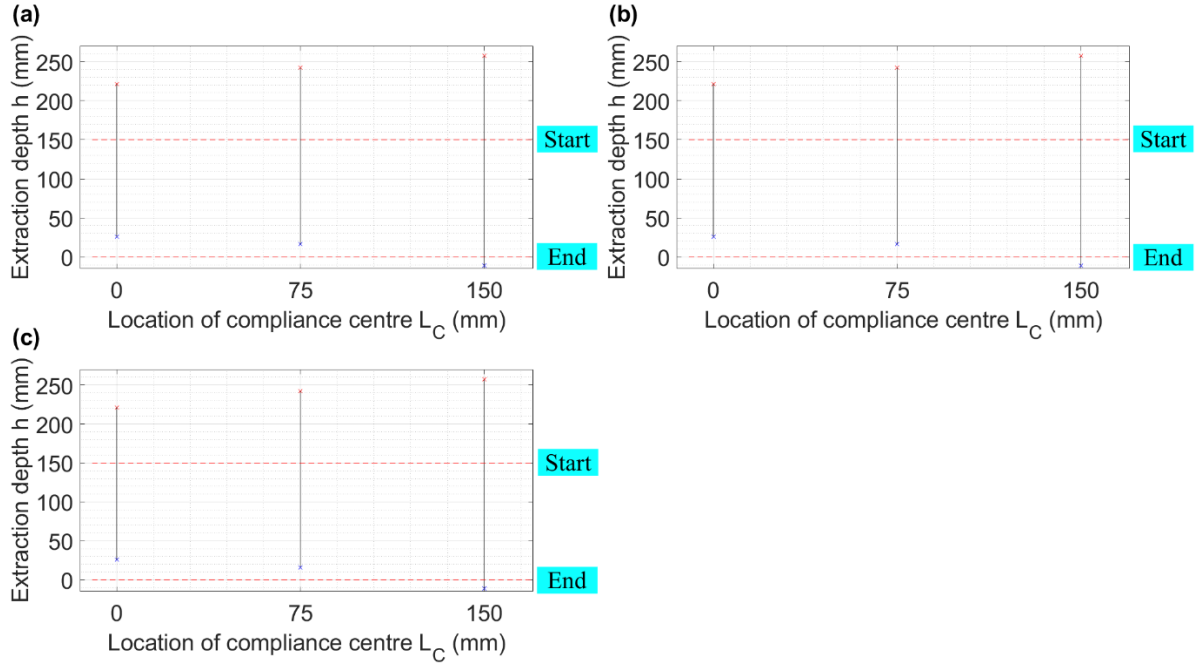

*Figure 3.41. The effect of the two-contact region the two-side contact on the structural parameters: (a) K_ψ =15*10^4 Nmm rad^{-1} ; (b) K_ψ =30*10^4 Nmm rad^{-1} ; (c) K_ψ =45*10^4 Nmm rad^{-1} with $K_X, K_Y = 0.3\ N\ mm^{-1}$, $K_\theta, K_\Phi = 30*10^4$ Nmm rad^{-1} $\delta_X, \delta_Y =$ 2 mm,$\delta_\theta, \delta_\Phi, \delta_\psi = 0$ rad.*

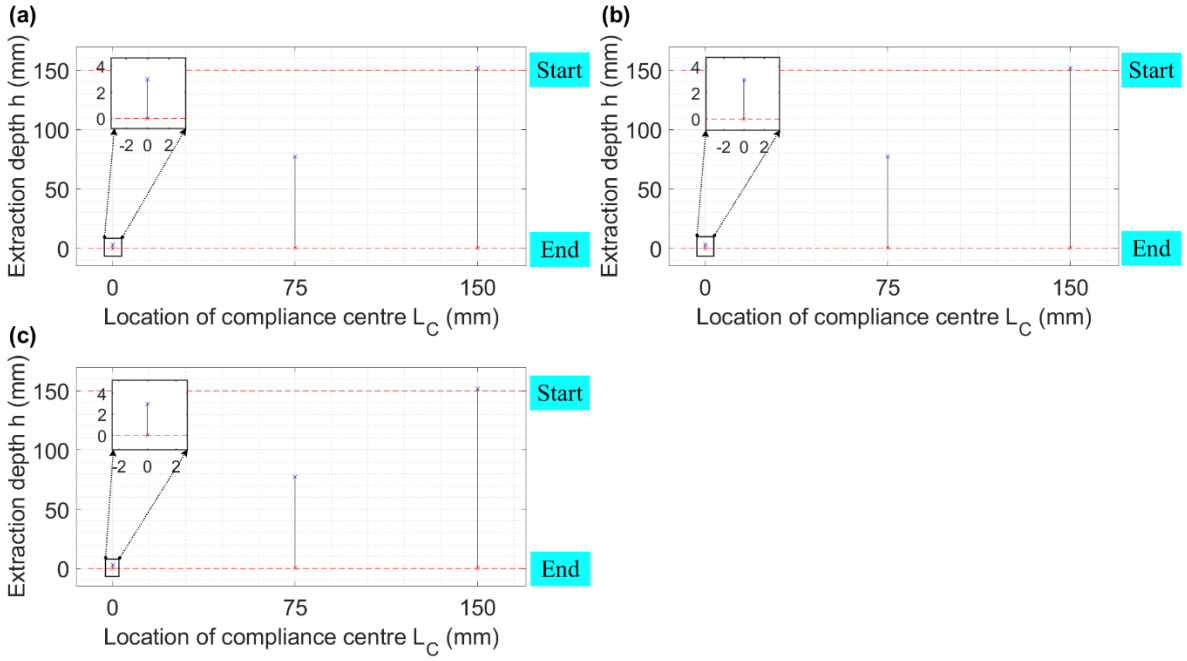

*Figure 3.42. The effect of the two-contact region the combined two-side and one-plane contact on the structural parameters: (a) K_ψ =15*10^4 Nmm rad^{-1} ; (b) K_ψ =30*10^4 Nmm rad^{-1} ; (c) K_ψ =45*10^4 Nmm rad^{-1} with $K_X, K_Y = 0.3\ N\ mm^{-1}$, $K_\theta, K_\Phi = 30*10^4$ Nmm rad^{-1} $\delta_X, \delta_Y =$ 2 mm,$\delta_\theta, \delta_\Phi, \delta_\psi = 0$ rad.*

3.4 Experiment

In this section, an experiment is performed with three samples with different dimensions to verify the results of the above analysis. Rectangle peg-hole has the following geometric dimensions (Table 3.2).

TABLE 3.2. Parameters for rectangle peg-hole

Category	**Parameter**	**Value**
Friction Characteristics	Static Coefficient of friction for PLA	$\mu = 0.266$
Geometrical parameters	Peg mass	m= 0.4 kg
	Peg dimensions	Sample 1: 59.5*39.5 mm, Sample 2: 60*40 mm, Sample 3: 60.5*40.5 mm
	Hole dimensions	60.1* 40.1 mm
	Peg length	L= 150 mm
Initial position/angle	Depth	$h_0 = 150$ mm
	Angle	$\theta_0 = -0.9$ rad

3.4.1 Experimental Design

The experimental setup described in this section employed a six-degree-of-freedom KUKA LBR iiwa robot [25] in conjunction with a wrist-mounted force/torque sensor (Figure 3.43). The video documenting the experiment is available at [26]. During the experiment, the force and moment data were recorded. The experimental setup involved placing a block with a hole on a table, with a peg affixed to the media flange of the robot arm. A noteworthy feature of this configuration is the deliberate exclusion of a gripper by attaching the workpiece to the robot's end effector, as the work by Zhang et al [11].

Both the peg and the hole were fabricated from thermoplastic material. The experiment was conducted 18 times for each sample, with six repetitions for each compliance centre location (L_C = 150 mm, L_C= 75 mm, L_C = 0 mm).

The tool centre point (TCP) was dynamically established through active compliance. In this context, the peg could rotate around the TCP. To experiment with diverse compliance centre locations, various TCP configurations were implemented [25].

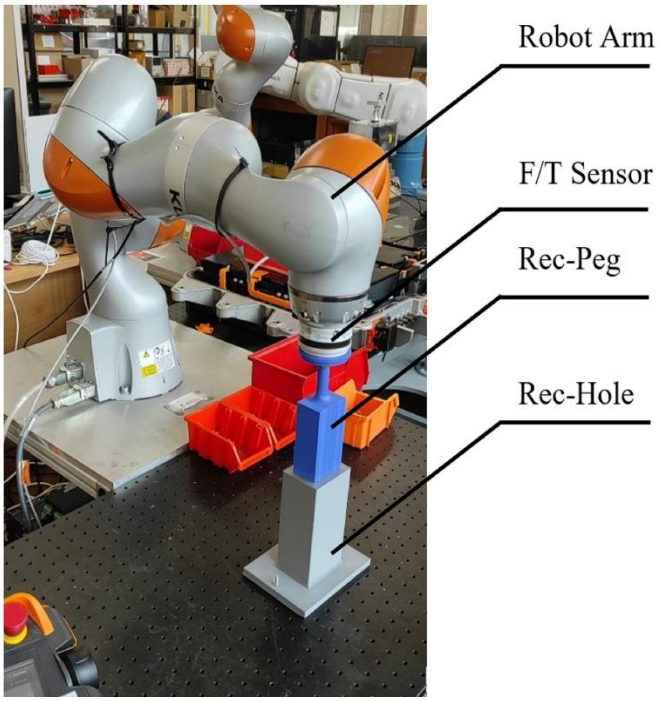

Figure 3.43. The experimental setup.

3.4.2 Experimental Result

The experimental parameters utilised in this study can be found in Table 3.2. To ensure consistency, a stiffness value of K_x , K_y = 0.3 N.mm^{-1}, was set along the extraction direction. Prior to plotting the extraction force measurements, a Savitzky-Golay filter was employed to effectively eliminate any noise present in the data.

Figure 3.44 visually presents the outcomes obtained from investigating the influence of the location of the compliance centre on extraction forces across various depths for three samples with different dimensions. As the extraction force increases, the area of the two-contact progressively expands. This observation highlights the significant disparity in contact states between theoretical predictions and practical implementations, depending on the position of the compliance centre.

Notably, the blue curve in Figure 3.44 clearly indicates that the two-point contact region attains its maximum extent when the compliance centre is situated far from the tip of the rectangle peg. On the other hand, the orange and green curves demonstrate narrower and lower peaks as the distance L_C decreases, thus corresponding to a diminished two-contact region.

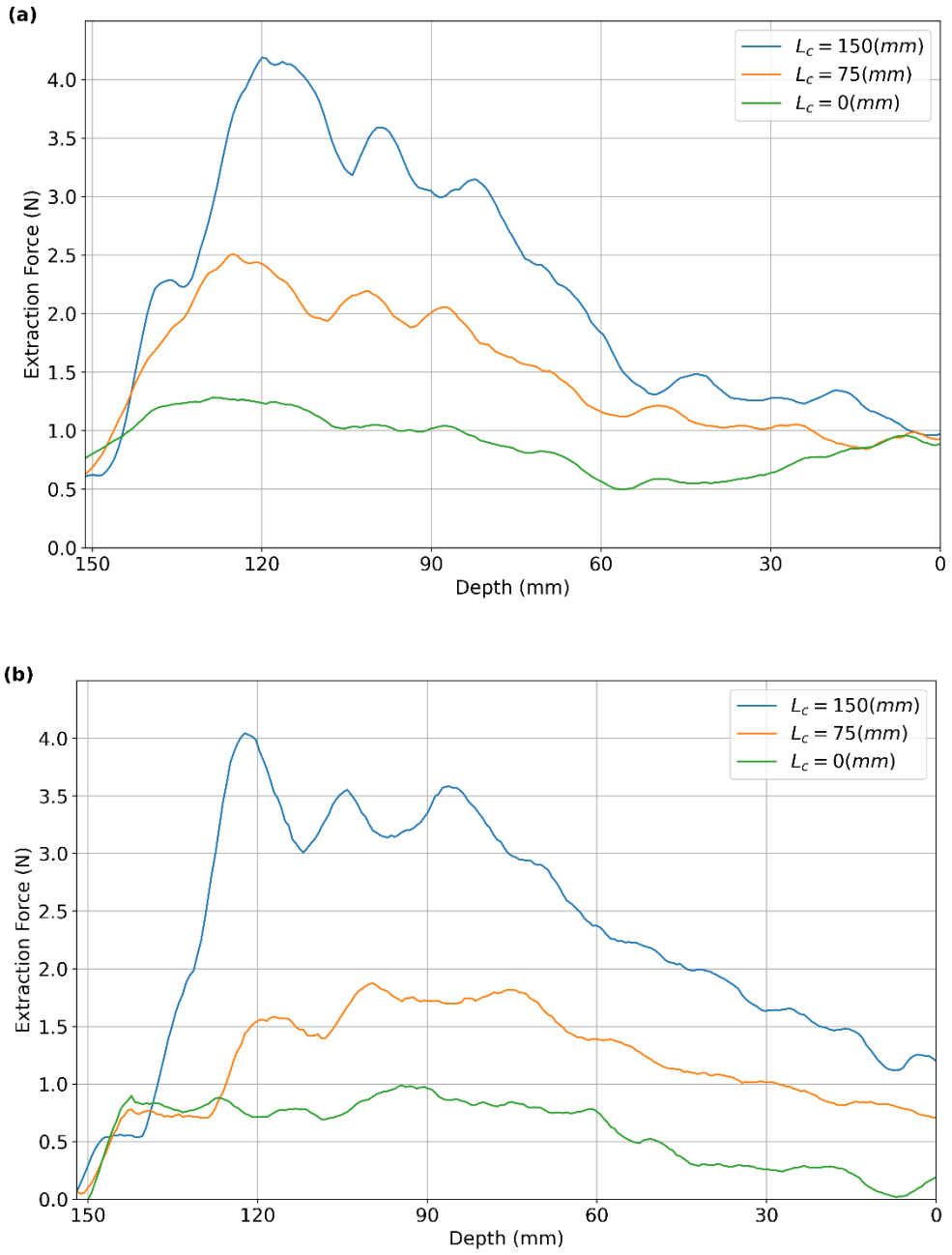

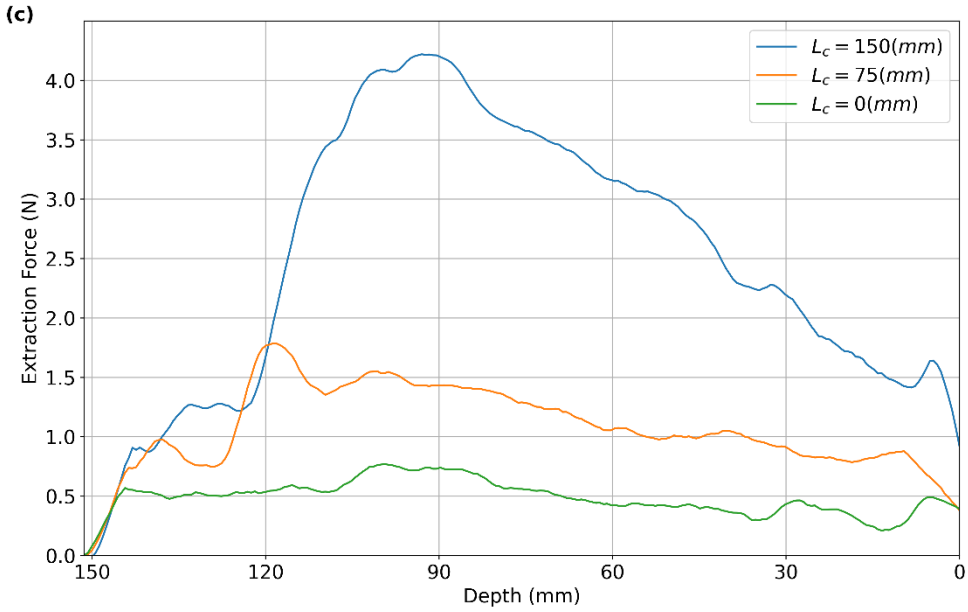

Figure 3.44. Extraction force curves based on compliance centre locations. a) $w' * v' = 59.5*39.5$ mm, b) $w' * v' = 60*40$ mm, and c) $w' * v' = 60.5*40.5$ mm

3.5 Conclusion

This paper has conducted a thorough examination of the challenges associated with extracting a rectangular peg from a hole, focusing on geometric and quasistatic force analysis. Identifying 26 potential contact states in this scenario highlights complexities relevant to both the assembly and disassembly of rectangular peg holes. The results of geometric and quasistatic force analysis provide valuable insights into the intricacies of jamming phenomena specific to rectangular peg-hole disassembly. Through systematic exploration involving factors such as compliance centre location, initial errors in lateral displacement or angular orientation, and manipulator stiffness, significant insights have been gained regarding their influence on two-contact states—emphasising the crucial role of optimising these aspects to enhance disassembly processes effectively.

Our findings demonstrated that positioning the ACC at the end of the peg results in the lowest extraction force compared to alternative ACC placements along the peg. Moreover, we have shown that allocating the ACC in this manner decreases or prevents the occurrence of jamming. To demonstrate the practical applications of our research, we utilised a 6-DOF

compliant manipulator, the KUKA LBR, in real-world settings. Over multiple experiments, we demonstrated that placing the ACC at the end of the peg reduced the average maximum extraction force by 77.1% compared to the top of the peg position, and by 55.6% compared to the centre of the peg position, which suggests a more efficient method for engineers in robotic disassembly operations. These findings suggest that a robot with a reduced payload could be effectively utilised, provided it employs an appropriate ACC strategy. This means that in many disassembly cases, lighter robots with lower payload capacities can be sufficient instead of heavy, high-payload robots with a good ACC strategy.

In conclusion, this study not only enhances the understanding of disassembly processes but also underscores how the application of robotic systems in remanufacturing and other related industries can be revolutionised by integrating these findings. Our research focused on rectangular peg-hole systems which is an elementary disassembly case. More complex disassembly cases, such as irregular geometries, can be investigated through combining this research into rectangular peg-hole systems and other elementary disassembly cases such as cylindrical peg-hole systems [11] and multi-peg–multi-hole systems [7], [22]. Future work could expand upon adhesive force by incorporating such effects, potentially enhancing the model's applicability to recycling and remanufacturing scenarios where such forces are more prominent. Additionally, the research could investigate systems with changeable stiffness, exploring how dynamically adjusting stiffness parameters could improve the efficiency and adaptability of robotic systems during disassembly processes. These extensions may open new avenues for optimising disassembly tasks in real-world applications.

Acknowledgement

This work was supported by the Engineering and Physical Sciences Research Council (EPSRC) under Grant EP/W00206X/1.

3.6 References

[1] F. Goli, Y. Wang, and M. Saadat, "Perspective of self-learning robotics for disassembly automation," in *2022 27th International Conference on Automation and Computing (ICAC)*, 2022, pp. 1–6. doi: 10.1109/ICAC55051.2022.9911085.

[2] J. Y. Mule, "Design for Disassembly Approaches on Product Development," 2012.

[3] W. L. Ijomah, C. A. McMahon, G. P. Hammond, and S. T. Newman, "Development of robust design-for-remanufacturing guidelines to further the aims of sustainable development," *Int J Prod Res*, vol. 45, no. 18–19, pp. 4513–4536, Sep. 2007, doi: 10.1080/00207540701450138.

[4] S. Vongbunyong and W. H. Chen, "Disassembly Automation," in *Disassembly Automation: Automated Systems with Cognitive Abilities*, S. Vongbunyong and W. H. Chen, Eds., Cham: Springer International Publishing, 2015, pp. 25–54. doi: 10.1007/978-3-319-15183-0_3.

[5] Y. Tang, M. Zhou, E. Zussman, and R. Caudill, "Disassembly modeling, planning, and application," *J Manuf Syst*, vol. 21, no. 3, pp. 200–217, 2002, doi: https://doi.org/10.1016/S0278-6125(02)80162-5.

[6] B.-H. Kim, B.-J. Yi, I. H. Suh, and S.-R. Oh, "Stiffness analysis for effective peg-in/out-hole tasks using multi-fingered robot hands," in *Proceedings. 2000 IEEE/RSJ International Conference on Intelligent Robots and Systems (IROS 2000) (Cat. No.00CH37113)*, 2000, pp. 1229–1236 vol.2. doi: 10.1109/IROS.2000.893187.

[7] F. Goli *et al.*, "Jamming problems and the effects of compliance in dual peg-hole disassembly," *Royal Society Proceedings A*, 2023, doi: https://doi.org/10.1098/rspa.2023.0364.

[8] R. Usubamatov and K. W. Leong, "Analyses of peg-hole jamming in automatic assembly machines," *Assembly Automation*, vol. 31, no. 4, pp. 358–362, Jan. 2011, doi: 10.1108/01445151111172943.

[9] D. E. Whitney, "Quasi-static assembly of compliantly supported rigid parts," *J Dyn Syst Meas Control*, vol. 104, no. 1, pp. 65–77, 1982.

[10] B. P. McNelly, R. Leary, S. Brennan, and K. Reichard, "Characterizing successful robotic insertion and removal from a dry storage cask using peg-like jamming and wedging analysis," in *Pressure Vessels and Piping Conference*, American Society of Mechanical Engineers, 2016, p. V06BT06A064.

[11] Y. Zhang *et al.*, "Peg–hole disassembly using active compliance," *R Soc Open Sci*, vol. 6, no. 8, p. 190476, 2019.

[12] H. Asada and Y. Kakumoto, "The dynamic RCC hand for high-speed assembly," in *Proceedings. 1988 IEEE International Conference on Robotics and Automation*, 1988, pp. 120–125 vol.1. doi: 10.1109/ROBOT.1988.12035.

[13] S. N. 'Simunovi, "an information approach to parts mating," Massachusetts Institute of Technology, Cambridge, MA, 1979.

[14] J. L. Nevins and D. E. Whitney, "Assembly Research," *IFAC Proceedings Volumes*, vol. 12, no. 10, pp. 195–214, 1979, doi: https://doi.org/10.1016/S1474-6670(17)65359-X.

[15] M. E. Caine, T. Lozano-Perez, and W. P. Seering, "Assembly strategies for chamferless parts," in *Proceedings, 1989 International Conference on Robotics and Automation*, 1989, pp. 472–477 vol.1. doi: 10.1109/ROBOT.1989.100031.

[16] R. H. Sturges, "A Three-Dimensional Assembly Task Quantification with Application to Machine Dexterity," *Int J Rob Res*, vol. 7, pp. 34–78, 1988, [Online]. Available: https://api.semanticscholar.org/CorpusID:32049730

[17] R. H. Sturges Jr. and S. Laowattana, "Virtual Wedging in Three-Dimensional Peg Insertion Tasks," *Journal of Mechanical Design*, vol. 118, no. 1, pp. 99–105, Mar. 1996, doi: 10.1115/1.2826863.

[18] R. H. Sturges Jr. and S. Laowattana, "Design of an Orthogonal Compliance for Polygonal Peg Insertion," *Journal of Mechanical Design*, vol. 118, no. 1, pp. 106–114, Mar. 1996, doi: 10.1115/1.2826840.

[19] D. R. Strip, "Insertions using geometric analysis and hybrid force-position control: method and analysis," in *Proceedings. 1988 IEEE International Conference on Robotics and Automation*, IEEE, 1988, pp. 1744–1751.

[20] W. Wang, R. N. K. Loh, and E. Y. Gu, "Passive compliance versus active compliance in robot-based automated assembly systems," *Industrial Robot: An International Journal*, vol. 25, no. 1, pp. 48–57, Jan. 1998, doi: 10.1108/01439919810196964.

[21] F. Lan, M. Castellani, D. Truong Pham, and Y. Wang, "On the correctness of using two-dimensional representations in the analysis of cylindrical peg–hole insertion and withdrawal," *R Soc Open Sci*, vol. 10, no. 8, Aug. 2023, doi: 10.1098/rsos.221021.

[22] F. Goli, Y. Zhang, Y. Wang, and M. Saadat, "An Analysis of Dual Peg-Hole Disassembly Problems," in *Advances in Remanufacturing*, M. Fera, M. Caterino, R. Macchiaroli, and D. T. Pham, Eds., Cham: Springer Nature Switzerland, 2024, pp. 483–500.

[23] K. Sathirakul and R. H. Sturges, "Jamming conditions for multiple peg-in-hole assemblies," *Robotica*, vol. 16, no. 3, pp. 329–345, 1998, doi: DOI: 10.1017/S0263574798000393.

[24] D. N. Trong, M. Betemps, and A. Jutard, "Analysis of dynamic assembly using passive compliance," in *Proceedings of 1995 IEEE International Conference on Robotics and Automation*, 1995, pp. 1997–2002 vol.2. doi: 10.1109/ROBOT.1995.525556.

[25] "System Software KUKA Sunrise.OS 1.11 KUKA Sunrise.Workbench 1.11 Operating and Programming Instructions for System Integrators," 2016.

[26] F. Goli *et al.*, *Rectangle peg-hole disassembly process with active compliance centre*, (2024). Accessed: Apr. 09, 2024. [Online Video]. Available: https://figshare.com/s/2f8db80aaa00a0eb60d2

[27] Y. Zhang *et al.*, "Peg–hole disassembly using active compliance," *R Soc Open Sci*, vol. 6, no. 8, p. 190476, 2019, doi: https://doi.org/10.1098/rsos.190476.

Chapter 4. DISASSEMBLY OF RECTANGLE PEG-HOLE STRUCTURES THROUGH COMPLIANCE STRATEGY AND REINFORCEMENT LEARNING

Authors Contributions:

This chapter of the alternative thesis format is published in the IEEE 20th International Conference on Automation Science and Engineering (2024). I am the first author of this publication. The paper's details and co-authors' contributions are outlined below.

Goli F[1], Wang Y[2] Saadat M[3]; Disassembly of Rectangle Peg-Hole Structures Through Compliance Strategy and Reinforcement Learning (2024).

https://ieeexplore.ieee.org/abstract/document/1071

[1] **Farzaneh Goli:** The main author, Designed and Simulated Reinforcement learning and executed experiments, performed all necessary data analysis and wrote the manuscript.

[2]**Yongjing Wang:** He provided ongoing supervision and meticulous proofreading support during the entire research process. Her oversight was key in maintaining the project's academic rigour, and her critical feedback helped ensure that the final manuscript was polished and well-structured.

[3] **Mozafar Saadat:** He provided ongoing supervision and meticulous proofreading support during the entire research process.

Disassembly of Rectangle Peg-Hole Structures Through Compliance Strategy and Reinforcement Learning

Abstract

Disassembling complex structures using robots is one of the fastest-growing areas of research at the cross-section of artificial intelligence (AI), robotics, and manufacturing. The ability to disassemble parts with efficiency, flexibility and adaptability is important for many sectors including remanufacturing and recycling sectors. This paper presents a new method of disassembling rectangle peg-hole structures by combining compliance strategies with reinforcement learning (RL).

This shows that the combination of compliance strategy with reinforcement learning improves the efficiency and adaptability of disassembly processes by reducing the force required to extract the peg. Reinforcement learning empowers the system to learn disassembly motions by recurrent learning, and dynamically adapting strategies by environmental feedback, such as force/torque sensing.

Experimental results confirm the effectiveness of the proposed method, showing that the extraction force is reduced by 29.6 % compared to the method described in chapters 2 & 3 when using the reinforcement learning-based compliance strategy. It is revealed that the RL agent with a compliance strategy learns optimised disassembly motions while considering material compliance and geometrical limitations.

Key words: Disassembly, compliance strategy, Reinforcement Learning, peg-hole, PyBullet.

4.1 Introduction

The development and growth of the economy and consumption are coupled with public concerns over waste product recycling [1]. Research shows that there are 1.3 billion tons of metal waste in the world, and by 2050, the amount might reach 27 billion tons [2]. The manufacturing sector which adapts to the environmental and resource challenges needs to emphasise environmental impact and resource efficiency, minimising the environmental hazards of end-of-life products while maximising the economic and social benefits of the products [3], [4], [5], [6].

A remanufacturing concept allows products to have a longer life cycle and utilise resources efficiently [7]. Disassembly is considered the first remanufacturing step, increasing product utilisation in the manufacturing sector, lowering the cost of remanufacturing, and reducing the average carbon consumption per product [8]. On the other hand, disassembly is also at the junction of recycling and remanufacturing, and there are several influencing factors such as product design [9], [10].

Using robots in contact-rich tasks is inherently complex due to the dynamic interactions between the robot and the object being assembled/disassembled [11]. It is imperative to employ impedance control strategies in these tasks since they enable robotic systems to adapt to uncertainties and variations inherent in real-world environments [12]. It effectively reduces the risk of damage to objects and improves the effectiveness of the disassembly process.

Impedance strategy is typically categorised into static and adaptive methodologies. In disassembly tasks, static impedance strategies often do not cope with the unpredictable nature of the process [13]. On the contrary, adaptive impedance strategies provide a more robust framework for dealing with the complexities of contact-rich tasks because they dynamically adjust gains according to task conditions [14].

In robotic disassembly, adaptive impedance is adopted in a variety of ways to select appropriate adaptive gains. Although traditional methods are effective in certain scenarios, they lack the adaptability necessary for complex disassembly tasks due to their reliance on heuristics. Data-driven insights can be leveraged for dynamic impedance optimisation by incorporating machine learning (ML) techniques [15].

Although adaptive impedance control is useful for robotic disassembly, there are some challenges involved. The complexity of modelling dynamic interactions and the diversity of object characteristics necessitate complex approaches to control strategy design [12], [16].

These challenges can be addressed through Reinforcement Learning (RL). With RL, control strategies can be designed that can adapt and optimise performance through trial and error, leveraging environment information to achieve optimal outcomes in even the most complex disassembly tasks [6], [17].

Recently, the rise of reinforcement learning (RL) in robotics provides an exciting new approach, where systems are learning and adapting to their environment through trial-and-error processes and optimising actions based on evaluation of the environment [18]. This paradigm is especially suited for robotic disassembly, in which the tasks are highly variable and therefore call for dynamism in responding to these variations in order to achieve efficiency and minimise damage [19].

Recent studies have demonstrated that robotic systems with RL are capable of dealing with variabilities by making real-time decisions that can help remanufacturing processes [20].

The use of compliance strategies in disassembly reduces the risk of damaging the parts and avoids contact problems such as jamming and wedging. Because of the feedback from the physical interactions, these methods enable the disengagement mechanism to change its motion dynamically, thereby increasing the precision of disassembly [21]. Hence, such a blend of RL and compliance with robotics addresses the shortcomings of conventional disassembly

techniques, such as using purely mechanical or pre-programmed robotic approaches, and works as a strategy that is adaptive and sensitive to the environment of the task [22].

The literature presents several cases where RL has been deployed successfully in robotic tasks from autonomous driving to robot manipulation tasks requiring high-level dexterity [23], [24], [25]. Nevertheless, RL lacks a specific focus on disassembly processes where clearance is small and contact conditions are complex. In particular, how the RL could be integrated with compliance strategies, a conventional technique supporting assembly and disassembly processes, is missing.

Our previous study examined the effect of the location of the compliance centre on the extraction of dual peg-holes and rectangle peg-holes [26]. As a result of considering the compliance centre at the end of the peg, less force is required to extract it [27], [28].

In this study, we intend to optimise the extraction process by integrating RL with compliance strategies for disassembly. More specifically, this development is carried out using rectangular peg-hole systems, which is seen as a classic challenging disassembly case study where contact conditions are complex and unknown, and contact processes are difficult to model using conventional analytical approaches (Figure 4.1).

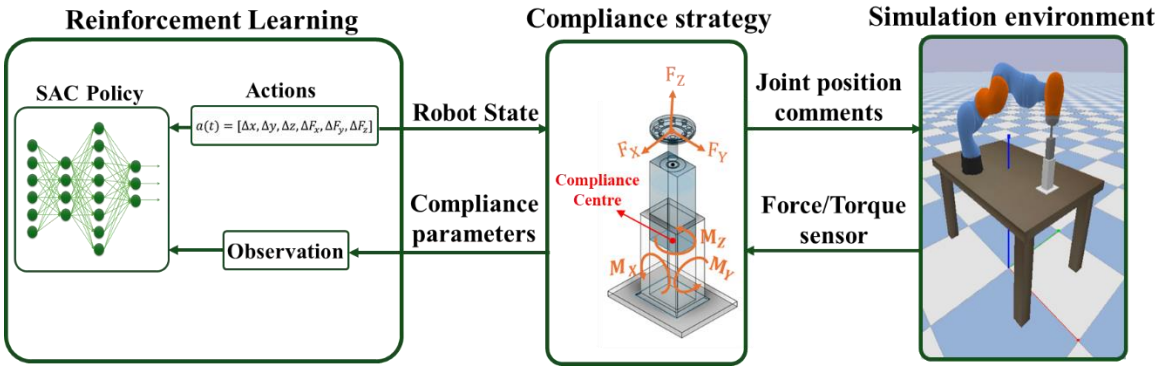

Figure 4.1 A graphic Overview of Disassembly with Active Compliance Strategy and Reinforcement Learning

4.2 Methodology

4.2.1 Peg-Hole disassembly task

Peg-out-hole is a classic disassembly process which demonstrates an array barrier of robotic manipulation. This task involves bringing the peg axes and the hole axes parallel to have the peg extracted to the specified depth. Even small misalignments at this point result in severe friction or even hinder the movement. As shown in Figure 4.2, the extraction phase can be divided into one-contact and two-contact states according to the contact state. In two-contact states, jamming can easily occur due to lateral and angular errors, even though the motion is small. Thus, to avoid the object's surface being scratched through jamming, admittance control was used to realise the compliance control in the robotic disassembly.

Farzaneh et al explore the details of jamming during the disassembly of the peg hole [27], [29]. While the friction and jamming effects are most likely the hardest to model, they complicate the task of maximising performance models-based approaches, making such options impractical. This effort is focused on the extraction stage, which is the most challenging part and requires fine force command.

In tasks where it's crucial to perfectly centre the peg in the hole, the actual depth of the hole may be unclear or unpredictable. Consequently, kinematic planning and position control by conventional means are not efficient enough to ensure a satisfactory task in this case. In this study, the rectangular peg-hole configuration is selected, and a manipulator pulls the peg out of the hole. Taking advantage of state feedback, a state-action controller is built to be highly tuned to help pilot the disassembly process.

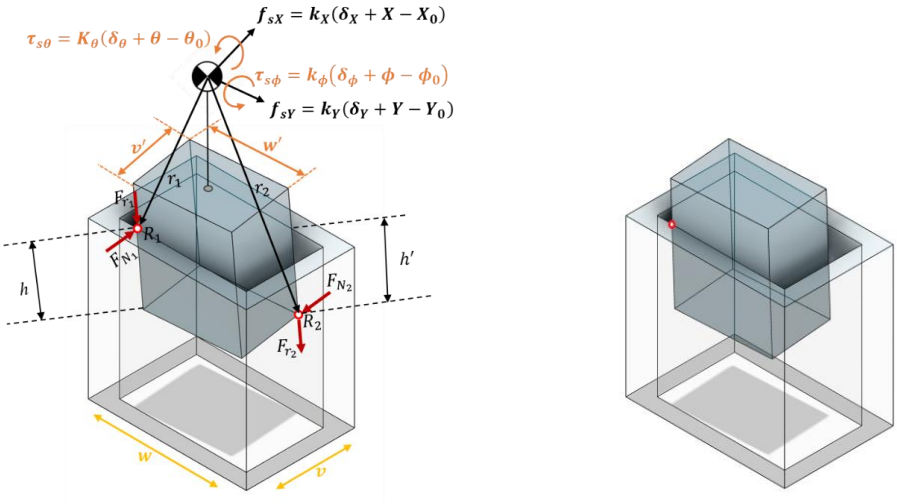

Figure 4.2. Contact stats of rectangle peg-hole disassembly[1]

4.2.2 Robotic disassembly simulation setup

Our research focuses on the intricate task of disassembling a rectangular peg from a corresponding hole using RL techniques with a compliance strategy. Our simulated environment incorporates realistic models of the rectangle peg and hole, ensuring accuracy and realism through the utilisation of CAD files (Figure 4.3) within the PyBullet simulation (Figure 4.4).

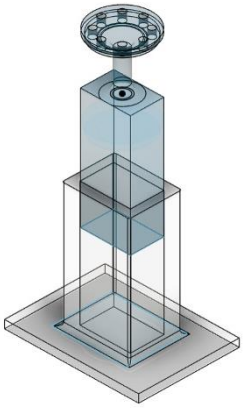

Figure 4.3. A 3D view of rectangle peg-hole

[1] More detail in chapter 3.

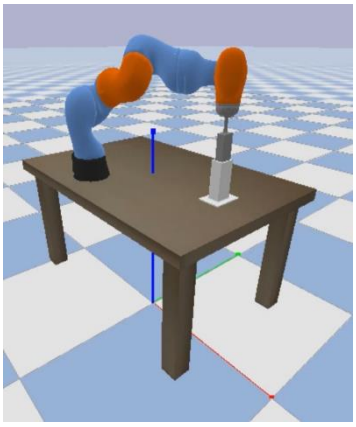

Figure 4.4 An environment simulated using PyBullet

We employ a powered KUKA iiwa robot equipped with a torque/force (T/F) sensor to discern and react to physical connections between the peg and the hole (Figure 4.4). The force/torque sensor integrated into the robot allows us to measure the applied force along the x and y axes during the peg extraction process.

To enhance the adaptability of our approach, we incorporate a compliance strategy within the RL framework. This strategy enables the robot to dynamically adjust its behaviour based on external forces and constraints encountered during the disassembly process.

4.2.3 Robotic Compliance and Adaptability

One of the most often used methods for compliance control [30] is impedance control [31], which aims to increase positioning precision. It is generally assumed that a robot moving slowly and smoothly in a constrained environment can be regarded as a quasi-static operation during disassembly.

In this case, a stiffness controller rather than an impedance controller is suitable due to the small speed and acceleration. When obstructions prevent the obedient robot from following the virtual trajectory, it will veer off course and pull itself back with the specified stiffness.

In other words, compliance refers to the robot's ability to dynamically adjust its stiffness and responsiveness to external forces and constraints encountered during the disassembly process.

The purpose of this research is to integrate RL with a compliance strategy aiming at the following goals:

• *Stiffness modulation:* The stiffness of the robot refers to its resistance to deformation when subjected to external forces. By incorporating compliance parameters into the RL algorithm, we enable the robot to modulate its stiffness dynamically. This modulation allows the robot to adapt its behaviour based on the nature and magnitude of external forces encountered during the disassembly task.

• *Responsiveness adjustment:* In addition to stiffness modulation, our compliance strategy empowers the robot to adjust its responsiveness to external stimuli. This responsiveness refers to the robot's ability to react to changes swiftly and accurately in the environment, such as variations in the position or orientation of the peg and hole.

• *Controlled disassembly process:* The overarching goal of integrating compliance into the RL framework is to promote a controlled and adaptable disassembly process. By dynamically adjusting its stiffness and responsiveness, the KUKA iiwa robot can effectively navigate uncertainties and variations in the environment while maintaining task objectives.

• *Real-time adaptation to environmental dynamics:* One of the key advantages of our compliance strategy is its real-time adaptability to environmental dynamics. As the robot interacts with the peg and hole, it continuously monitors and responds to changes in force, torque, and spatial relationships. This real-time adaptation allows the robot to optimise its disassembly strategy based on the evolving conditions of the task environment.

• *Precision and stability emphasis:* Central to the compliance strategy is the emphasis on precision and stability during the disassembly process. By dynamically modulating its stiffness and responsiveness, the robot can achieve precise and stable interactions with the peg and hole, minimising errors and maximising task success rates.

4.2.4 Reinforcement learning algorithm with compliance strategy

Robotic RL involves a robot acting sequentially over a sequence of time steps in a stochastic environment in order to learn. The RL agent is to learn how to accomplish the goal of selecting actions that will result in maximum cumulative reward, meet the safety constraints, and do efficient disassembly within the simulated environment. An agent can conduct actions $a \in A$ and observe the environment through observations $o \in O$ that may or may not equal. The environment is characterised by a state $s \in S$. With a maximum of T time steps per episode, we examined an episodic interaction of finite time steps. To control the dynamical system, the agent seeks to identify a policy $\pi(a(t)|o(t))$ that chooses actions $a(t)$ conditioned on observations $o(t)$. With γ acting as a discount factor, the goal is to identify a policy $\pi*$ that maximises the expected sum of future rewards provided by

$$R(t) = \sum_i^{\infty} \gamma r(s(t), a(t)) \tag{4.1}$$

given stochastic dynamics $p(s(t+1)|s(t), a(t))$ and reward function $r(s, a)$ [18].

For this study, we define the problem of dismantling a rectangular peg from a matching hole using an RL algorithm called soft actor-critic (SAC) with the "MlpPolicy" for policy representation. SAC is renowned for its capability to address continuous environments and event-driven structures, making it an ideal choice for our complex disassembly objectives. Utilising the MlpPolicy algorithm, which is based on a multilayer perceptron architecture, facilitates the learning of intricate, nonlinear policies required for the disassembly task. The main goal of this technique is to complete the task as successfully as possible while acting randomly. As an off-policy algorithm, SAC reuses information from recent rollouts for sample-efficient training by using a replay buffer [32].

Based on the equation (4.1) , we define the state $S(t)$ as a vector containing key variables that characterise the robot's operational state:

$$S(t) = [x, y, z, F_x, F_y, F_z, \theta, \phi, \Psi] \tag{4.2}$$

In the context of the robot's operations, the variables x, y, and z represent the Cartesian coordinates of its flange, whereas θ, ϕ, and Ψ represent the flange's rotational angles. Additionally, F_x, F_y and F_z indicate the forces and torques exerted along the x, y, and z axes, respectively, as measured by the force/torque sensor. Meanwhile, the controller issues the action $a(t)$, defined as a set comprising changes in position (Δx, Δy, Δz) and changes in force ($\Delta F_x, \Delta F_y, \Delta F_z$).

$$a(t) = [\Delta x, \Delta y, \Delta z, \Delta F_x, \Delta F_y, \Delta F_z] \tag{4.3}$$

This action dictates the movement commanded to the robot by the controller at each sequential time step.

4.2.5 Training Parameters

Effective configuration of training parameters significantly influences the learning process and eventual performance of the agent. Throughout the training process, we adjusted the number of successful programs of the *train_freq* parameter, set to time step 50, enabling the model to adapt its strategy based on accumulated experience. Moreover, setting the size of our replay buffer as a *buffer_size* parameter of 100,000 plays a crucial role in storing and replaying past interactions, enabling the model to analyse various scenarios encountered during training.

To explore and learn efficiently in the simulated environment, it is crucial to ensure an appropriate range of *total_timesteps*. We verify and adjust the total timestep range to optimise the training process. Table 4.1 shows other parameters of the learning algorithm.

TABLE 4. 1. The Leaning Agent's Specific Parameters

Parameter	Value
γ	0.99
α	0.2
r_{end}	+1 ; if the trial is successful -1 ; if the trial is not successful
w_d	Rectangle Peg-Hole: 1
w_f	1
w_{stf}	Rectangle Peg-Hole: 0.1

4.2.6 Reward System and Analysis

The reward system serves as a pivotal component of reinforcement learning, incentivising behaviour conducive to successful peg-hole disassembly.

To train the extraction controller, the environment provides a reward $r(s,a)$ after $a(t)$ is executed. The reward function is defined as follows based on the desired behaviour in the extraction task:

$$r(s,a) = -w_d.\Delta z - w_f.\left\|f_{xy}\right\| - w_{stf}.\left\|k_{xy}\right\| + r_{end} \quad (4.4)$$

These first three represent the immediate rewards at each stage, according to the depth of the hole, the average contact forces in the x-y direction, and the stiffness. The relative weights of these terms can be set by moving w_d , w_f , w_{stf}.

A reward design starts with encouraging upward movement of the peg while discouraging actions requiring large contact forces or high stiffness. In the last step of this episode r_{end} is provided to the network if the trial succeeds or fails before reaching the maximum number of steps.

Our reward function incorporates several critical parameters, including:

- *Z-directional distance:* The Z-directional distance reflects the successful removal of the peg from the hole. As the robot progresses through the disassembly task, minimising the Z-directional distance signifies effective extraction of the peg without causing disruptions or deviations from the desired trajectory. Achieving this objective leads to higher rewards.
- *Average forces along X and Y Axes:* Stability and precision during disengagement are crucial for successful peg-hole disassembly. To emphasise these aspects, the reward system considers the average forces exerted along the X and Y axes. Lower forces indicative of stable and controlled interactions between the robot, peg, and hole result in higher rewards.
- *Robot compliance and adaptability:* The compliance strategy encourages the robot to dynamically adjust its stiffness and responsiveness to external forces and constraints encountered during the disassembly process. A higher reward is assigned when the robot demonstrates adaptive behaviour and adjust its compliance parameters to navigate varying environmental conditions.

4.2.7 Simulation Result

In this section, we want to investigate the performance criteria of an RL project on separating a rectangular peg from a hole using a focused matching strategy.

Figure 4.5 shows the comparative results of the extraction forces (F_z) required to extract a rectangular peg from a hole using two approaches: reinforcement learning (RL) and reinforcement learning with compliance strategy (CS). The horizontal axis represents the number of episodes and the vertical axis represents the extraction force (N).

As shown, the extraction force required by the RL method fluctuates significantly in the previous episodes and tends to stabilise with higher peaks as the learning progresses. This behaviour indicates that the method tries to optimise the extraction process, but struggles to achieve a constant force reduction. On the other side, the RL method integrated with the adaptive strategy shows a more stable and lower extraction force throughout the episodes. The

extraction force is smoother, indicating that the integration of compliance strategy with the reinforcement learning algorithm effectively reduces the sudden force changes and thus reduces the overall force demand. This improvement can be attributed to the ability of the adaptation strategy to dynamically adapt to environmental constraints, reducing resistance forces during the peg extraction process.

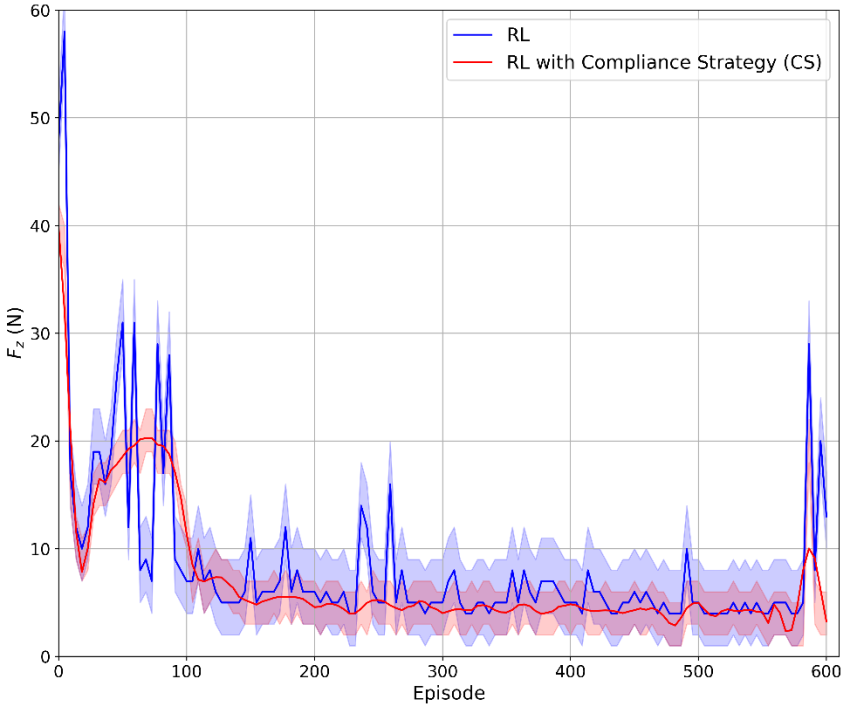

Figure 4.5. Comparison of extraction forces (F_z) using RL and RL with compliance strategy (CS)

Another performance metric is the average X-Y force (N) during the episodes. Figure 4.6 shows the average force exerted along the X and Y axes throughout the episodes. As can be seen, over time, the average force decreases sharply and then continues to fluctuate at a lower level.

This reduction indicates that the RL algorithm has improved in employing an efficient strategy, which can imply a more delicate and controlled interaction between the robot and the environment. Figure 4.7 shows the discounted cumulative reward of each episode. A decrease in the negative value over time indicates that the agent is learning and improving its performance, making fewer mistakes or more optimal actions while learning.

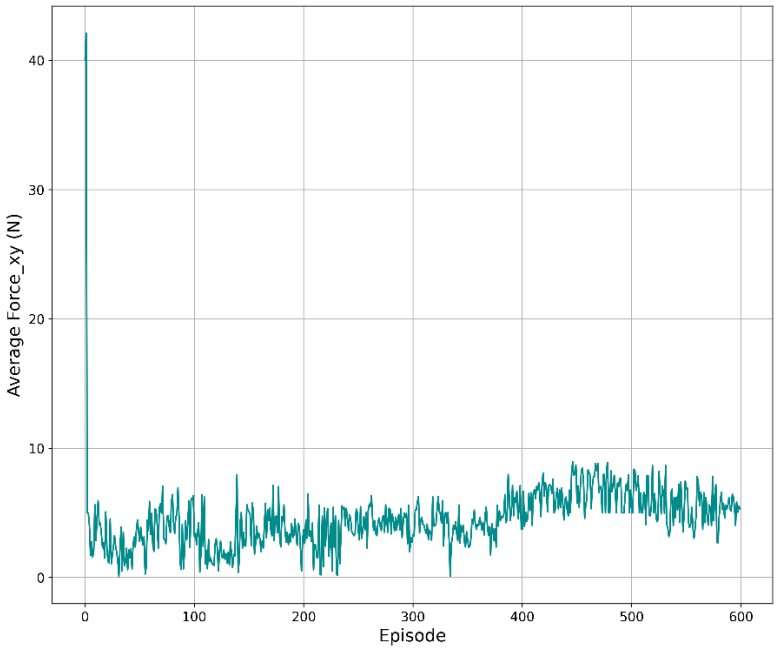

Figure 4.6. The average force exerted along the X-Y axis during each episode

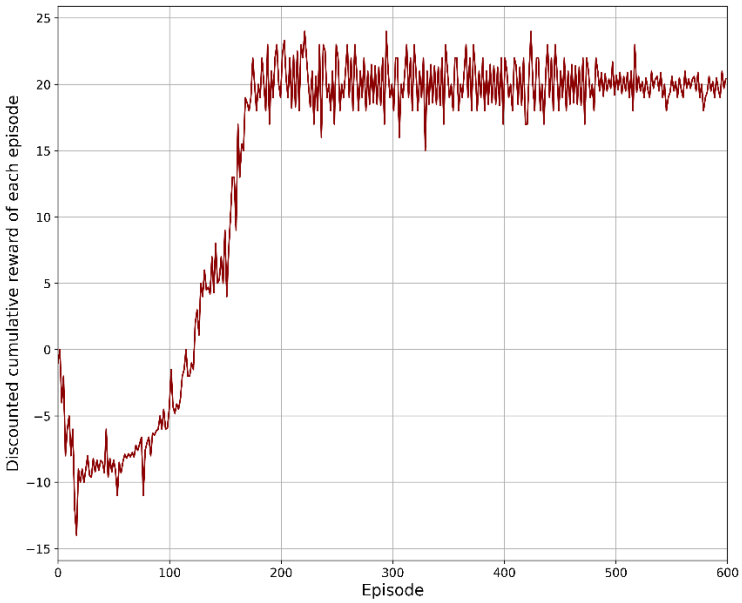

Figure 4.7. The discounted cumulative reward of each episode

Figure 4.8 represents different observations from an RL algorithm during a training phase. These observations typically include positional data and force measurements over a number of time steps or iterations.

The top graph plots the positions of a peg in a 3-dimensional space over time. The positions

are measured along the X, Y, and Z axes. The X-axis of the graph represents the time steps or iterations during the training. The Y-axis represents the normalised position values, which range from 0 to 1, suggesting that the positions have been scaled or normalised for the purpose of the analysis.

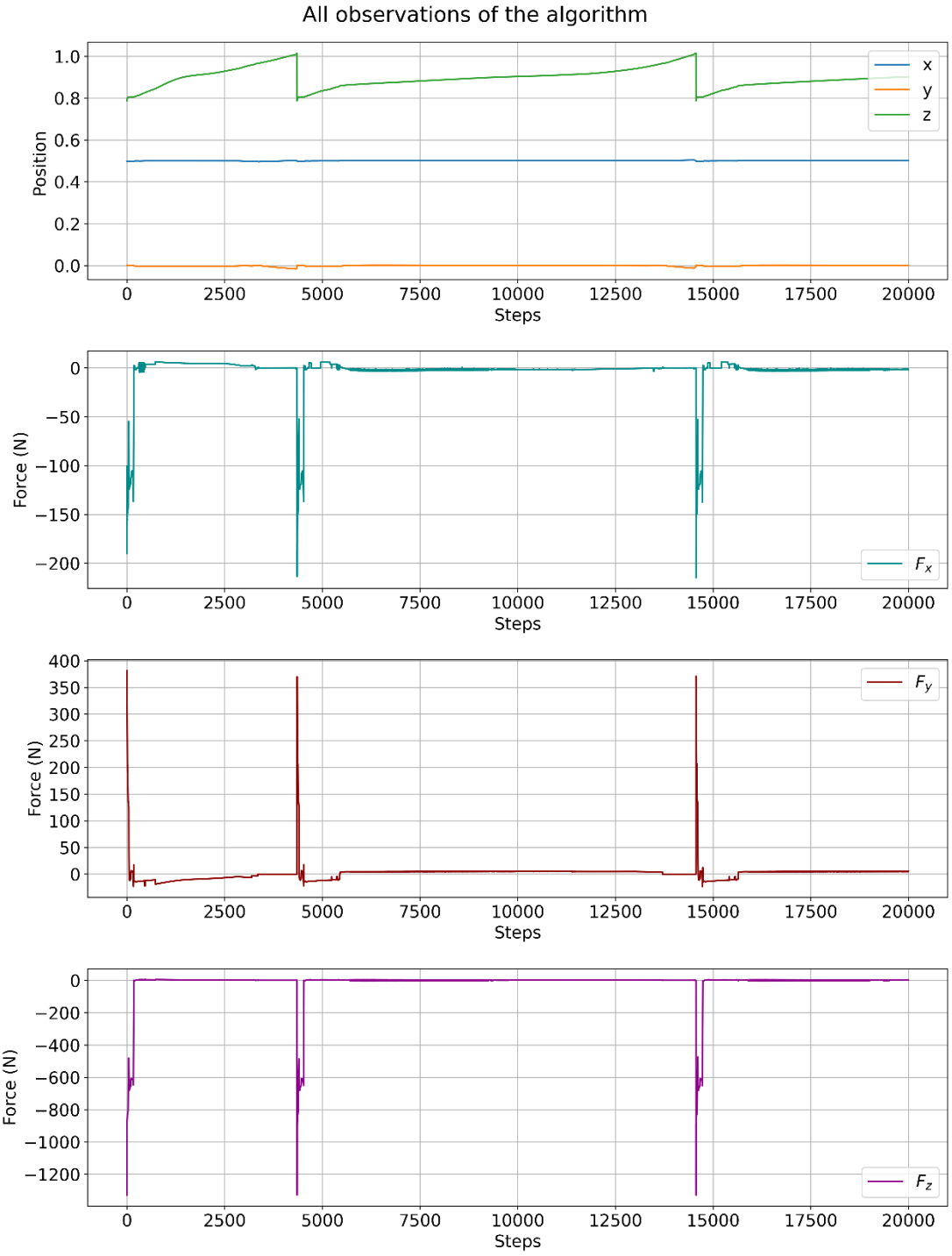

Figure 4.8. Trajectory and force dynamics in an RL-controlled disassembly task for Rectangle Peg-Hole

The graph shows that the position along the Z-axis increases over time, which could indicate a successful disassembly motion. The relatively flat lines for the X and Y positions suggest stability in the horizontal plane, which is typically desired in a disassembly task to avoid lateral forces that could jam the peg.

Results represent a typical learning curve of an agent that improves over time. They also show stabilisation as the number of episodes increases, which is a correct behaviour in RL, as the agent begins to converge toward a more stable policy.

In addition, the agent's performance improves as the robot adapts better to the compliance strategy based on the reduction in force. Therefore, the RL algorithm quickly identified strategies that require less force, which demonstrates the agent's ability to learn and adapt.

Also, the results suggest that the compliance strategy is effectively integrated into the learning process. The reduction in the force applied indicates that the robot adjusts its stiffness and responsiveness in real-time to adapt to the environment, which is a complex task that reflects advanced learning capabilities. The cumulative reward process suggests that compliance parameters are adjusted to achieve the desired task while maximising efficiency and minimising force interactions.

In conclusion, the technical details and trends in the plots suggest that our RL algorithm can handle the task with a compliance and controlled strategy.

4.3 Experimental and Result

In this section, we describe the experiment setup and the results and discussions.

4.3.1 Experimental Setup

To validate the effectiveness of the proposed methodologies in this chapter, we conducted rectangular peg-hole disassembly experiments utilizing a KUKA iiwa collaborative robot, which was securely mounted on a table. A HEX 6-axis force/torque sensor was affixed to the robot's flange at the end-effector.

A rectangular peg (dimensions 60 mm by 40 mm) was made with a 3D printer and attached beneath the sensor with screws. As depicted in Figure 4.9, a corresponding rectangular hole, measuring 60.1 mm by 40.1 mm, was positioned at an arbitrary location on the table. The reinforcement learning (RL) agent's environment was trained on a system equipped with an Intel i9-13900HX CPU and an NVIDIA GeForce RTX 4080 GPU with 12 GB of GDDR6 memory. SunriseWorkbench (KUKA Software) was employed to control the robotic agent. Figure 4.9 illustrates the physical setup of the real-robot experimental environment.

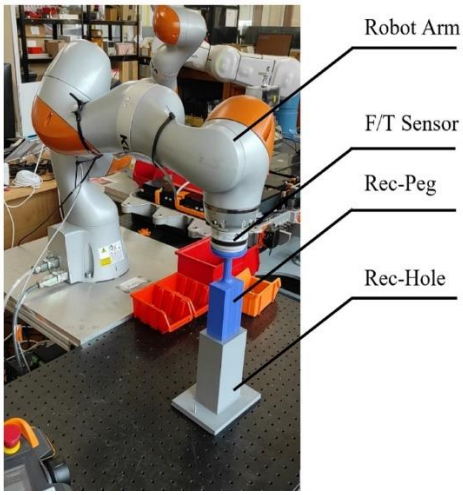

Figure 4.9 Overview of Kuka robot with F/T sensor and peg-hole

The parameters for our methodology are defined as outlined in Table 4.2. To prevent unintentional damage to both the components and the disassembly system, maximum allowable Cartesian force and torque limits were established within the experimental setup. At the outset, the robot was configured in teach mode and positioned within the designated hole.

To ensure experimental safety during the robotic disassembly process, the velocity of the robot was restricted to a maximum of 0.1 m/s. Furthermore, a contact force threshold of 20 N was established for both the X and Y axes to prevent excessive force during interaction. In each adjustment step, the translation offset was limited to a maximum of 0.1 mm along the X and Y axes, with a rotational offset constraint of 5 degrees. These parameters were selected to maintain precise control over movement and contact forces throughout the disassembly process.

TABLE 4. 2. Parameters of rectangle peg-hole disassembly

Parameter	***Values***
Stiffness Gains (N/m)	[50, 50, 50]
Damping Gains (N*s/m)	[0.05, 0.05, 0.05]
Contact force threshold (N)	10
Maximum cartesian torque (Nm)	[3,3,1]

4.3.2 Experimental Result

This section presents the results of the experiment. To ensure accuracy and efficiency in the results, the experiment was repeated 10 times. Figure 4.10 compares the extraction force (F_z) based on reinforcement learning and compliance strategies (CS) with the method described in chapters 2 & 3. The method described in chapters 2 & 3, depicted by the red line, shows consistently higher forces throughout the process, which fluctuates significantly and has prominent peaks. There is a sharp increase in force with the method described in chapters 2 & 3, reaching over 12 N with more oscillations.

In contrast, the RL with a compliance strategy, shown by the green line, maintains a more stable and lower force profile throughout the entire depth range. The RL method's peak forces never exceed 8 N, which reflects that the system has to overcome initial resistance, such as static friction. In this process, the force slowly decreases to stabilise at 5 N and display smaller oscillations compared to the method described in chapters 2 & 3. This decrease in force proves that the compliance strategy of RL is adaptive; it optimises the application of force after the initial resistance is overcome. The middle phase shows steady-state behaviour with slight oscillations in the force, which indicates that the RL system continuously adapts to changes in either stiffness or contact points for smooth and controlled extraction. These results evidence that RL with compliance strategy allows reaching very good precision and high efficiency under variable conditions.

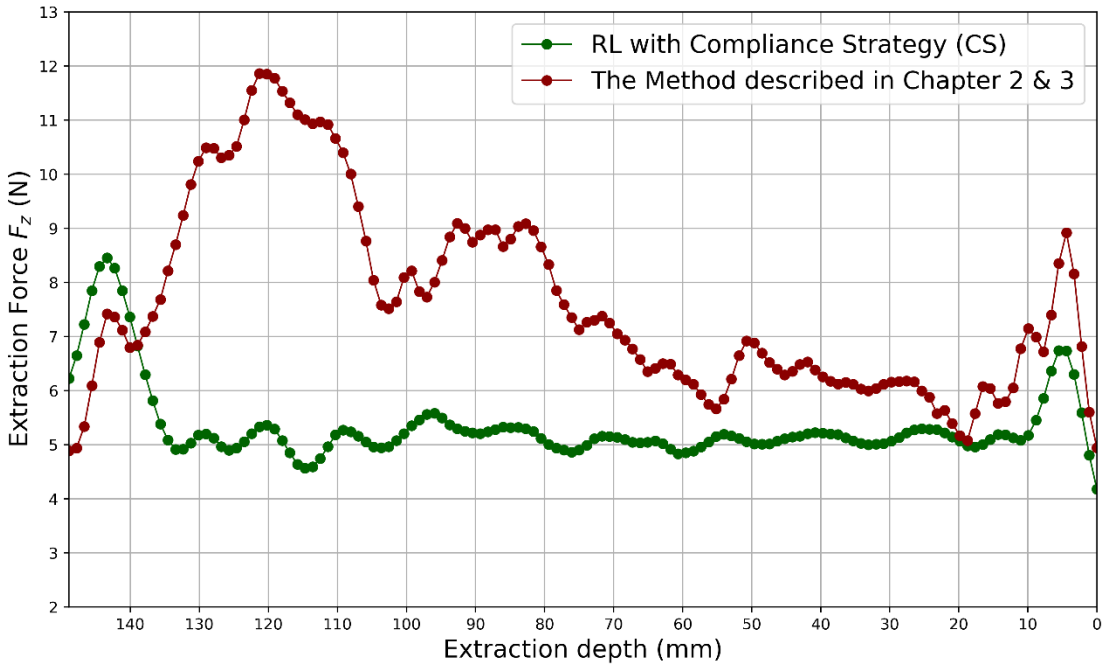

Figure 4.10. Extraction force (F_z) using a reinforcement learning compliance strategy

Figure 4.11 Comparing the extraction force (F_z) for two methods: between the method described in chapters 2 & 3 and an RL-based compliance strategy. The IQR is represented by a box, with the average median force shown as the horizontal line inside the box. The whiskers

portray the full range of recorded forces, while the triangles in green represent the measured mean forces.

It can also be clearly seen from this graph that the forces for the RL-based strategy are lower and more consistent than those of the method described in chapters 2 & 3. The median and mean of the RL method are significantly lower, with a reduced IQR showing less variability. Conversely, the method described in chapters 2 & 3 results in higher average and peak forces, with greater variability.

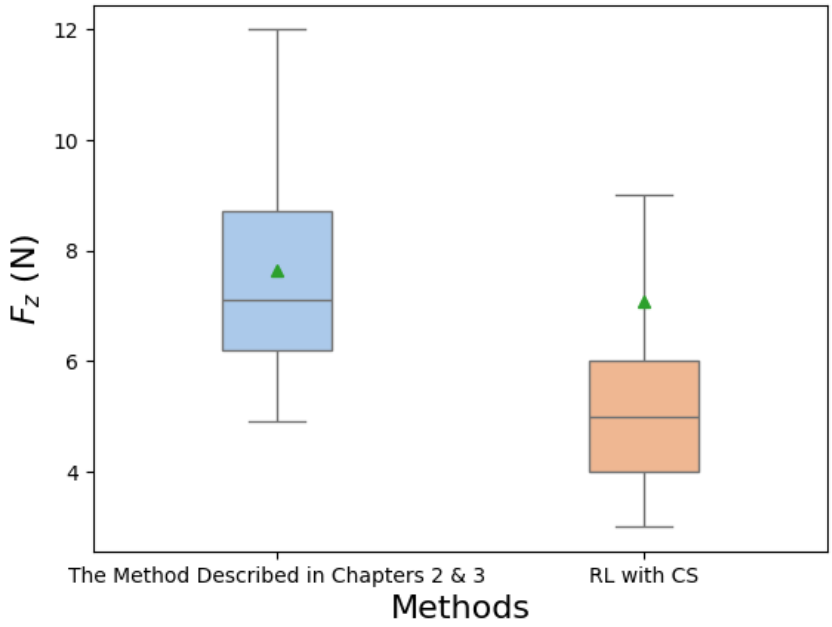

Figure 4.11. Comparison of F_z for the method described in chapters 2 & 3 and compliance strategy using reinforcement learning.

Figure 4.12 shows the time taken for the method described in chapters 2 & 3 and RL-based compliance methods to complete the extraction process. The RL-based compliance strategy has constantly recorded shorter times, both in terms of its median and mean, which are less than that of the method described in chapters 2 & 3. On the other hand, this RL method has shown reduced variability with a narrower IQR and with whiskers barely as short as the range, whereas the method described in chapters 2 & 3 has mostly higher times with greater inconsistency. This illustrates how the RL strategy optimises the extraction process, making it time-effective with reliability.

These findings point out that the proposed RL-based compliance strategy is efficient and stable in maintaining controlled force application during the extraction process, hence having the potential to outperform the method described in chapters 2 & 3, especially in applications where precision and consistency are crucial. Based on RL policy, the disassembly success rate is 94%, and the average disassembly time needed is 7.6 seconds.

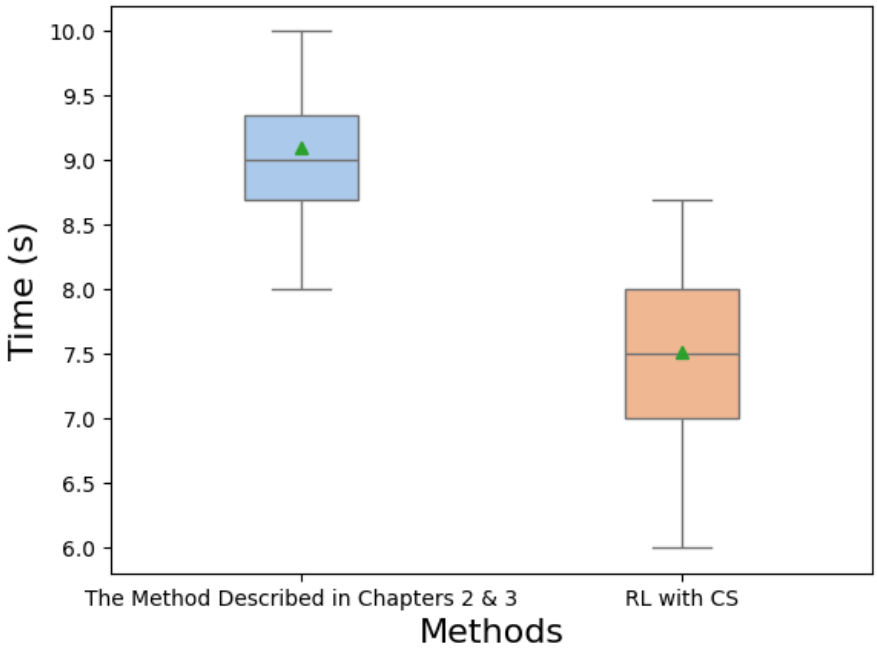

Figure 4.12. Extraction Time Comparison for The Method Described in Chapters 2 & 3 vs. RL-Based Compliance Approaches

4.4 Conclusion

In this research, a compliance strategy integrated with reinforcement learning was used to disassemble rectangular hole structures, increasing their efficiency, flexibility, and adaptability. This approach shows significant reductions in force required for disassembly with high accuracy and adaptation to dynamic environments using the SAC algorithm in PyBullet's simulated environment. The compliance strategy empowers the robot to modulate its stiffness and responsiveness to external forces, facilitating adaptive and robust disassembly manoeuvres.

Experimental results demonstrate the effectiveness of the proposed method, with the extraction force reduced by 29.6% compared to the the method described in chapters 2 & 3, validating the combined use of reinforcement learning and compliance strategies. By dynamically adjusting compliance parameters, such as stiffness coefficients and force thresholds, the robot can effectively navigate uncertainties and variations in the environment while maintaining task objectives. Results confirm that reinforcement learning algorithms combined with compliance strategies are effective for disassembly.

Future work will investigate various shapes of peg-holes using this algorithm and undertake comprehensive laboratory experiments to validate the results. It would significantly increase the robustness and reliability of our results, thereby facilitating the understanding and application of this innovative approach.

4.5 References

[1] Z. Y. Liu, C. Li, X. Y. Fang, and Y. B. Guo, "Energy Consumption in Additive Manufacturing of Metal Parts," *Procedia Manuf*, vol. 26, pp. 834–845, 2018, doi: https://doi.org/10.1016/j.promfg.2018.07.104.

[2] A. Azaria, A. Richardson, S. Kraus, and V. S. Subrahmanian, "Behavioral Analysis of Insider Threat: A Survey and Bootstrapped Prediction in Imbalanced Data," *IEEE Trans Comput Soc Syst*, vol. 1, no. 2, pp. 135–155, 2014, doi: 10.1109/TCSS.2014.2377811.

[3] K. Igarashi, T. Yamada, S. M. Gupta, M. Inoue, and N. Itsubo, "Disassembly system modeling and design with parts selection for cost, recycling and CO2 saving rates using multi criteria optimization," *J Manuf Syst*, vol. 38, pp. 151–164, 2016, doi: https://doi.org/10.1016/j.jmsy.2015.11.002.

[4] S. Baazouzi, F. P. Rist, M. Weeber, and K. P. Birke, "Optimization of Disassembly Strategies for Electric Vehicle Batteries," *Batteries*, vol. 7, no. 4, 2021, doi: 10.3390/batteries7040074.

[5] S. S. H. S. M. M. Olga Battaïa Alexandre Dolgui and M. K. Tiwari, "Design for manufacturing and assembly/disassembly: joint design of products and production systems," *Int J Prod Res*, vol. 56, no. 24, pp. 7181–7189, 2018, doi: 10.1080/00207543.2018.1549795.

[6] X. Guo, Z. Bi, J. Wang, S. Qin, S. Liu, and L. Qi, "Reinforcement learning for disassembly system optimization problems: A survey," *International Journal of Network Dynamics and Intelligence*, pp. 1–14, 2023.

[7] R. T. Lund, "Remanufacturing : the experience of the United States and implications for developing countries," 1985. [Online]. Available: https://api.semanticscholar.org/CorpusID:109190894

[8] G. Tian, M. Zhou, and P. Li, "Disassembly Sequence Planning Considering Fuzzy Component Quality and Varying Operational Cost," *IEEE Transactions on Automation Science and Engineering*, vol. 15, no. 2, pp. 748–760, 2018, doi: 10.1109/TASE.2017.2690802.

[9] X. Guo, Z. Zhang, L. Qi, S. Liu, Y. Tang, and Z. Zhao, "Stochastic Hybrid Discrete Grey Wolf Optimizer for Multi-Objective Disassembly Sequencing and Line Balancing Planning in Disassembling Multiple Products," *IEEE Transactions on Automation Science and Engineering*, vol. 19, no. 3, pp. 1744–1756, 2022, doi: 10.1109/TASE.2021.3133601.

[10] X. Guo, M. Zhou, S. Liu, and L. Qi, "Multiresource-Constrained Selective Disassembly With Maximal Profit and Minimal Energy Consumption," *IEEE Transactions on Automation Science and Engineering*, vol. 18, no. 2, pp. 804–816, 2021, doi: 10.1109/TASE.2020.2992220.

[11] L. Rozo, S. Calinon, D. Caldwell, P. Jiménez, and C. Torras, "Learning collaborative impedance-based robot behaviors," in *Proceedings of the AAAI conference on artificial intelligence*, 2013, pp. 1422–1428.

[12] S. Hjorth, E. Lamon, D. Chrysostomou, and A. Ajoudani, "Design of an Energy-Aware Cartesian Impedance Controller for Collaborative Disassembly," *arXiv preprint arXiv:2302.03587*, 2023.

[13] H.-C. Cho, *A Strategy for Connector Assembly using Impedance Control for Industrial Robots*. 2012.

[14] H. Cao, X. Chen, Y. He, and X. Zhao, "Dynamic Adaptive Hybrid Impedance Control for Dynamic Contact Force Tracking in Uncertain Environments," *IEEE Access*, vol. 7, pp. 83162–83174, 2019, doi: 10.1109/ACCESS.2019.2924696.

[15] E. Mobedi, N. Villa, W. Kim, and A. Ajoudani, "An Adaptive Control Approach to Robotic Assembly with Uncertainties in Vision and Dynamics," in *2020 29th IEEE International Conference on Robot and Human Interactive Communication (RO-MAN)*, 2020, pp. 144–150. doi: 10.1109/RO-MAN47096.2020.9223515.

[16] Y. Michel, R. Rahal, C. Pacchierotti, P. R. Giordano, and D. Lee, "Bilateral Teleoperation With Adaptive Impedance Control for Contact Tasks," *IEEE Robot Autom Lett*, vol. 6, no. 3, pp. 5429–5436, 2021, doi: 10.1109/LRA.2021.3066974.

[17] J. Jones and J. Smith, "Ethnography: challenges and opportunities," *Evidence Based Nursing*, vol. 20, no. 4, p. 98, Oct. 2017, doi: 10.1136/eb-2017-102786.

[18] R. S. Sutton and A. G. Barto, *Reinforcement learning: An introduction*. MIT press, 2018.

[19] D. Silver and D. Hassabis, "Alphago: Mastering the ancient game of go with machine learning," *Research Blog*, vol. 9, 2016.

[20] A. Allagui, I. Belhadj, R. Plateaux, M. Hammadi, O. Penas, and N. Aifaoui, "Reinforcement learning for disassembly sequence planning optimization," *Comput Ind*, vol. 151, p. 103992, 2023, doi: https://doi.org/10.1016/j.compind.2023.103992.

[21] H. Zhu, A. Gupta, A. Rajeswaran, S. Levine, and V. Kumar, "Dexterous Manipulation with Deep Reinforcement Learning: Efficient, General, and Low-Cost," in *2019 International Conference on Robotics and Automation (ICRA)*, 2019, pp. 3651–3657. doi: 10.1109/ICRA.2019.8794102.

[22] Q. Liu, Z. Ji, W. Xu, Z. Liu, B. Yao, and Z. Zhou, "Knowledge-guided robot learning on compliance control for robotic assembly task with predictive model," *Expert Syst Appl*, vol. 234, p. 121037, 2023, doi: https://doi.org/10.1016/j.eswa.2023.121037.

[23] P. Mirowski *et al.*, "Learning to navigate in complex environments," *arXiv preprint arXiv:1611.03673*, 2016.

[24] M. Andrychowicz *et al.*, "Hindsight Experience Replay," in *Advances in Neural Information Processing Systems*, I. Guyon, U. Von Luxburg, S. Bengio, H. Wallach, R. Fergus, S. Vishwanathan, and R. Garnett, Eds., Curran Associates, Inc., 2017. [Online]. Available:

https://proceedings.neurips.cc/paper_files/paper/2017/file/453fadbd8a1a3af50a9df4df899537b5-Paper.pdf

[25] F. Goli, Y. Wang, and M. Saadat, "Perspective of self-learning robotics for disassembly automation," in *2022 27th International Conference on Automation and Computing (ICAC)*, 2022, pp. 1–6. doi: 10.1109/ICAC55051.2022.9911085.

[26] F. Goli *et al.*, "Characterizing the mechanics of rectangular peg–hole disassembly and the effect of the active compliance centre on the extraction force," *R Soc Open Sci*, vol. 11, no. 11, p. 240956, 2024.

[27] F. Goli *et al.*, "Jamming problems and the effects of compliance in dual peg-hole disassembly," *Royal Society Proceedings A*, 2023, doi: https://doi.org/10.1098/rspa.2023.0364.

[28] F. Goli, Y. Zhang, Y. Wang, and M. Saadat, "An Analysis of Dual Peg-Hole Disassembly Problems," in *Advances in Remanufacturing*, M. Fera, M. Caterino, R. Macchiaroli, and D. T. Pham, Eds., Cham: Springer Nature Switzerland, 2024, pp. 483–500.

[29] Goli F, "Dual peg-hole disassembly process with active compliance centre." [Online]. Available: https://youtube.com/shorts/hDh6vXg1Vx4

[30] A. O. Albu-Schäffer and G. Hirzinger, "Cartesian impedance control techniques for torque controlled light-weight robots," *Proceedings 2002 IEEE International Conference on Robotics and Automation (Cat. No.02CH37292)*, vol. 1, pp. 657–663 vol.1, 2002, [Online]. Available: https://api.semanticscholar.org/CorpusID:15056647

[31] N. Hogan, "Impedance Control: An Approach to Manipulation: Part I—Theory," *J Dyn Syst Meas Control*, vol. 107, no. 1, pp. 1–7, Mar. 1985, doi: 10.1115/1.3140702.

[32] D. Horgan *et al.*, "Distributed prioritized experience replay," *arXiv preprint arXiv:1803.00933*, 2018.

Chapter 5. GENERAL DISCUSSION

5.1 Discussion

In this thesis, geometric and quasistatic force issues related to robotic disassembly tasks are evaluated, with a special focus on dual-peg assemblies and rectangular peg holes. The study systematically develops the jamming phenomenon and compliance strategies and includes advanced techniques such as reinforcement learning to further understand and optimise robotic disassembly processes.

In the second chapter, this work addresses the geometric and static force analysis for the dual-peg extraction jamming problem, considering all geometric variations. The identification of 13 distinct contact states in the dual-peg jamming problem is a pivotal contribution, highlighting the complexity of this task. The quasi-static force analysis demonstrates its effectiveness in examining the jamming phenomenon, offering significant insights applicable to a variety of assembly and disassembly problems.

In Section 2.2, we simplify the dual peg-hole disassembly by assuming (i) circular, axisymmetric components, (ii) perfect alignment, (iii) no tilt, and (iv) a clearance smaller than the peg size. These assumptions, supported by prior work (e.g., Lan et al. [1]), enable a tractable two-dimensional analysis that captures the essential physics of jamming and extraction. Although real manufacturing may exhibit slight misalignments or tilts, modern precision techniques and active compliance effectively mitigate these, making our assumptions realistic approximations for many industrial applications.

Compliant manipulators integrated into the study further improve the geometric and force/moment conditions for each of the contact states, therefore opening ways to develop

more accurate and reliable robotic systems that could be applied to disassembly and remanufacturing. The research study also identifies some factors that are critical in determining the two-point contact area, including the compliance centre location, initial errors in both lateral and angular displacements, and manipulator stiffness. First and foremost, this study identifies a new technique on how the location of the compliance centre might become very critical, considering compliance centre strategies that have been developed based on single peg-hole systems, which can be implemented successfully in dual peg-hole disassembly tasks.

From this theoretical model, experimental tests justify these findings by showing how carefully adjusted compliance strategies, involving compliance at any appropriate variable of stiffness and remote centre compliance, effectively lower disassembly forces. While the jamming conditions for dual peg-hole assemblies are different from the single peg-hole assemblies, the remote strategy for compliance proves to effectively reduce the disassembly force in both cases. In addition, the experimental result not only confirms the predictions made from the theoretical model but also gives weight to reliability and practicality in applying the findings of this study.

Figure 5.1 illustrates the measured extraction force (vertical axis) as a function of depth (horizontal axis) for three samples with different radii and three compliance centre locations. (L_C =0 mm, 25 mm, and 55 mm). Each solid curve represents the average of six repeated measurements (18 total experiments, with six repetitions per compliance centre location). The shaded regions around each curve denote the range of observed values across all repetitions, highlighting the variability in the experimental data. As the compliance centre moves away from the tip of the dual-peg, the two-point contact region increases, while the orange and green curves show narrower and lower peaks, indicating a smaller two-point contact region (as discussed in section 2.5.2).

a)

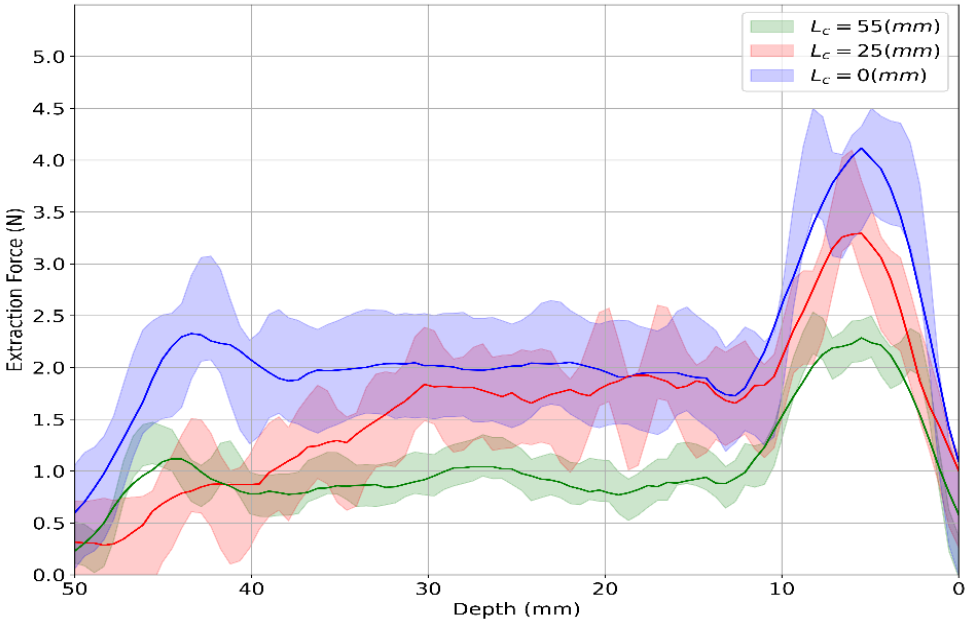
$L_c = 55(mm)$
$L_c = 25(mm)$
$L_c = 0(mm)$
Extraction Force (N)
Depth (mm)
0.0
0.5
1.0
1.5
2.0
2.5
3.0
3.5
4.0
4.5
5.0
50
40
30
20
10
0

b)

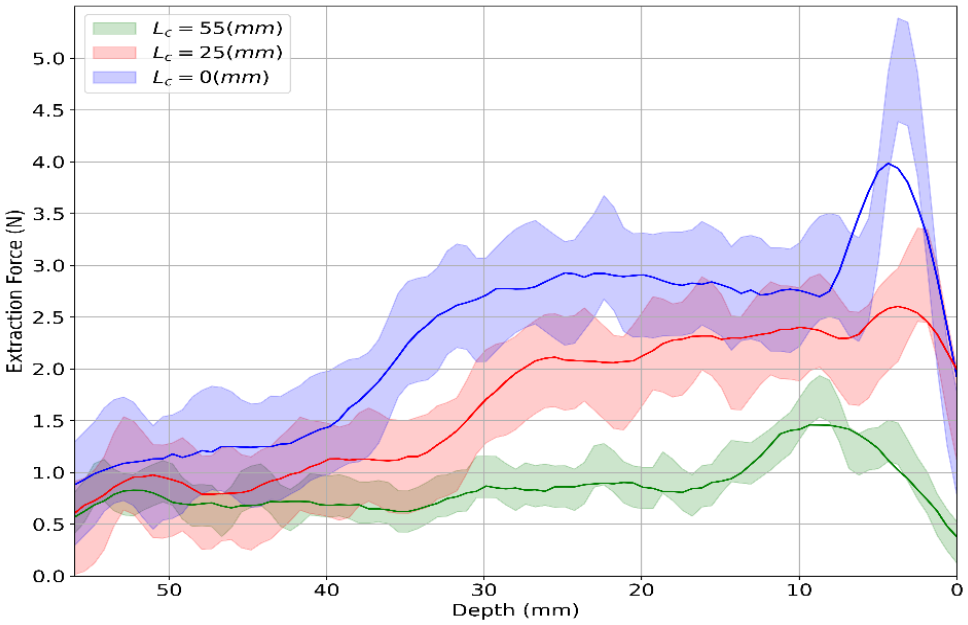
$L_c = 55(mm)$
$L_c = 25(mm)$
$L_c = 0(mm)$
Extraction Force (N)
Depth (mm)
0.0
0.5
1.0
1.5
2.0
2.5
3.0
3.5
4.0
4.5
5.0
50
40
30
20
10
0

c)

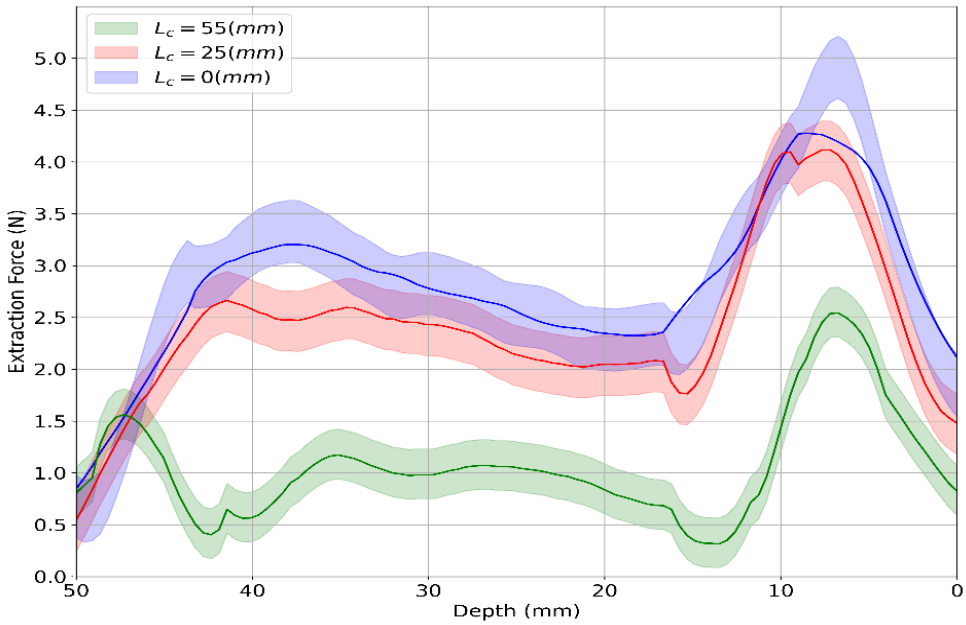

Figure 5.1 Extraction force curves based on compliance centre locations in dual peg-hole with a) r= 5.7 mm, b) r= 6 mm, and c) r=6.5 mm

Figure 5.2 presents a boxplot comparing the distribution of measured extraction forces for three different compliance centre locations (L_C=55 mm, 25 mm, and 0 mm). Each box depicts the interquartile range (the distance between the first and third quartiles), while the horizontal line within the box represents the median. The whiskers indicate the minimum and maximum observed values, and the triangular markers denote the mean extraction force. This representation highlights both the central tendency (median and mean) and the variability (range and interquartile spread) of the extraction force for each compliance centre location.

a)

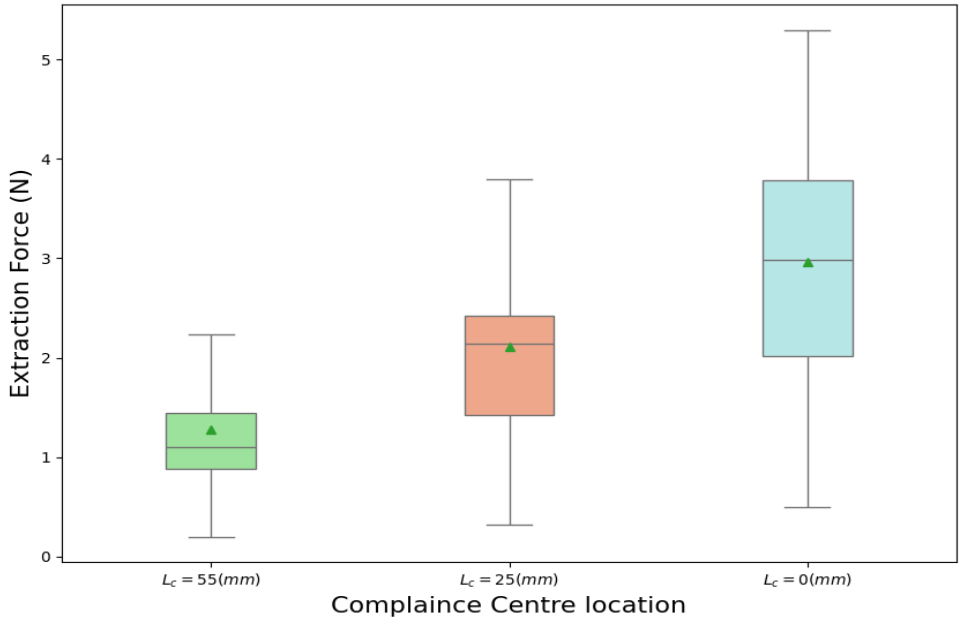
Extraction Force (N)
0
1
2
3
4
5
$L_c = 55(mm)$
$L_c = 25(mm)$
$L_c = 0(mm)$
Complaince Centre location

b)

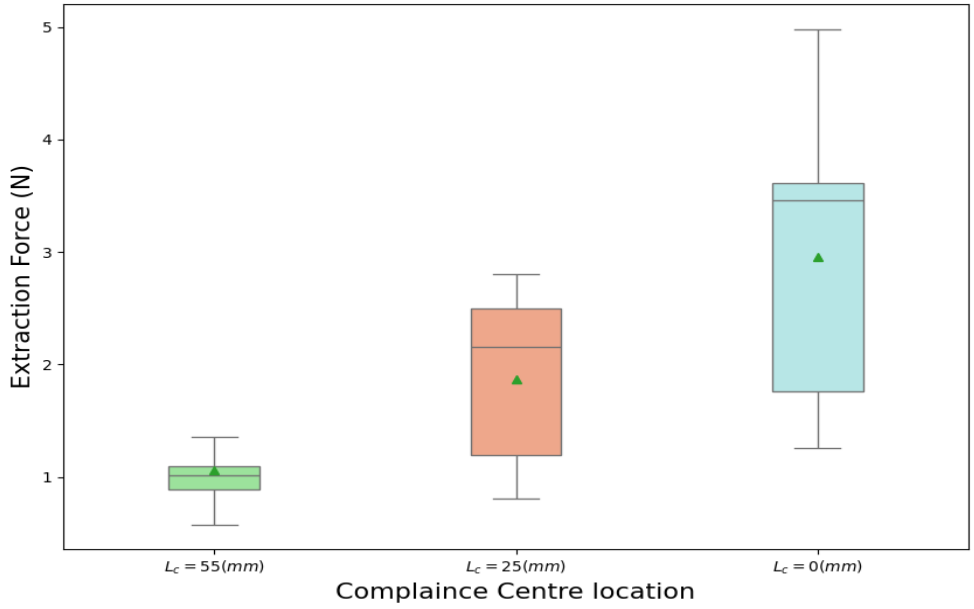
Extraction Force (N)
1
2
3
4
5
$L_c = 55(mm)$
$L_c = 25(mm)$
$L_c = 0(mm)$
Complaince Centre location

c)

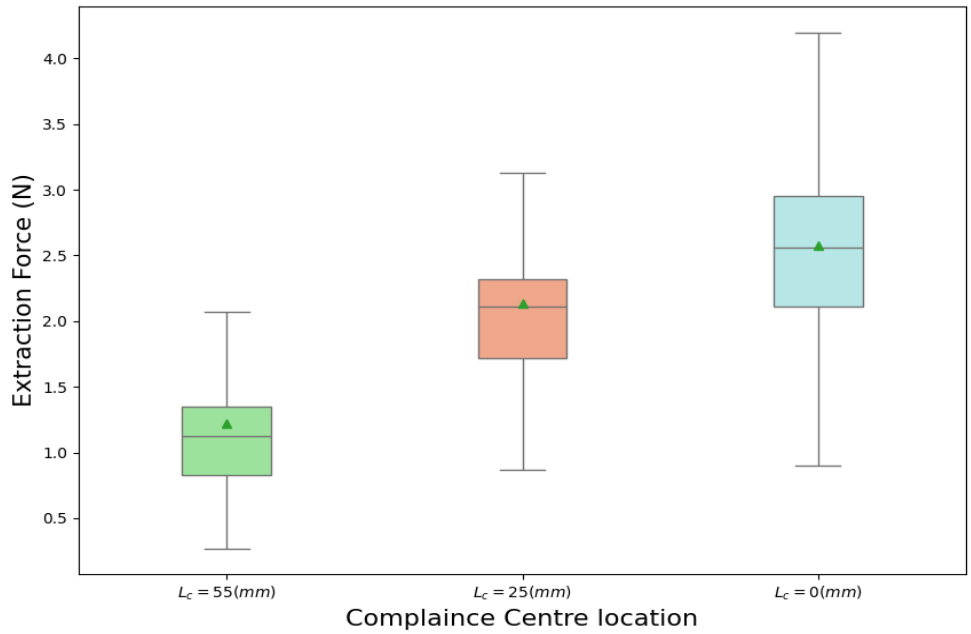

Figure 5.2 Comparison of the extraction force in dual peg-hole based on compliance centre locations with a) r= 5.7 mm, b) r= 6 mm, and c) r=6.5 mm.

The third chapter of the thesis addresses rectangular peg dislodgment from a hole, invoking geometric and quasistatic force analyses to identify possible contact states at 26 in that setting. By highlighting this intrinsic complexity within the setting of rectangular peg-hole disassembly, some new views concerning jamming phenomena will come into consideration. This work investigates the influence of compliance centre location, initial errors in lateral displacement and angular orientation, and manipulator stiffness on the disassembly process and identifies these factors as very important in optimising effective disassembly. It also presents results indicating that locating the ACC (Active Compliance Centre) at the end of the peg greatly reduces the magnitude of extraction forces compared to other positions along the peg. This finding suggests a more efficient disassembly strategy for robotic systems. In real-world experiments with a 6-DOF compliant manipulator, KUKA LBR, this setup achieved a 77.1% reduction in maximum extraction force relative to the top of the peg and a 55.6% reduction with respect to the centre of the peg, suggesting

that robots with lower payload capacities can be put into effective use for disassembly tasks as long as the appropriate ACC strategy is applied.

The theoretical contribution to disassembly processes makes this research an important element in the remanufacturing industry. While focusing on a rectangular peg-hole system, one of the most elementary cases of a disassembly problem, the work provides the basis upon which more complicated geometries would be addressed, like irregular shapes and multi-peg-hole systems. The addition of adhesive forces to this model is further work that could be done to extend these findings to recycling and remanufacturing processes, where adhesive forces are commonly found. Further research might involve the development of variable stiffness systems whose stiffness varies dynamically during the disassembly, potentially enabling more efficient and adaptable disassembly processes.

Figure 5.3 illustrates the outcomes obtained from investigating the influence of the location of the compliance centre on extraction forces across various depths for three samples with different dimensions. Each solid curve represents the average of six repeated measurements (18 total experiments, with six repetitions per compliance centre location). The shaded regions around each curve denote the range of observed values across all repetitions, highlighting the variability in the experimental data. As the compliance centre moves away from the end of the rectangle-peg, the two-contact region grows, while the orange and green curves show narrower peaks, indicating a smaller two-contact region (as discussed in section 3.4.2).

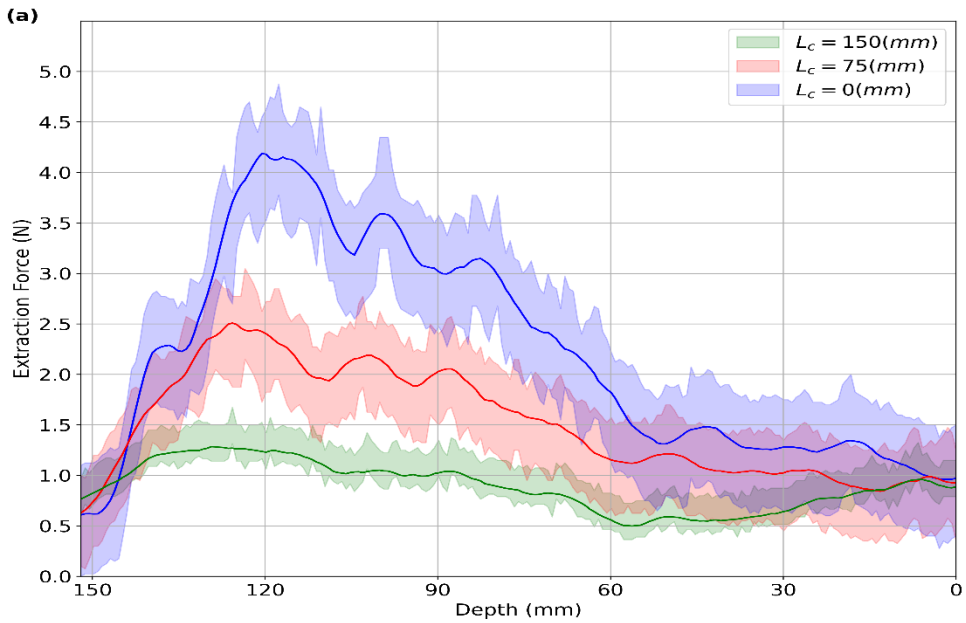
(a)
$L_c = 150(mm)$
$L_c = 75(mm)$
$L_c = 0(mm)$
Extraction Force (N)
0.0
0.5
1.0
1.5
2.0
2.5
3.0
3.5
4.0
4.5
5.0
150
120
90
60
30
0
Depth (mm)

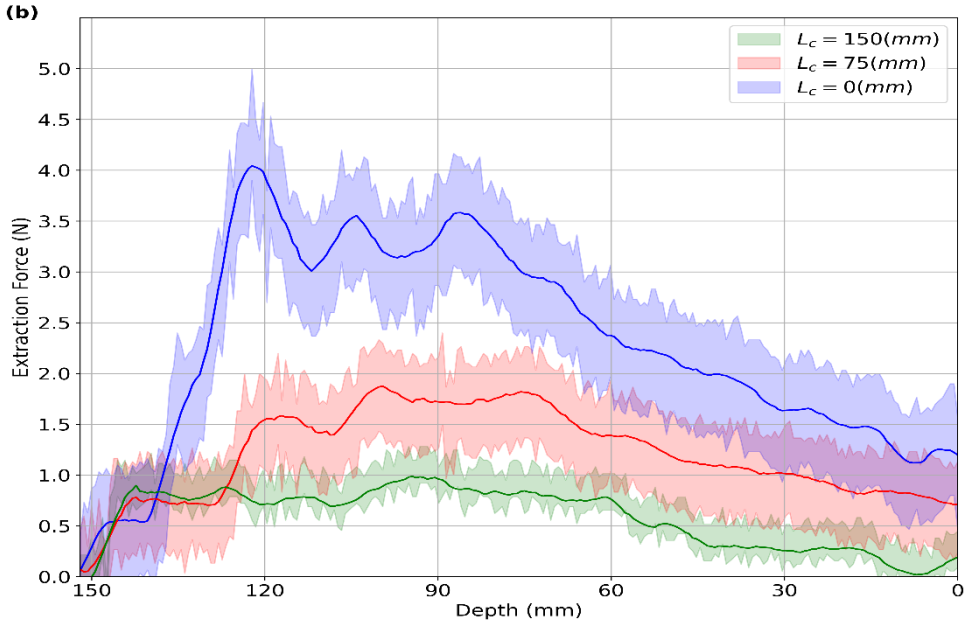
(b)
$L_c = 150(mm)$
$L_c = 75(mm)$
$L_c = 0(mm)$
Extraction Force (N)
0.0
0.5
1.0
1.5
2.0
2.5
3.0
3.5
4.0
4.5
5.0
150
120
90
60
30
0
Depth (mm)

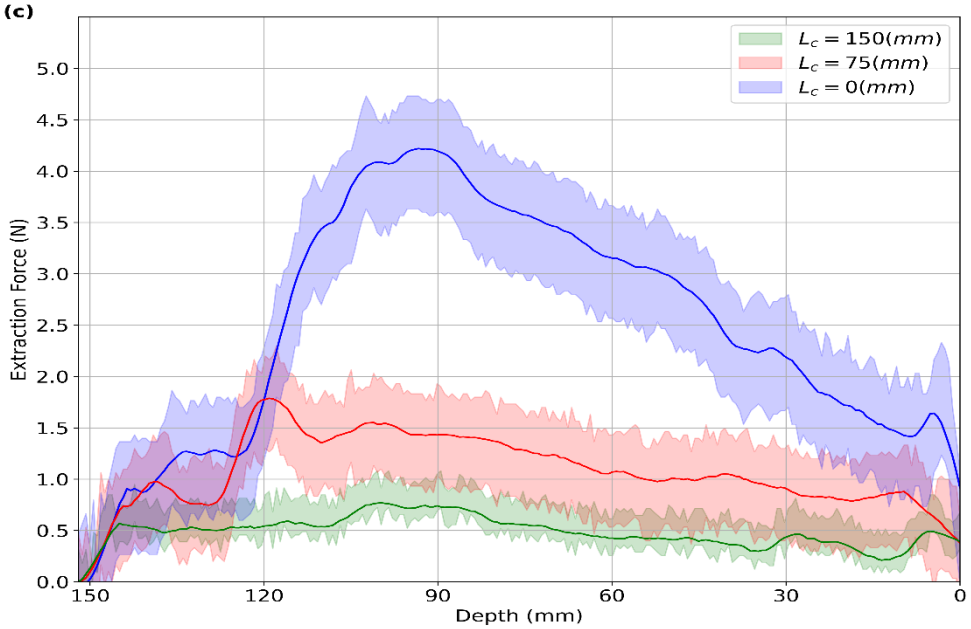

*Figure 5.3 Extraction force curves based on compliance centre locations in the rectangle peg-hole with a) w'*v'= 59.5*39.5 mm, b) w'*v'= 60*40 mm, and c) w'*v'=60.5*40.5 mm*

Figure 5.4 presents a boxplot comparing the distribution of measured extraction forces in the rectangle peg-hole for three different compliance centre locations (L_C =150 mm, 75 mm, and 0 mm). Each box depicts the interquartile range (the distance between the first and third quartiles), while the horizontal line within the box represents the median. The whiskers indicate the minimum and maximum observed values, and the triangular markers denote the mean extraction force. This visualisation effectively demonstrates both the central tendency (through median and mean) and the variability (via the range and interquartile spread) in extraction force measurements for the different compliance centre locations.

We acknowledge that the current experimental setup does not allow for the direct measurement of the exact number and locations of contact points between the peg and the hole. While the simulations provided detailed predictions of various contact states, the practical tests do not capture all the complexities of the peg–hole interaction, particularly regarding the precise number and locations of contact points. However, both the simulation

and experimental results consistently indicate that positioning the compliance centre at the identified optimum location yields the best performance in terms of reducing extraction forces and mitigating jamming. This convergence of results reinforces the validity of the compliance centre location as a critical factor in enhancing disassembly efficiency.

a)

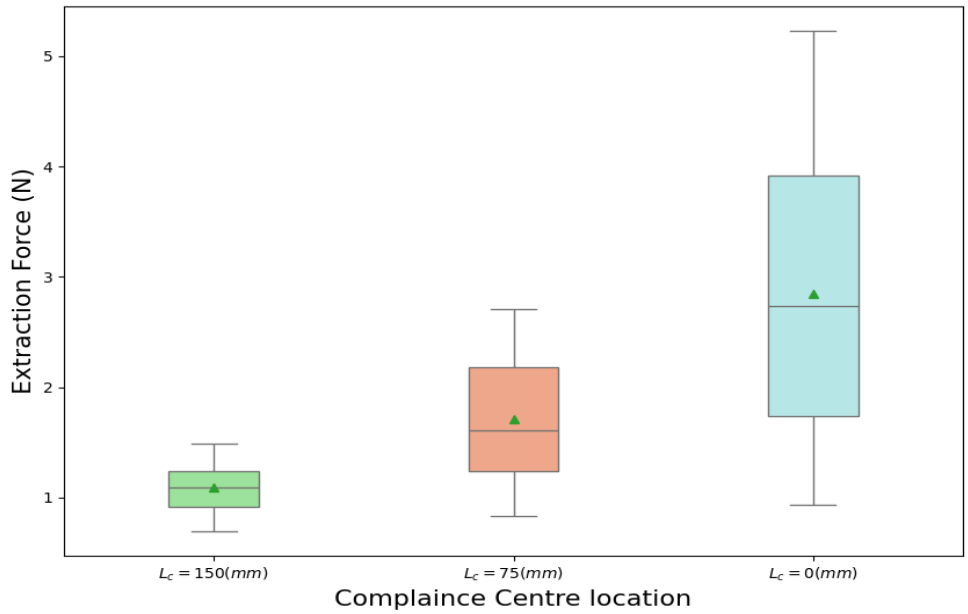

b)

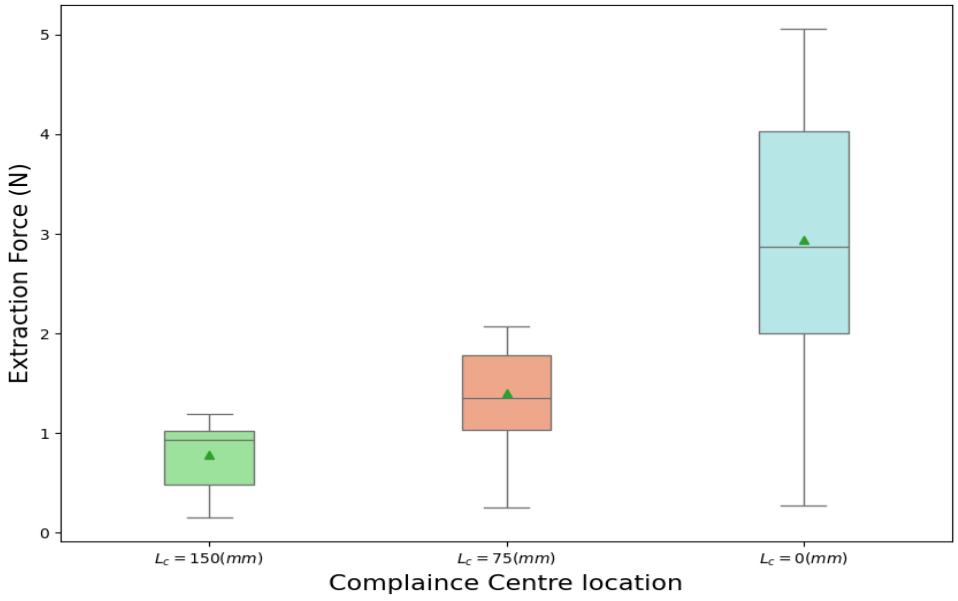

c)

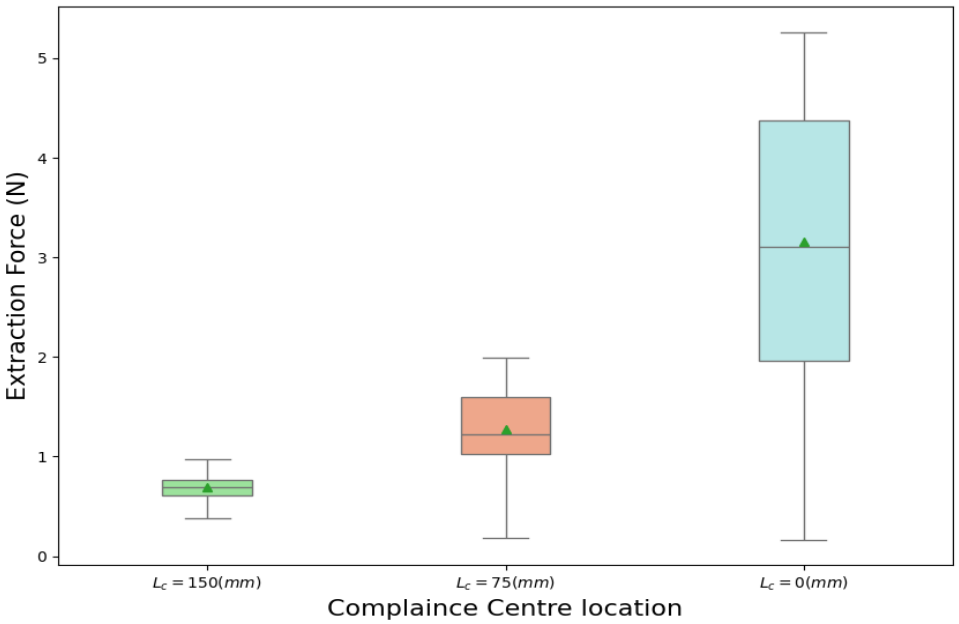

*Figure 5.4 Comparison of the extraction force in rectangle peg-hole based on compliance centre locations with a) w'*v'= 59.5*39.5 mm, b) w'*v'= 60*40 mm, and c) w'*v'=60.5*40.5 mm*

The fourth chapter introduces the development of a compliance strategy integrated with reinforcement learning to improve disassembly efficiency, flexibility, and adaptability. The innovative approach significantly reduces the forces needed for disassembly, which is highly accurate and adaptive to dynamic environments using the Soft Actor-Critic algorithm in PyBullet's simulated environment. The ability of the robot to modulate stiffness in response to external forces enables adaptive disassembly manoeuvres, which makes it more robust in uncertain and changing conditions. Experimental results confirm that by integrating reinforcement learning and compliance strategies, the extraction forces were reduced by 29.6% compared to the method described in chapters 2 & 3, which confirms the potential of this combined approach for improving disassembly tasks. By dynamically adjusting key parameters, such as stiffness coefficients and force thresholds, the robot can effectively navigate uncertainties and variations in the environment while meeting task objectives.

5.2 Conclusion

The findings of this research significantly advance our understanding of robotic disassembly by combining theoretical analysis with experimental validation. The work provides a deeper insight into the mechanics of disassembly in both dual-peg and rectangular peg-hole systems by systematically identifying the various contact states and associated jamming conditions. This comprehensive understanding has enabled the development of advanced compliance strategies, where the critical positioning of the Active Compliance Centre (ACC) plays a pivotal role in reducing disassembly forces. The experiments demonstrate that such strategies not only mitigate jamming but also make disassembly more reliable and efficient.

Moreover, the integration of reinforcement learning with compliance control has proven to be an innovative approach, allowing the robotic system to adapt dynamically to varying conditions. By learning optimal disassembly motions and adjusting its stiffness in response to external forces, the robot achieves a significant reduction in extraction force compared to the method described in chapters 2 & 3. Overall, these contributions establish a strong foundation for the development of more efficient, robust, and adaptable robotic systems for remanufacturing and recycling applications.

5.3 Future Work

Future research should broaden the scope of this study by extending the developed methodologies to more complex and varied disassembly scenarios. One promising direction is to investigate the applicability of the current models to irregular shapes and multi-peg-hole systems, thereby generalising the findings beyond the elementary cases examined here. Additionally, future work should incorporate adhesive forces into the analytical framework to

better simulate realistic conditions encountered in recycling and remanufacturing processes, where such forces can significantly influence disassembly dynamics. Another exciting avenue is the development of variable stiffness systems that can dynamically adjust their mechanical properties during the disassembly process, potentially leading to even greater efficiency and adaptability in robotic operations. Moreover, future work should explore techniques for directly observing and quantifying the contact points during experiments. Possible approaches include integrating a transparent window into the experimental fixture, employing high-speed imaging, or using advanced force/torque sensors. These methods could provide valuable insights into the exact nature and location of the contact points, enabling a more accurate validation and refinement of the simulation models. Finally, further validation through extensive laboratory experiments in diverse real-world settings will be crucial to refining the reinforcement learning algorithms and compliance strategies, ensuring their robustness and broad applicability across a range of disassembly tasks.

5.4 References

[1] F. Lan, M. Castellani, D. Truong Pham, and Y. Wang, “On the correctness of using two-dimensional representations in the analysis of cylindrical peg–hole insertion and withdrawal,” *R Soc Open Sci*, vol. 10, no. 8, Aug. 2023, doi: 10.1098/rsos.221021.